LOCAL EFFECTS IN RECTANGULAR HOLLOW SECTION JOINTS

by

© PIOTR KAZIMIERZ OSTROWSKI M.Sc., M.Eng.

A Thesis
Submitted to the School of Graduate Studies
in Partial Fulfilment of the Requirements
for the degree
Doctor of Philosophy

McMaster University
November 1988

LOCAL EFFECTS IN RECTANGULAR HOLLOW SECTION JOINTS

DOCTOR OF PHILOSPHY

(Civil Engineering
and Engineering Mechanics)

McMASTER UNIVERSITY

Hamilton, Ontario

TITLE: **LOCAL EFFECTS IN RECTANGULAR HOLLOW SECTION JOINTS**

AUTHOR: Piotr Kazimierz Ostrowski
(M.Sc. - Technical University of Wroclaw, Poland)
(M.Eng. - McMaster University, Hamilton, Canada)

SUPERVISORS: Dr. R.M.Korol and Dr. F.A.Mirza

NUMBER OF PAGES: xx, 268

ABSTRACT

LOCAL EFFECTS IN RECTANGULAR HOLLOW SECTION JOINTS

A theoretical and experimental study of RHS joints is presented, with particular attention being devoted to RHS gap K joints due to their popularity and complex behaviour.

The theoretical aspects include the derivation of a nine-node general shell element with six degrees of freedom per node, capable of modelling multiple intersections between plates and shells. The material behaviour is described using the Von Mises yield criterion and the Prandtl-Reuss flow equations. The plasticity algorithm allows a sampling point to yield within a load increment and traces both the elastic and inelastic stress increments accordingly. Refined numerical analyses allow for an accurate tracing of the yield surface in every iteration. Each sampling point within an element is capable of carrying individually specified material properties. This makes it possible to account for a strain-hardened zone near the corners of an RHS or for the material properties of the weldment.

The experimental investigation included 26 isolated RHS joints which were subconfigurations of a gap K joint. The testing program made it feasible to assess the effects of the angle of branch inclination and the flexibility of the base. Numerous strain gauges and rosettes mounted on the branch walls near the weldment, provided load-strain characteristics at the toe, the heel and the sidewall for the entire history of loading. The effectiveness of the heel area and the type of failure mode were found to depend strongly on the angle of branch inclination. The rigid or flexible base conditions affected the stress distribution in the branch walls and the direction of the principal axes.

The developed finite element model was used in the numerical simulation of the behaviour of RHS joints. All the joint configurations tested were subjects of the numerical simulation in three independent stages which allowed for the model to be thoroughly verified. A very good agreement between the experimental and numerical results was achieved in all stages. The numerical analysis provided complementary results towards better understanding of the behaviour of tested joints. The same numerical model was utilized in a parametric study of a gap K joint which included the effects of : the angle of branch inclination, the width ratio, the gap size and the chord width to thickness ratio. The results are presented by means of stresses in the branch member walls and the local deflections of the chord connecting face. A number of new observations are made which result in recommendations for the design of RHS joints.

ACKNOWLEDGEMENTS

The author would like to thank his research directors Dr. R.M. Korol and Dr. F.A. Mirza, for their guidance and advice during the course of this study .

Participation in the experimental program was possible thanks to Dr. J.A. Packer from Department of Civil Engineering , University of Toronto, who also devoted his time and shared his expertise in the area of design of Hollow Section Joints.

The author would like to thank the members of his Supervisory Committee Dr. G.Æ.Oravas and Dr R.Sowerby for their valuable advice.

Thanks are also due to Mr. G.S. Frater, M.A.Sc. student at the University of Toronto at the time of the experimental project, and to the technical support staff in the Structures Laboratories at the University of Toronto for making my participation in the experiments a most enjoyable experience.

Help from my collegues, Ray Luft and Brad Koziey, with writing a grid generator for stage 1 of numerical work and for plotting of some of the graphs is very much appreciated.

The author expresses his deepest gratitude to Krystyna and Alexandra, who filled his private life with meaning.

To my Parents Janusz and Ewa

TABLE OF CONTENTS

PAGE

Abstract iii

Acknowledgements v

Table of Contents vii

List of Figures xi

List of Tables xx

List of Symbols xxi

CHAPTER 1 INTRODUCTION 1

- 1.1 General 1
- 1.2 Objective and Scope 3
- 1.3 Originality of the Research 5
- 1.4 Overview of the Study 7
- 1.5 Literature Review 8
  - 1.5.1 Experimental Investigations 9
  - 1.5.2 Analytical and Numerical Studies 13

CHAPTER 2 BEHAVIOUR OF RECTANGULAR HOLLOW SECTION JOINTS 24

- 2.1 Introduction 24
- 2.2 Joint Configurations 26
  - 2.2.1 Material and Section Size Restrictions 27
  - 2.2.2 K and N Joints 28
- 2.3 Gap K Joint 29

TABLE OF CONTENTS (continued)

PAGE

2.4 Joint Strength 30

2.4.1 Modes of Failure 31

2.4.2 Effective Width 32

2.4.3 Limits for Gap Size 34

2.5 Serviceability Limit State of Joint Deformation 36

2.5.1 Local Joint Behaviour 38

2.5.2 Redistribution of Bending Moments 42

CHAPTER 3 FINITE ELEMENT ANALYSIS 52

3.1 Description of the Problem 52

3.2 Selection of the Element 53

3.3 Modelling of Shell Intersections 55

3.4 Shell Element 58

3.4.1 Geometry 59

3.4.2 Displacement Field 60

3.4.3 Displacement Derivatives 61

3.5 Derivation of the Element Matrices 64

3.5.1 Strains and Stresses 64

3.5.2 Stiffness Matrix 66

3.6 Elasto-Plastic Problem 67

3.6.1 Governing Equations 67

3.6.2 Matrix Formulation 70

3.6.3 Numerical Algorithm 71

TABLE OF CONTENTS (continued)

PAGE

3.7 Numerical Procedure 72

3.7.1 Choice of Solution Method 72

3.7.2 Numerical Integration 73

3.7.3 Convergence Criteria 73

3.8 Verification Examples 75

CHAPTER 4 EXPERIMENTAL PROGRAM 87

4.1 Introduction 87

4.2 General Description 88

4.3 Instrumentation 89

4.4 Strain Measurements 90

4.5 Results for Rigid and Flexible Bases 97

4.6 LVDT Measurements 99

4.7 Material Properties 99

4.8 Yielding Patterns 100

4.9 Summary of Experimental Results 102

CHAPTER 5 NUMERICAL SIMULATION OF RECTANGULAR HOLLOW SECTION JOINTS 144

5.1 Introduction 144

5.2 Display of Numerical Results 145

5.3 Stage 1: Two RHS Sections in Tension Separated by a Plate 147

5.4 Stage 2: Two RHS Sections Welded to RHS Chord at 90° 151

5.5 Stage 3: Two RHS Sections Welded to RHS Chord at Angles 60°, 45° and 30° 153

TABLE OF CONTENTS (continued)

PAGE

5.6 Summary of Numerical Results from Stages 1,2,3 165

CHAPTER 6 PARAMETRIC STUDY FOR GAP K-JOINT 175

6.1 Introduction 175

6.2 Selected Parameters 175

6.3 Effect of Angle of Inclination θ 178

6.4 Effect of Width Ratio β 181

6.5 Effect of Gap Size g 184

6.6 Effect of Chord Width to Thickness Ratio b_o / t_o 185

6.7 P-Delta Curves 186

6.8 Conclusions from Parametric Study 188

6.8.1 Distribution of Stresses in Branch Walls 188

6.8.2 Local Deflections 190

6.9 Design Implications 191

CHAPTER 7 SUMMARY AND CONCLUSIONS 230

7.1 Summary 230

7.2 Conclusions 232

REFERENCES 236

APPENDIX A SHAPE FUNCTIONS FOR 9 NODE SHELL ELEMENT 242

APPENDIX B FORMATION OF THE ORTHOGONAL BASIS 243

APPENDIX C TRANSFORMATION MATRICES 244

APPENDIX D EXPERIMENTAL RESULTS FOR SPECIMENS 17 AND 19 245

APPENDIX E RESULTS OF A PARAMETRIC STUDY 255

LIST OF FIGURES

FIGURE	DESCRIPTION	PAGE
1.1	Warren Truss and Gap K Joint	19
1.2	Correspondence Between Experimental Phases 1-3 and Joints used in Planar Trusses	20
2.1	Joint Configurations	44
2.2	Gap and Overlap Joints	44
2.3	Geometry of Gap K Joint	45
2.4	Plan View of Chord Connecting Face	46
2.5	Joint Strength at Different Load Levels	46
2.6	Effective Width for Gap K Joint	47
2.7	Current Limits for Gap Size	47
2.8	Measurement of Joint Deformation according to Wardenier et al. (1978)	48
2.9	Load vs. Deformation Graph for RHS T and K Joints	48
2.10	Load vs. Deflection Curves for a Frame at Different Width Ratios	49
3.1	Possible Methods of Discretization for Intersections	77
3.2	Weld geometry	78
3.3	Shell Element	79
3.4	Plasticity Algorithm	80
3.5	Incremental Stresses in Elasto-Plastic Space	81

LIST OF FIGURES (continued)

FIGURE	DESCRIPTION	PAGE
3.6	Macro Flowchart for Computer Program	82
3.7	Distribution of Sampling Points in Corner Zone	83
3.8	Distribution of Sampling Points in Weld Zone	83
3.9	Load-Deflection Curves for Elasto-Plastic Plate	84
3.10	Plate-to-RHS Verification Exampl	85
3.11	Load-Deflection Curves for Plate-to-RHS Connection	86
4.1	General View of a Specimen Tested	105
4.2	Summary of Experimental Program (after Frater 1986)	106
4.3	Strain Gauges at Toe of Specimen 12	107
4.4	Rosettes on Sidewall of Specimen 15	107
4.5	Specimen 12	108
4.6	Load vs. Strain Graph at Toe of Specimen 12	109
4.7	Load vs. Strain Graph at Heel of Specimen 12	109
4.8	Load vs. Major Principal Strain Graph for Rosettes 1,2,3 in Test 12	110
4.9	Load vs. Minor Principal Strain Graph for Rosettes 1,2,3 in Test 12	110
4.10	Specimen 14	111
4.11	Load vs. Strain Graph at Toe of Specimen 14	112
4.12	Load vs. Strain Graph at Heel of Specimen 14	112
4.13	Load vs. Major Principal Strain Graph for Rosettes 1,2,3 in Test 14	113

LIST OF FIGURES (continued)

FIGURE	DESCRIPTION	PAGE
4.14	Load vs. Minor Principal Strain Graph for Rosettes 1,2,3 in Test 14	113
4.15	Specimen 18	114
4.16	Load vs. Strain Graph at Toe of Specimen 18	115
4.17	Load vs. Strain Graph at Heel of Specimen 18	115
4.18	Load vs. Major Principal Strain Graph for Rosettes 1,2,3 in Test 18	116
4.19	Load vs. Minor Principal Strain Graph for Rosettes 1,2,3 in Test 18	116
4.20	Specimen 25	117
4.21	Load vs. Strain Graph at Toe of Specimen 25	118
4.22	Load vs. Strain Graph at Heel of Specimen 25	118
4.23	Load vs. Major Principal Strain Graph for Rosettes 1,2,3 in Test 25	119
4.24	Load vs. Minor Principal Strain Graph for Rosettes 1,2,3 in Test 25	119
4.25	Specimen 26	120
4.26	Load vs. Strain Graph at Toe of Specimen 26	121
4.27	Load vs. Strain Graph at Heel of Specimen 26	121
4.28	Load vs. Major Principal Strain Graph for Rosettes 1,2 in Test 26	122

LIST OF FIGURES (continued)

FIGURE __ DESCRIPTION PAGE

4.29 Load vs. Minor Principal Strain Graph for Rosettes 1,2 in Test 26 122
4.30 Directions of Principal Axes of Strain and Magnitudes of Strains near Failure: a- Test 12 (θ = 60°), b- Test 14 (θ = 30°) 123
4.31 Failure Mode in Test 10 124
4.32 Failure Mode in Test 13 125
4.33 Directions of Principal Axes of Strain and Magnitudes of Strains near Failure in Test 18 (θ = 90°) 126
4.34 Directions of Principal Axes of Strain and Magnitudes of Strains near Failure: a- Test 25 (θ = 60°), b- Test 26 (θ = 30°) 127
4.35 Failure Mode in Test 25 128
4.36 Failure Mode in Test 26 129
4.37 Comparison of Strain Values between Rigid Base Conditions (Test 12) and Flexible Base Conditions (Test 25) for Toe and Heel Locations (θ = 60°) 130
4.38 Comparison of Strain Values between Rigid Base Conditions (Test 14) and Flexible Base Conditions (Test 26) for Toe and Heel Locations (θ = 30°) 131
4.39 Comparison of Strain Values at Heel Location from Phases 3A, 3B and 3C 132

LIST OF FIGURES (continued)

FIGURE	DESCRIPTION	PAGE
4.40	Yielding Pattern near Failure in Test 18	133
4.41	Yielding Pattern near Failure in Test 25	134
4.42	Yielding Pattern near Failure in Test 26	135
5.1	Comparison of Experimental and Numerical Programs	158
5.2	Locations of Toe and Heel for Stages 1-4	159
5.3	Convention for Display of Stresses	160
5.4	Finite Element Grid for Stage 1	161
5.5	P - Delta Curves for Stage 1 :a- Stage 1A, b- Stage 1B, c- Stage 1C,d- Stage 1D, e- First Yield and Section for Various Angles θ, f- Simulated Joint	162
5.6	Verification Example for Stage 1	163
5.7	Display of Perpendicular Stresses in Branch Walls for Stage 1	164
5.8	Display of Tangential Stresses in Branch Walls for Stage 1	165
5.9	Display of Effective Stresses in Branch Walls for Stage 1	166
5.10	Finite Element Grid for Stage 2	167
5.11	Verification Example for Stage 2	168
5.12	Display of Stresses in Branch Walls for Stage 2	169
5.13	Finite Element Grid for Stage 3	170
5.14	Verification Example for Stage 3	171
5.15	Display of Perpendicular Stresses in Branch Walls for Stage 3	172
5.16	Display of Tangential Stresses in Branch Walls for Stage 3	173

LIST OF FIGURES (continued)

FIGURE DESCRIPTION PAGE

5.17 Display of Effective Stresses in Branch Walls for Stage 3 174

6.1 Finite Element Grid for Gap K Joint 192

6.2 Summary of Parametric Study for Gap K Joints 193

6.3 List of Subsets of Parametric Study 194

6.4 Effect of Angle θ at $\beta=0.44$, Perpendicular Stresses. 195

6.5 Effect of Angle θ at $\beta=0.44$, Tangential Stresses. 196

6.6 Effect of Angle θ at $\beta=0.44$, Effective Stresses. 197

6.7 Effect of Angle θ at $\beta=0.63$, Perpendicular Stresses. 198

6.8 Effect of Angle θ at $\beta=0.63$, Tangential Stresses. 199

6.9 Effect of Angle θ at $\beta=0.63$, Effective Stresses. 200

6.10 Effect of Angle θ at $\beta=0.88$, Perpendicular Stresses. 201

6.11 Effect of Angle β at $\beta=0.88$, Tangential Stresses. 202

6.12 Effect of Angle θ at $\beta=0.88$, Effective Stresses. 203

6.13 Effect of Width Ratio β at $\theta=30°$, Perpendicular Stresses. 204

6.14 Effect of Width Ratio β at $\theta=30°$, Tangential Stresses. 205

6.15 Effect of Width Ratio β at $\theta=30°$, Effective Stresses. 206

6.16 Effect of Width Ratio β at $\theta=45°$, Perpendicular Stresses. 207

6.17 Effect of Width Ratio β at $\theta=45°$, Tangential Stresses. 208

6.18 Effect of Width Ratio β at $\theta=45°$, Effective Stresses. 209

6.19 Effect of Width Ratio β at $\theta=60°$, Perpendicular Stresses. 210

6.20 Effect of Width Ratio β at $\theta=60°$, Tangential Stresses. 211

6.21 Effect of Width Ratio β at $\theta=60°$, Effective Stresses. 212

LIST OF FIGURES (continued)

FIGURE	DESCRIPTION	PAGE
6.22	Effect of Gap Size, Perpendicular Stresses.	213
6.23	Effect of Gap Size, Tangential Stresses.	214
6.24	Effect of Gap Size, Effective Stresses.	215
6.25	Effect of b_o/t_o , Perpendicular Stresses.	216
6.26	Effect of b_o/t_o , Tangential Stresses.	217
6.27	Effect of b_o/t_o , Effective Stresses.	218
6.28	Effect of Angle θ at $\beta=0.44$, Load-Deflection Curves.	219
6.29	Effect of Angle θ at $\beta=0.63$, Load-Deflection Curves.	220
6.30	Effect of Angle θ at $\beta=0.88$, Load-Deflection Curves.	221
6.31	Effect of Width Ratio β at $\theta=30°$, Load-Deflection Curves.	222
6.32	Effect of Width Ratio β at $\theta=45°$, Load-Deflection Curves.	223
6.33	Effect of Width Ratio β at $\theta=60°$, Load-Deflection Curves.	224
6.34	Effect of Gap Size, Load-Deflection Curves.	225
6.35	Effect of b_o/t_o , Load-Deflection Curves.	226
D1	Specimen 17	247
D2	Load-Strain Graph for Gauges 1,2,3 of Specimen 17	248
D3	Load-Strain Graph for Gauges 7,8,9 of Specimen 17	248
D4	Load-Angle of Inclination Graph for Major Principal Direction in Rosettes 4,5,6	249
D5	Load-Strain Graph for Gauges 11,12,13 of Specimen 17	249
D6	Specimen 19	250

LIST OF FIGURES (continued)

FIGURE	DESCRIPTION	PAGE
D7	Load-Strain Graph at Heel of Specimen 19	251
D8	Load-Strain Graph at Toe of Specimen 19	251
D9	Load-Major Principal Strain Graph for Rosettes 1,2,3 in Test 19	252
D10	Load-Minor Principal Strain Graph for Rosettes 1,2,3 in Test 19	252
D11	Load-Angle of Inclination Graph for Major Principal Direction for Rosettes 1,2,3	253
D12	Load-Major Principal Strain Graph for Rosettes 4,5,6 in Test 19	253
D13	Load-Minor Principal Strain Graph for Rosettes 4,5,6 in Test 19	254
D14	Load-Angle of Inclination Graph for Major Principal Direction for Rosettes 4,5,6	254
E1	Stresses for Stage 4 Case 1	256
E2	Stresses for Stage 4 Case 2	257
E3	Stresses for Stage 4 Case 3	258
E4	Stresses for Stage 4 Case 4	259
E5	Stresses for Stage 4 Case 5	260
E6	Stresses for Stage 4 Case 6	261
E7	Stresses for Stage 4 Case 7	262
E8	Stresses for Stage 4 Case 8	263

LIST OF FIGURES (continued)

FIGURE	DESCRIPTION	PAGE
E9	Stresses for Stage 4 Case 9	264
E10	Stresses for Stage 4 Case 10	265
E11	Stresses for Stage 4 Case 11	266
E12	Stresses for Stage 4 Case 12	267
E13	Stresses for Stage 4 Case 13	268

LIST OF TABLES

TABLE	TITLE	PAGE
1.1	Tests on RHS K and N Joints	21
1.2	Girder Tests	23
2.1	Ultimate Strength Equations for RHS Gap K Joints (CIDECT 1986)	50
4.1	Summary of Test Results	136
4.2	Summary of Instrumentation for Specimens 10-12	137
4.3	Summary of Instrumentation for Specimens 13-15	138
4.4	Summary of Instrumentation for Specimens 16-19	139
4.5	Summary of Instrumentation for Specimens 21,22,24	140
4.6	Summary of Instrumentation for Specimens 20,23,25,26	141
4.7	Material Properties (after Frater 1986)	142
4.8A	Simplified Stress-Strain Curve	143
4.8B	Parameter Values for Simplified Stress Strain Curve	143
6.1	Joint Characteristics in Parametric Study	227
6.2	Summary of Results for Effects of θ and β	228
6.3	Joint Strength Compared with Serviceability Load	229

CHAPTER 1

INTRODUCTION

1.1 General

The enormous popularity of tubular sections in structural applications is a result of the recognition of their superior load-resisting properties in torsion, high radius of gyration and multi-axial symmetry of the cross section. Many practical features such as welding without gusset plates, good structural integrity during the construction stages, weight savings in comparison with conventional steel sections and the low cost of fire and corrosion protection make them very attractive to designers, project engineers and those responsible for the maintenance of structures. In many applications aesthetically pleasing appearance of tubular sections is a deciding factor in their selection by architects for such exposed structures as spatial frames, pedestrian bridges and roof trusses.

Hollow Structural Sections (HSS) made of steel do not present any major difficulty in member design, even under a complex external load. Thus far, the designer's concern has been mostly devoted to connections, which have been the subject of an ongoing international research effort for the last twenty years. Most of the research and analysis of hollow section joints in the past concentrated on the strength aspects, which were the most crucial from the practical point of view. Today, a general consensus exists in the area of the design strength equations for HSS joints. However, a need has arisen for further research directed towards the deformation aspects including local deflections of the chord connecting face and strain distribution around the joint. An in-depth knowledge of the joint deformation will allow one to define the serviceability state of localized deflections and also identify the critical regions with respect to excessive local deformations leading to cracking of the material. The optimized design of joints is possible only when the strength and deformation aspects are both properly taken into account in the design process.

Rectangular Hollow Sections (RHS) are preferred to **Circular Hollow Sections (CHS)** for most on-shore structures because they only require straight cuts which leads to savings in the end preparation costs. Among the RHS joints, there are gap or overlap joints with equal or unequal width of the branch and chord members. The RHS gap joints require the least amount of preparatory work due to single cuts at the ends of branch members and are therefore preferred in design and construction. The unequal width connections are associated with higher flexibility of the chord connecting face and present highly non-uniform stress distributions around the joint. Therefore, the present study focuses attention mainly on **RHS gap joints of unequal width**, between the branch and the chord members. However, many aspects of the joint analysis and design for the RHS gap joints of unequal width are directly related to other RHS joints.

For example, the effects of the angle of inclination for the branch , the base flexibility or the presence of the weld gap between the web members can also be interpreted for overlap joints where one bracing is welded to another instead of to the chord member (100% overlap).

1.2 Objective and Scope

The objective of the present study is to add to the understanding of the behaviour of RHS joints based on a combination of experimental and theoretical investigations. The methods employed are not considered mutually exclusive tools but rather one approach which draws inspiration from both sides in order to end up with a more complete picture of a joint's behaviour. The formulation of a theoretical model of a structural joint along with first hand exposure to its experimental performance added considerably to the reliability and credibility of the model with a direct impact on the quality of the results presented.

This research project is concerned with the local behaviour of RHS joints. The main emphasis is on quantitative assessment of such local effects as the joint localised deflections and the strain distribution in the walls of a branch member, as well as the qualitative description of the load transfer mechanism within a joint as a function of the angle of the branch inclination, rigidity of the base under the branch and the presence of the weld gap.

The local behaviour of RHS joints is analyzed through a series of **experimental** steps called **phases** and **numerical** steps called **stages**. The

RHS gap K joint was selected for a detailed study. It is one of the most complex planar joints. An example of a gap K joint and a Warren truss consisting of K joints are shown in Figure 1.1 .

The development of the finite element model of HSS joints involved: the derivation of an element which could be used for the modelling of shell intersections, the implementation of an accurate and efficient elasto-plastic algorithm and a proper interpretation of boundary conditions. The element used in the analysis originated from the Ahmad shell element which was modified to account for non-smooth transitions between the elements. The elasto-plastic problem was solved with the use of the Von Mises yield criterion and the Prandtl-Reuss flow equations. The numerical algorithm involved the tangential stiffness method and the use of the frontal solution technique. Particular attention was devoted to an adequate discretization of the joints and realistic distribution of material properties including the weldment and the corners of an RHS affected by strain hardening.

The purpose of the experimental program was to gather information about the joint behaviour in order to: obtain a realistic description of the strain distribution in the walls of the branch; assess the influence of the branch angle θ and the flexibility of the base under the branch; find the extent of the yielded regions at different stages of loading; and provide data for the verification of the numerical model. This was achieved by placing numerous strain gauges and rosettes on the branch member walls and Linearly Varying Displacement Transducers (LVDT's) in the vicinity of the weldment. The extent of the yielded regions at different stages of loading was assessed through visual inspection of the layer of whitewash which was peeling off with plastic deformation on the joint surface. The experimental program was divided into stages which are briefly illustrated in Figure 1.2 along with their geometrical relevance to the joints used in practice.

A general finite element model for HSS joints was used for the simulation of all the joint configurations included in the experimental program. The purpose was to validate the computer model in a variety of applications and supplement the limited experimental data with numerically generated strain and stress distributions. After the model was thoroughly validated, an RHS gap K joint became the subject of a parametric study which included the following effects: the angle of inclination between the chord and a branch θ, the width ratio between the branch and chord, $\beta = b_i/b_o$, the weld gap size g and the chord width to thickness ratio b_o / t_o. In all cases both the stresses in the branch member walls and the load vs. local deflection were analyzed and conclusions included practical recommendations for the design of RHS gap K joints.

1.3 Originality of the Research

The finite element model presented in this study is one of the first known approaches to a full three dimensional elasto-plastic modelling of RHS joints. The universality of the developed numerical model allows for modelling of a variety of structures such as plates, shells, folded plates and any combination of these. Either circular or rectangular hollow sections can be used in such a discretization of a structural joint.

The numerical analysis involved the derivation of a general shell element capable of modelling multiple shell intersections. An efficient numerical algorithm for elasto-plastic analysis includes such features as: the possibility of yielding at a sampling point within a load increment, possibility of elastic unloading and accurate tracing of the yielding surface.

Testing of the RHS joint sub-configurations allowed for isolation of the two major effects: an angle of inclination for the branch and a flexibility of the base under the bracing.

A close interaction between experimental and theoretical investigations, where all the joint configurations tested found their corresponding numerical model, proved to be an effective method for identifying any discrepancies between the theory and practice and validating the numerical model. A theoretical parametric study performed on an RHS gap K joint included the records of the stress distribution in the walls of the branch member and load vs. local deflection curves. The conclusions from the parametric study describe the effects of four major parameters. The stresses in the branch member walls are given in the directions parallel and perpendicular to the weldment. This has a direct implication on the assessment of additional bending moments at the end of the branch and on forces affecting the design of weldments. The deflections of the chord connecting face are used in the evaluation of the serviceability limit state of localised deflections.

The design recommendations presented at the end of this study uncover past misconceptions about the behaviour of RHS joints. It has been revealed that the effectiveness of the heel area in the branch member of a gap K joint depends on the angle θ. The same was found to be true for the location of stress concentrations in the branch near failure. A substantial difference exists in the directions of the major principal axes of strain for the rigid and flexible base conditions.

1.4 Overview of the Study

Chapter 1 presents a general introduction and a literature review which includes the experimental, analytical and numerical studies on the subject of RHS N- and K- joints.

Background information about the behaviour of RHS joints and a discussion of the joint strength and the joint deformation aspects is given in chapter 2. Particular attention is devoted to the gap K joint as this is the subsequent topic of the thesis.

The finite element model of HSS joints is presented in Chapter 3. It contains modelling of intersections, derivation of a general shell element, an elasto-plastic analysis and verification examples.

The description of the experimental program which includes instrumentation, strain measurements, a list of material properties and evaluation of the yielding patterns is presented in Chapter 4, along with evaluation of the yielding patterns is presented in Chapter 4, along with the relevant conclusions and a discussion of the experimental results.

The joint configurations tested are subsequently simulated numerically and the outcome is presented in Chapter 5. The verification of the model is carried out based on the strain distribution in the branch member walls. The complementary numerical results include the distribution of stresses in the branch near the weldment and load-localised deflection graphs.

A numerical parametric study for the gap K joint is carried out after a good correspondence between experimental results and the numerical simulation is established . Four different parameters are included : angle of inclination, width ratio, a gap size and a chord width to thickness ratio. Axial load in the bracing versus local deflection curves are also presented. Chapter 6, which contains details about the parametric study, is completed with conclusions and recommendations for the designer.

The whole study is brought to a conclusion with a summary of findings on the behaviour of Rectangular Hollow Section Joints.

1.5 Literature Review

A survey of the literature includes sub-sections of experimental investigations as well as analytical and numerical studies. An extensive review of experimental work on HSS joints and trusses has been summarized by Wardenier (1982) and CIDECT (1986). Here, only an outline of tests carried out on RHS gap K and N joints will be presented since these are of prime interest to the present study.

1.5.1 Experimental Investigations

A summary of tests carried out on isolated K and N joints with RHS chord and bracings is included in Table 1.1 . The tests on full scale trusses are listed in Table 1.2 .

Intensive experimental work on the behaviour of RHS joints started under the sponsorship of CIDECT (Comité International pour le Développement et l'Etude de la Construction Tubulaire) about twenty years ago. The first CIDECT-sponsored experimental program on RHS N and K joints was undertaken at Sheffield University by Eastwood et al. (1970) . It was concluded that the strength of the joint increases with the amount of overlap and higher values of the branch width to the chord width ratio.

A few years later CIDECT originated a major experimental program on HSS joints which was carried out in Great Britain, the Netherlands and Germany. The primary aim of the series of tests was the development of design recommendations for HSS joint strength equations. The CIDECT Program 5EC was carried out by the British Steel Corporation at Corby (Davie and Giddings 1971). The first part was an extension of work from Sheffield University and involved tests on joints mostly of N configuration. Next, a series of tests was performed on isolated joints (Markarian 1977) in connection with the full truss testing at the

University of Pisa. All the joints tested at Corby had the branch member angle equal to either 45° or 90°.

The most extensive testing of RHS joints was carried out at Delft University of Technology in the Netherlands (Wardenier et al. 1978) . Series A through L of these tests investigated effects such as: orientation of bracings, depth/width ratio for the chord, bracing angle, gap and overlap size, chord axial load, purlin load, material properties, relative thickness of bracing to chord walls, weld shape, member size and slenderness of the chord walls. Apart from one series of tests, the angle of inclination between bracings and a chord was either 45 or 90 degrees.

In 1968 at the Mannesmann Research Institute in Duisburg (West Germany) a number of RHS joints with different bracing angles and various types of joint reinforcement methods were tested (Mannesmann 1968). A research project at the University of Karlsruhe in West Germany focused on a few specific design aspects such as: high strength steel (see Table 1.1, CIDECT Program 5R) or high slenderness ratio for the chord walls in K joints (see Table 1.1, CIDECT Program 5T) . Finally, each of the research centres at Corby, Delft and Karlsruhe tested two RHS joints in order to check equivalence between the testing rigs (see Table 1.1, CIDECT Program 5S. Aside from CIDECT sponsored research there was a significant number of tests performed by Mostostal (Poland). This research project included RHS K joints. A total of 186 specimens of four different types were investigated: a gap joint, a lap joint and two joints with gusset plates between bracing members. The results of this experimental program are presented by Zycinski et al. (1982) who concluded that for gap K joints with large width ratio the increase in the gap size is associated with lower joint strength.

A few complete trusses were tested at the University of Nottingham (Dasgupta 1970), the University of Pisa (British Steel Corporation 1977a), the University of Delft (De Koning et al. 1979) and by Mostostal in Poland (Czechowski et al. 1984). A listing of test information on RHS girders is included in Table 1.2 . The main objective was to establish correspondence between tests on isolated joints and joints in girders, and hence to develop or verify design recommendations. Consequently, most girders tested consisted of joints already tested in isolation. The truss joints at Nottingham were similar to those tested in Sheffield. Eight panel trusses were loaded at three nodes on the top chord. The tests at Pisa (British Steel Corporation 1977a) included a series of eight N braced girders with RHS or CHS bracings. The joint configurations were similar to those tested at Corby (British Steel Corporation 1977b). One half of the girder had gapped joints and the other half had overlapped joints. The truss configuration was similar to those tested at Nottingham with the same pattern of loading. In Delft, four Warren trusses were tested. Both the bracings and the chord were made of square hollow sections. Three girders had the bracings inclined at 45° and in one girder the bracing angle was 30° . Joints on one side of the girder were gapped while on the other side they were overlapped. The loading was applied at the centre of the truss. Recently, eight trusses were tested by Mostostal in Poland

(Czechowski et al. 1984). Both gap and overlap joints were used (see Table 1.2). The magnitude of localised deflections was found to be much smaller than for equivalent joints tested in isolation. Also, the overall truss deflections were noticeably higher than calculated from a pin-connected truss model. The last reported tests on complete trusses were performed by Philiastides (1988) who investigated the behaviour of seven Warren trusses.

In summary, over four hundred RHS joints and about twenty five complete girders have been tested in experimental research programs around the world during the last twenty years. A great deal of experimental data has become available on the strength of HSS joints, thus allowing for the formulation of the design strength recommendations of RHS joints (IIW 1981, CIDECT 1986). However, the angle of inclination for the bracing members in most cases is either 45° or 90°. Very few joints had the bracings inclined at angles of 30° or 60°. There are reasons to believe that the joints with these angles are associated with high stress concentrations either at the heel or the toe (as will be documented later in this study). It seems that the joints of such configurations should be included in future experimental programs since the results may affect present design recommendations predominantly based on test results.

The main objective of previous test programs in the area of RHS joints was the determination of their strength. A limited number of tests involved the measurements of the joint deformation over the entire history of loading up to the joint failure. Joints tested for fatigue analysis did have comprehensive strain measurements but the history of loading was usually limited to an elastic range of the joint behaviour. Hence, there is a need for further testing which would include the local deformation measurements of the joint and truss deflections throughout the entire history of loading.

1.5.2 Analytical and Numerical Studies

A review will be presented of the major directions in which methods of analysis for tubular joints have evolved over the last several decades.

Classical Shell Analysis

Most of the early studies of tubular joints are based on classical thin shell equations for cylindrical shells such as those derived by Donnell (1934) or Flugge (1967). Donnell's approach was used by Hoff et al. (1953) for stress analysis for cylindrical vessels due to various attachments such as small pipes. In 1955 Bijlaard developed an equation similar to Donnell's which was utilized in stress and deflection analysis of tubular chords under radial load from attached pipes. Kellogg (1956) presented a method which allowed for the analysis of tubes under uniform circumferential line loads. A specific method applied to tubular joints was developed by Dundrova (1965) who imposed compatibility of displacements at an intersection of a chord and a bracing assuming that only axial forces from the bracings are transferred to the chord. This was the first attempt to model a branch directly. However, it did not include bending of the branch member walls.

The major disadvantages of methods which used the classical shell theory for analysis of tubular joints were exclusion of bending components in the branch and limitation of the scope to the elastic region. However, these methods provided an initial estimate of stress levels which could be used for joint design including the predictions of peak stresses for fatigue analysis (Hoff 1953, Bijlaard 1955).

Finite Difference Method

The finite difference method was a practical numerical method used for the analysis of tubular joints which did not require extensive computation. This method was used by Blockley (1967), Mee (1969) and Redwood (1965) who analyzed tubular joints utilizing the theory of thin plates. Korol and Mansour (1979) used the finite difference technique for the solution of a T joint represented by the chord connecting face resting on uncoupled springs which reflected the action of the chord webs. The use of a finite difference method was quite popular in the 1960s and early 1970s and was proven to give satisfactory results for simple joint geometries and the elastic range of analysis.

Yield Line Method

The yield line method was originally published by Johansen (1962) for concrete slabs. The method was first used in analysis of tubular joints by Jubb and Redwood (1966) for RHS T joints. Davies and Roper (1975) employed the method to the analysis of gap N joints and later improved the model to include shear action (Davies and Roper 1977). Patel et al. (1975) utilized the method for strength predictions in RHS T joints. The geometry of a K joint was considered by Mouty (1976) . Packer (1978) extended the yield line method for large deflection effects and also incorporated local yielding at the toes of branch members in the chord connecting face including strain hardening of the material. Currently the yield line method provides the joint strength expressions for RHS T,Y and X configurations in CIDECT (1986) Monograph No. 6.

The yield line method gained its popularity mainly due to its simplicity in the estimation of the ultimate joint strength. It provides an upper bound solution to the yield load. It is used mostly in the strength predictions for simple RHS joints which consist of an assembly of plates. The major drawbacks of the yield line method include its inability to describe the deformation characteristics or location of stress concentrations. In more rigorous analysis it should be used in conjunction with techniques such as the finite element method.

Finite Element Method

The finite element method emerged as a reliable tool for stress analysis of tubular joints in the late 1960s and early 1970s . One of the first analyses of tubular joints using the finite element method was presented by Greste (1970). His computer program was developed for CHS K joints with equal bracings and one plane of symmetry. Similar analyses of HSS joints were carried by Dasgupta (1970) and Roper (1974). Most recently, Mirza and Korol (1982) presented the finite element model of a T joint with two coupled springs along the edge of the chord top plate and included non linear material effects. Subsequently, Mirza et al. (1982)

extended the elasto-plastic model by including frame action of the webs and bottom flanges and applied the model to single and double chord T joints. The same model was utilized by Ostrowski (1984) who introduced geometrically nonlinear effects and analyzed gap K joints.

A number of researchers have used commercial finite element programs. Ogle and Kulak (1981) utilized SAPIV for the elastic analysis of RHS gap K joints. Strommen (1982) used ABAQUS for the nonlinear analysis of K joints with the bracings modeled by rigid inclusions in the chord connecting face. Irving (1982) employed LUSAS for the nonlinear analysis of CHS T joints.

Conclusions from Analytical and Numerical Studies of Tubular Joints

The analytical studies of tubular joints in the past were often restricted to the elastic range of loading, simple joint geometry and a membrane action in the branch members. The finite difference method was the first numerical technique which provided satisfactory results but was also limited to elastic analysis and simple joints. The nature of the yield line method does not allow for accurate joint deformation analysis and therefore cannot provide reliable stress concentration factors. However, it may be used for the estimation of the ultimate joint strength of simple geometry.

The behaviour of tubular joints at the ultimate load level necessitates the incorporation of material and geometrical nonlinearities in any model which is to be both accurate and reliable in the joint strength predictions. It is only possible with the use of high speed computers and modern numerical methods such as the finite element technique. This method is currently the only reliable approach which may be used for the analysis of tubular joints including deformation aspects and stress analysis regardless of the geometrical complexity. It is capable of providing a complete picture of the stress flow within a structure.

The use of a finite element method in analysis of RHS joints adds considerably to the understanding of joint behaviour especially when joint flexibility, strain or stress distributions are involved. It is often regarded as a complementary method to experimental investigations in order to cover a full range of the joint parameters. The cost of testing in many situations makes the numerical analysis a viable and more economical approach.

Design recommendations for tubular joints in the past have been based predominantly on the results of experiments. The theoretical joint strength predictions either were too complex or did not match the empirical values due to assumed failure modes different to those observed in testing. Consequently the analytical tools were primarily used as an estimation of the effect of certain parameters on the joint strength. Final expressions were then calibrated based on results obtained from experiments.

The availability of accurate numerical methods and the ever decreasing cost of computer analysis soon will make these methods the dominant tool in prediction of both the strength and deformation of tubular joints. However, the analyst must be familiar with the physical behaviour of joints in order to properly recognize different failure modes and simplify the output down to comprehensible data which can be used in design recommendations.

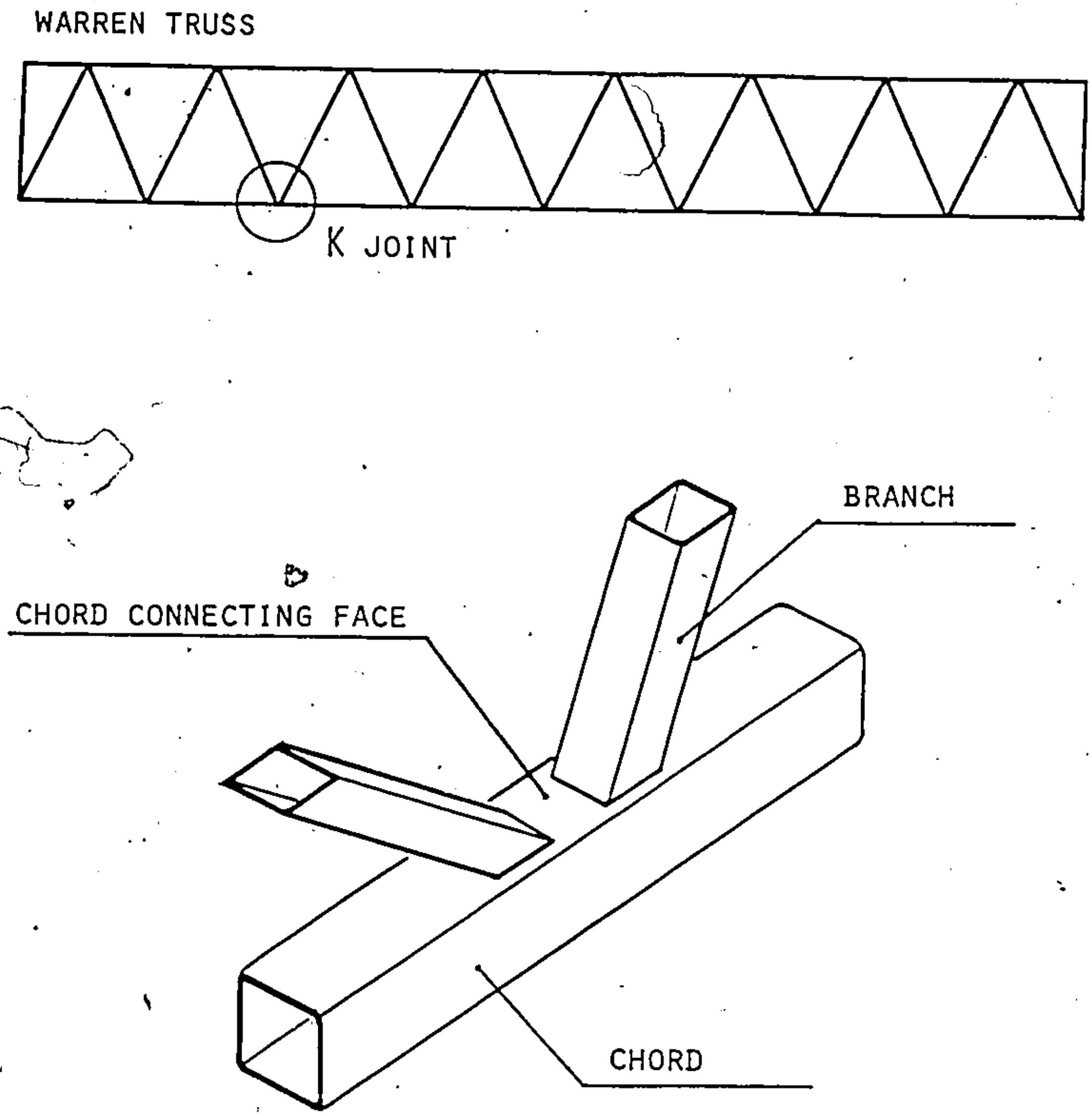

FIGURE 1.1 Warren Truss and Gap K Joint

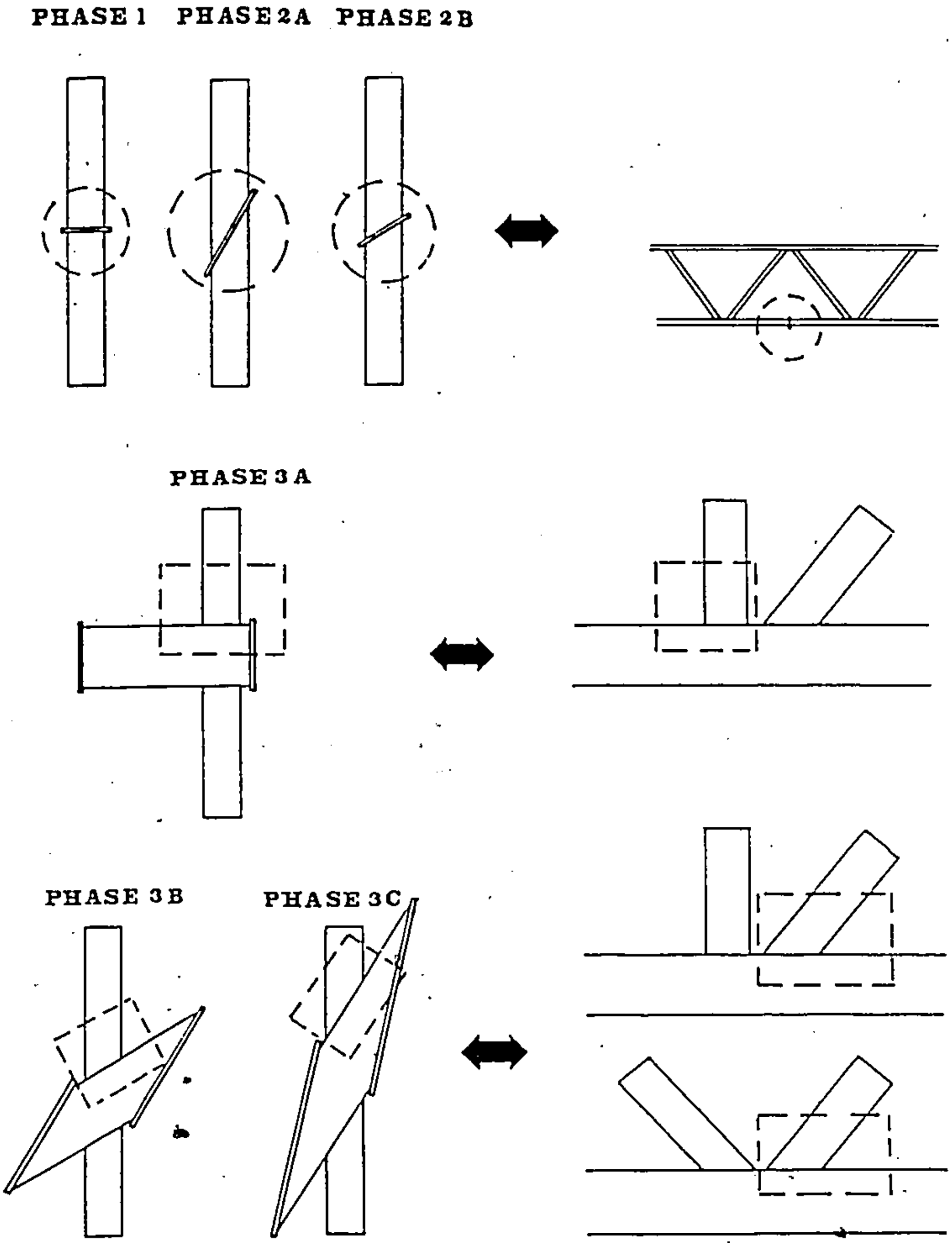

FIGURE 1.2 Correspondence Between Experimental Phases 1-3 and Joints used in Planar Trusses

TABLE 1.1 Tests on RHS K and N Joints (to be continued...)

TEST CENTRE	JOINT	No. of tests	CHORD SIZES	BRANCH SIZES	BRANCH ANGLE θ	b_o/t_o	WIDTH RATIO β	gap g
Univ. of Sheffield UK , Mee (1969) CIDECT Program 5A	N	18 gap 39 lap	203x203 ⇓ 89x89	127x127 ⇓ 38x38	90,45	14 ⇓ 55	0.43 ⇓ 0.73	nominal gap or 100% OL
BSC Tubes Division UK , Davie (1971) CIDECT Program 5EC	N	5 gap	127x127 ⇓ 254x254	101x101 ⇓ 203x203	90,45	14 ⇓ 40	0.8 ⇓ 0.875	nominal 25 mm gap
BSC Tubes Division. UK.Markarian(1977) CIDECT Program 5FC	N	6 gap 6 lap	152x152 ⇓ 254x254	50x50 ⇓ 152x152	90,45	24 ⇓ 40	0.33 ⇓ 0.67	nominal 25 mm gap
BSC Tubes Division UK,Yeomans(1977) CIDECT Program 7A	N K	2 lap 2 gap 4 lap 4 gap	100x100	40x40 and 60x60	90,45	25	0.4 ⇓ 0.6	50mm gap to 118% OL
Univ. of Delft Netherlands Wardenier (1978) CIDECT Program 5Q	N K	4 lap 28 gap 230 gap 11 lap	100x100 + 50x50 - 305x305	30 ⇓ 100	90,45 45,45	8.8 ⇓ 33.8	0.36 ⇓ 0.76	0.2b ⇓ 30% OL

TABLE 1.1 Tests on RHS K and N Joints (continued)

Mannesmann (1968) Germany		41 gap &lap	100x100 and 140x70	40x40,60x60 100x60,80x40	30,45, 60	25 ⇓ 17.5	0.4 ⇓ 1.0	various gap&lap cond.
Univ. of Karlsruhe Germany,Hohl(1974) CIDECT Program 5M	K	3 gap 9 lap	260x260	260x260 ⇓ 100x100	45,45	30	0.38 ⇓ 1.0	nominal gap or 50% OL
Univ. of Karlsruhe Germany,Mang(1978a) CIDECT Program 5R	K	4	120x120	90x90 ⇓ 120x120	45,45	13.3	13.3	
Univ. of Karlsruhe Germany,Mang(1978b) CIDECT Program 5T	K	4	420x420 and 330x330	160x160 and 140x140	45,45	38.1 ⇓ 52.4	0.38 ⇓ 0.67	
Univ. of Delft and Karlsruhe CIDECT Program 5S Wardenier (1976)	K	3 gap 3 lap	258x258	100x100	45,45	14.6 ⇓ 16.8	0.39	
Mostostal, Poland Zycinski et al. (1982)	4 types of K	182	100x100x4 100x100x5	70x70x3.6 70x70x5 40x40x3.2	45,60	20-25	0.4 0.7 1.0	gap 0.1-1.0 b 29-75%OL *
Univ. of Trondheim Strommen (1982)	K	13	120x200x6.3 200x200x6.3	80x80x5 - 120x120x5	45	19-32	0.4-1.0	gap 0.04 -0.44

* - inadequately documented and not used by CIDECT or IIW
OL - overlap

TABLE 1.2 Girder Tests

TEST CENTRE	Girder type	No. of tests	CHORD SIZES	BRANCH SIZES	BRANCH ANGLE θ	b_o/t_o	WIDTH RATIO β
University of Nottingham UK	N , loaded at centre & quarter points	3	89x89	34.1 dia - 60.3 dia	90,45	24	0.38 0.68
University of Pisa Italy CIDECT Program 5FP BSC 1977a	N , loaded at centre & quarter points	6	127x127 ⇓ 254x254	42.4 dia - 194 dia 51x51 - 152x152	90,45	16 - 40	0.3 - 0.76
University of Delft Netherlands CIDECT Program 5Qg	K , loaded at centre	4	80x80 ⇓ 120x120	60x60	45/45 30/30	22.4 ⇓ 27.9	0.5 ⇓ 0.75
Kulak and Ogle 1981	K , loaded at two points	9	152x102	152x152 outer web 89x89 inner web	53	24	0.6 1.0
MOSTOSTAL, Poland Czechowski 1984	K , loaded at two points	8	100x100 80x80	80x80 50x50 40x40	45,60	33 20	
Philiastides 1988	K , loaded at one point	7	100x100 150x150	40x40 60x60	45,60	20 24	0.4 0.6

CHAPTER 2

BEHAVIOUR OF RECTANGULAR HOLLOW SECTION JOINTS

2.1 Introduction

Since the late nineteen sixties intensive research work on HSS joints has been carried out around the world. Much of the on-shore work has been sponsored by CIDECT whose mandate is promotion of the use of steel hollow sections. Large diameter CHS joints were promoted by the offshore industry where research was sponsored mainly by oil exploration and production companies. The primary reasons for the divergence of the offshore/onshore research are environmental requirements and structural size. However, a number of issues are of common concern to the experts from CIDECT, the offshore industry and another organization - the International Institute of Welding (IIW) who collectively provide a stimulating environment for international cooperation in sharing research findings in both the general area of HSS and in the more complex area of CHS and RHS joints. The present state of the art in the design of HSS joints is mostly the result of cooperation between CIDECT, the offshore industry and IIW.

The design of HSS joints has traditionally been based on their strength, calculated by dividing the ultimate level attained in experiments by a suitable safety factor. For some joints such as RHS T, X or

Y joints (Figure 2.1), the strength equations were derived based on the yield line method with the results calibrated with experiments. Present design recommendations for RHS joints do not require the serviceability limit state of local deflections for the chord connecting face to be checked independently from the design strength. Instead, the range of validity for some geometric joint parameters has been restricted in such a way that local deflections are not critical. This approach was dictated by the lack of comprehensive measurements directed towards the serviceability criterion and a relatively small number of theoretical studies devoted to the deformation aspects of joint performance.

Today, there is general concurrence with satisfactory design strength equations for many planar type RHS joints. However, a need exists for studies which could give further insight into joint behaviour, including its deformation and various mechanisms of the load transfer. This should lead in the future to a separation of the two limit states and a relaxation of some restrictions currently imposed on the validity of joint parameters which accompany the present design strength equations.

Within the current design recommendations for RHS joints a few aspects which need further attention are: the limits of validity for the gap size in gap K joints, stress concentration factors for fatigue design of RHS joints, and local load transfer within a joint which includes the effect of bending moments due to joint geometry and joint stiffness. There is insufficient experimental data on the subject of local joint behaviour, including joint flexibility and stress flow in the walls of RHS members. The present study addresses these issues and provides experimental and numerical evidence of basic mechanisms which take place around the joint.

This chapter presents background on research work leading to the current design recommendations for RHS joints with special emphasis on gap N and K joints. A review of the most common concepts in the design of RHS joints is divided into strength and deformation aspects of joint behaviour.

2.2 Joint Configurations

A number of different joint configurations can be identified in lattice structures made with HSS. The most common are T, Y, X, N, K or KT joints which derive their names from a similarity in shape to letters of the alphabet. Figure 2.1 illustrates planar configurations isolated from the rest of a structure. Three factors of the joint configuration are: the angle of inclination for bracings, the number of bracing members attached to the chord and whether both the top and bottom flanges of the chord participate in the load transfer. The influence of all of the above will be discussed in the present study. Although the main focus is on a gap K joint, an independent assessment of each of the above effects is also given adequate treatment in experimental and numerical joint analysis. Hence, a synthesis of the joint behaviour can be built for almost every joint configuration.

2.2.1 Material and Section Size Restrictions

Hollow structural sections are manufactured from low carbon weldable steels which may be hot finished, cold formed or cold formed and stress relieved. According to CIDECT Monograph No. 6 (1986), the following restrictions apply to the material properties of HSS joints in order for the current design recommendations to be valid:

- yield strength should be within the 235-355 MPa range
- % elongation on a gauge length of $5.65 \sqrt{(So)}$ should be > 18, where So is the cross sectional area (in mm^2) over the gauge length (in mm)
- ratio of yield stress to ultimate stress should be less than 0.8 .

A departure from the above restrictions does not mean that the current design recommendations cannot be used. In such cases additional experimental or analytical work may be necessary to describe the joint behaviour under the new material limitations. For example, the restriction imposed on the yield strength was deemed necessary because higher strength steels often exhibit brittle behaviour of the material, a response contrary to the assumption of proper redistribution of internal forces used in the joint strength equations.

In many instances the production method restricts the range of available sections and material properties. For example, square sections manufactured in Canada are limited in the size of the external cross section dimensions by 25.4 x 25.4 mm and 304.8 x 304.8 mm for the lower and upper limits respectively. The thicknesses range between 2.41 and 15.9 mm (SONCO 1983, STELCO 1981). Available test results (Wardenier et al. 1978) did not show any significant scale effects which may allow us to use even larger sections when such become available.

2.2.2 K and N Joints

Among K and N joints one has a choice of using gap or overlap joints. Both types of joints are defined in Figure 2.2 . The amount of overlap is often given as a percentage of the distance $p = h_1/\sin\theta_1$. A gap which is separating branch members allows for simple fabrication of a joint with only a single cut at the end of a bracing. Often an overlap joint is preferred, especially if joint eccentricity becomes a critical factor. Current design recommendations (IIW 1981) for the design of HSS joints restrict eccentricity to:

$$-0.55 < e/h_o \text{ (or } e/d_o\text{) } < 0.25 \qquad (2.1)$$

where: e - eccentricity

h_o - depth of RHS chord

d_o - diameter of CHS chord .

Positive and negative eccentricities are illustrated in Figure 2.2 for the gap and overlap joints with which they are typically associated. The absolute value of the positive limit for eccentricity is lower than a negative limit because it is believed that positive eccentricity increases the overall truss deflections and therefore is less desirable. It is recommended by CIDECT (1986) that within the allowable limits the effect of nodal eccentricity be neglected in the joint design. However, it should be taken into account in the design of the members for any eccentricity. Outside the allowable limits the equivalent bending moment must be redistributed among the members meeting at the joint, and taken into account in the joint design. It is a frequent practice to allocate one half of the moment to the chord on each side of the joint, for equal panel spacing, providing the chord's bending stiffness is much greater than that of the bracings.

2.3 Gap K-Joint

The main thrust of the present study is on RHS joints with a particular focus on gap joints. For the reasons described in Section 1.1 the K joint was selected for a detailed investigation in the present study. A geometry of gap K joints with typical parameters used in design as recommended by CIDECT (1986) is illustrated in Figure 2.3 . The major parameters that affect the design characteristics are as follows:

- angle of inclination for a bracing, θ_i
- width ratio between a bracing and a chord, β
- gap size or overlap between two bracings, g or q
- bracing width to thickness ratio, b_i / t_i
- chord width to thickness ratio, b_o / t_o
- bracing thickness to chord thickness ratio, t_i / t_o
- yield stress of the material, F_y

Other parameters defined in Figure 2.3 are utilized in designing the layout of a joint and express certain properties. Thus, α gives an indication of the chord beam characteristics, γ denotes the chord's slenderness, τ provides a measure of chord or brace wall failure and ζ is a nondimensional gap parameter.

Throughout this study a consistent terminology is used for describing the strain and stress distributions around the joint. Such terms as : the toe, the heel or the sidewall as well as the weldment lengths a, b, c and d are defined in Figure 2.4. The same figure is an example of a joint geometry believed to possess good redistribution properties for internal forces (Wardenier 1982). In such cases the value of $b_o - b_i$ is set equal to g which will be further explained in Section 2.4.3.

2.4 Joint Strength

Current design recommendations for RHS joints advocated by CIDECT (1986) are provided in a limit states design format. A summary of the design equations for RHS gap K and N joints is summarized in Table 2.1 . The joint strength equations are expressed by a characteristic strength based on test results at a presumed 95 % confidence level. In order to arrive at the design strength as required by the European standards, the characteristic strength is further divided by joint factors γ_m, γ_c where γ_m is a material factor and γ_c depends on the nature of the structure and includes uncertainties associated with local effects, construction stages or other factors. A combination of the two joint factors $\gamma_m \gamma_c$ in general reflects the type of expected failure and the amount of joint ductility. A graphical illustration of interdependence between joint strengths at different load levels is shown in Figure 2.5. The joint strength at the working load level in CIDECT notation is given as N^*/γ_s, where N^* is the joint design strength expressed as a load in a particular bracing and γ_s is the appropriate load factor.

According to Canadian standards the ultimate strength equations given in CIDECT (1986) must be multiplied by a suitable resistance factor (φ) in order to arrive at the design strength of a joint. The selection of those resistance factors is described by Packer et al. (1984) in "Canadian Implementation of CIDECT Monograph No. 6" which introduced all changes necessary to make the design recommendations consistent with existing Canadian standards.

2.4.1 Modes of Failure

As a result of an extensive experimental program at Delft University, Wardenier (1982) identified the following failure modes for RHS joints:

a - yielding of the chord connecting face or the chord cross section
b - crack initiation around the tension bracing in the chord top face
    (often termed as "punching shear")
c - cracking in the welds or in the tension bracing
d - local buckling of the compression web member
e - shear failure of the chord
f - chord wall bearing failure or local buckling of the chord under
    the compression web member

g - local buckling of the chord face behind the heel of the tension web
    member .

Failure modes "c" and "d" are also termed "effective width" failures in the current CIDECT (1986) Monograph No. 6 . Failure mode "a" takes place for joints with width ratios in the range 0.4 - 0.8 . It is the most common failure mode for RHS K and N type Joints. The same failure mode is often accompanied by cracking in the chord (mode "b") or in the bracing (mode "c") when the width ratio is within the range 0.6 - 0.8 . Mode "c" usually takes place in joints with relatively thin walled bracings, while mode "d" may occur for lap joints. When the width ratio approaches 1.0, then mode "e" is often observed. Local buckling (modes "f" and "g") occurs especially in joints with a high chord width to thickness ratio. In many cases the joint failure may be a combination of a few different failure modes. Detailed descriptions of the failure modes observed during testing of RHS joints were described by Wardenier and Stark (1978) and Wardenier (1982).

The punching shear failure mode (mode "b") and the effective width failure modes (modes "c" and "d") use the concept of effective width to determine the length of the bracing wall which is fully participating in the load transfer mechanism.

2.4.2 Effective Width

An effective width concept is often used in the design of plates when a stress distribution across the width of a plate is highly nonlinear. An assumption that only part of the plate width is fully effective significantly simplifies the design. It is recognized that whenever only one bracing is attached to the chord connecting face (T or X joints and part of a Y joint), both cross walls of the bracing are not fully effective. An expression for an effective width of these walls was initially derived from the results of plate to RHS connections by Rolloos (1969). Recent studies by Wardenier et al. (1981) and Davies et al. (1981) on plate to RHS, and RHS to RHS connections respectively, concluded that the effective width b_e is directly dependent on the chord thickness t_o and can be assumed as 13.5 t_o for Fe 360 and Fe 430 steels and 11.5 t_o for Fe 510 steel (Fe 360, Fe 430 and Fe 510 are European grades of steel equivalent to the yield strength in MPa of about 240, 300 and 360 respectively). If the branch thickness or the yield stress is different from that of the chord, then the above expressions can be modified by by the linear factor $\frac{F_{yo}\, t_o}{F_{yi}\, t_i}$, and the chord thickness to width ratio $\frac{t_o}{b_o}$ to obtain the following:

$$b_e = C \left(\frac{t_o}{b_o} \right) b_i \left(\frac{F_{yo}\, t_o}{F_{yi}\, t_i} \right) \qquad (2.2)$$

where C is the effective width factor equal to 13.5 for Fe 360 or Fe 430 steels and 11.5 for Fe 510. Recently, IIW recommended that the value of C be set equal to 10.0 for all grades of steel (Packer 1988).

The effective width definition above is recommended in the current design recommendations CIDECT (1986) for the cross walls of the RHS branch member in T, X or Y joints whenever the branch is inclined to the chord at 90°. For angles other than 90° the effective width of the cross walls may change but lack of sufficient experimental or analytical evidence in this area makes the above recommendations valid for other angles as well. In the case of RHS gap K and N joints it is recognized that the gap region will make the adjacent cross faces of both bracings fully effective. Hence, each bracing has only one cross-wall (in the heel area) which is not fully effective. Figure 2.6 illustrates the effective width of the cross wall in the heel area for an RHS gap K joint.

2.4.3 Limits for the Gap Size

The size of a gap is deemed to have no significant effect on the joint strength and therefore does not enter into the current design strength equations. However, the restrictions imposed on the gap size are included in the limits of validity for the current design equations shown in Table 2.2 . Hence , the appropriate gap size is a necessary condition for the joint strength equations to be valid. The limits imposed on the gap size are thus very important because of a possible exclusion of a joint in the design of a truss if this parameter is outside the allowable range.

According to CIDECT (1986) three walls of the RHS bracing in a gap joint are fully effective in the load transfer and the fourth, at the heel, is only partially effective. Wardenier (1982) considers three sides of a bracing in a gap joint as fully effective when "a good distribution of stiffness" exists. Such a state hypothetically takes place when the gap size is equal to $b_o - b_i$. The condition of "a good distribution of stiffness" is illustrated in Figure 2.4 . It appears that in the above reasoning the distribution of stresses in the chord connecting face is closely linked to the stress distribution in the walls of the branch member.

The notion of "good distribution of stiffness" is currently used by CIDECT in the definition of the allowable gap size limits given by the following expression:

$$0.5\,(b_o - b_i) < g < 1.5\,(b_o - b_i) \qquad (2.3)$$

An additional limit of $g \geq 2t_o$ is also imposed to allow for the weldment between the bracings. As can be seen in Equation 2.3 one half of the gap size is being subtracted from and added to the gap size at which a good distribution of stiffness hypothetically takes place (see Figure 2.4). The limits of validity for the gap size are displayed in Figure 2.7 . A practical range for the width ratio β of 0.4-0.8 has been selected for illustration of geometrical proportions between the size of a bracing, a gap and a width of a chord for the lower and upper limits of the gap size. As an example, two square bracings of the same size are used with an angle of inclination for the bracings of 45° which determines the length of the line of contact between the branch and the chord. A few comments about the lower and upper limits for the gap size based on visual inspection are listed below.

Joints with a small width ratio (~0.4) appear to provide a good stiffness distribution because the size of the branch is of the same order as the size of the gap as well as the distance between the sidewalls of the branch and the chord. However, an upper limit for the gap size may lead to the two branches working independently with no interaction in the gap region.

For joints with high width ratio (~0.8) either of the gap size limits is much smaller than any dimension of the branch cross section. Therefore it is questionable whether a good stiffness distribution can be achieved with the present limits for this width ratio. A substantial non-uniformity in stress distribution between the toe and the heel may lead to a re-distribution of forces in either of those areas rather than along the entire perimeter of the branch.

It appears that the basic notion that a good redistribution of internal forces should be selected as a criterion in setting the limits for the gap size may be violated for high width ratios. In situations with small width ratio the upper limit for the gap size may be a reason for lack of interaction between the bracings in RHS gap joints.

2.5 Serviceability Limit State of Joint Deformation

The deformation limit of 1% b_o has been generally accepted as a serviceability limit for RHS joints, with the displacement expressed as a vertical deflection of the chord connecting face (Figure 2.8 , gauges 1-4). In experiments, chord local deformation has also been measured as an axial displacement of a bracing in the vicinity of the connection as measured by gauges 5 and 6 in Figure 2.8 (Wardenier and Stark 1978), and such a displacement is often resolved into vertical and horizontal components. The design strength equations currently advocated by CIDECT (CIDECT 1986) often take the deformation limit into account indirectly, as for example in the case of yielding of the chord face for T, Y and X joints (see Wardenier 1982 , p.5-41). Other failure modes for these joints occur without the deformation at the serviceability level being critical. For RHS gap K and N joints, additional restrictions are imposed for the validity of the joint parameters, partly in order to limit the joint deformation at service loads to $0.01\ b_o$:

$b_o/t_o < 40$, and , $b_i/b_o > 0.4$.

For RHS overlap joints, the local joint deflections at the serviceability load level are not critical and therefore do not have to be verified.

One can conclude that the serviceability limit state is currently embodied in the design recommendations for the ultimate limit state of RHS joints. The main reason for such an arrangement is the lack of experimental or analytical bases for a rational method of predicting the joint local deflections. One advantage of this indirect inclusion of the serviceability limit state of localized deflections within the joint strength calculations is a reduced number of steps in the design process. However, the serviceability limit state is very much different in nature from the ultimate limit state and so should be defined separately with a sound theoretical basis for its existence.

2.5.1 Local Joint Behaviour

RHS joints are characterized by properties which are not typical for most joints fabricated with the use of open section members. Relatively thin walls and direct welding without the use of gusset plates or stiffeners cause substantial local deformations. In addition, localised stresses imposed on the nominal stress field lead to a highly nonlinear variation of internal forces in the vicinity of the connection.

It is a common assumption in the design of trusses with the use of RHS sections that the members are pin-connected. Very often some bending moments will arise at the end of bracing members due to both nodal eccentricities and the specific geometry of a joint where the toe or the heel position may cause undue stress concentrations. The bending moments due to noding eccentricities are neglected in the design of connections, provided they are relatively modest and fall within a specified range (see Table 2.1), because the empirically derived joint strength equations account for the nonuniform stress distribution. However, according to CIDECT (1986) the same bending moments should be accounted for in the design of <u>members</u> framing into the joint. The bending moments due to the continuity of the frame and the local stiffness of the joint in general are not accounted for in the design of members. It is essential to describe the stress distribution around the joint in order to be able to predict the joint strength in other ways which are not empirical. The limited experimental results cannot provide a consistent and complete description of the behaviour of RHS joints.

The characteristic points on the load vs. local joint deformation graph for typical RHS T and K joints are illustrated in Figure 2.9. The compression and tension characteristics for a T joints refer to two separate joints while both characteristics for a K joints refer to one joint. It has been found that the deflections under the compression bracing are often higher (in absolute value) than for the tension bracing. This was noticed in experiments (Wardenier et al. 1978) and confirmed by finite element analysis (Ostrowski et al. 1985). A physical explanation for a non-symmetrical configuration of vertical deflections can be found through a nonlinear analysis of a rectangular closed section under inward and outward loadings (Ostrowski et al 1985). An outward force acting on the top plate leads to stretching of the side walls which limits outward displacements. A force acting inwardly causes both compression and bending of the side walls which displace out-of-plane with the upper edges moving downwards. Thus, the chord connecting face is more prone to inward than to outward displacements resulting in higher flexibility under the strut rather than under the tie. The region around the tension bracing is thus stiffer with high concentration of stresses in the vicinity of the gap. Among other points on the load-deflection curves in Figure 2.9, point **m** indicates a separation of load-deflection curves for tension and compression bracing. At the same time the membrane action starts to affect the joint behaviour. The deformation limit of 1% b_o is marked by point **d** which typically appears early on the nonlinear curves. Cracking around the tension bracing may develop around point **c**. The ultimate load reached in a T joint in tension is often higher than in compression. Both limits are marked by **u**. Figure 2.9 illustrates typical load - deflection graphs with the characteristic points described, but their positions on the curves may be altered due to different joint geometry and loading conditions.

It was established in a previous study by Ostrowski (1984) that numerical analysis of RHS joints beyond the service load level should incorporate the large deflection effect as well as elasto-plastic material response. Also, it has been shown that geometric nonlinearity (large deflection effect) is responsible for a departure from a perfect anti-symmetric profile of localised deflections for the chord connecting face, as observed when only material nonlinearity is included in the analysis. A simple numerical experiment outlined below can show how significant the membrane stresses are at the working load level, for a typical RHS section used in Canada.

A study was undertaken on the deformation of a closed rectangular frame under an inward (compression) and outward (tension) loading and was carried out for three different width ratios. The purpose of this analysis was to determine a separation point between small deflection and large deflection curves. This limit will indicate that membrane stresses affect joint behaviour.

A square hollow section 254 x 254 x 9.53 mm was selected for the computer study in which the loading was applied to the top flange and the deflection measured as shown in Figure 2.10 . A two node, six degrees of freedom finite element was used for the analysis which involved both large deflection and material nonlinearity effects. A total of 14 elements were used in modelling one-half of the cross-section. The basic parameters were as follows:

$E = 2*10^5$ MPa , ET= 2400 MPa , $F_y = 350$ MPa

A plate rigidity of $Et^3/(1-\nu^2)$ was used in all elements. A uniform loading was distributed over the contact width which was to simulate the action of a mated branch to chord RHS joint. The width ratios of 0.4 , 0.6 and 0.8 were considered for an inward and outward loading. For small deflections, both an inward and outward loading produced the same load-displacement curves. Therefore no distinction is made in this case. However, for the large deflection case an inward loading produced higher deflections than for an outward loading. The three curves are presented for each width ~~ratio~~ in Figure 2.10 .

The effect of membrane stresses in the behaviour of a typical RHS joint can be assessed for the three different width ratios. For $\beta = 0.8$ the effect of membrane stresses is negligible. These become more significant for the smaller width ratios ($\beta = 0.4$). At the level of local deflections equal to 1% of b_o a difference does not exist between the large and small deflection curves, for all three width ratios. An immediate conclusion is that for a study of the behaviour of RHS joints at low deformation level it is sufficient to use <u>small</u> deflection elasto-plastic analysis. For any investigation of the joint behaviour beyond the service loads it is absolutely necessary to recognize the distinction between the magnitudes of absolute deflections under the tension and compression members with the latter becoming critical, and also to use large deflection elasto-plastic analysis.

2.5.2 Redistribution of Bending Moments

CIDECT Monograph No. 6 (CIDECT 1986) states that the secondary bending moments due to the end fixities of the members can be neglected in the design of joints, provided there is adequate deformation and rotation capacity in both the joints and members to allow the redistribution of stresses at the ultimate limit state or after local yielding of the joint. Limitations imposed on the slenderness of the bracings as well as the minimum requirements for the weld sizes are seen as the means of achieving adequate deformation and rotation capacity. However, it is not clear how one can determine a sufficient deformation and rotation capacity for a joint. The rotation capacity for a structural member is defined as the ratio of inelastic rotation over a unit length and the elastic rotation over a unit length, between $M=M_p$ (based on a simple plastic theory) and a point where the experimentally measured M drops below M_p. Korol (1972) proposes a deformation capacity of 4 for HSS members. The required deformation capacity depends on the structure and the type of loading. The physical meaning of a deformation capacity can be explained as a rotation of a section between attaining M_p and such a time as the development of a mechanism within a structure occurs. In the case of RHS trusses those definitions do not apply directly. Such a truss design is governed by the strength of joints rather than members. The joints in a truss fail due to high stress concentrations which cause yielding of the chord connecting face rupturing of an RHS wall; or cracking in a weldment. Buckling of members and shear failure are also possible (see Section 2.4.1). The deformation capacity of a joint remains a difficult and unresolved issue to be addressed in this study.

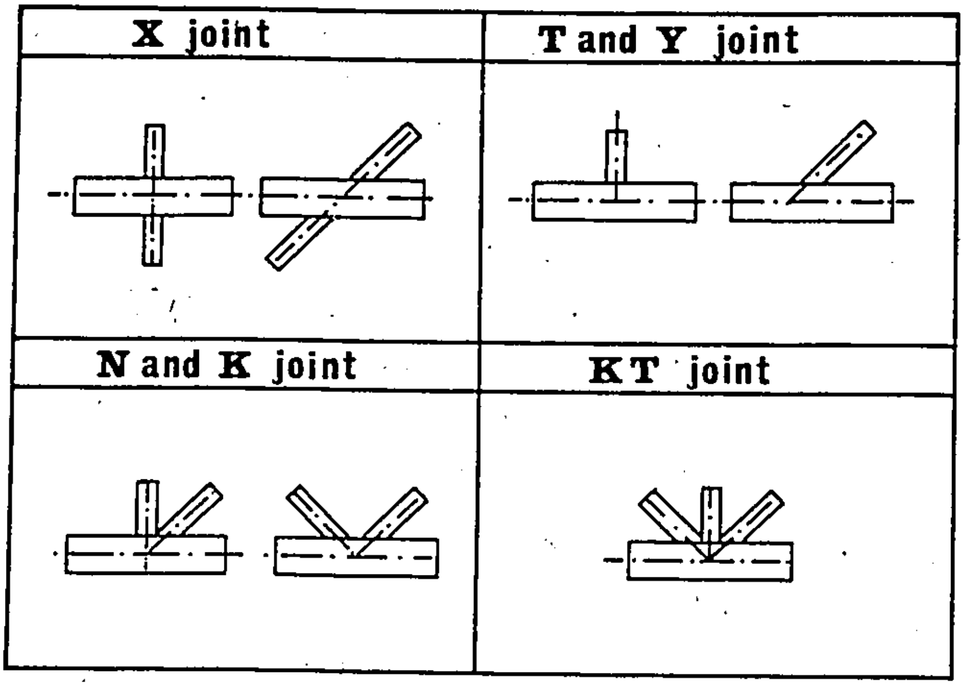

FIGURE 2.1 Joint Configurations

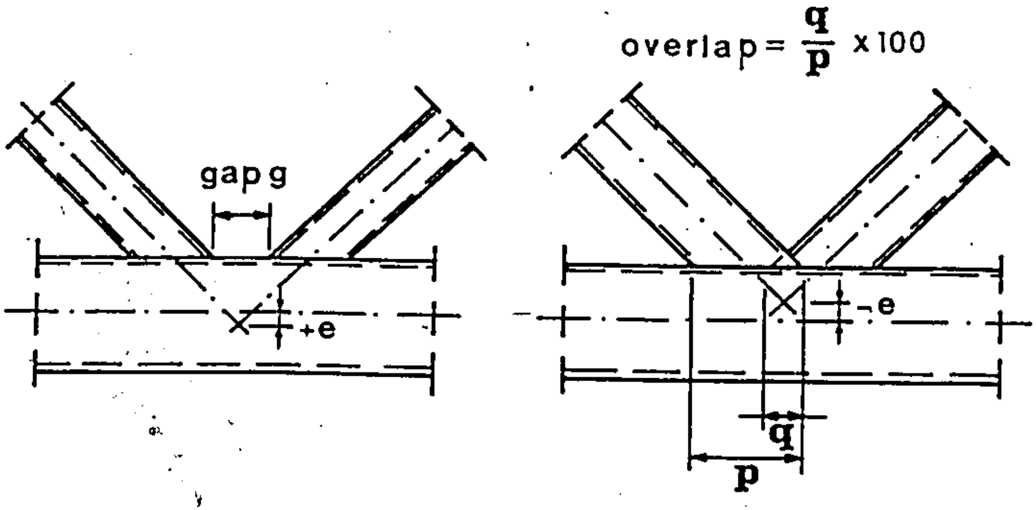

FIGURE 2.2 Gap and Overlap Joints

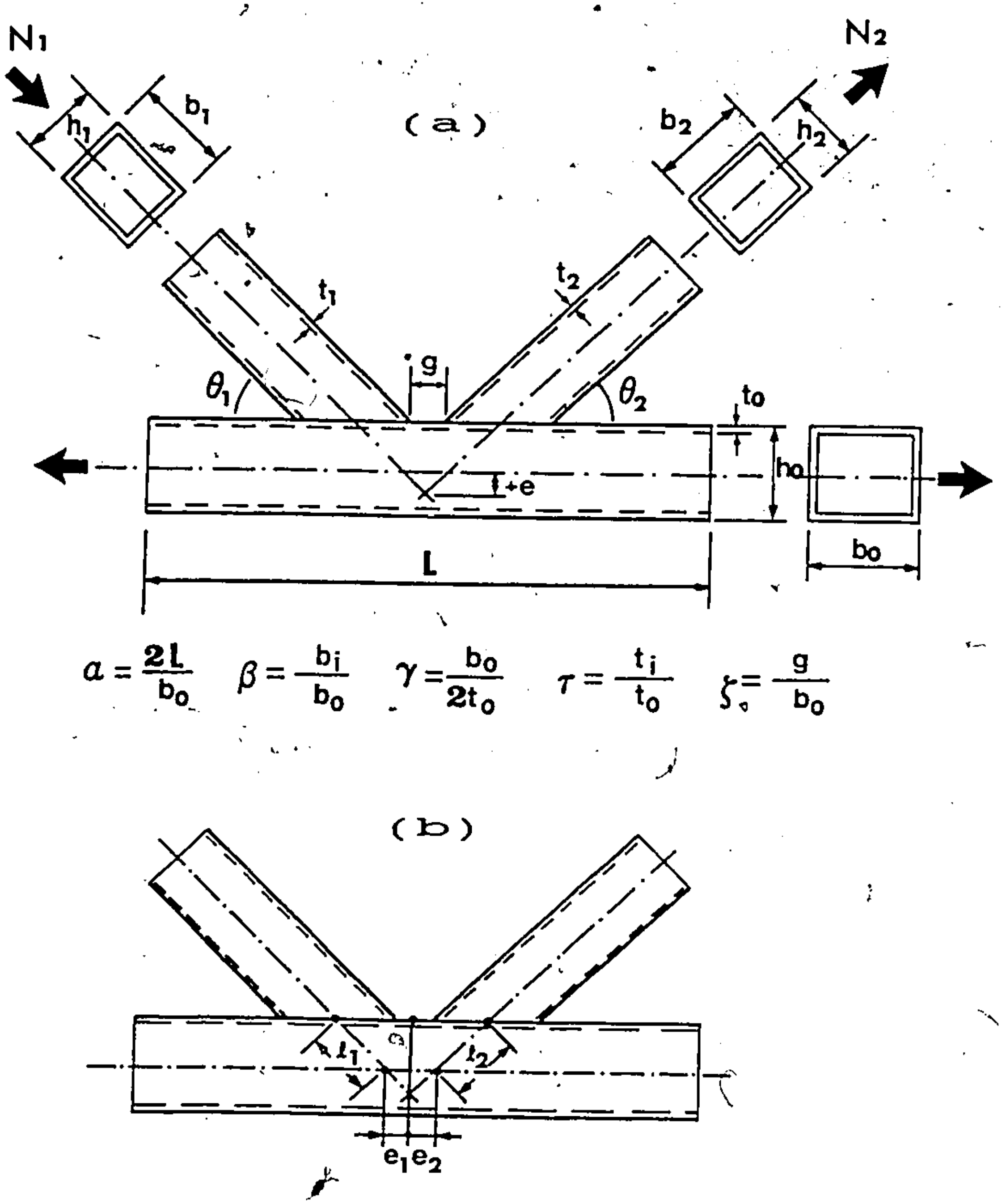

FIGURE 2.3 Geometry of Gap K Joint

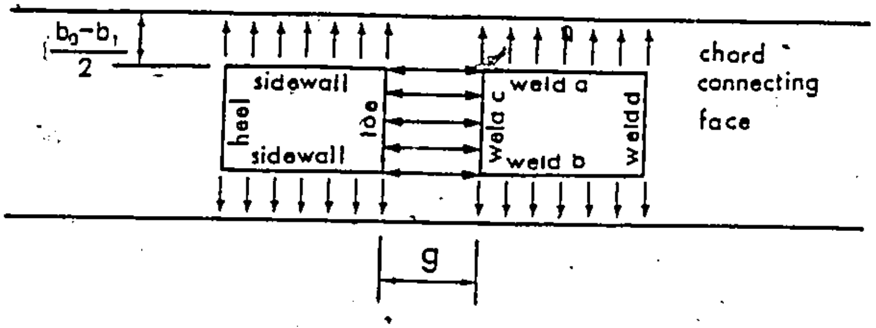

FIGURE 2.4 Plan View of Chord Connecting Face

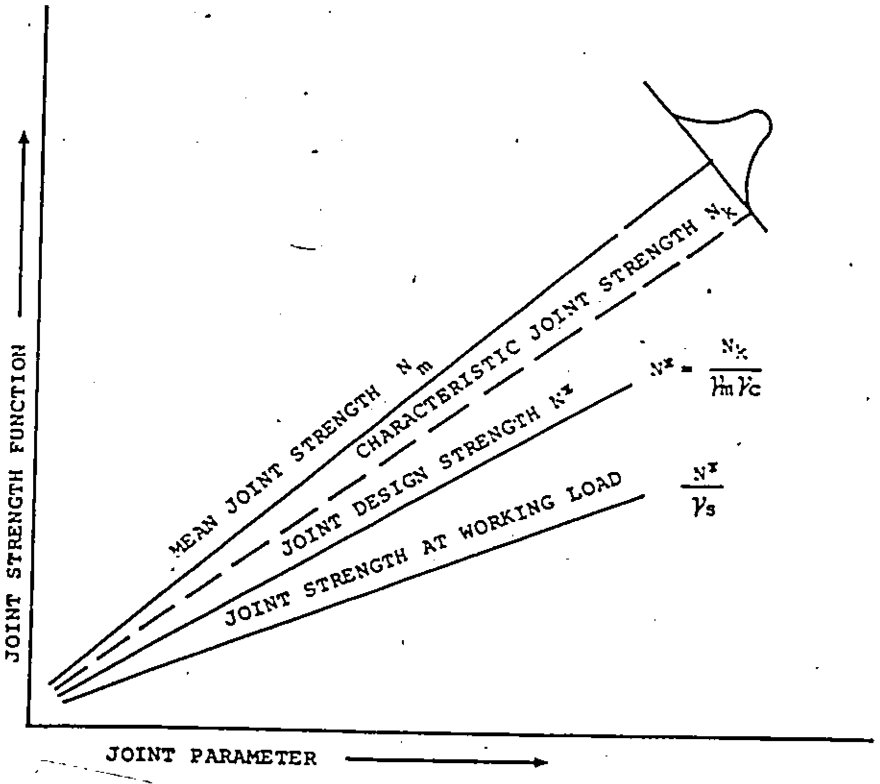

FIGURE 2.5 Joint Strength at Different Load Levels

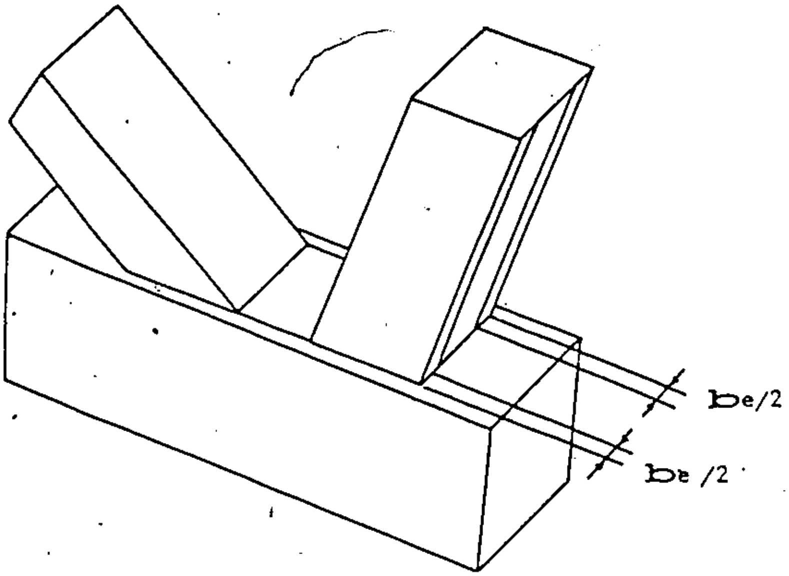

FIGURE 2.6 Effective Width for Gap K Joint

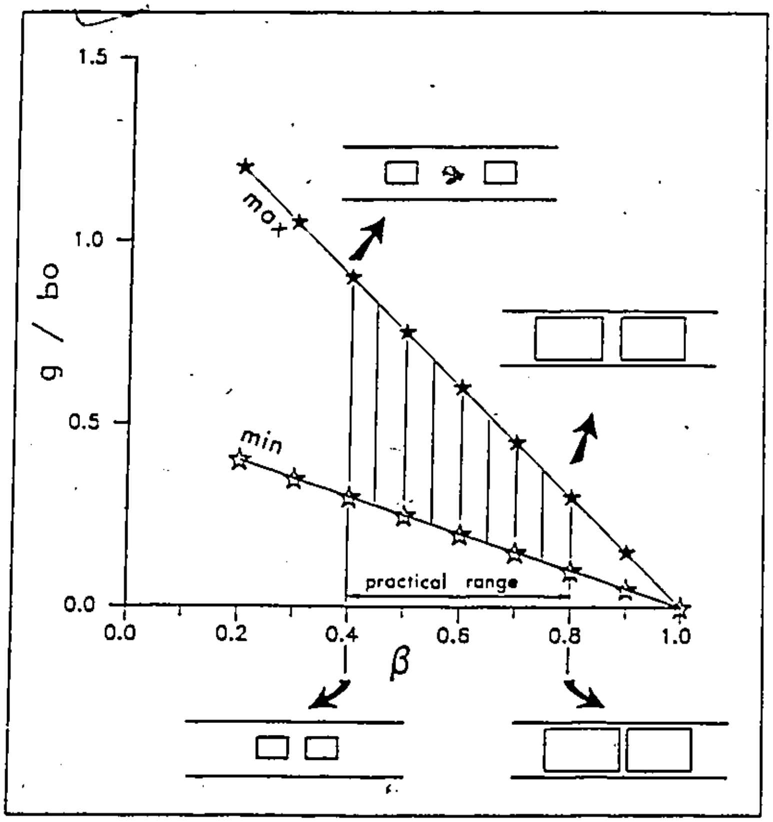

FIGURE 2.7 Current Limits for Gap Size

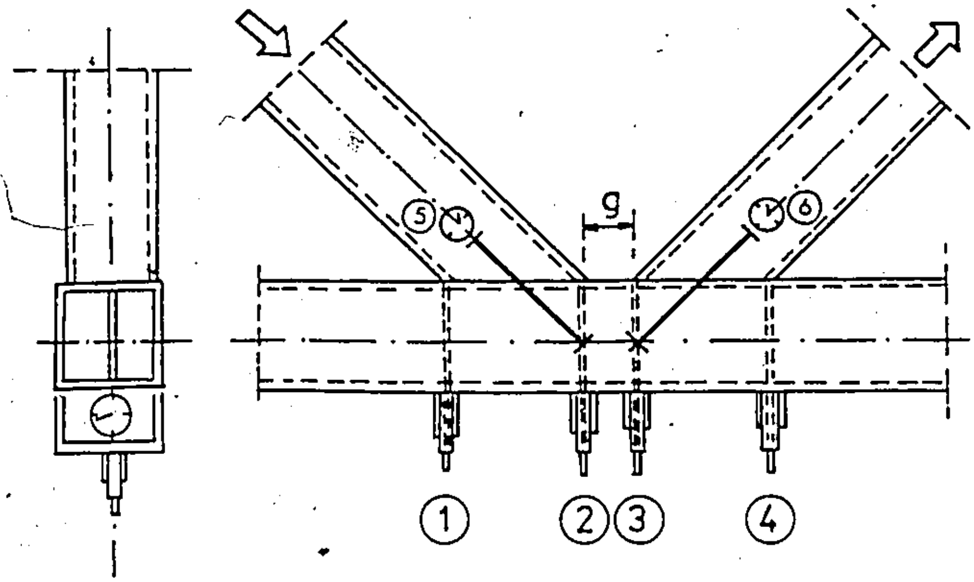

FIGURE 2.8 Measurement of Joint Deformation according to Wardenier et al. (1978)

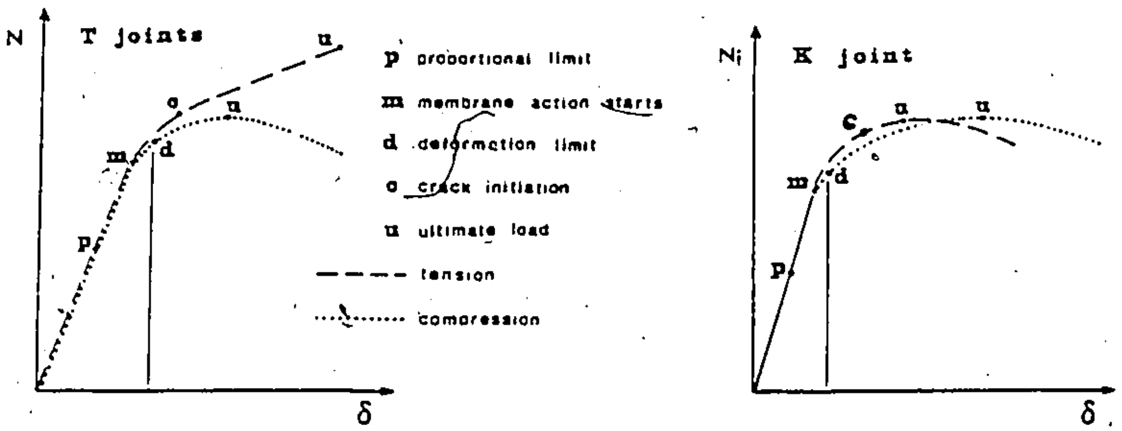

FIGURE 2.9 Load vs. Deformation Graph for RHS T and K Joints.

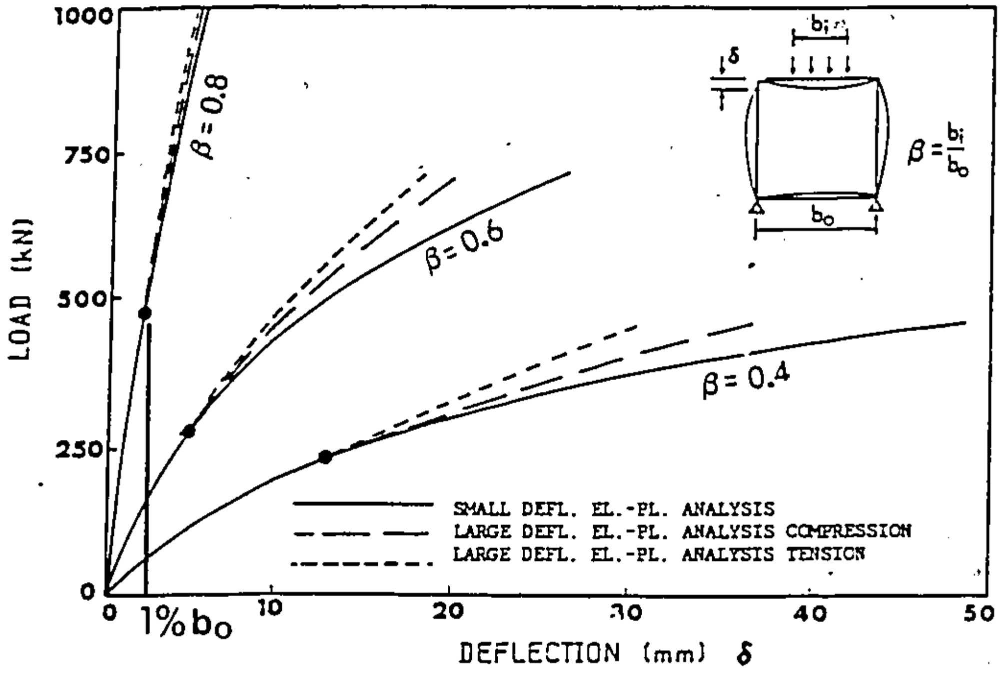

FIGURE 2.10 Load vs. Deflection Curves for a Frame at Different Width Ratios

TABLE 2.1 Ultimate Strength Equations for RHS Gap K Joints (CIDECT 1986)

	GENERAL LIMITS $0.4 < \beta < 1.0$ $\quad 30° < \theta < 90° \quad \sigma_e < 360\ \mathrm{N/mm}^2$ $\frac{b_o}{t_o}, \frac{h_o}{t_o} < 40 \quad 0.5 < \frac{h_o}{b_o} < 2.0 \quad \frac{\sigma_e}{\sigma_u} > 0.8$		
FAILURE MODE	BASIC ULTIMATE STRENGTH EQUATION	PARAMETER DEFINITION	ADDITIONAL LIMITS
Chord Face Failure	$N_{1m} = \frac{7.7\sigma_{eo}t_o^2\,\beta^*}{\sin\theta_1}\left(\frac{b_o}{t_o}\right)^{0.5} f\left(\frac{b_o}{t_o}\right)^{\mu}$ Ultimate strength $N_{1k} = 0.9\,N_{1m}$ Characteristic strength	$\beta^* = \frac{b_1+h_1+b_2+h_2}{4b_o}$ $f\left(\frac{b_o}{t_o}\right) = 1 + \frac{1.25}{3000}\left(\frac{b_o}{t_o} - 30\right)(90° - \theta_1 - \theta_2)$ $f\left(\frac{b_o}{t_o}\right) = 1.0$ when $\frac{b_o}{t_o} < 30$ $f\left(\frac{b_o}{t_o}\right) \leq 1.0$ $\mu = 1.3 - \frac{0.4}{\beta}\left\|\frac{\sigma_o}{\sigma_{eo}}\right\|$ for chord in compression $= 1.0$ for chord in tension	$\frac{b_1}{t_1} > 1.1*\sqrt{\frac{E}{\sigma_e}}$ $\frac{b_2}{t_2} < 35$ $\frac{g}{b_o} \geq \frac{1-\beta}{2}$ $\frac{g}{b_o} \leq \frac{3(1-\beta)}{2}$

σ_e - yield stress ; σ_u - ultimate stress ; σ_{eo} - chord yield stress

TABLE 2.1 Continued

FAILURE MODE	BASIC ULTIMATE STRENGTH EQUATION	PARAMETER DEFINITION	ADDITIONAL LIMITS
Chord Shear	$N_Q = \frac{\sigma_{eo}}{\sqrt{3}} \cdot A_Q$	$A_Q = 2h_o t_o + \alpha b_o t_o$ where $\alpha = \sqrt{\frac{1}{1+(4g^2/3t_o^2)}}$	
Chord Punching Shear	$N_{QP} = \frac{\sigma_{eok} t_o}{\sqrt{3}\sin\theta_i} \left(\frac{2h_i}{\sin\theta_i} + b_i + b_{ep} \right)$	$b_{ep} = \left(\frac{c}{b_o/t_o} \right) b_i$	C=13.5 for Fe360 Fe430 C=11.5 for Fe510 $b_e \leq b_i$ $\sigma_{eok} t_o > \sigma_{eik} t_i$
Bracing Effect. Width	$N_{ei} = \sigma_{ei} t_i \, [2h_i - 4t_i + b_i + b_e]$	$b_e = \left(\frac{c}{b_c/t_o} \right) \left(\frac{\sigma_{eok} t_o}{\sigma_{eik} t_i} \right) b_i$	
Combined Shear & End Load in Chord	$N_{FQ} = (A_o - A_Q) \sigma_{eo} + A_Q \sigma_{eo} \sqrt{(1-(Q/N_Q)^2)}$	N_{FQ} - reduced axial load capacity of chord in presence of shear N_Q - shear strength of chord cross section Q - shear force	
Combined Moment Shear & Axial Load	$\left(\frac{F_o}{N_{FQ}} \right)^{1.5} + \left(\frac{M_o}{M_{FQ}} \right) \leq 1.0$	$M_{FQ} = (A_o - A_Q)(h_o - t_o)\sigma_{eo} + 0.5(h_o - t_o) * A_Q \sigma_{eo} \sqrt{(1-(Q/N_Q)^2)}$ N_{FQ} - reduced axial load capacity due to shear	

σ_{eok} - chord characteristic yield strength ; σ_{ei} - minimum yield strength of member i

A_i - cross sectional area of member i

CHAPTER 3

FINITE ELEMENT ANALYSIS

3.1 Description of the Problem

The purpose of this numerical study is to model the three dimensional behaviour of an RHS joint up to the serviceability load level. One can classify the problem in terms of continuum mechanics as a small strains, small displacements, elasto-plastic analysis. The specific problems under investigation include the distribution of stresses in the branch member walls in the vicinity of the connection, the description of the load transfer mechanism within a joint and the evaluation of the local deflection criterion.

The finite element method has been selected as a tool for the analysis because of its accuracy and flexibility in modelling structures. The essential aspects in modelling of a tubular joint include the satisfaction of displacement compatibility at intersections, a proper account of the progression of plasticity, a realistic interpretation of boundary conditions and appropriate discretization of the hollow section members. This study introduced a newly derived general shell element which originated from the Ahmad shell element. A nine node element with six degrees of freedom per node including three global translations and three global rotations allowed for an accurate modelling of the multiple shell intersections typically found in RHS joints. The material behaviour is described using the Von Mises yield criterion and the Prandtl-Reuss flow equations. The plasticity algorithm implemented in this study allows a sampling point to yield within a load increment and accounts for both elastic and inelastic stress increments accordingly. It traces the current position of the yield surface and brings the stress level to the yield surface at the end of each iteration. The uniaxial stress-strain relationship of the material is described by a piece-wise linear scheme which with an unlimited number of points on the curve can approximate any nonlinear function. Each sampling point is capable of carrying individually specified material properties which allows for drawing a line between a strain-hardened zone near the corners and the flat portion of an RHS within the boundaries of an element.

3.2 Selection of Finite Element

The factors to be considered in selecting a proper shell element include accuracy, an ability to model general shell structures of arbitrary geometry, and satisfactory numerical performance in terms of cost and memory requirements.

The facet elements were the first to be used in analysis of tubular joints (Greste 1970). The element introduced geometrical errors due to a curved surface being replaced by a number of flat elements. Membrane and bending actions are uncoupled within a single element. Some applications such as the modelling of a cylinder under internal pressure, which results in a purely membrane state of stress, may nevertheless show some bending moments at the element intersections. Among true curved shell elements one has a choice of formulating the element based on a particular theory such as Donnell or Reissner shell theories. However, such formulations do not provide the desired versatility in modelling joints with varying geometry. Another possibility is the use of a three dimensional element, which has the advantage of representing the complex stress field that often occurs at intersections between plates or shells. However, the discretization of the entire structure, which comprises plates and shells, using only three dimensional elements is highly inefficient because of a large number of degrees of freedom and a substantial demand on memory requirements during the computation. Besides, the stress field at some distance away from the intersection is mostly two dimensional, and it is not necessary to include more than one node in the thickness direction of the element.

The three dimensional elements can be reduced to plate and shell elements after imposing additional assumptions on the element behaviour. The following two assumptions simplify the description of the shell geometry and the displacement field by the definition of direction cosines of the normal vectors at the nodal points:

- particles originally on a straight line in the direction of the normal vector to the middle surface of the element remain on a straight line after the shell has deformed;

- the stress in the direction of the normal vector to the shell middle surface is zero.

After introducing these two assumptions, the twenty-node three dimensional element is reduced to a nine-node shell element which is still capable of including the shear deformations typical for thick shells. Often such elements are called degenerated three dimensional elements, mainly due to ~~the~~ procedure used in their derivation. This concept was originally introduced by Ahmad et al. (1970). It was further expanded for the nonlinear range by Ramm (1977) and Krakeland (1978). Bathe and Bolourchi (1980) also used this concept in deriving their family of isoparametric shell elements. The Ahmad element is particularly suitable for modelling shells and plates because of its simplicity, numerical efficiency and the fact that it possesses the same degree polynomial approximations for the in-plane and out-of-plane variables. This element was selected for the present study to model the plate and shell surfaces in tubular joints. However, a new element had to be derived for modelling the intersections. This originated with the Ahmad shell element. Instead of five degrees of freedom per node it has six degrees of freedom with three global rotations replacing the previous two rotations with respect to locally defined axes.

3.3 Modelling of Shell Intersections

Modelling of shell intersections using the finite element technique has recently attracted the attention of many researchers (Bathe and Ho 1980, Crisfield 1985, Panagiotopoulos 1986). Bathe and Ho (1980) outlined four different possibilities for discretizing of an intersection between two plates meeting at an angle of 30° , namely through a two dimensional finite element mesh, shell elements with constraint equations, the average normal technique or by using transition elements. In RHS joints as many as four plates may share a common node. Two dimensional finite element mesh is a planar discretization of a cross section and cannot be used to model tubular joint intersections because of their three dimensional geometry. The average normal technique leads to substantial distortions of the elements in a typical application for tubular joints. The solution with transition elements is acceptable for intersections of more than two plates providing that an additional three dimensional element is used to join the transition elements. Hence, of the above four methods only the shell element with constraint equations can be directly adopted for the modelling of general tubular joints.

Intersections between an assembly of plates were analyzed by Crisfield (1985), who extended the technique of selective shear-constraints initially introduced as a remedy against the locking phenomenon in a Mindlin-Reissner element with reduced thickness. The unconstrained variables are adopted at the plate intersections with the constrained variables located elsewhere. This leads to numerical difficulties and requires special numerical treatment of the problem. In addition, the suggested method cannot be extended to general shell applications.

Panagiotopoulos (1986) used Ahmad's shell element for the modelling of an intersection between two very thin cylinders under internal pressure. In addition to the Ahmad element he included solid incompatible elements and transition elements. His approach is valid for intersections where any given node at the junction is part of no more than two surfaces. The solid element should be replaced by a compatible three dimensional element if a more general solution is needed.

With the use of the Ahmad shell element, two possible solutions emerge for the modelling of intersections found in a typical tubular joint. One is based on constrained equations and the other makes use of three dimensional elements in combination with transition elements. Both methods are illustrated in Figure 3.1 .

A close look at the intersection between the walls of two RHS members connected by welding is essential to an understanding of the basic mechanisms of load transfer that take place at the junction. Photographs of typical intersections of RHS to RHS connections taken during the experiments reported herein are illustrated in Figure 3.2 . It is apparent that the amount of weldment with a throat thickness greater than the smaller thickness of the two connected walls adds substantially to the rigidity of the connection. It is reasonable to assume that for any imaginary point along the intersection, the three linear displacements and three global rotations are the same for either of the connecting walls. The extent of the weldment ensures that this condition is satisfied.

The physical arrangement of the welded connection makes the constrained equations approach to modelling intersections more appropriate than the use of a three dimensional element with transition elements on each side. The latter method would be more appropriate if the end sections of the tubular branch were cemented to the chord connecting face rather than welded which provides more rigidity at the intersection. In addition, the method of constrained equations is associated with substantial savings in cost and computer memory requirements. The same method can also be applied to the corners of an RHS member where substantial work hardening takes place during the forming process.

This study uses the same underlying assumptions as the method of constrained equations in the modelling of intersections. This is achieved by a derivation of a general shell element with six degrees of freedom per node. It is not necessary to constrain any degrees of freedom because the nodal points at an intersection have three translations and three rotations; all expressed in terms of the global Cartesian axes.

3.4 Shell Element

The shell element used in this analysis is derived from the Ahmad shell element which was extensively documented in the literature by Ahmad et al. (1970), Zienkiewicz (1977) and Irons and Ahmad (1980). The present formulation of a general shell element is different because two rotations with respect to local axes are replaced by three rotations with respect to global Cartesian axes.

3.4.1 Geometry of the Element

There are three sets of operative coordinate systems (see Figure 3.3):

- global Cartesian axes X , Y , Z adopted for the representation of the entire structure;
- local Cartesian axes x′ , y′ , z′ defined at each sampling point within an element, mainly for the representation of the states of strain and stress;
- curvilinear axes ξ , η , ζ which are inherent to an isoparametric formulation and are essential in the description of the element curved geometry.

The element geometry is described using local curvilinear coordinates in the non-dimensional form which is typical for the representation of isoparametric elements. The middle surface of the element is defined by coordinates ξ and η, while ζ is used in the out-of-plane direction (Figure 3.3). A position of a point within an element in the global Cartesian system is given by Ahmad et al. (1970) :

$$\begin{bmatrix} X \\ Y \\ Z \end{bmatrix} = \sum_{i=1}^{9} N_i(\xi,\eta) \frac{1+\zeta}{2} \begin{bmatrix} X_i \\ Y_i \\ Z_i \end{bmatrix}_{top} + \sum_{i=1}^{9} N_i(\xi,\eta) \frac{1-\zeta}{2} \begin{bmatrix} X_i \\ Y_i \\ Z_i \end{bmatrix}_{bot} \qquad (3.1)$$

N_i (ξ,η) are the shape functions for the middle surface which are listed in Appendix A. The vector connecting the points on the top and bottom surfaces is called the thickness vector and is defined as follows:

$$V_{3i} = v_{3i}\ t_i = \begin{bmatrix} X_i \\ Y_i \\ Z_i \end{bmatrix}_{top} - \begin{bmatrix} X_i \\ Y_i \\ Z_i \end{bmatrix}_{bot} \qquad (3.2)$$

where v_{3i} is a unit vector in the direction of the thickness vector.

Hence, Equation (3.1) can be written in the following form:

$$\begin{bmatrix} X \\ Y \\ Z \end{bmatrix} = \sum_{i=1}^{9} N_i(\xi,\eta) \begin{bmatrix} X_i \\ Y_i \\ Z_i \end{bmatrix}_{mid} + \frac{1}{2} \sum_{i=1}^{9} N_i(\xi,\eta)\, \zeta\, t_i\, v_{3i} \qquad (3.3)$$

where : t_i is the distance between the points on the top and bottom surfaces;

X , Y , Z are global Cartesian coordinates of a point (ξ,η,ζ);

X_i , Y_i , Z_i are global Cartesian coordinates of node i .

An algorithm leading to formation of the orthogonal basis $[v_{1i}, v_{2i}\ v_{3i}]$ is presented in Appendix B.

The global coordinates of points on the middle surface are given by:

$$\begin{bmatrix} X_i \\ Y_i \\ Z_i \end{bmatrix}_{mid} = \frac{1}{2} \left\{ \begin{bmatrix} X_i \\ Y_i \\ Z_i \end{bmatrix}_{top} + \begin{bmatrix} X_i \\ Y_i \\ Z_i \end{bmatrix}_{bot} \right\} \qquad (3.4)$$

The first term of Equation (3.3) takes into account the position of points on the middle surface which are identical with the nodal points of the element under consideration. The second term includes the effect of rotation of the thickness vector.

3.4.2 Displacement Field

Each nodal point within an element possesses six degrees of freedom (DOF) : three nodal displacements and three rotations with respect to global Cartesian axes. The displacement field within an element in the directions of the global Cartesian axes is defined by:

$$\begin{bmatrix} U \\ V \\ W \end{bmatrix} = \sum_{i=1}^{9} N_i(\xi,\eta) \begin{bmatrix} U_i \\ V_i \\ W_i \end{bmatrix} + \frac{1}{2} \sum_{i=1}^{9} N_i(\xi,\eta)\, \zeta\, t_i\, \Phi_i \begin{bmatrix} A_i \\ B_i \\ \Gamma_i \end{bmatrix} \qquad (3.5)$$

where: U , V , W are displacements at a point (ξ, η, ζ) within an element expressed in terms of the global Cartesian coordinates;

U_i , V_i , W_i are global Cartesian displacements at node i;

Φ_i is a transformation matrix derived in Appendix C;

A , B , Γ are rotations about the global Cartesian axes.

3.4.3 Displacement Derivatives

The displacement derivatives in the local Cartesian system are necessary in order to find strains and stresses within an element. A method of finding local Cartesian base vectors is described in Appendix B.

For an isoparametric shell element the displacement derivatives in the global Cartesian system are related to the same derivatives in the curvilinear system in the following way:

$$\begin{bmatrix} \frac{\partial U}{\partial X} & \frac{\partial V}{\partial X} & \frac{\partial W}{\partial X} \\ \frac{\partial U}{\partial Y} & \frac{\partial V}{\partial Y} & \frac{\partial W}{\partial Y} \\ \frac{\partial U}{\partial Z} & \frac{\partial V}{\partial Z} & \frac{\partial W}{\partial Z} \end{bmatrix} = J^{-1} \begin{bmatrix} \frac{\partial U}{\partial \xi} & \frac{\partial V}{\partial \xi} & \frac{\partial W}{\partial \xi} \\ \frac{\partial U}{\partial \eta} & \frac{\partial V}{\partial \eta} & \frac{\partial W}{\partial \eta} \\ \frac{\partial U}{\partial \zeta} & \frac{\partial V}{\partial \zeta} & \frac{\partial W}{\partial \zeta} \end{bmatrix} \qquad (3.6)$$

where the Jacobian matrix is given by:

$$J = \begin{bmatrix} \frac{\partial X}{\partial \xi} & \frac{\partial Y}{\partial \xi} & \frac{\partial Z}{\partial \xi} \\ \frac{\partial X}{\partial \eta} & \frac{\partial Y}{\partial \eta} & \frac{\partial Z}{\partial \eta} \\ \frac{\partial X}{\partial \zeta} & \frac{\partial Y}{\partial \zeta} & \frac{\partial Z}{\partial \zeta} \end{bmatrix} \qquad (3.7)$$

The components of the Jacobian matrix are obtained by taking appropriate derivatives of Equation (3.3) .

The Equation (3.6) can be transformed to local Cartesian axes by the following transformation:

$$[e_u \; e_v \; e_w] = \begin{bmatrix} \frac{\partial u'}{\partial x'} & \frac{\partial v'}{\partial x'} & \frac{\partial w'}{\partial x'} \\ \frac{\partial u'}{\partial y'} & \frac{\partial v'}{\partial y'} & \frac{\partial w'}{\partial y'} \\ \frac{\partial u'}{\partial z'} & \frac{\partial v'}{\partial z'} & \frac{\partial w'}{\partial z'} \end{bmatrix} = \theta^T \begin{bmatrix} \frac{\partial U}{\partial X} & \frac{\partial V}{\partial X} & \frac{\partial W}{\partial X} \\ \frac{\partial U}{\partial Y} & \frac{\partial V}{\partial Y} & \frac{\partial W}{\partial Y} \\ \frac{\partial U}{\partial Z} & \frac{\partial V}{\partial Z} & \frac{\partial W}{\partial Z} \end{bmatrix} \theta \qquad (3.8)$$

where θ is the transformation matrix described in Appendix C .

Equation (3.8) can also be expanded with the use of the r.h.s of Equation (3.6); i.e. :

$$[e_u \ e_v \ e_w] = \theta^T J^{-1} \begin{bmatrix} \frac{\partial U}{\partial \xi} & \frac{\partial V}{\partial \xi} & \frac{\partial W}{\partial \xi} \\ \frac{\partial U}{\partial \eta} & \frac{\partial V}{\partial \eta} & \frac{\partial W}{\partial \eta} \\ \frac{\partial U}{\partial \varsigma} & \frac{\partial V}{\partial \varsigma} & \frac{\partial W}{\partial \varsigma} \end{bmatrix} \theta \qquad (3.9)$$

After finding the appropriate displacement derivatives with respect to the curvilinear axes from Equation (3.5) the results are:

$$\begin{bmatrix} e_u \\ e_v \\ e_w \end{bmatrix} = \sum_{i=1}^{9} [\bar{B}_i \ \theta^T \ \frac{1}{2} \ t_i \ (\varsigma \ \bar{B}_i + \bar{C}_i) \ \theta^T \ \Phi_i \ ] \begin{bmatrix} U_i \\ V_i \\ W_i \\ A_i \\ B_i \\ \Gamma_i \end{bmatrix} \qquad (3.10)$$

where

$$\bar{B}_i = \begin{bmatrix} B_1 & 0 & 0 \\ B_2 & 0 & 0 \\ 0 & 0 & 0 \\ 0 & B_1 & 0 \\ 0 & B_2 & 0 \\ 0 & 0 & 0 \\ 0 & 0 & B_1 \\ 0 & 0 & B_2 \\ 0 & 0 & 0 \end{bmatrix}, \quad \bar{C}_i = \begin{bmatrix} 0 & 0 & 0 \\ 0 & 0 & 0 \\ C_1 & 0 & 0 \\ 0 & 0 & 0 \\ 0 & 0 & 0 \\ 0 & C_1 & 0 \\ 0 & 0 & 0 \\ 0 & 0 & 0 \\ 0 & 0 & C_1 \end{bmatrix} \quad \Phi_i = \begin{bmatrix} 0 & 1 & 0 \\ -1 & 0 & 0 \\ 0 & 0 & 1 \end{bmatrix}. \qquad (3.11)$$

The elements of matrices $\bar{B}_i$ and $\bar{C}_i$ in Equation (3.12) are defined by the following:

$$\begin{aligned} B_{1i} &= A_{11} N_{i,\xi} + A_{12} N_{i,\eta} \\ B_{2i} &= A_{21} N_{i,\xi} + A_{22} N_{i,\eta} \\ C_{1i} &= A_{33} N_i \end{aligned} \tag{3.12}$$

where:

$$A = \theta^T J^{-1} = \begin{bmatrix} A_{11} & A_{12} & 0 \\ A_{21} & A_{22} & 0 \\ 0 & 0 & A_{33} \end{bmatrix} \tag{3.13}$$

3.5 Derivation of Element Matrices

The principle of virtual work is used in derivations of the expressions necessary for solving the problem by the finite element method. The incremental form of the virtual work equation is given by:

$$\int_V \Delta\epsilon^T D \delta\Delta\epsilon dV = \int_A T^T \delta\Delta u dA + \int_V F^T \delta\Delta u dV - \int_V \sigma^T \delta\Delta\epsilon dV \tag{3.14}$$

where: **T** is a vector of surface tractions ;

F is a vector of body forces ;

u is a displacement vector.

Other quantities are introduced in the next section.

3.5.1 Strains and Stresses

The vector of linear strains ϵ and Cauchy stresses σ which appear in Equation 3.15 can be expanded to:

$$\epsilon = \begin{bmatrix} \epsilon_{x'} \\ \epsilon_{y'} \\ \gamma_{x'y'} \\ \gamma_{x'z'} \\ \gamma_{y'z'} \end{bmatrix} = \begin{bmatrix} \frac{\partial u'}{\partial x'} \\ \frac{\partial v'}{\partial y'} \\ \frac{\partial \phi'}{\partial y'} + \frac{\partial v'}{\partial x'} \\ \frac{\partial u'}{\partial z'} + \frac{\partial w'}{\partial x'} \\ \frac{\partial v'}{\partial z'} + \frac{\partial w'}{\partial y'} \end{bmatrix} , \quad \sigma = \begin{bmatrix} \sigma_{x'} \\ \sigma_{y'} \\ \tau_{x'y'} \\ \tau_{x'z'} \\ \tau_{y'z'} \end{bmatrix} \qquad (3.15)$$

$\epsilon_{z'}$ and $\sigma_{z'}$ being neglected due to introduced shell assumptions which are also reflected in the derivation of the elasticity matrix **D** from the three dimensional case by requiring $\sigma_{z'} = 0$ and eliminating $\epsilon_{z'}$:

$$\mathbf{D} = \frac{E}{1-\nu^2} \begin{bmatrix} 1 & \nu & 0 & 0 & 0 \\ \nu & 1 & 0 & 0 & 0 \\ 0 & 0 & \frac{1-\nu}{2} & 0 & 0 \\ 0 & 0 & 0 & \frac{1-\nu}{2k} & 0 \\ 0 & 0 & 0 & & \frac{1-\nu}{2k} \end{bmatrix} \qquad (3.16)$$

The constant k in Equation 3.16 accounts for the difference between the assumed constant shear distribution through the thickness of the element and the actual distribution which is parabolic. The value of k is set to be 1.2 .

The linear strain vector ϵ in Equation 3.15 can be computed from the nodal displacements in the following way:

$$\epsilon = \sum_{i=1}^{9} \left[B_i \, \theta^T \, , \, \frac{1}{2} t_i \, (\zeta \, B_i + C_i) \, \theta^T \, \Phi_i \right] \begin{bmatrix} U_i \\ V_i \\ W_i \\ A_i \\ B_i \\ \Gamma_i \end{bmatrix} \tag{3.17}$$

where

$$B_i = \begin{bmatrix} B_1 & 0 & 0 \\ 0 & B_2 & 0 \\ B_2 & B_1 & 0 \\ 0 & 0 & B_1 \\ 0 & 0 & B_2 \end{bmatrix}_i \qquad C_i = \begin{bmatrix} 0 & 0 & 0 \\ 0 & 0 & 0 \\ 0 & 0 & 0 \\ C_1 & 0 & 0 \\ 0 & C_1 & 0 \end{bmatrix}_i \tag{3.18}$$

and B_1 , B_2 , C_1 are defined in Eq. (3.12).

3.5.2 Stiffness Matrix

The small displacement stiffness matrix for an element is computed by numerical integration. The contributions from all sampling points within an element are in the following form:

$$\bar{K}_{ij} = \begin{bmatrix} {B_i}^T \\ {B_i}^T \zeta + {C_i}^T \end{bmatrix} D \left[\, B_j \, , \, \zeta B_j + C_j \, \right] \tag{3.19}$$

$\bar{K}_{ij}$ is a 6 x 6 matrix expressed in local Cartesian coordinates and i, j are appropriate node numbers for the element. The element stiffness matrix is given by:

$$K_{ij} = \int_{-1}^{1} \int_{-1}^{1} \int_{-1}^{1} \begin{bmatrix} \theta & 0 \\ 0 & 1/2 \; t_i \; \Phi_i^T \; \theta \end{bmatrix} \bar{K}_{ij} \begin{bmatrix} \theta^T & 0 \\ 0 & 1/2 \; t_i \; \theta^T \; \Phi_i \end{bmatrix} \det(J) d\xi d\eta d\zeta \tag{3.20}$$

Kij is expressed in global Cartesian coordinates. The transformation matrices θ , Φ_i were introduced in Section 3.4.2 .

3.6 Elasto-Plastic Problem

The elasto-plastic stress analysis of plates and shells in this study is based on the Von Mises yield criterion and the Prandtl-Reuss equations. The evolution of the yield surface is described through an isotropic hardening model. The numerical algorithm is based on the tangential stiffness approach.

3.6.1 Governing Equations

The yield criterion determines the stress level at which plastic deformation begins. In general it can be expressed in the form:

$$f(\sigma_{ij}) = k(\kappa) \tag{3.21}$$

where f is a particular function of stress and k is a material parameter. The stress level at which plastic deformation begins according to the Von Mises yield criterion can be expressed by:

$$(J_2')^{1/2} = k \tag{3.22}$$

where J_2' is the second deviatoric stress invariant which can be explicitly written as:

$$J_2' = 1/2 \, (\sigma_{ij}' \, \sigma_{ij}') \; . \tag{3.23}$$

This numerical study defines a state of stress at a sampling point in terms of local Cartesian axes x', y' z' which conforms to plane stress conditions. Hence, J_2' can be written in the form:

$$J_2' = 1/2 \, (\sigma_{x'}'^2 + \sigma_{y'}'^2) + \tau_{x'y'}^{\,2} + \tau_{y'z'}^{\,2} + \tau_{x'z'}^{\,2} \, . \qquad (3.24)$$

Equation 3.21 can be also expressed as:

$$\bar{\sigma} = \sqrt{3} \, (J_2')^{1/2} = \sqrt{3} \, k \qquad (3.25)$$

where $\bar{\sigma}$ is the effective stress. In uniaxial tension $\bar{\sigma} = \sigma$ and therefore

$$k = 1/\sqrt{3} \, \sigma_o \qquad (3.26)$$

which represents a relation between the material parameter k and the yield stress in uniaxial tension σ_o .

The addidivity postulate is used in the definition of the incremental strains in the inelastic region:

$$d\epsilon_{ij} = (d\epsilon_{ij})_e + (d\epsilon_{ij})_p \qquad (3.27)$$

The elastic part is given by:

$$(d\epsilon_{ij})_e = \frac{d\sigma_{ij}'}{2\mu} + \frac{(1-2\nu)}{E} \, \delta_{ij} \, d\sigma_{kk} \qquad (3.28)$$

where ν is Poisson's ratio,

μ is Lame constant,

δ_{ij} is Kronecker delta .

The plastic flow after yielding is defined by:

$$(d\epsilon_{ij})_p = d\lambda \, \frac{\partial f}{\partial \sigma_{ij}} \qquad (3.29)$$

where $d\lambda$ is the plastic multiplier and f is a function which describes the yield surface. For $f = J_2'$ we have :

$$\frac{Zf}{\partial\sigma_{ij}} = \frac{\partial J_2'}{\partial\sigma_{ij}} = \sigma_{ij}' \tag{3.30}$$

Hence, Equation 3.29 becomes:

$$(d\epsilon_{ij})_p = d\lambda\ \sigma_{ij}' \tag{3.31}$$

which are known as the Prandtl-Reuss equations.

The evolution of the yield surface is described by isotropic strain hardening with the hardening parameter κ defined as:

$$\kappa = \bar{\epsilon}_p \tag{3.32}$$

where $\bar{\epsilon}_p$ is the effective plastic strain obtained by the integration of the incremental effective plastic strain given by:

$$d\bar{\epsilon}_p = \sqrt{(2/3)}\ [(d\epsilon_{ij})_p\ (d\epsilon_{ij})_p]^{1/2} \tag{3.33}$$

over the strain path.

The hardening law k = k(κ) can alternatively be expressed in terms of the effective stress $\bar{\sigma}$ as a function of $\bar{\epsilon}_p$:

$$\bar{\sigma} = H(\bar{\epsilon}_p) \tag{3.34}$$

or after differentiating

$$\frac{d\bar{\sigma}}{d\bar{\epsilon}_p} = H'(\bar{\epsilon}_p) \tag{3.35}$$

The hardening function H' can be determined from a simple uniaxial test when $\bar{\sigma}$ and $\bar{\epsilon}_p$ become σ and ϵ_p . Hence

$$H'(\bar{\epsilon}_p) = \frac{d\sigma}{d\epsilon_p} = \frac{d\sigma_o}{d\epsilon - d\epsilon_e} = \frac{1}{d\epsilon/d\sigma - d\sigma_e/d\sigma} \tag{3.36}$$

or

$$H' = \frac{1}{1/E_T - 1/E} = \frac{E_T}{1 - E_T/E} \qquad (3.37)$$

where E and E_T are tangential moduli for the uniaxial stress-strain relationship in the elastic and inelastic regions respectively.

3.6.2 Matrix Formulation

The theoretical relations presented in Section 3.6.1 were translated into matrix notation before being implemented in the computer program. This study follows the developments and notation from Owen and Hinton (1980) which are modified for the current analysis.

Equation 3.21 can be written as

$$f(\sigma) = k\ (\kappa) \qquad (3.38)$$

which can also take the following form:

$$F(\sigma,\kappa) = f(\sigma) - k(\kappa) \qquad (3.39)$$

The consistency condition requires that

$$dF = \frac{\partial F}{\partial \sigma} d\sigma + \frac{\partial F}{\partial \kappa} d\kappa = 0 \qquad (3.40)$$

which can also be written as:

$$a^T d\sigma - Ad\lambda = 0$$

with a^T and A given by:

$$a^T = \frac{\partial F}{\partial \sigma} = \left[\frac{\partial F}{\partial \sigma_x}, \frac{\partial F}{\partial \sigma_y}, \frac{\partial F}{\partial \sigma_z}, \frac{\partial F}{\partial \tau_{yz}}, \frac{\partial F}{\partial \tau_{zx}}, \frac{\partial F}{\partial \tau_{xy}} \right] \qquad (3.39)$$

$$A = -\frac{1}{d\lambda}\frac{\partial F}{\partial \kappa}d\kappa \quad . \tag{3.41}$$

Hence, Equation 3.27 can be expressed in matrix notation as

$$d\epsilon = D^{-1}\,d\sigma + d\lambda\,\frac{\partial F}{\partial \sigma} \quad . \tag{3.42}$$

The plastic multiplier $d\lambda$ is given by (Owen and Hinton 1981) :

$$d\lambda = a^T D\,d\epsilon \,/\, (A + a^T Da) \quad . \tag{3.43}$$

The value of A for conditions outlined in Section 3.6.1 is equal to H' which is defined by Equation 3.37 (Owen and Hinton 1980) . Hence, the elasto-plastic incremental stress-strain relation can be written as:

$$d\sigma = D_{ep}\,d\epsilon \tag{3.44}$$

where $D_{ep} = D - d_D\, d_D^{\,T} \,/\, (A + d^T a)$.

$d_D = D\,a$

3.6.3 Plasticity Algorithm

The abbreviated version of the plasticity algorithm used in this study is shown in Figure 3.4 . Graphical illustration of the equations included in Figure 3.4 is given in Figure 3.5 . The algorithm does the following:

- properly accounts for strain hardening;
- allows the integration point to yield within a load increment and then accounts for elastic and plastic components independently;

- monitors the evolution of the yield surface in order to reflect the current stress level for yielded points;
- keeps track of plastic strains;
- allows for unloading;
- makes large load steps possible without penalty in accuracy, convergence or drifting from equilibrium.

3.7 Numerical Procedures

A general macro flow chart of a computer program is presented in Figure 3.6. The names of major subroutines are printed using capital letters and further expanded with small letters to provide a self-explanatory layout of the program.

3.7.1 Choice of a Solution method

A few solution methods are implemented in the computer program:

- Initial Stiffness Method ;
- Newton-Raphson Method ;
- Modified Newton-Raphson Method ;
- re-computation of a stiffness matrix after the first iteration of each load increment ;
- re-computation of a stiffness matrix after the first and second iterations of each load increment.

Most of the numerical examples presented in this study used the Newton-Raphson Method.

3.7.2 Numerical Integration

A Gaussian integration method was used in numerical evaluation of surface and volume integrals. A 3x3 scheme of sampling points was found to be both necessary and sufficient to integrate the required quantities exactly. Each of the sampling points within an element was allowed to carry an independent set of material properties. An example of the distribution of material properties within elements which are located in the corner zone of an RHS and are affected by strain hardening during the forming process is illustrated in Figure 3.7 . One row of sampling points near the corner carried the material properties of the coupons removed from this area after the testing of RHS joints. The rest had the properties of flat portions of RHS. The properties of of the weldment were carried by three integration points as shown in Figure 3.8.
The material properties of the RHS used in this experimental study are listed in Table 4.8. The same properties are later implemented in the numerical simulation of RHS joint configurations which are identical to those seen in testing.

3.7.3 Convergence Criteria

The following convergence criteria were used in the present finite element analysis:

energy tolerance

$$\frac{\Delta \underline{U}^T \left({}^{t+\Delta t}\underline{R} - {}^{t+\Delta t}\underline{F} \right)}{\Delta \underline{U}^T \left({}^{t+\Delta t}\underline{R} - {}^{t}\underline{F} \right)} \leq \text{ETOL} \quad , \qquad (3.45)$$

where: $\Delta \underline{U}$ is a vector of nodal point incremental displacements ;

$^{t+\Delta t}\underline{R}$ is a vector of externally applied nodal point loading at time t+Δt ;

$^{t+\Delta t}\underline{F}$ is a vector of nodal point forces corresponding to internal stresses at time t+Δt ;

ETOL is an energy convergence tolerance

force tolerance

$$\frac{\| {}^{t}\underline{R} - {}^{t+\Delta t}\underline{F} \|_2^F}{\text{RNORM}} \leq \text{RTOL} \qquad (3.46)$$

where $\| \ldots\ldots \|_2^F$ denotes the Euclidean norm and only the nodal point forces are included.

RNORM is a reference force

RTOL is a force convergence tolerance

moment tolerance

$$\frac{\| {}^{t}\underline{R} - {}^{t+\Delta t}\underline{F} \|_2^M}{\text{RMNORM}} \leq \text{RTOL} \qquad (3.47)$$

where RMNORM is a reference moment

and only the nodal points are included.

In addition , two other quantities were monitored throughout the analysis:

- maximum value of incremental displacements
- ratio of maximum value of displacement in the n-th iteration to the maximum value of a displacement in first iteration of a given load increment.

The dominant criterion used throughout the analysis was the energy criterion. The ETOL was usually in the range of 0.001 to 0.005 . In general a slower convergence was noticed in the analysis of three dimensional structures with non-smooth transitions between the elements than in smooth plates and shells.

3.8 Verification Examples

Two verification examples which check the validity of the numerical model are presented in this section. The first example, shown in Figure 3.9, verifies the elasto-plastic model through a comparison of the load-deflection curve at the centre of a simply supported plate 0.254x0.254x0.010 m with the results presented by Stanton and Schmit (1970) . A 4 x 4 finite element grid for one quarter of a plate was used. The material properties are as follows: E= 689.5 MPa; E'= 0.1 and σ_y = 206.85 kPa . The results of the present study and those of Stanton and Schmit remain in satisfactory agreement throughout the loading history. The second example is for a plate-to-RHS connection tested by Dixon (1982). The dimensions of the plate and RHS are shown in Figure 3.10a. A finite element grid of one quarter of the the structure is illustrated in Figure 3.10b . A comparison of the results of the present study and the experimental measurements obtained by Dixon (1982) is shown in Figure 3.11. A satisfactory agreement was found between the two curves within the validity of the model; i.e. for elasto-plastic, small deformation analysis. It is believed that a discrepancy starts to appear once the membrane stresses become significant in the walls of an RHS, which is beyond the scope of this study.

A verification of the numerical model of HSS joints with the present experimental program will be included in Chapter 5.

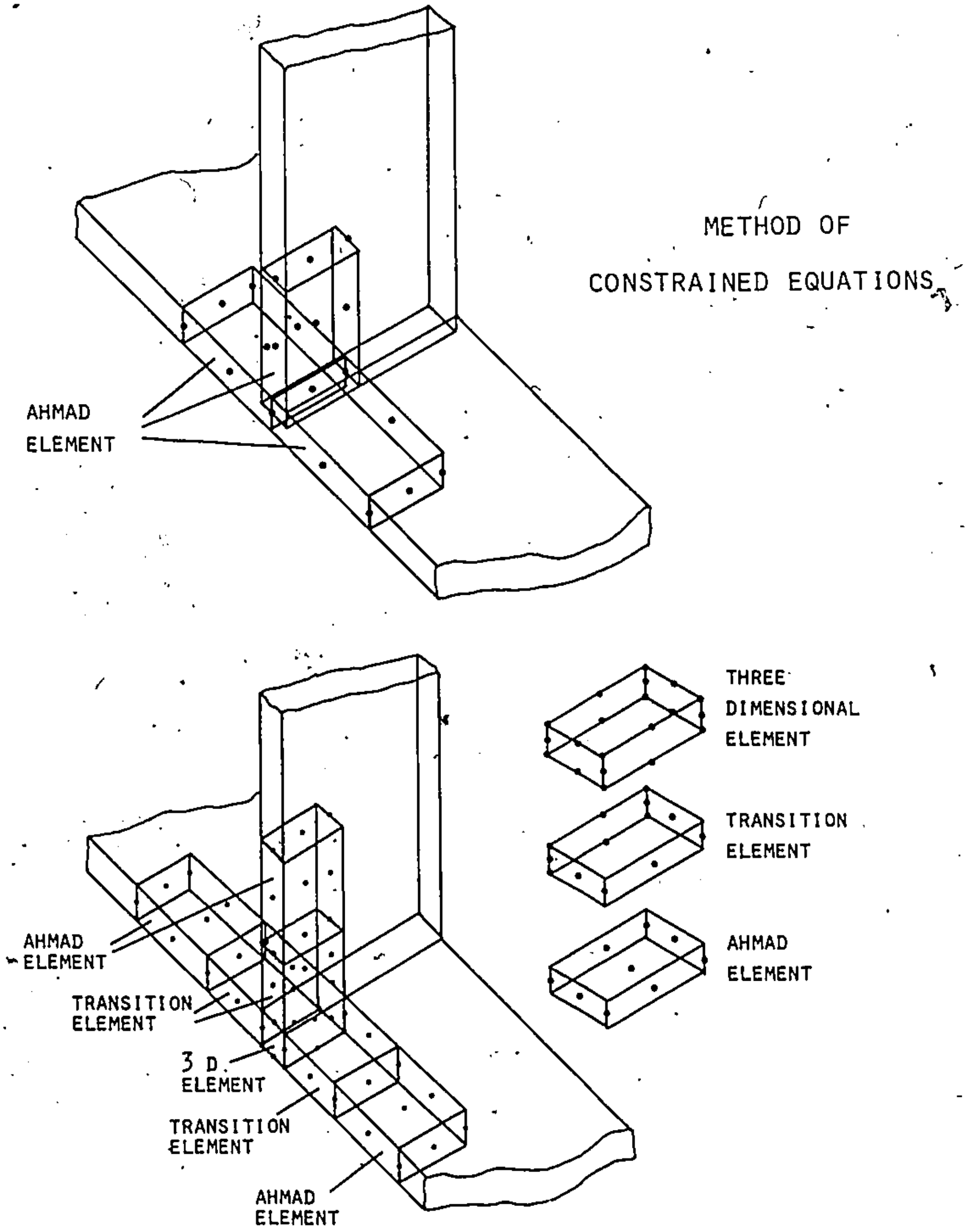

Figure 3.1 Possible Methods of Discretization for Intersections

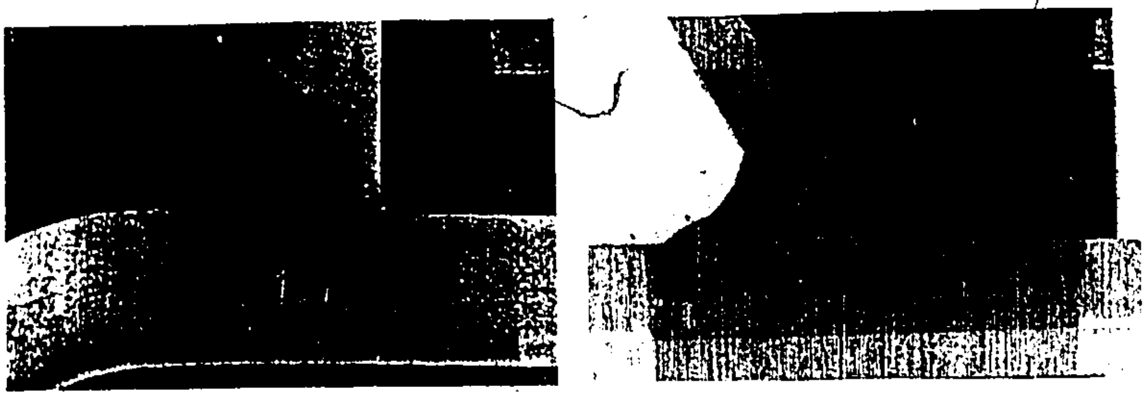

Figure 3.2 Weld geometry

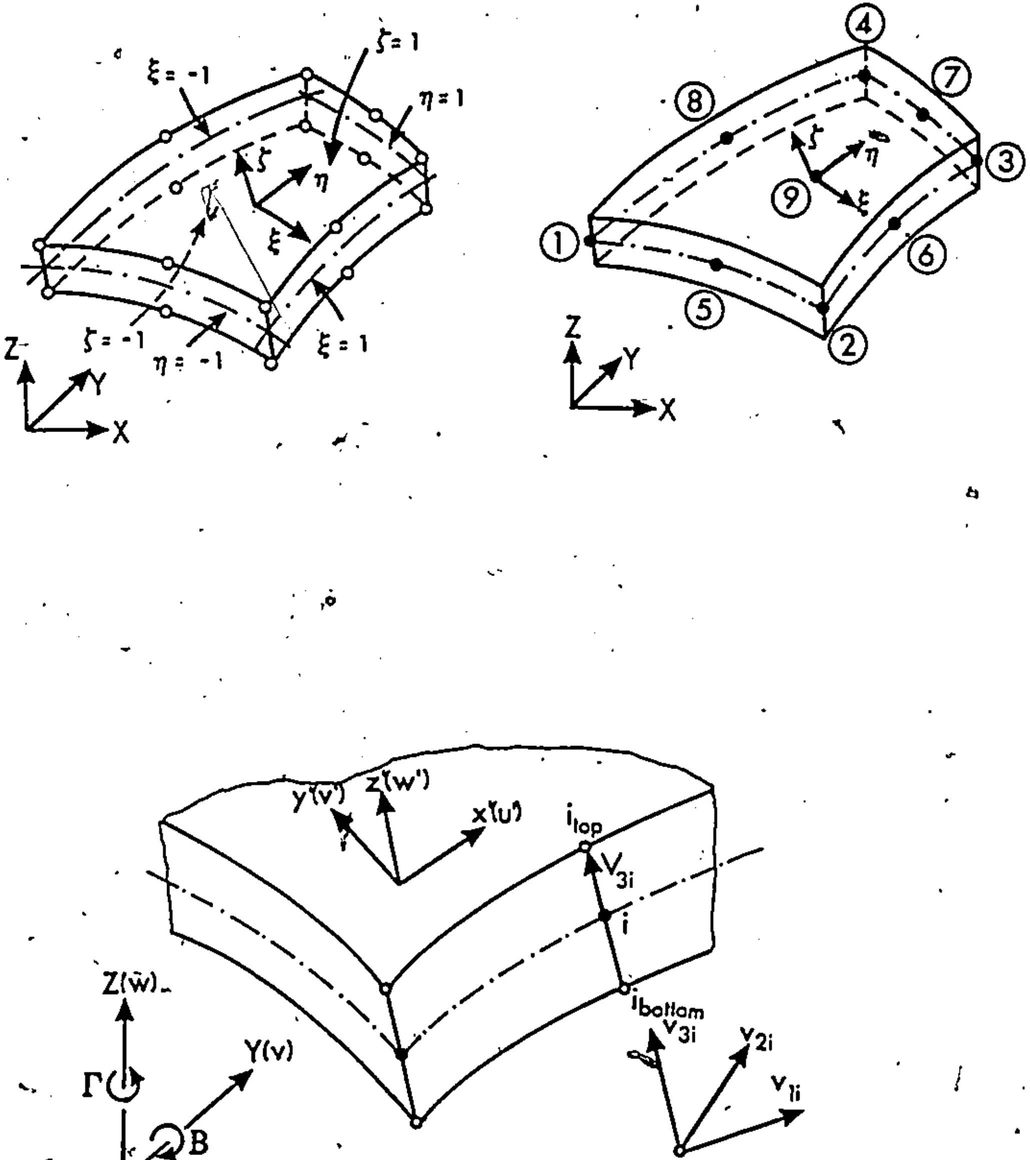

Figure 3.3 Shell Element

```
apply residual forces $\Phi^{r-1}$
compute $du^r$ and $d\epsilon^r$
compute $d\sigma_e^r = D\,d\epsilon^r$
find $\sigma_e^r = \sigma^{r-1} + d\sigma_e^r$
check $\bar{\sigma}^{r-1} > \sigma_y = \sigma_y^o + H'\bar{\epsilon}_p^{r-1}$
Y ⇓
    point previously yielded
    check $\bar{\sigma}_e^r > \bar{\sigma}^{r-1}$
    Y ⇓
        stress is increasing
        $\sigma^r = \sigma^{r-1} + d\sigma_e^r - d\epsilon_p^r$
        find $d\bar{\epsilon}_p^r$ and add to $\bar{\epsilon}_p^{r-1}$
        scale stresses $\sigma^r = \sigma^r(\sigma_y^o + H'\bar{\epsilon}_p^r)/\sigma^r$
    N ⇓
        elastic unloading
        $\sigma^r = \sigma^{r-1} + d\sigma_e^r$
N ⇓
    point not previously yielded
    check $\bar{\sigma}_e^r > \bar{\sigma}_y^o$
    Y ⇓
        point just yielded
        $\sigma^r = \sigma^{r-1} + (1-R)d\sigma_e^r$
        where
        $R = (\bar{\sigma}_e^r - \sigma_y)/(\bar{\sigma}_e^r - \bar{\sigma}^{r-1})$
        compute $d\epsilon_p^r$ corresponding to $Rd\sigma_e^r$
        update stresses $\sigma^r = \sigma^r + Rd\sigma_e^r - Dd\epsilon_p^r$
        find $d\bar{\epsilon}_p^r$ and add to $\bar{\epsilon}_p^{r-1}$
        scale stresses $\sigma^r = \sigma^r(\sigma_y^o + H'\bar{\epsilon}_p^r)/\bar{\sigma}^r$
    N ⇓
        point is still elastic
        $\sigma^r = \sigma^{r-1} + d\sigma_e^r$
```

Figure 3.4 Plasticity Algorithm

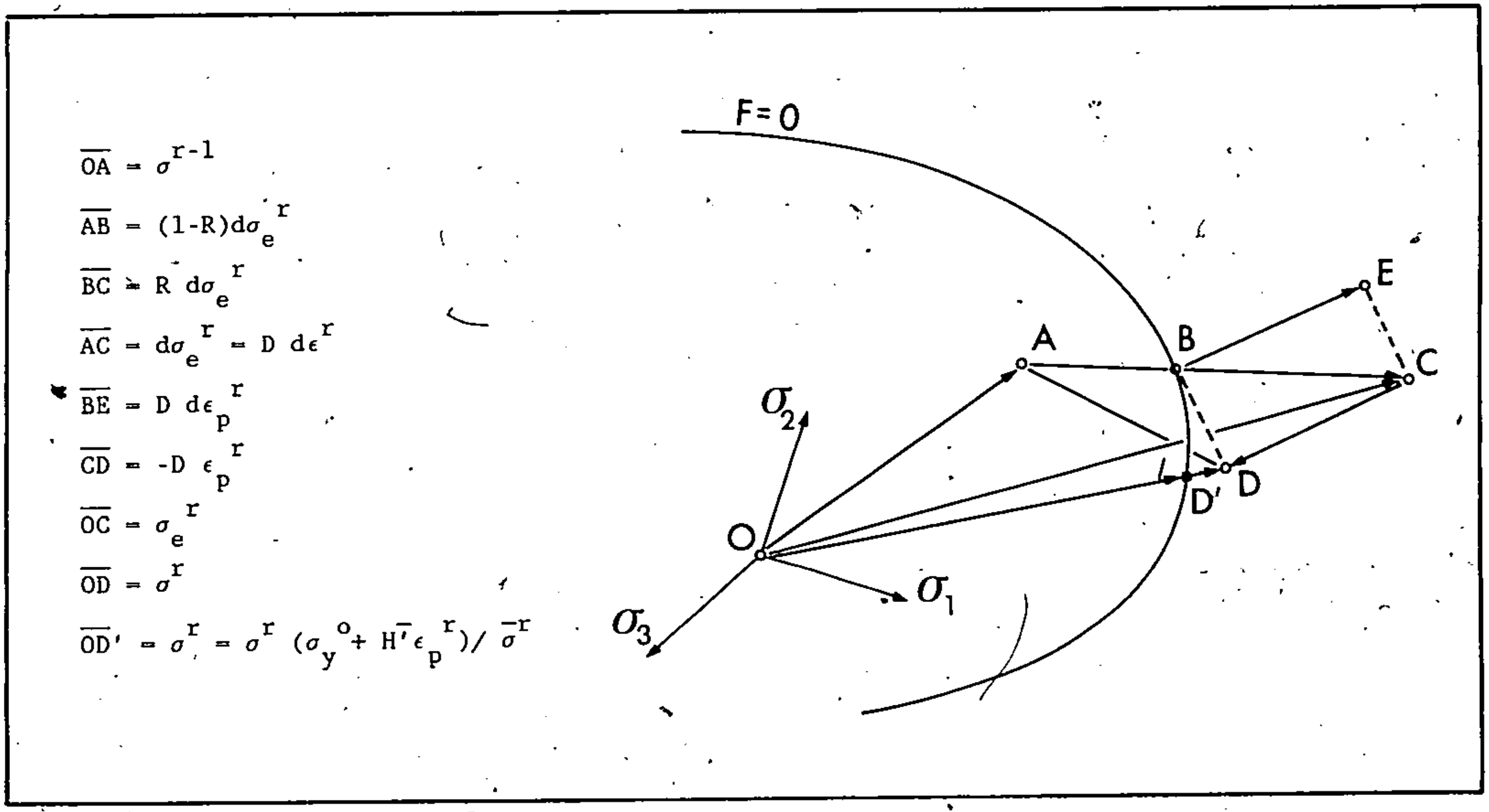

$\overline{OA} = \sigma^{r-1}$

$\overline{AB} = (1-R)d\sigma_e^{\,r}$

$\overline{BC} = R\ d\sigma_e^{\,r}$

$\overline{AC} = d\sigma_e^{\,r} = D\ d\epsilon^r$

$\overline{BE} = D\ d\epsilon_p^{\,r}$

$\overline{CD} = -D\ \epsilon_p^{\,r}$

$\overline{OC} = \sigma_e^{\,r}$

$\overline{OD} = \sigma^r$

$\overline{OD}' = \sigma^r = \sigma^r\ (\sigma_y^{\,o} + H'\bar{\epsilon}_p^{\,r})/\ \bar{\sigma}^r$

Figure 3.5 Incremental Stresses in Elasto-Plastic Space

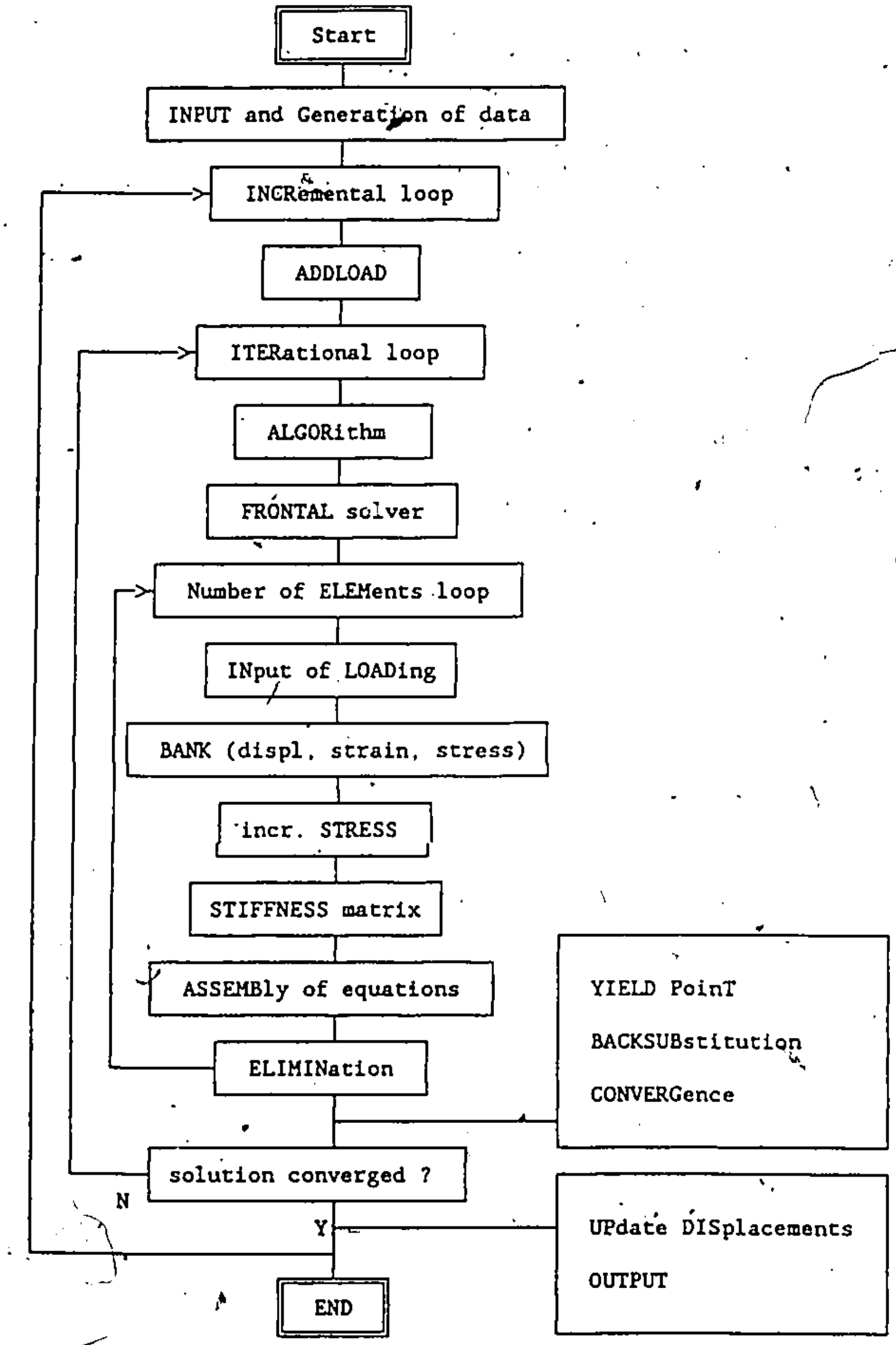

Figure 3.6 Macro Flowchart for Computer Program

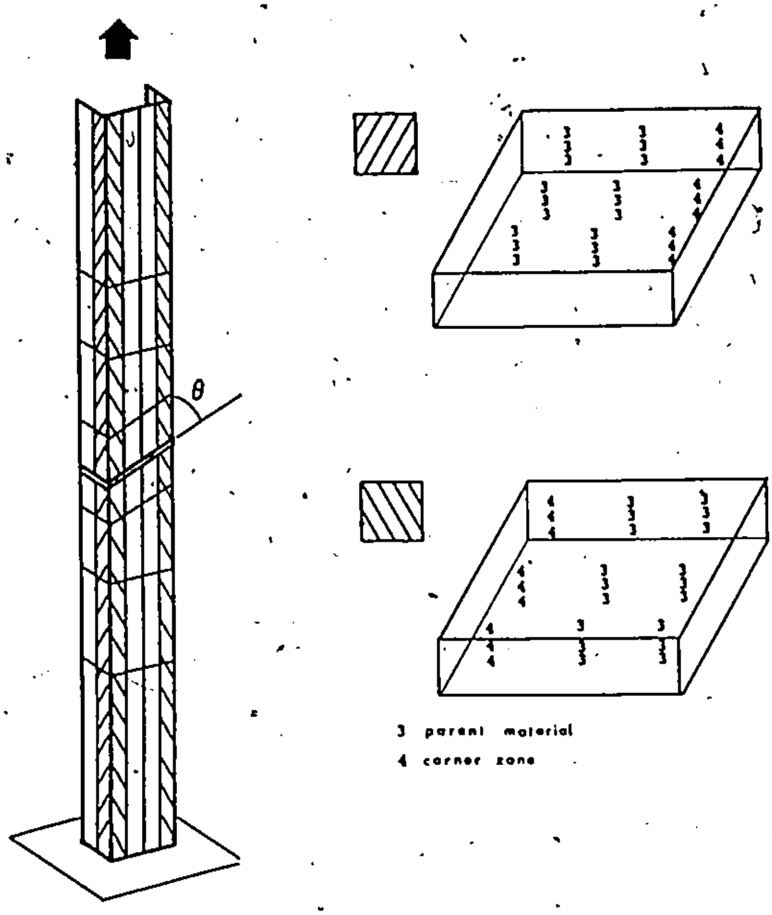

Figure 3.7 Distribution of Sampling Points in Corner Zone

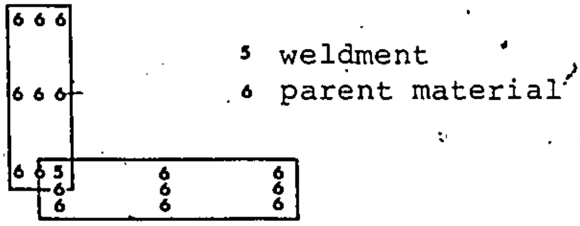

Figure 3.8 Distribution of Sampling Points in Weld Zone

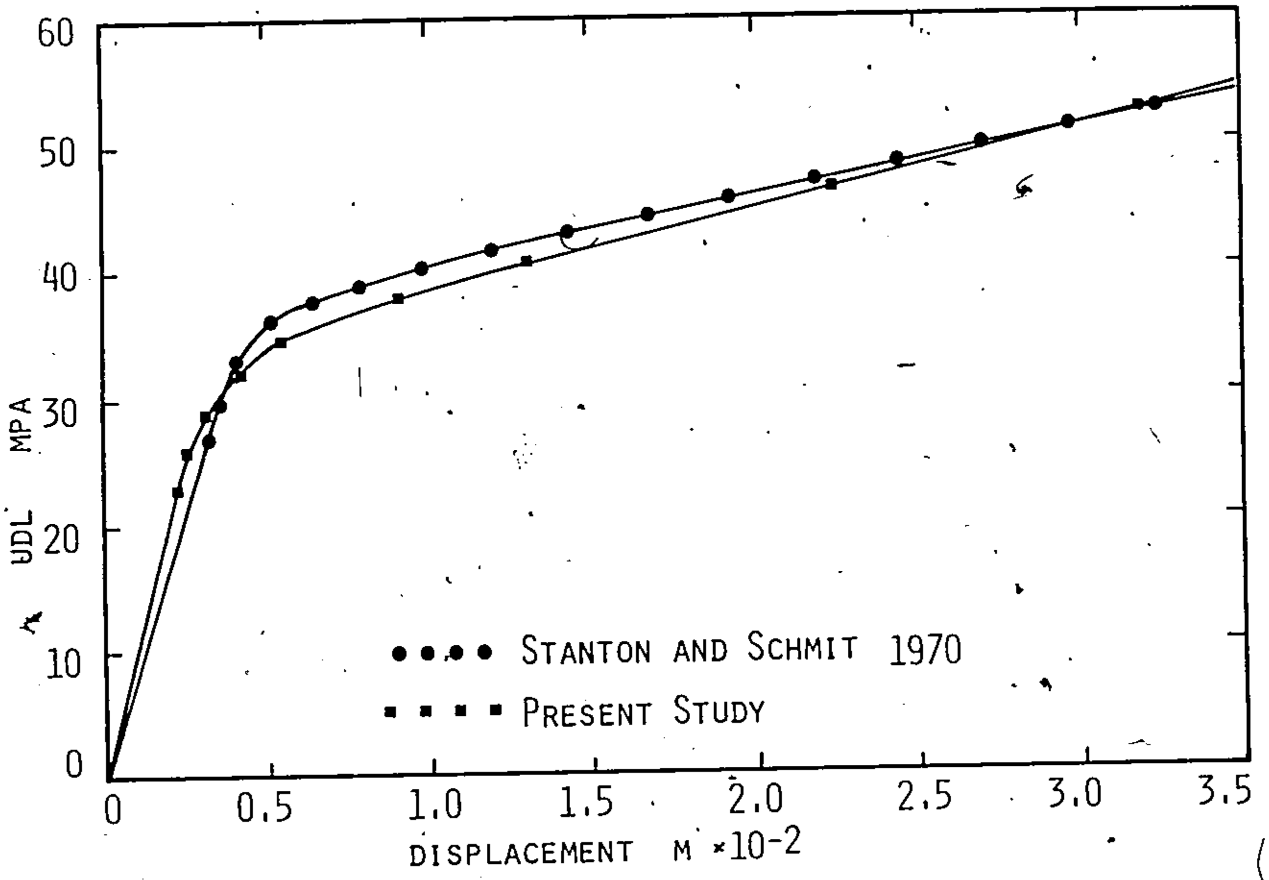

Figure 3.9 Load-Deflection Curves for Elasto-Plastic Plate

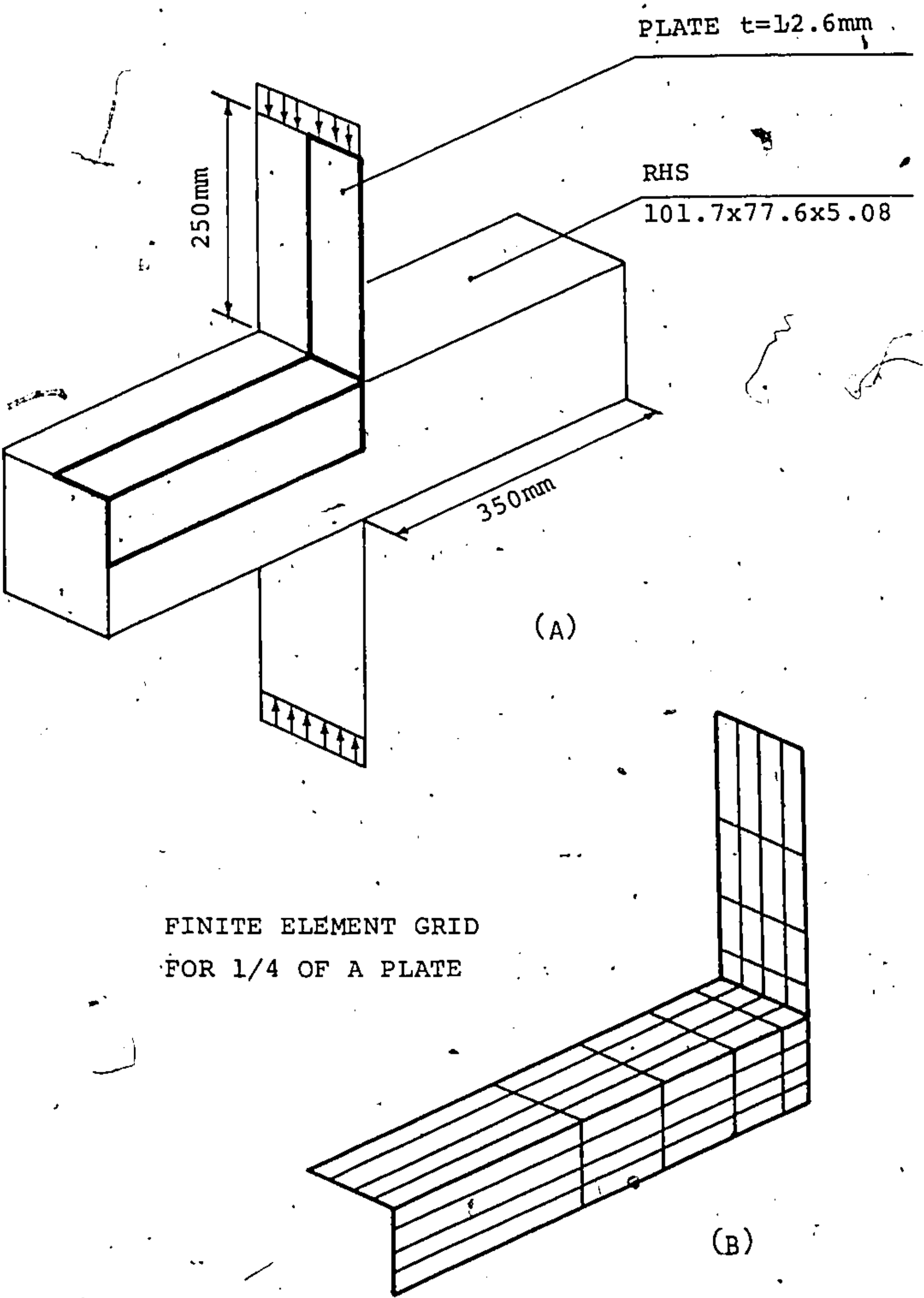

Figure 3.10 Plate-to-RHS Verification Example

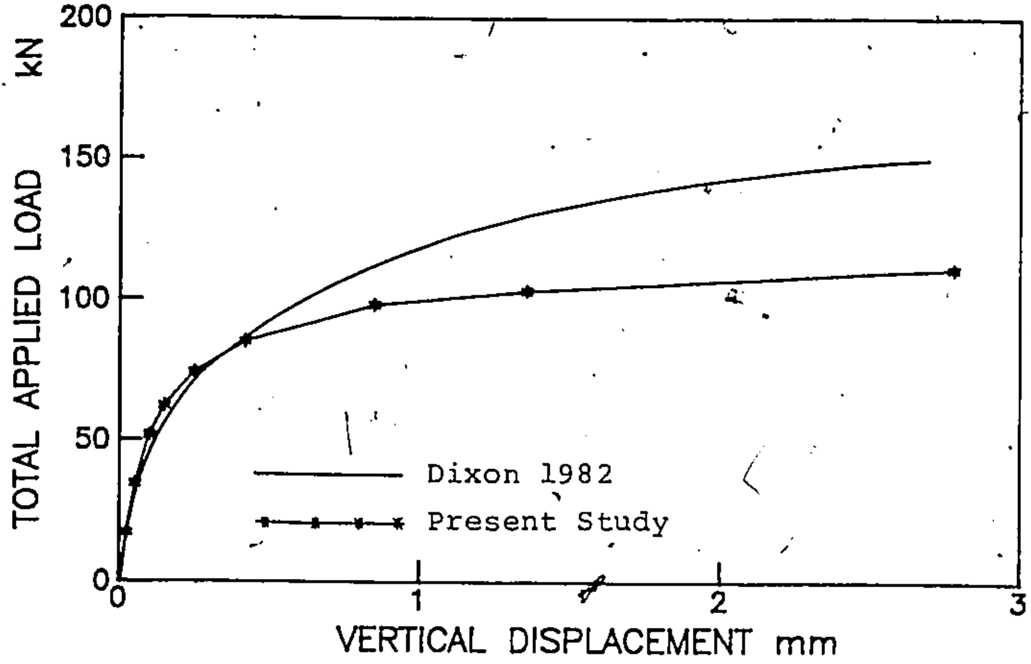

FIGURE 3.11 Load-Deflection Curves for Plate-to-RHS Connection

CHAPTER 4

EXPERIMENTAL PROGRAM

4.1 Introduction

The experimental program reported herein was part of an investigation entitled "Weldment Design for Hollow Structural Section Joints" at the University of Toronto (Frater 1986). It included 26 isolated RHS joints as part of a study on connections in Warren or Pratt trusses. The testing arrangement used only two branch members, separated by a plate or RHS, and subjected the branches to axial tensile forces to simulate the tension branch to chord member weld junction in an RHS truss joint. The framework of the testing made it possible to investigate the effects of a few main parameters which influence the response of a branch in the vicinity of the chord. The testing started with two branch members in tension separated by a rigid plate. In the next step, a square hollow section was substituted for the plate to simulate the action of a chord. In both cases the angle of inclination for the branch member was varied over the values of 90°, 60° and 30° .

A previous analytical study of a gap K-joint by the author (Ostrowski 1984) has shown that it is essential to know the stress distribution around the perimeter of a branch in order to model the joint without the three dimensional representation of the branch members. An experimental program dedicated to a rational design of weldments provided a suitable base for comprehensive strain measurements around the joint. These measurements were used to obtain a better understanding of the flow of internal forces, and hence the distribution of stresses, in the branch member walls.

This chapter presents the results obtained in experiments as well as their interpretation relative to current design recommendations for RHS gap joints. The material included gives a full history of loading up to failure. In this way the experimental and the numerical results are complementary because the numerical model describes the joint behaviour at the initial loading stages up to the serviceability load level. The strain measurements collected during the experiments will form the basis for the verification of numerical results in Chapter 5.

4.2 General Description

The testing program included 26 joint sub-assemblies, an example of which is shown in Figure 4.1 . A summary of the experimental program is illustrated in Figure 4.2 . Table 4.1, which was compiled based on Frater (1986), lists all the joints tested, the ultimate load attained , the weld size measurements, and the types of failure modes. Further details of the tests are given elsewhere (Frater 1986, Packer and Frater 1986 , Packer and Frater 1987), with an analysis of the weldment performance and weldment recommendations.

The joints were grouped according to their basic characteristics in three phases. Phase 1 represented two square hollow sections in tension separated by a 19 mm plate which was welded at a 90° angle to the member axis. In Phases 2A and 2B the same plate was inclined at angles of 60° and 30° . In Phase 3 the plate was replaced by a square hollow section of dimensions 203.2 x 203.2 x 12.7 mm with the branch members inclined at 90° , 60° and 30° for Phases 3A , 3B and 3C respectively. Additional chord end stiffening plates were used in Phase 3 to prevent the deformation of the chord cross section (see Figure 4.2). The object in Phase 3 was to simulate the action of a gap region in a gapped K-joint (see Section 2.3) at one side of the branch member and a remote end of the chord at the other side of the branch member. In all three phases the branch members were made from 127.0 x 127.0 x 9.53 mm hollow section. Both HSS sections used were made of 350 W grade steel, class H.

4.3 Instrumentation

The experiments were performed in a 2750 kN capacity MTS Universal Testing Machine under displacement control (see Figure 4.1). All the specimens were subjected to a static tension load with a stroke rate between 0.005 mm/s and 0.01 mm/s .

Measurements on the test specimens were collected by means of strain gauges, 45 degree strain gauge rosettes and Linearly Varying Displacement Transducers (LVDT's). The strain gauges and rosettes were used to detect the distribution of strains in the walls of a branch member in close proximity to the weld. Additional strain gauges were mounted longitudinally on the branch member and at midwall locations remote from the joint to check the axial load distribution between the branch member walls in areas remote from the connection. The LVDT's provided an estimate of the weld deformation in the direction parallel to the member axis. The experiment was monitored by real-time plots of the applied load versus time and the applied load versus the machine stroke displacement. Occasionally the current values of strains at different locations were printed to control the progress of the experiment.

4.4 Strain Measurements

Tables 4.2 through 4.6 summarize the locations of strain gauges and rosettes on the specimens tested. The total number of mounted strain gauges listed in the table may vary from those illustrated on a sketch because only the strain gauges in the vicinity of the weld are shown. Each of the last four columns of every table corresponds to one face of a branch member . Each face is described by numbers that are allocated to corner positions of the square branch. The location of the strain gauges and rosettes is given only in a schematic representation. An example of the sets of strain gauges and rosettes used is shown in Figures 4.3 and 4.4 . Sketches of selected specimens and plots of representative test results for Phases 2A, 2B, 3A, 3B and 3C are illustrated in Figures 4.5-4.9, 4.10-4.14, 4.15-4.19, 4.20-4.24 and 4.25-4.29 respectively. The initial figure for each specimen shows detailed positions of the strain gauges and rosettes; load vs. strain graphs for the toe and heel areas (strain gauges) and load vs. major and minor principal strains graphs for the sidewalls (rosettes) follow in sequence. Each of the examples illustrates the essential trends in the response of the specimens to the applied loading. The terminology used in this section is analogous to that used in Chapter 2. In most cases the distance between a strain gauge and the weld toe was in the order of 5-10 mm . The gauge length of the strain gauges used was 10 mm. Hence, the centre point of a strain gauge was positioned about 10-15 mm from the weld toe. The length of one leg of the fillet varied between 5 and 15 mm. The total distance between the centre point of the gauge and the intersection of the external surfaces of the branch and the chord (or the plate) was, therefore, in the range of 15 to 30 mm .

During the experimental program the strain gauges and rosettes were positioned at different locations. After each batch of specimens (2-3 joints) the results were analyzed and new positions for strain gauges were recommended. Near the end of the testing program a typical arrangement included 3-5 strain gauges on the branch member walls at the toe and the heel (see the strain gauges at the toe of Specimen 12 in Figure 4.3) as well as three 45 degree rosettes mounted on the sidewalls of the branch (see the sidewall of Specimen 14 in Figure 4.4). Early in the experimental program it was revealed that the direction of the major principal axis at sidewall locations varied with the loading.

Phase 1 included two RHS members in tension separated by a 19 mm plate welded transversely to the branch member axis at an angle θ = 90°. Details of this series are described in Frater (1986).

Phase 2A is represented by Specimen 12 shown in Figure 4.5 with an angle θ of 60° . The strains measured near the failure load for the toe were higher than the values of strains for the heel (see Figures 4.6 and 4.7).* This indicates that the toe area is the critical region of the joint in such a configuration. The rosettes located on the sidewalls of the branch allowed for monitoring of the variation of the strain values along the principal axes as illustrated in Figures 4.8 and 4.9 for major and minor principal axes respectively. The directions of the major principal axes of strain were initially co-linear with the branch member axis. When the loading increased, these directions changed continuously; near failure their positions were as illustrated in Figure 4.30a . The rosettes located on the sidewall near the toe and at the midwall location indicated higher major principal strains than near the heel. However, the rosette near the toe registered a negative value of strain along the minor principal axis, clearly indicating that this location is the most critical of the three positions for the rosettes located on the sidewall of Specimen 12.

Phase 2B consisted of specimens with an angle of inclination of 30°, an example of which is shown in Figure 4.10 for Specimen 14 . A comparison similar to that made for Phase 2A can be made for the toe (Figure 4.11) and the heel (Figure 4.12) areas. It is apparent that the strains at the heel are higher than those at the toe. This conclusion is opposite to the one above for Specimen 12. Moreover, this difference existed throughout the loading history and not only near failure as in Test 12 (see Figures 4.6 and 4.7). It should be stressed that the only parameter other than the weld size that is different for the two joints is the angle θ. The history of strain values in the direction of the major and minor principal axes for Specimen 14 is shown in Figures 4.13 and 4.14 . The position of the principal axes at failure is illustrated in Figure 4.30b . It is clear that the most critical region on the sidewall of Specimen 14 is near the heel.

The direction of the major principal axis of strain near failure did not deviate substantially from the direction of the longitudinal axis of the branch member in either Specimen 12 or Specimen 14 . This feature appears to be characteristic of specimens in Phase 2 with the branch connected to a rigid base (19 mm plate). Examples of failure modes that occurred in Phase 2 are shown in Figure 4.31 for Specimen 10 (same configuration as Specimen 12) and in Figure 4.32 for Specimen 13 (same configuration as Specimen 14). It is important to notice that the failure was initiated near the toe for Specimen 10 (θ=60°) and near the heel for Specimen 13 (θ=30°). Exactly the same regions were found to be critical based on an analysis of the strain measurements.

<u>Phase 3A</u> is represented by Specimen 18 (Figure 4.15). The difference between the strain values at the toe and the heel is illustrated in Figures 4.16 and 4.17 . It was characteristic of Phase 3A

specimens that the strains in the middle of the wall at the heel were negative (compression), despite the branch member being loaded in tension. Only corner positions at the heel experienced tensile strains. The comparison of values for the major and minor principal strains for rosettes located on the sidewalls of the branch are shown in Figures 4.18 and 4.19 . It is evident that all three major principal strains were of approximately equal value throughout the loading history. However, among the minor principal strain values only the midwall location shows a monotonic increase up to the ultimate load. The corner positions of rosettes indicate that near the failure load the minor principal strain values become negative. The directions and magnitudes of the principal strains near failure for Specimen 18 are illustrated in Figure 4.33 . The direction of the major principal strains in the corner locations on the sidewall bisect the 90° angle between the branch wall and the chord wall.

Additional strain measurements were collected on Specimens 17 and 19 which were of the same nature as Specimen 18. The sketches of both specimens and the relevant graphs are included in Appendix D along with a brief interpretation of the results. Specimen 17 carried three rosettes in the toe area. The main objective was to reveal the direction of the major principal axis of strain in the corner positions of the toe. It was found that the directions of the major principal axis of strain are inclined to the longitudinal branch member axis at an angle of about 45° for most of the loading history. In Test 19 rosettes were positioned on both sidewalls of the branch to check for symmetry in the distribution of strains. The graphs presented in Appendix D indicated an almost perfect symmetry in the strain distribution on both sides of Specimen 19. The major trends observed for Specimen 18 were also confirmed for Specimen 17 and 19.

Phase 3B included Specimen 25 shown in Figure 4.20 . In testing, the highest values of strain at the toe and the heel were at about the same level. However, the three middle strain gauges at the heel showed consistently lower strain levels. This result clearly indicates that only the corner zones at the heel are fully effective in resisting the load. At the toe, up to a level of about 5000 microstrain, all strain gauges showed comparable strain levels. From then on only the corner positions deformed monotonically up to failure. The values of the strains along the major and minor principal axes for rosettes 1,2 and 3 along the branch member sidewall are shown in Figures 4.23 and 4.24 . At a load level of about 1100 kN, which corresponds to first yielding in the corner zones at the heel (see Figure 4.22), the value of strain along the major principal axis of strain for rosette 3 suddenly dropped (see Figure 4.23). Shortly after, a similar drop occurred for rosette 2 (see Figure 4.23) and only rosette 1 (near the toe) indicated a monotonic increase of strains along the major principal axis. This can be explained by a redistribution of internal forces at the heel and the shift of a resultant force towards the toe area which thus became ~~a~~ critical region in Test 25 . This is confirmed in Figure 4.34a by an illustration of directions and magnitudes for principal strains near failure.

Phase 3C is represented by Specimen 26 shown in Figure 4.25 . All three strain gauges at the heel (see Figure 4.27) showed the same levels of strains throughout the loading history. At the toe (see Figure 4.26), the centre strain gauge indicated consistently lower values than strain gauges at the corner locations. Hence, the toe appears not to be fully effective in resisting the load. Near failure the strains at the heel became higher than at the toe with the latter dropping in value near the limit. Only two rosettes were mounted on Specimen 26 as shown in Figure 4.25 . The values of strains along the principal axes of strain are illustrated in Figures 4.28 and 4.29 for the major and minor principal axes of strain respectively. The strain values along the major principal axis for rosette 2 (near the heel) were substantially higher than for rosette 1 (near the toe). In addition, the strains along the minor principal axes are compressive for most of the loading history with the strains for rosette 2 being lower than for rosette 1. This brings one to the conclusion that the heel area is the critical region, which is confirmed by the illustration of strain values along the principal axes of strain near failure as shown in Figure 4.34b.

The failure modes for specimens 25 and 26 are illustrated in Figures 4.35 and 4.36 respectively. As in Phase 2, (see Figures 4.31 and 4.32), the specimen with the angle of inclination for the branch member being 60° failed first near the toe (Test 25) while the specimen with the angle of 30° ruptured near the heel (Test 26).

It is worth pointing out that the direction of the major principal axis in the critical regions for Specimen 25 with θ = 60° (at the toe), and Specimen 26 with θ = 30° (at the heel), almost matched the directions which bisect the angles of consideration.

4.5 Results for Rigid and Flexible Bases

The effect of a rigid base versus a flexible base condition on the distribution of strains in the walls of a branch was ascertained from the results of several tests. The rigid base condition was simulated in Phases 1, 2A and 2B of the experiments by inserting a thick plate between two RHS branch members. The flexible base condition was simulated by welding two RHS branch members to a larger size RHS chord which took place in Phases 3A, 3B and 3C.

For rigid base (Test 12) and flexible base conditions (Test 25) the following observations were made for an angle θ = 60° (see Figure 4.37):

- in both instances the centre gauge at the toe shows higher strains than the gauges near the corners
- the centre gauge at the heel of the flexibly connected branch registered much lower strains than near the corners.

A similar comparison was made for an angle θ = 30° (see Figure 4.38), which involved Test 14 (rigid base) and Test 26 (flexible base). It was noted that:

- the centre gauge at the toe location for both tests near failure indicated a lower level of strains than near the corners

- the heel area for $\theta = 30^\circ$ in both conditions was fully effective.

The effectiveness of the toe area does not appear to depend on the flexibility of the base. It depends on the angle of inclination of the branch member and either increases ($\theta = 60^\circ$) or decreases ($\theta = 30^\circ$) from the point where the load vs. strain curve becomes nonlinear shortly before failure. Hence, one can assume that within the working load range, the toe area is fully effective for both the rigid and flexible conditions.

The heel area for the rigid base conditions is also fully effective. The effectiveness of the heel area for the flexible base conditions is illustrated in Figure 4.39 . For $\theta = 90^\circ$ (Phase 3A) the strain levels at the heel indicate compression. With a reduction in θ the strains gradually changed to an almost no strain situation for $\theta = 60^\circ$ (Phase 3B), and to a fully effective heel area for $\theta = 30^\circ$ (Phase 3C).

Rigid or flexible base conditions also affect the distribution of stresses on the sidewalls of the branch members as discussed in the previous section. The directions of the major principal axes are almost parallel to the branch member's longitudinal axis for the rigid base conditions of Specimens 12 and 14. The flexible base substantially alters the flow of internal forces in the sidewalls of the branch in the vicinity of the connection compared with a rigid base. Near failure, the direction of the major principal axis of strain in the critical region tends to bisect the angle of consideration, θ.

4.6 LVDT Measurements

Linearly Varying Displacement Transducers were introduced to measure the weld deformation over a 50 mm length which included the weld and part of the RHS wall. The displacement obtained at three sides of a branch: at the toe, the heel, and one side, gave a good estimate of a relative displacement between the base and a point located on a branch wall 50 mm above. However, it is difficult to extract exactly the deformation of the branch walls beyond the weld toe. The strain gauges located within the 15-30 mm range of the plunger of the LVDT often indicated strains in the order of 5000-10000 microstrain, i.e. several times the elastic limit. Nevertheless, the recorded LVDT displacements are useful in determining the effect of the weld size on the deformation of a branch in the immediate vicinity of a connection.

The conclusions based on the LVDT readings are consistent with those for strain readings for the toe and heel locations. For example, with the angle of inclination of the branch of 60° the toe experiences higher deformation than the heel; with the angle of 30° the opposite takes place. Examples of measurements recorded by LVDT's in the current experimental program can be found in Frater (1986).

4.7 Material Properties

The material properties were measured for both RHS sections, a 19 mm plate (used in Phases 1 and 2), and for the weld consumables.

A standard tensile coupon test was performed for the plate coupons and the flat portions of the HSS sections. The RHS corner coupons were prepared to ensure unchanged cross-section geometry of the corner zone. The weld consumable coupons were prepared for two different electrode diameter sizes (D=1.2 mm and D=1.6 mm) according to existing standards. All material properties obtained are listed in Table 4.7 . A typical trilinear stress-strain relationship for the materials from which coupons were tested is illustrated in Table 4.8. It includes the characteristic parameters for each stress-strain curve (see Table 4.8B), which will be later implemented in the numerical analysis. The values of the yield stress for the RHS corner zones were 15 to 30 percent higher than the yield stress for the flat coupons. The ratio of the ultimate stress to the yield stress for the RHS material, at various places around the cross-section, was in the range of 1.13 to 1.38. The yield stress for the weld consumables reached almost twice the value for RHS. The stress-strain curve for the weld consumables was bilinear as opposed to trilinear for the RHS.

4.8 Yielding Patterns

Among the specimens in Phase 1 and Phases 2A and 2B (see Figure 4.2), only the regions close to the weldment showed any signs of yielding, which was indicated by cracking of whitewash. First signs of yielding appeared in the corners of the branch. For small weld sizes no further yielding took place because the failure occurred early in the loading stage. The specimens with larger weld sizes showed some signs of yielding along the weldment around the branch member. In either case only a region of 25-50 mm from the weldment was affected by yielding. The strain gauges positioned on the sidewalls of the branch away from the joints recorded strains lower than 2200 microstrain which was equivalent to an elastic limit for the HSS material. It is believed that the yielding in the vicinity of the weldment was caused by three independent factors: stress concentrations in the corner zones of the branch, the local bending near the weld and the residual stresses due to welding. The 19 mm plate separating the branch members in Phases 1 and 2 did not show any signs of yielding.

A few common observations can be made about the progression of plastic zones around the joints in specimens of Phase 3. Again the corners of the branch in the vicinity of the weldment were the first to show signs of yielding. Subsequently, parts of the sidewall of a chord member, near the transition between the flat portions of the chord and the corners, started yielding with cracks in the whitewash parallel to the chord axis. The corner regions of the chord did not show any signs of yielding until near the ultimate load. An illustration of the plastic zones is shown in Figures 4.40 , 4.41 and 4.42 for Phases 3A, 3B and 3C respectively. In each case the figure shows the yielded regions close to the failure load. For specimens with sufficient weld sizes extensive yielding of the chord sidewall and its connecting face was evident as the loading reached the ultimate level. Each of the specimens representing different phases of the experiment displayed a distinct pattern of yielding on the sidewalls of the chord which indicates the significance of the normal and horizontal components of the branch member forces in the progression of plastic zones around the joint.

4.9 Summary of Experimental Results

The distribution of strains in the walls of a branch near the weld has been found to depend on the angle of inclination and on rigid or flexible base conditions.

Three different angles θ were represented by the specimens included in this chapter, namely 30° , 60° and 90°. A comparison of strain levels between the toe and the heel indicated that for θ = 30° the heel area is the critical region of the joint. For θ = 60°, it was the toe which experienced the highest strains. These findings have been confirmed for both the rigid and flexible base conditions by means of strain measurements at the toe and the heel and on the sidewalls of a branch as well as by inspection of the failure modes after testing.

The rigidity of the base has an impact on the effectiveness of the heel area in resisting the load and on the change in direction of the principal axes of strain in the branch sidewalls.

For the rigid base conditions all four walls of the branch can be regarded as fully effective in resisting the load. For the flexible base conditions the toe area can also be assumed to be fully effective. Moreover, the heel is fully effective for θ = 30°. However, for the flexible base, with an increasing angle of inclination of the branch member, the effectiveness of the heel area decreases. For θ = 90° the strains recorded at the heel were negative despite the branch being under tensile load.

The directions of the major principal strain axis on the branch member sidewall were nearly parallel to the branch longitudinal axis for the rigid base conditions throughout the loading history. The same directions in the flexible base conditions were parallel to the branch axis at the beginning of loading and then changed constantly up to failure when they bisected the angles of consideration. In Phase 3 (flexible base) in the toe area, the directions of the major principal axis of strain in the corner locations bisected the angle of consideration for most of the loading history.

The yielding patterns were identified by brushing the peeling-off layers of whitewash painted on a specimen. In Phase 2 (rigid base) the first locations to show signs of yielding were the corner positions of the branch in contact with the weld. Next, the yielding spread along the weldment. Neither the plate nor the rest of the branch showed any sign of yielding. In Phase 3 (flexible base) the corners of the branch near the weld yielded first. Next, some yielding was observed on the sidewalls of the chord close to the rounded corners. For specimens with large weld sizes an extensive yielding of the chord sidewall and the chord connecting face was observed in the ultimate stages of the testing.

Current IIW (1981) recommendations assume that the heel area in a gap K joint is not fully effective. A formula for the effectiveness of this crosswall is based on plate to RHS experiments which do not include any function of an angle of inclination θ. The current experimental program revealed that the effectiveness of the heel is strongly dependent on θ ; in fact , for an angle of 30° the heel could be regarded as fully effective.

The positions of the major principal axis of strain indicate that for the rigid base conditions the dominating component of strain is parallel to the branch longitudinal axis, but for the flexible base conditions the values of strains in the direction parallel to the weldment were of the same order as in the direction of the longitudinal branch member axis. This conclusion affects the design of weldments as well as the determination of the strain and stress concentration factors around the joint.

FIGURE 4.1 General View of a Specimen Tested

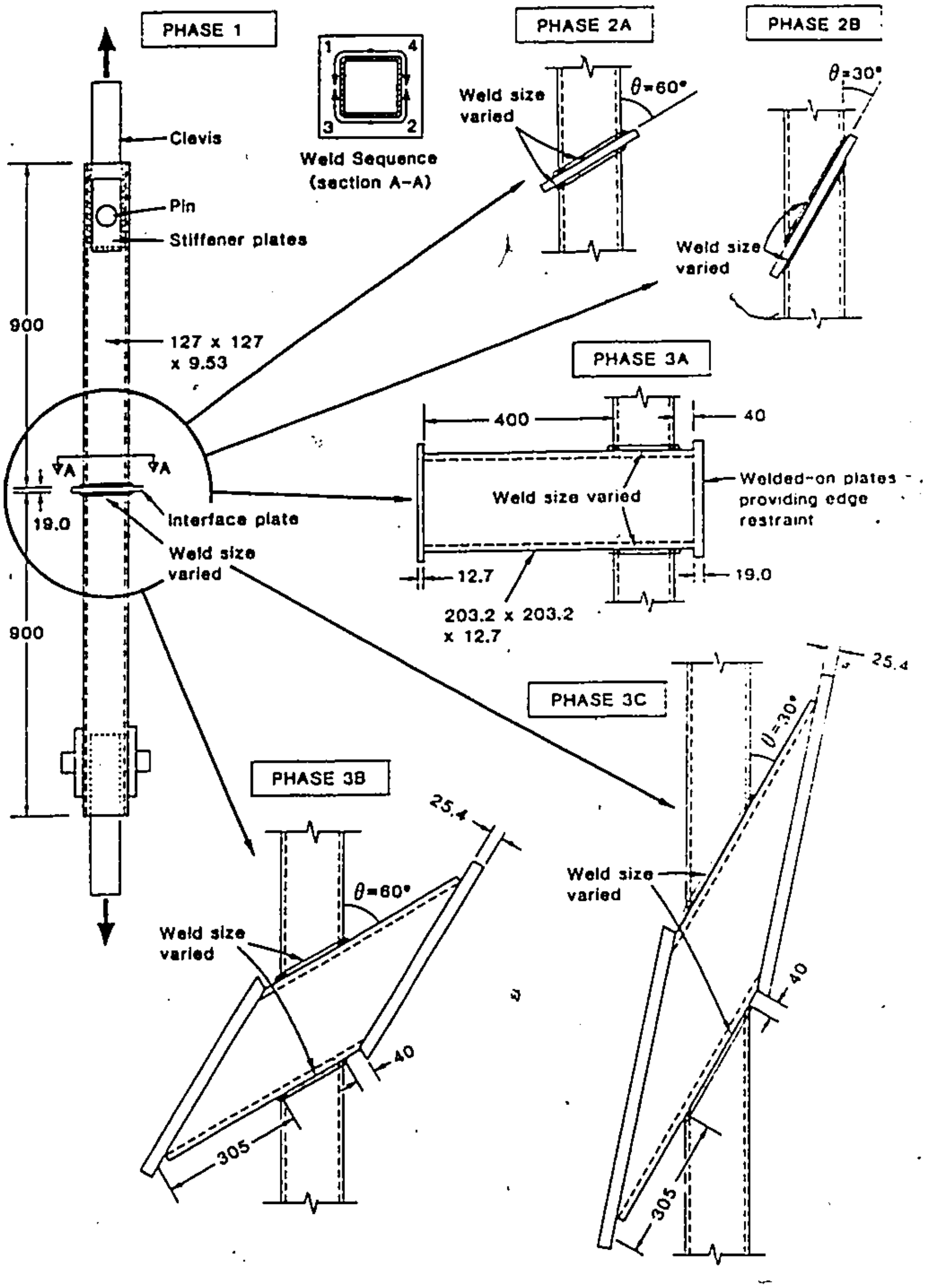

FIGURE 4.2 Summary of Experimental Program (after Frater 1986)

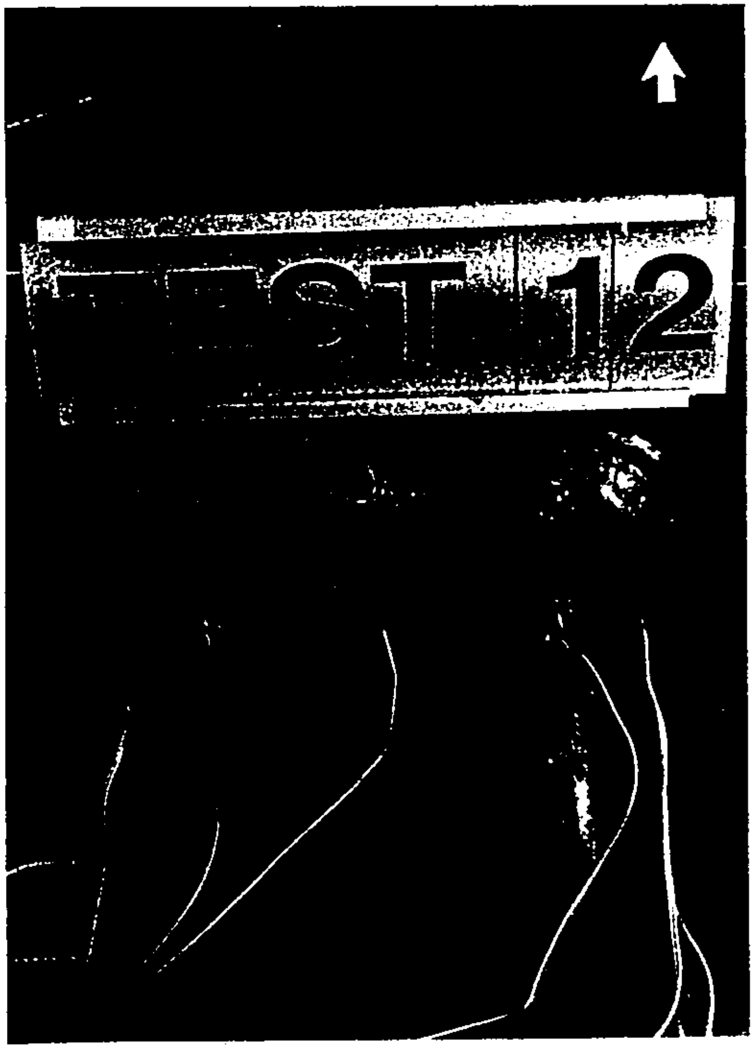

FIGURE 4.3 Strain Gauges at Toe of Specimen 12

FIGURE 4.4 Rosettes on Sidewall of Specimen 15

TEST 12

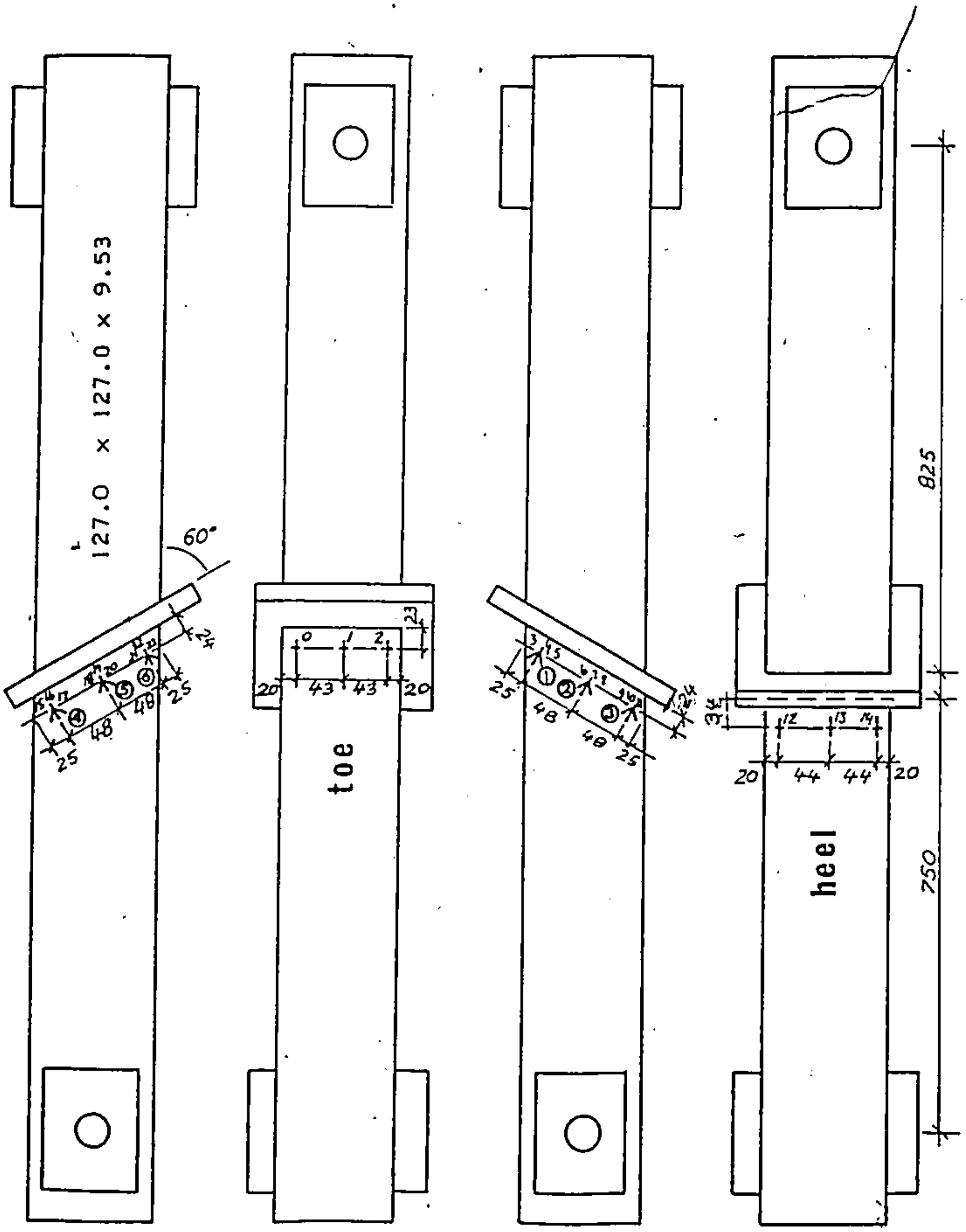

FIGURE 4.5 Specimen 12

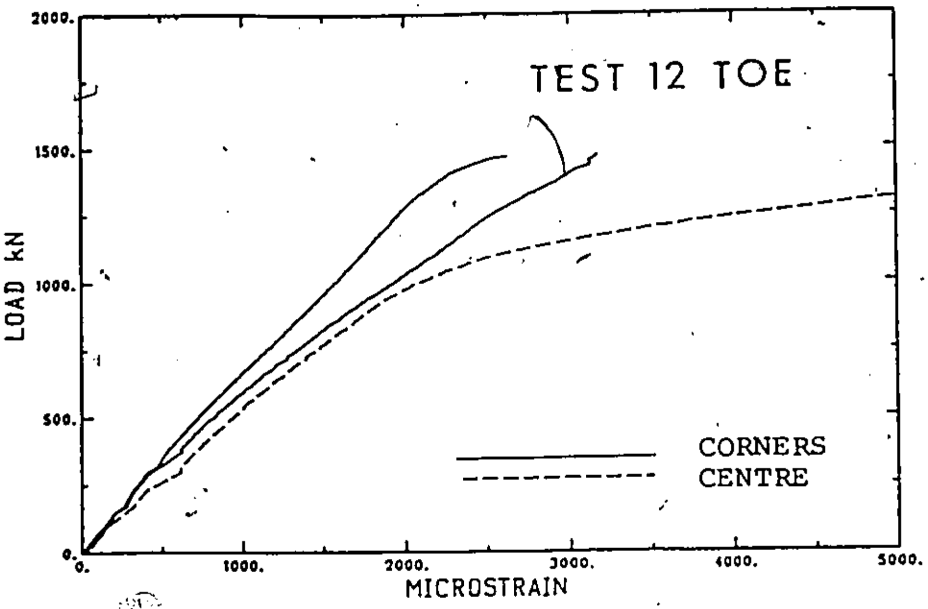

FIGURE 4.6 Load vs. Strain Graph at Toe of Specimen 12

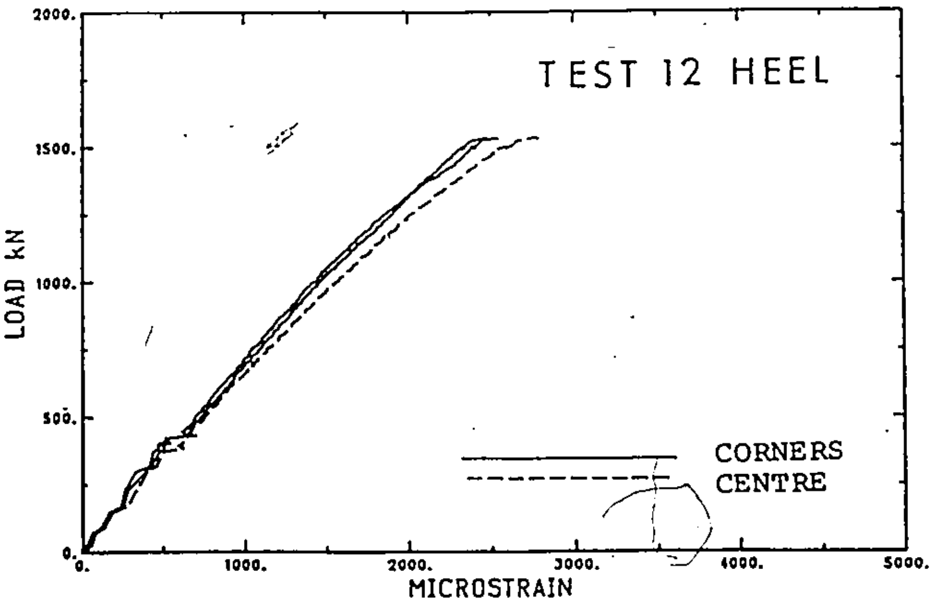

FIGURE 4.7 Load vs. Strain Graph at Heel of Specimen 12

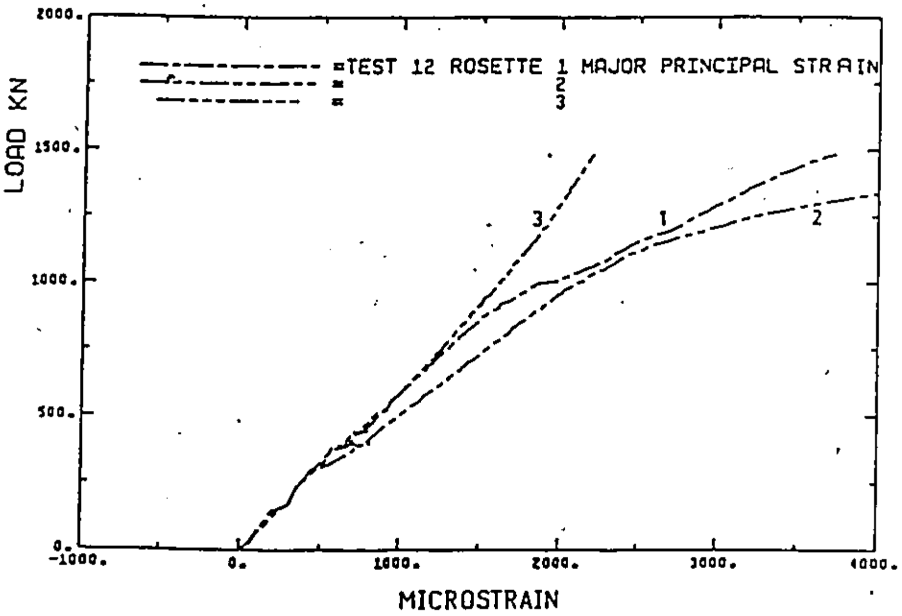

FIGURE 4.8 Load vs. Major Principal Strain Graph for Rosettes 1,2,3 in Test 12

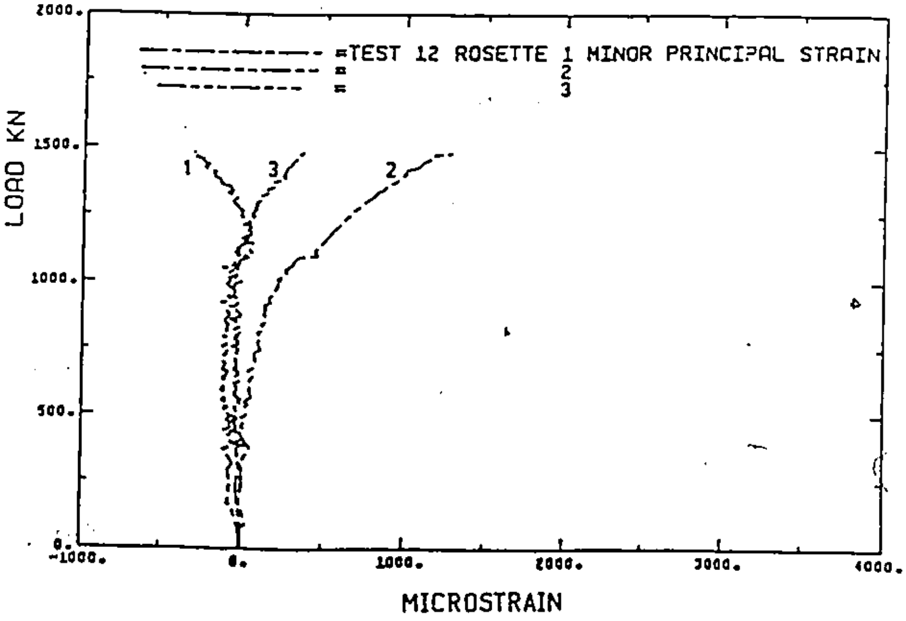

FIGURE 4.9 Load vs. Minor Principal Strain Graph for Rosettes 1,2,3 in Test 12

TEST 14

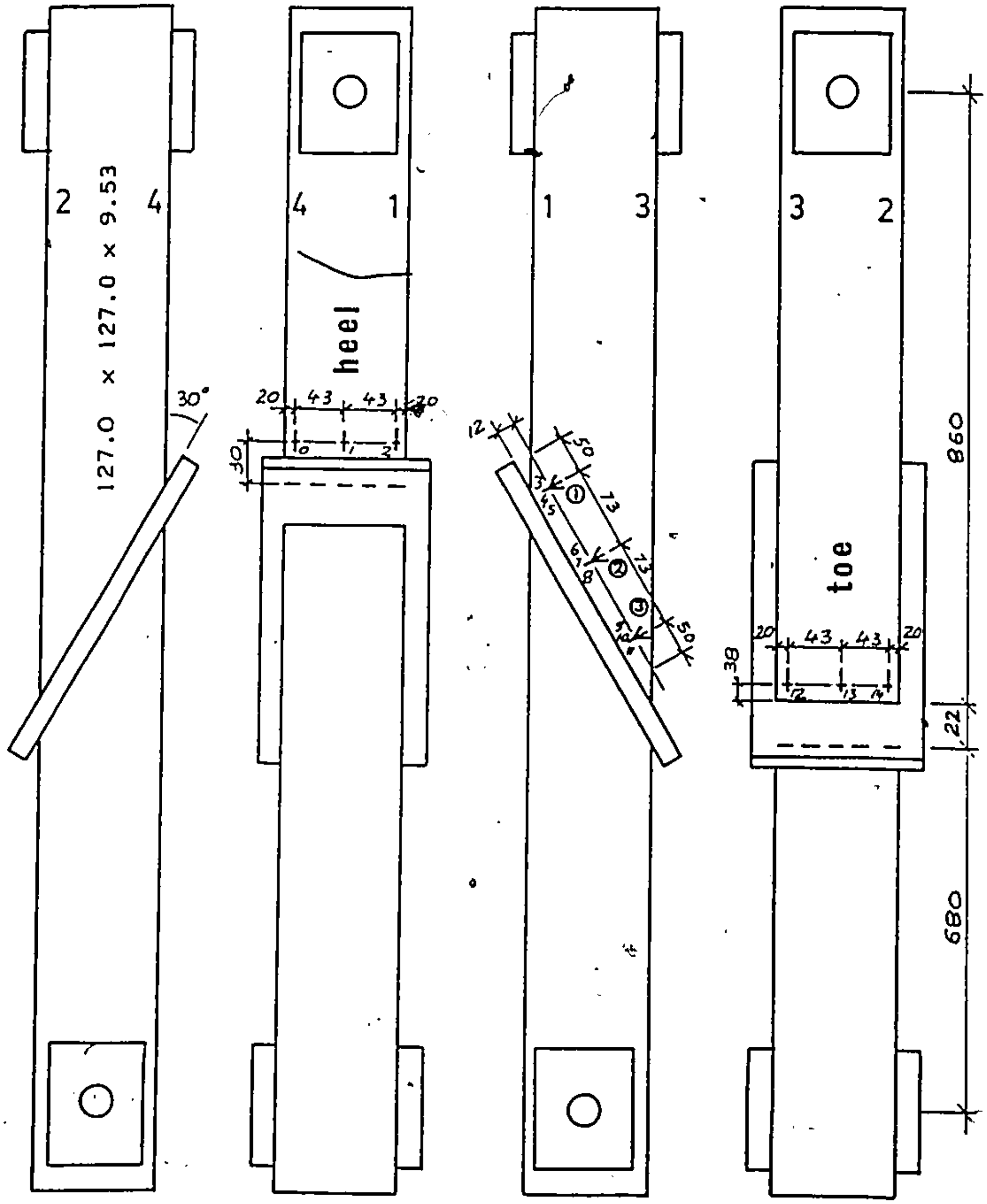

FIGURE 4.10 Specimen 14

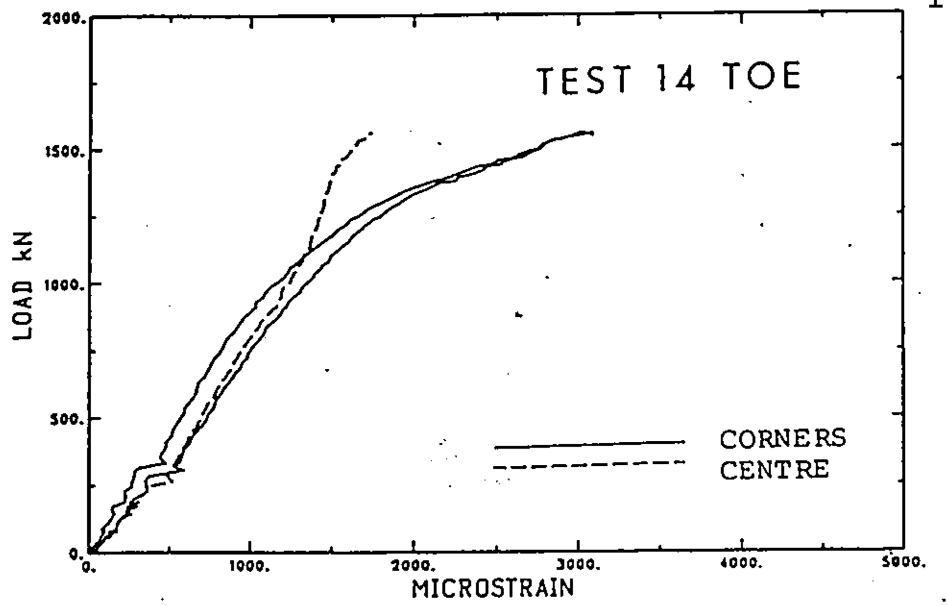

FIGURE 4.11 Load vs. Strain Graph at Toe of Specimen 14

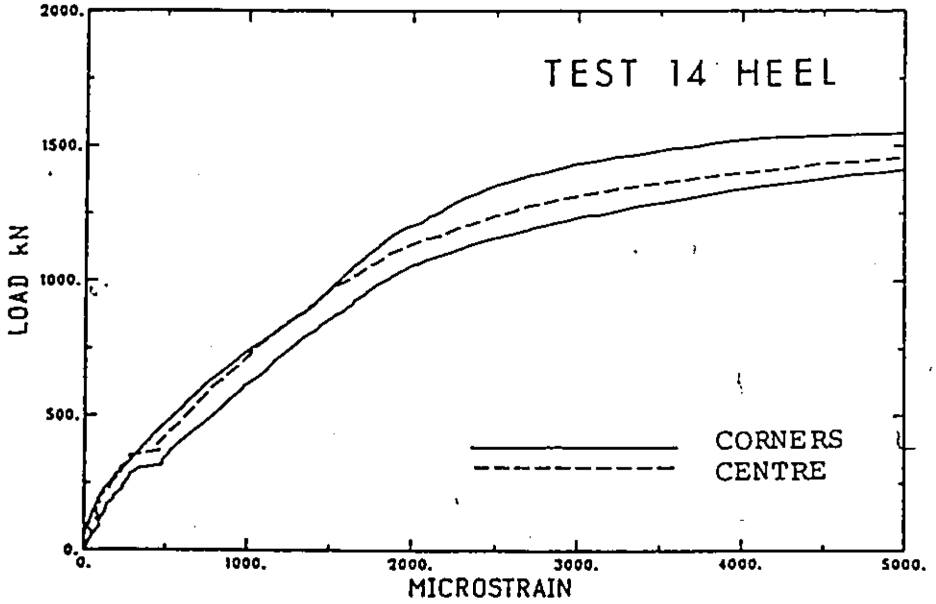

FIGURE 4.12 Load vs. Strain Graph at Heel of Specimen 14

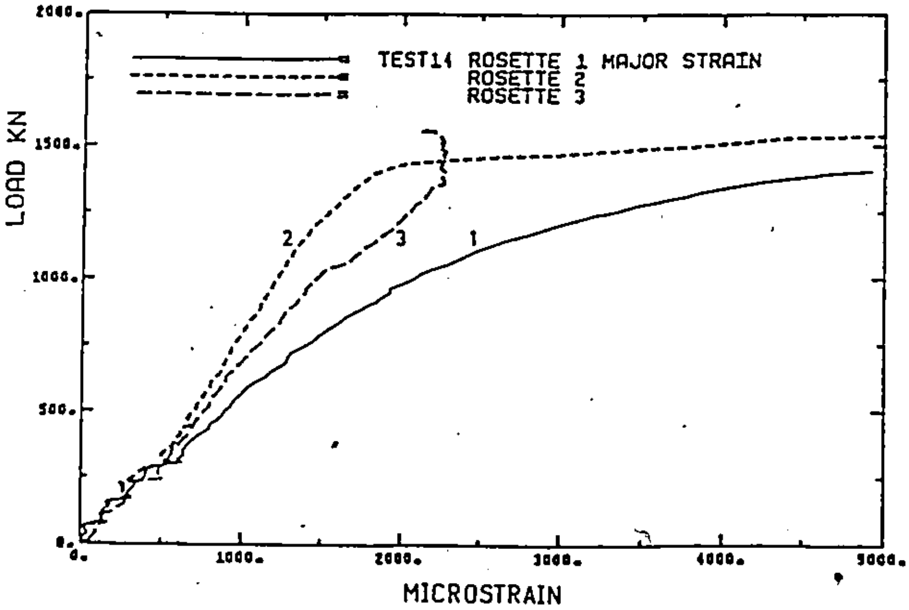

FIGURE 4.13 Load vs. Major Principal Strain Graph for Rosettes 1,2,3 in Test 14

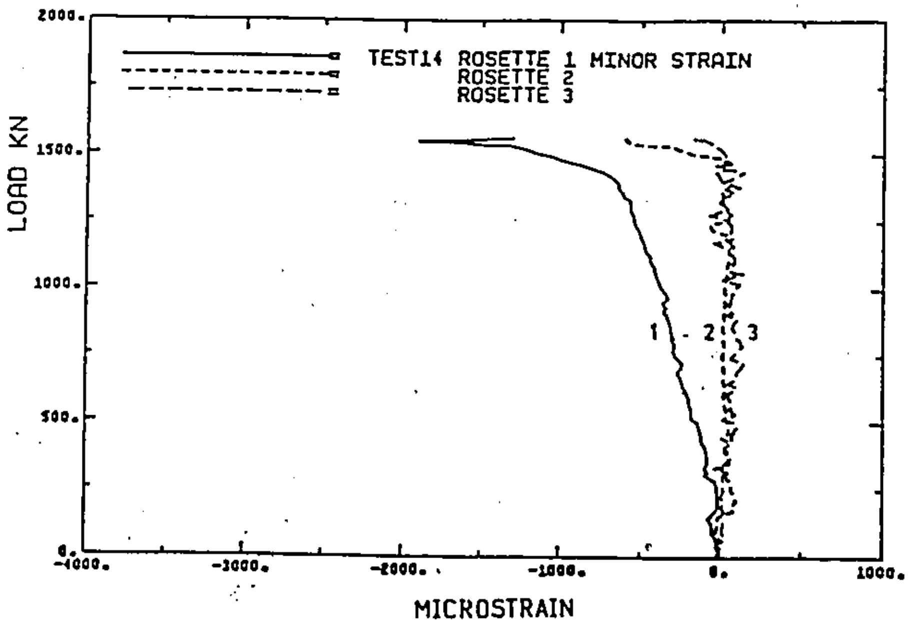

FIGURE 4.14 Load vs. Minor Principal Strain Graph for Rosettes 1,2,3 in Test 14

TEST 18

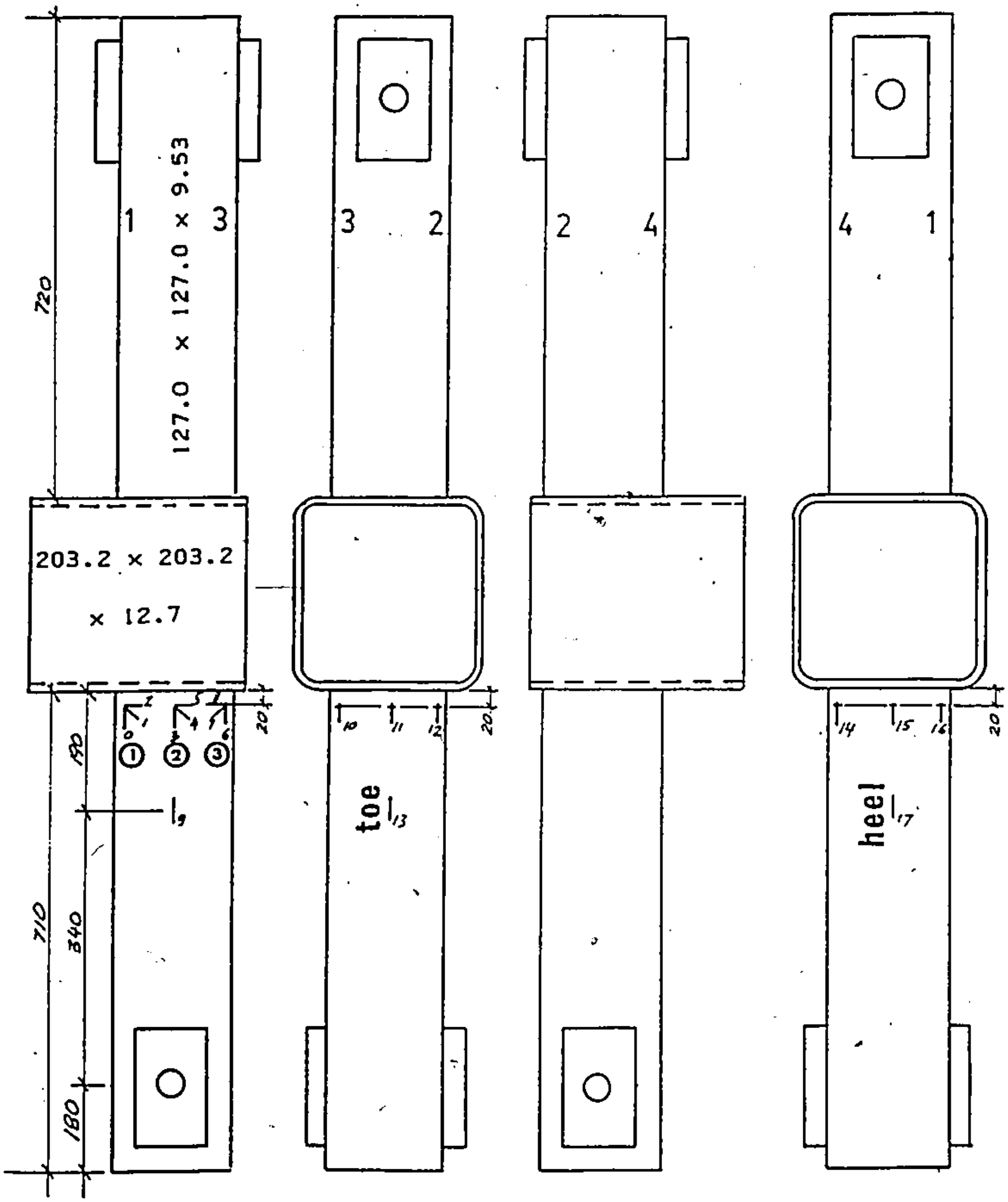

FIGURE 4.15 Specimen 18

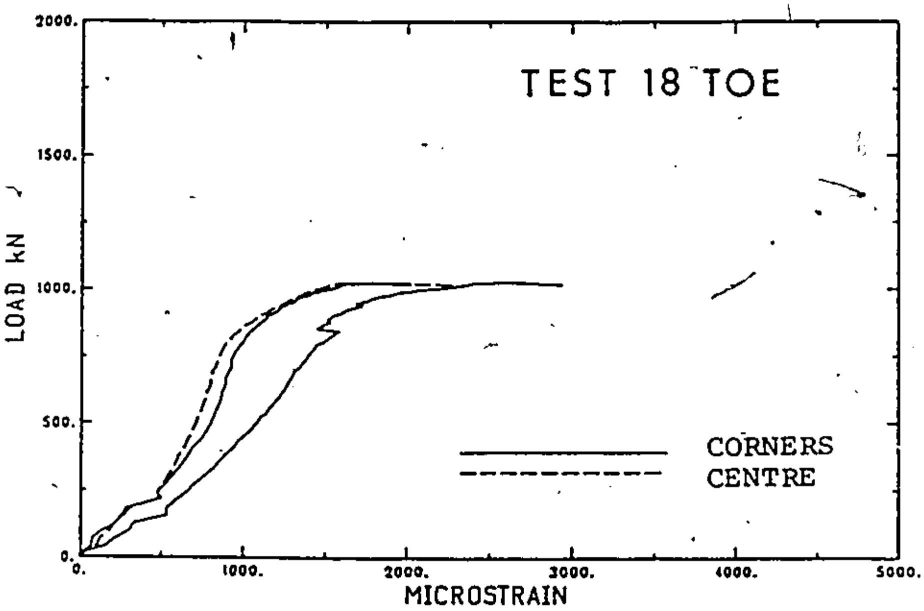

FIGURE 4.16 Load vs. Strain Graph at Toe of Specimen 18

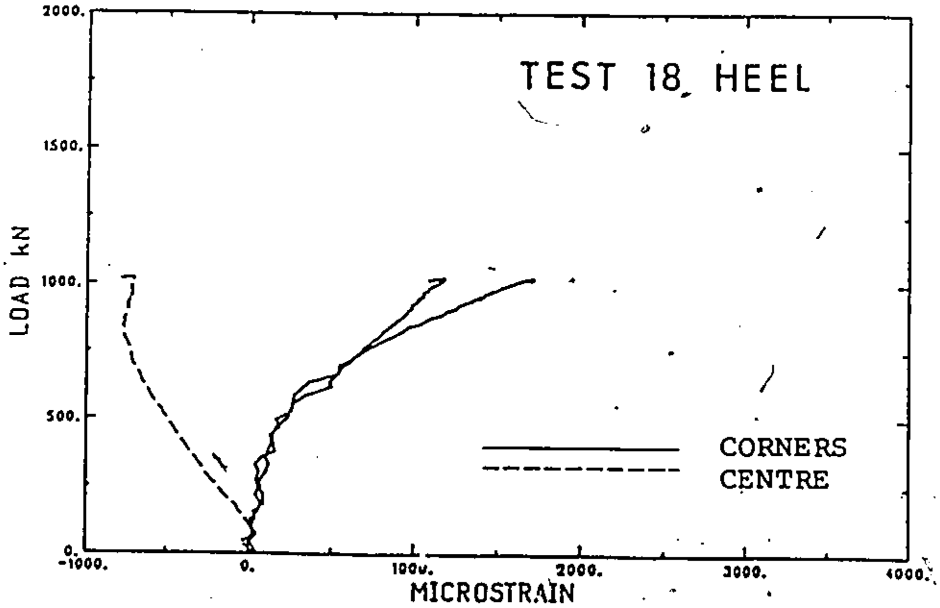

FIGURE 4.17 Load vs. Strain Graph at Heel of Specimen 18

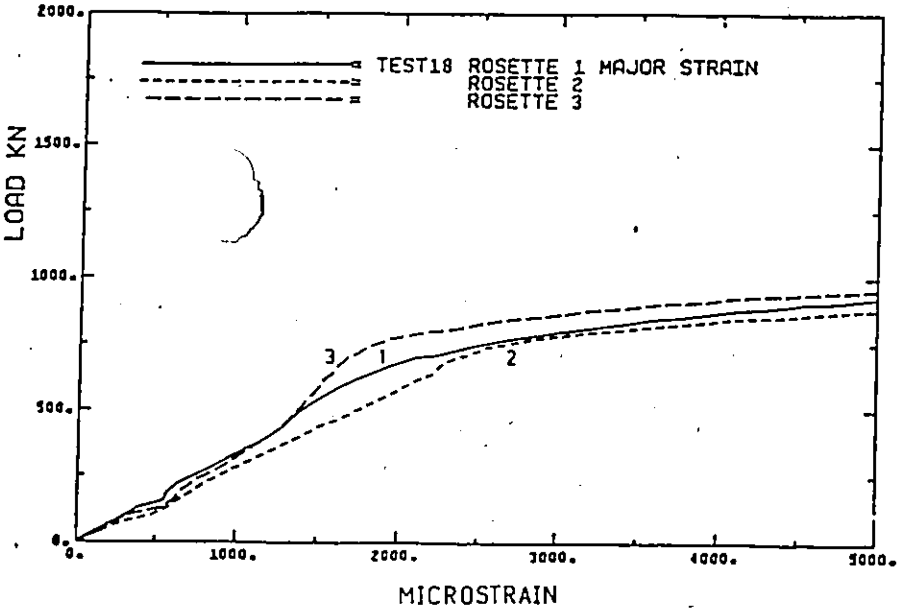

FIGURE 4.18 Load vs. Major Principal Strain Graph for Rosettes 1,2,3 in Test 18

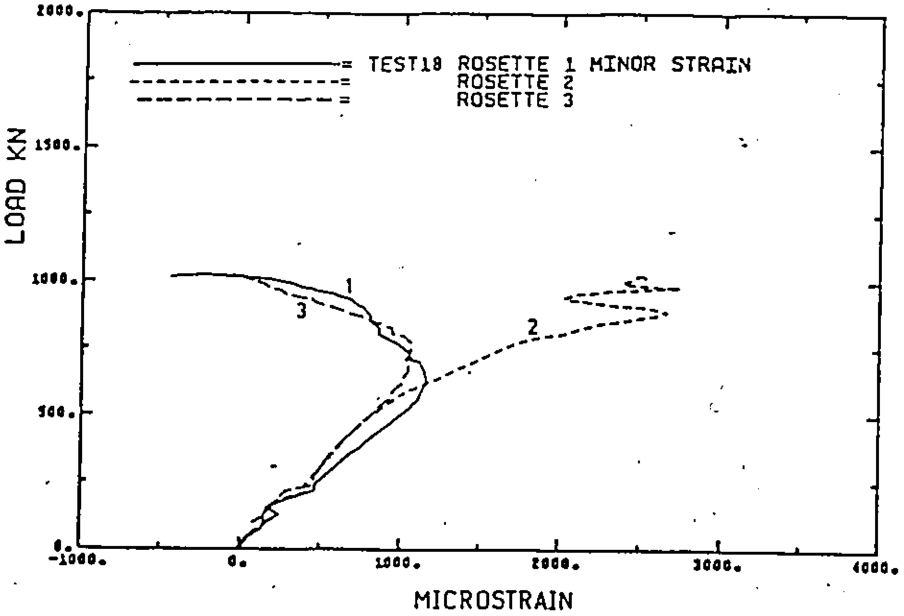

FIGURE 4.19 Load vs. Minor Principal Strain Graph for Rosettes 1,2,3 in Test 18

TEST 25

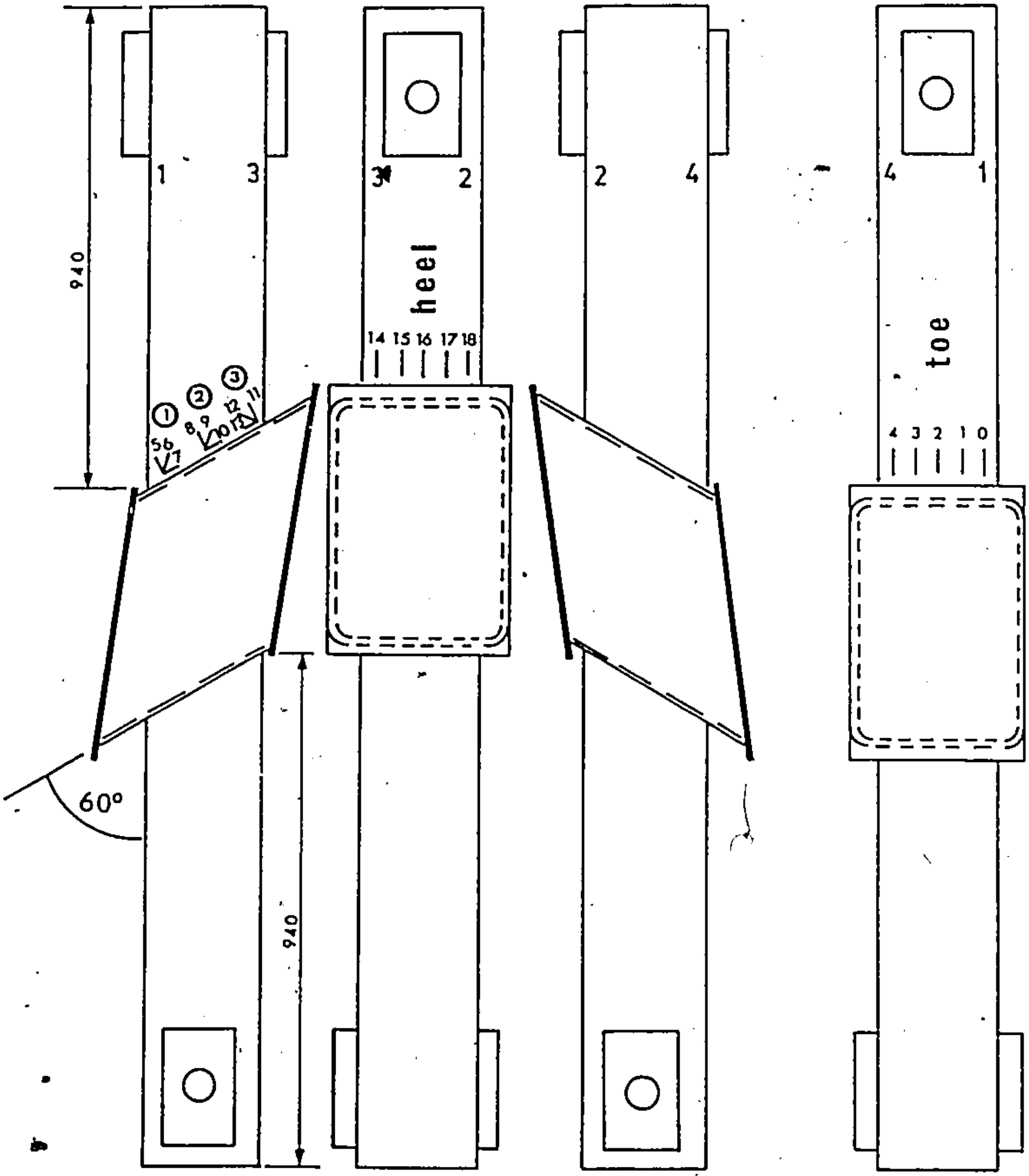

FIGURE 4.20 Specimen 25

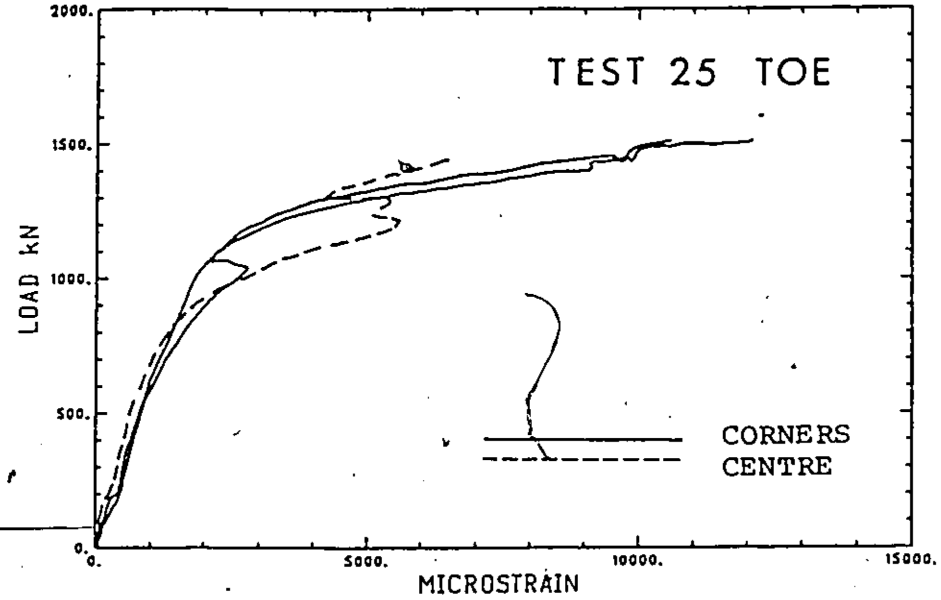

FIGURE 4.21 Load vs. Strain Graph at Toe of Specimen 25

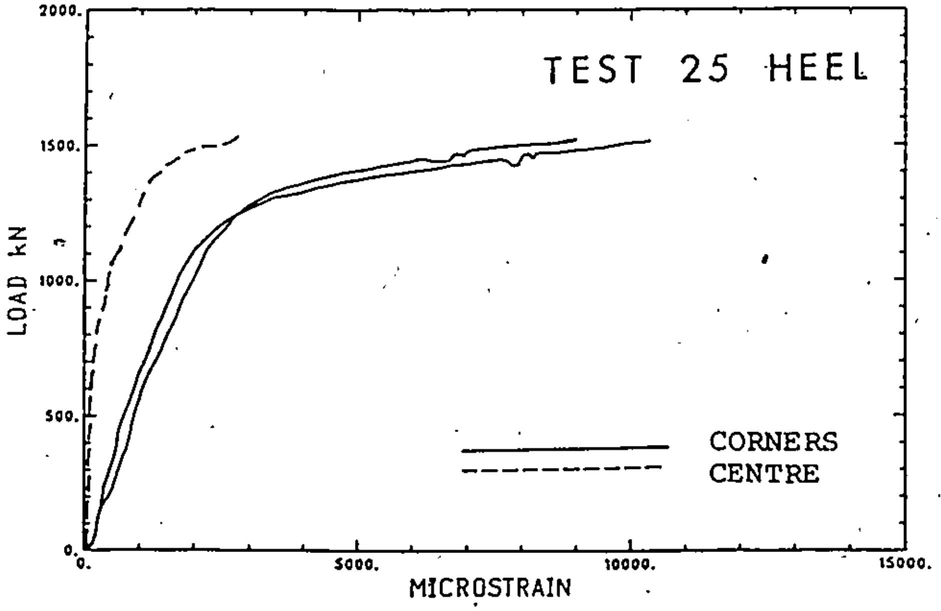

FIGURE 4.22 Load vs. Strain Graph at Heel of Specimen 25

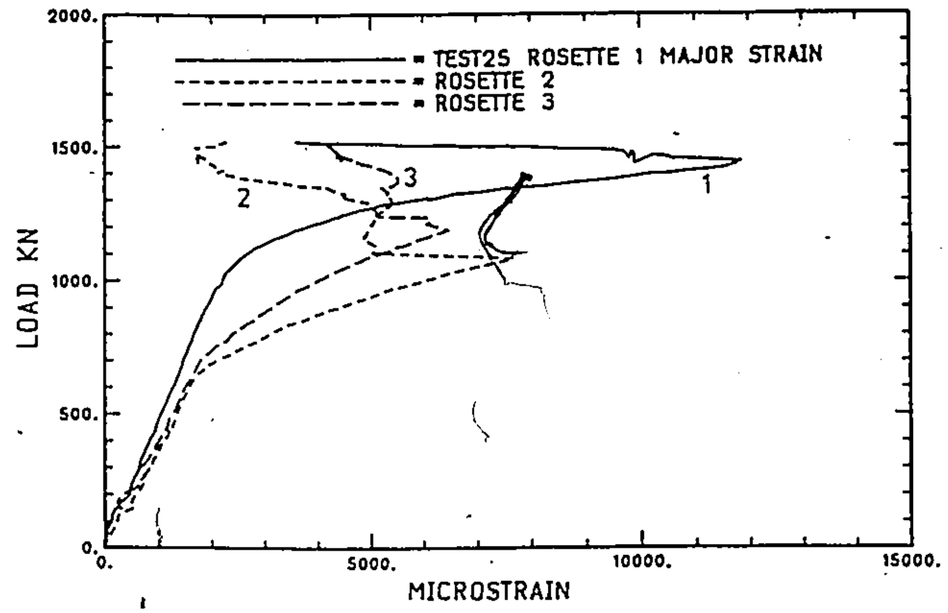

FIGURE 4.23 Load vs. Major Principal Strain Graph for Rosettes 1,2,3 in Test 25

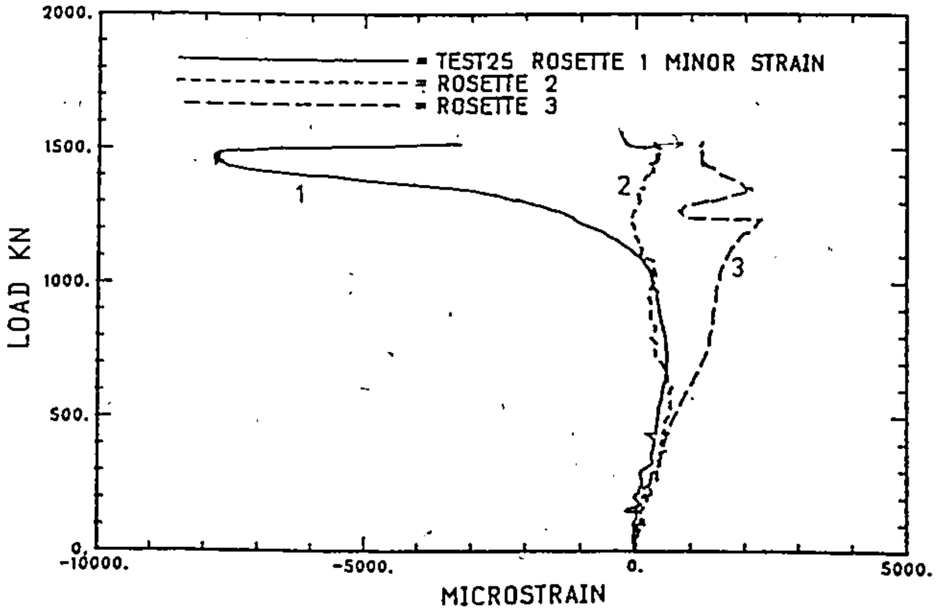

FIGURE 4.24 Load vs. Minor Principal Strain Graph for Rosettes 1,2,3 in Test 25

TEST 26

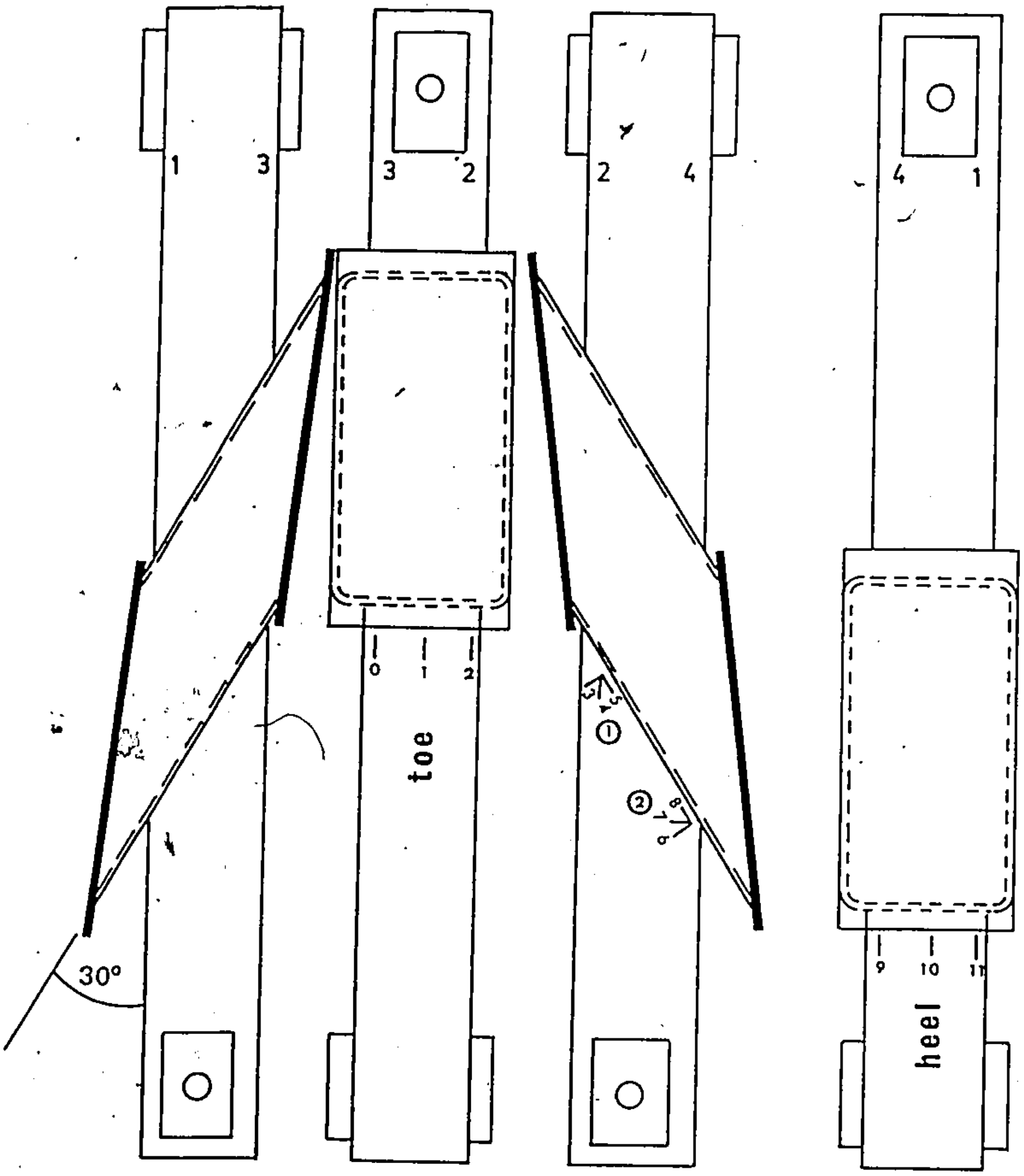

FIGURE 4.25 Specimen 26

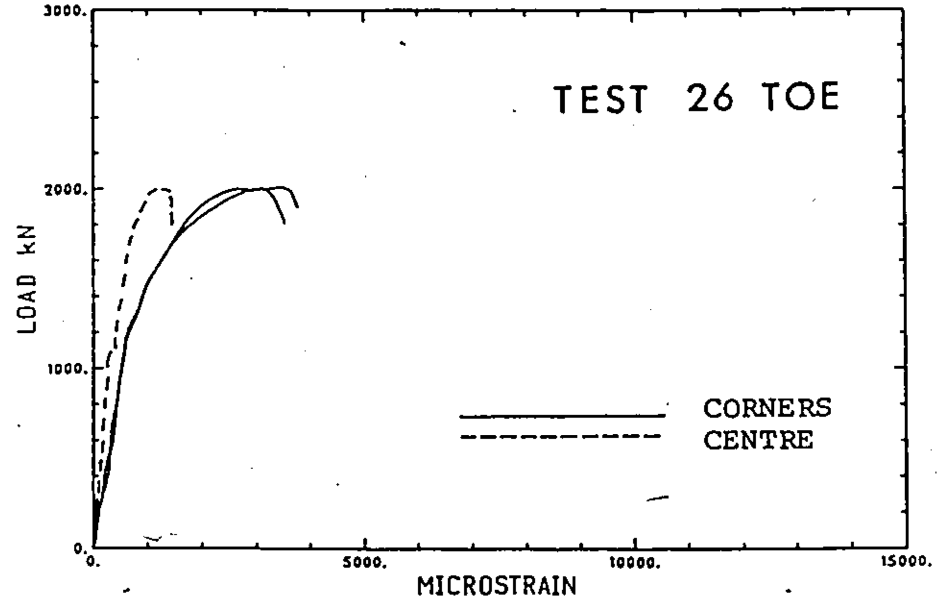

FIGURE 4.26 Load vs. Strain Graph at Toe of Specimen 26

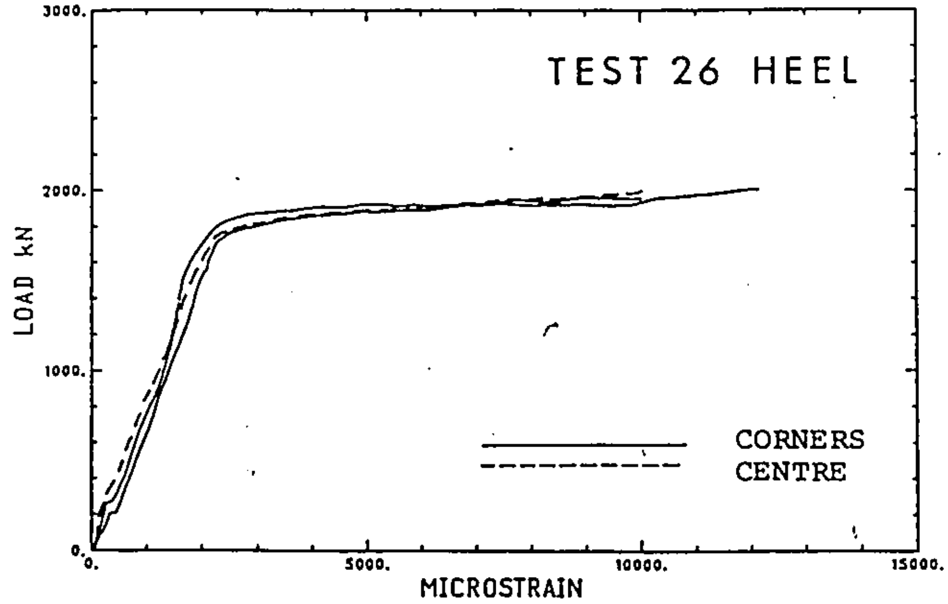

FIGURE 4.27 Load vs. Strain Graph at Heel of Specimen 26

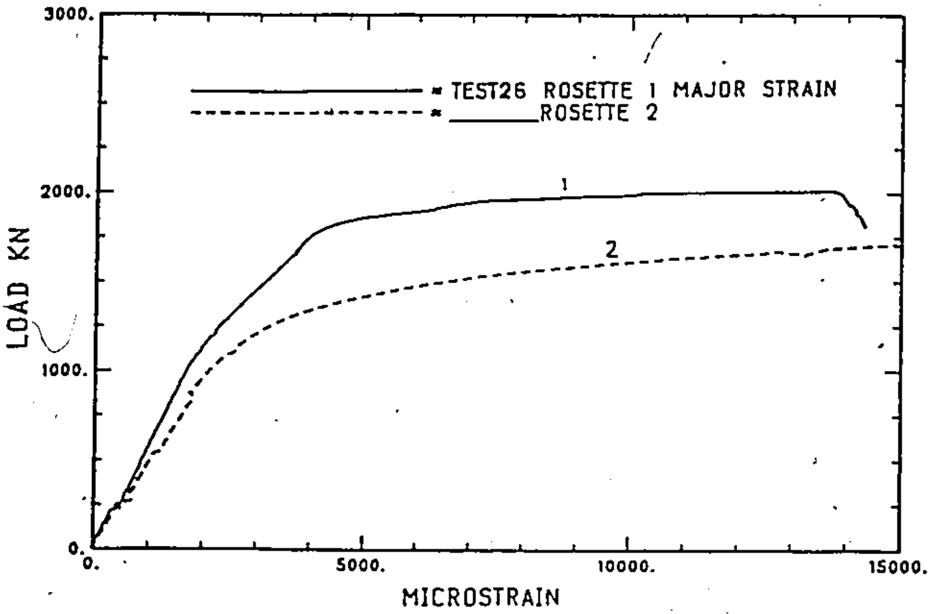

FIGURE 4.28 Load vs. Major Principal Strain Graph for Rosettes 1,2 in Test 26

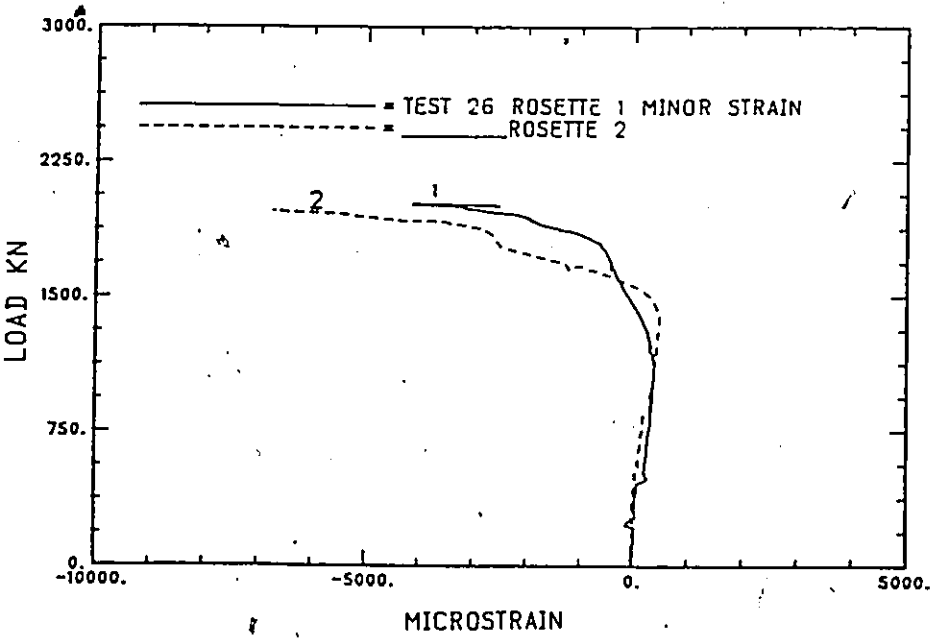

FIGURE 4.29 Load vs. Minor Principal Strain Graph for Rosettes 1,2 in Test 26

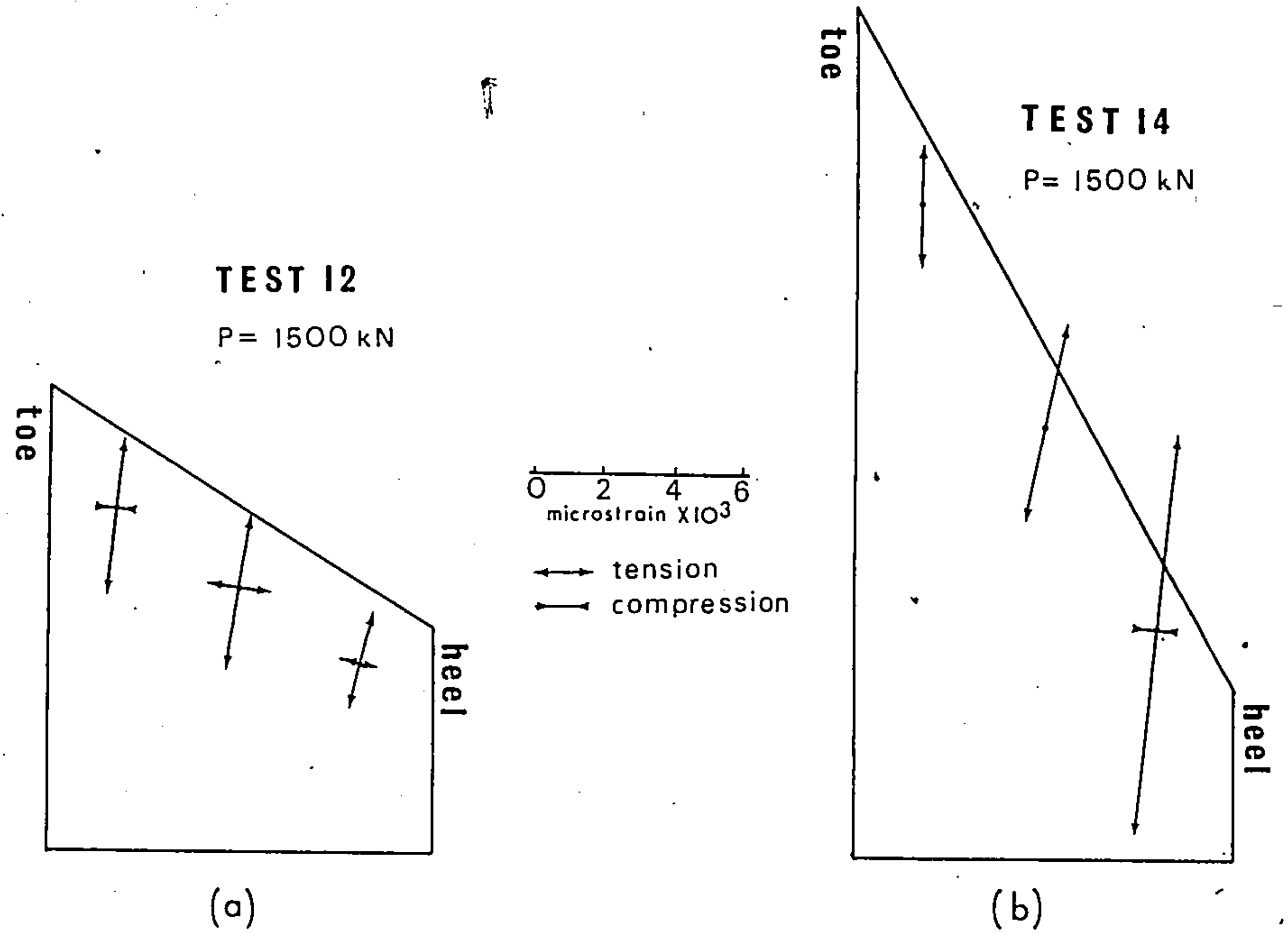

FIGURE 4.30 Directions of Principal Axes of Strain and Magnitudes of Strains near Failure: a- Test 12 (θ = 60°), b- Test 14 (θ = 30°)

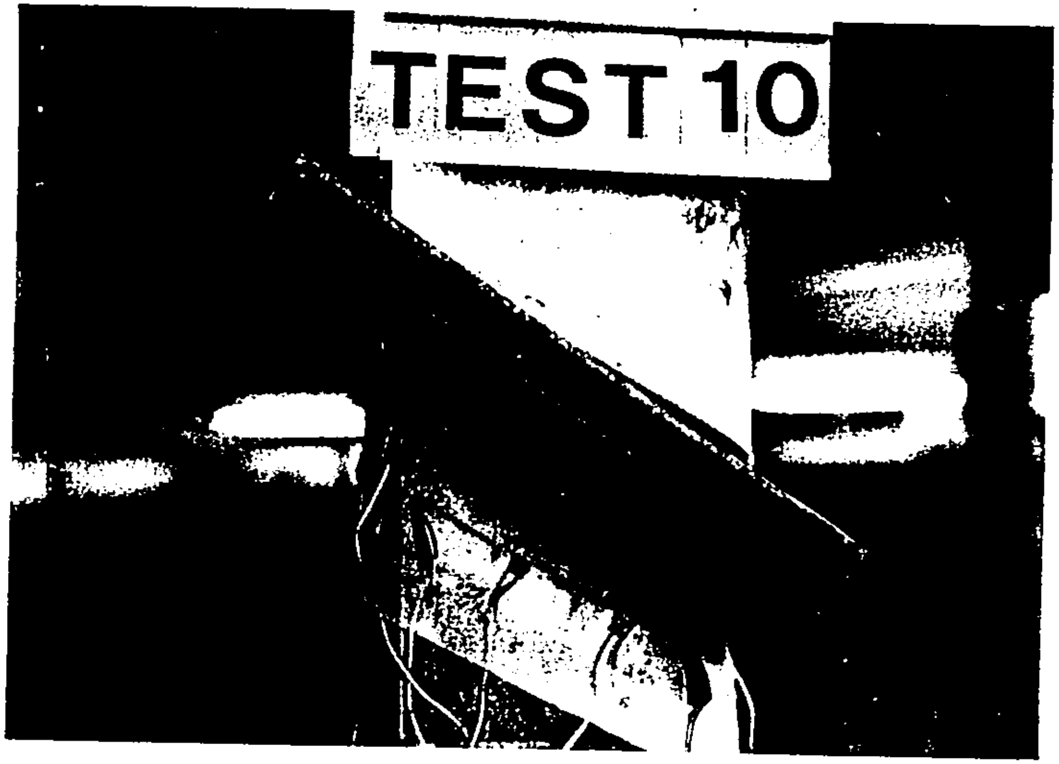

FIGURE 4.31 Failure Mode in Test 10

FIGURE 4.32 Failure Mode in Test 13

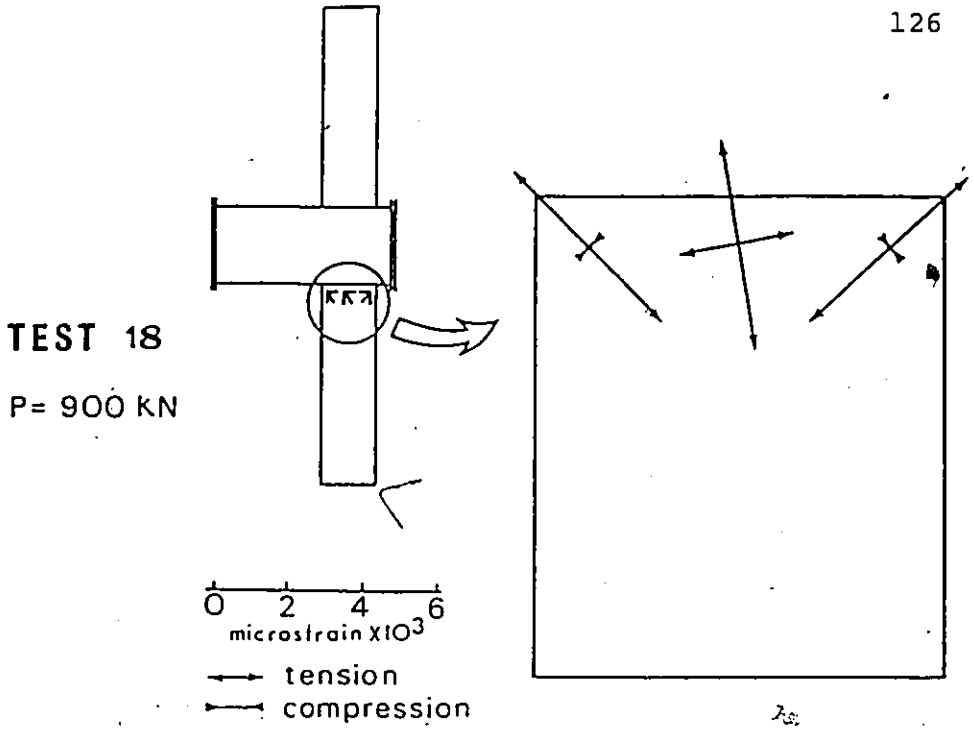

FIGURE 4.33 Directions of Principal Axes of Strain and Magnitudes of Strains near Failure in Test 18 (θ - 90°)

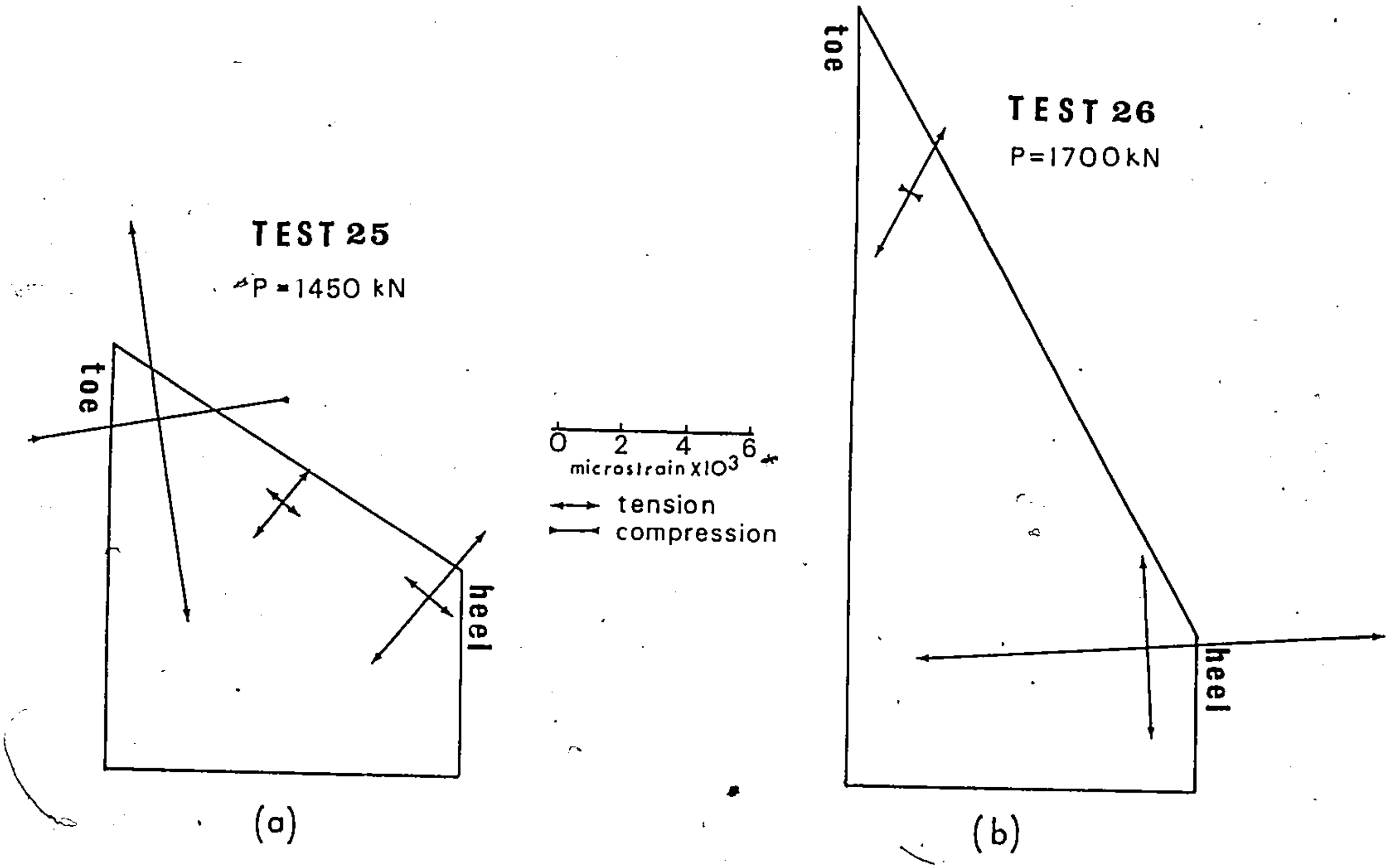

FIGURE 4.34 Directions of Principal Axes of Strain and Magnitudes of Strains near Failure: a- Test 25 (θ = 60°), b- Test 26 (θ = 30°)

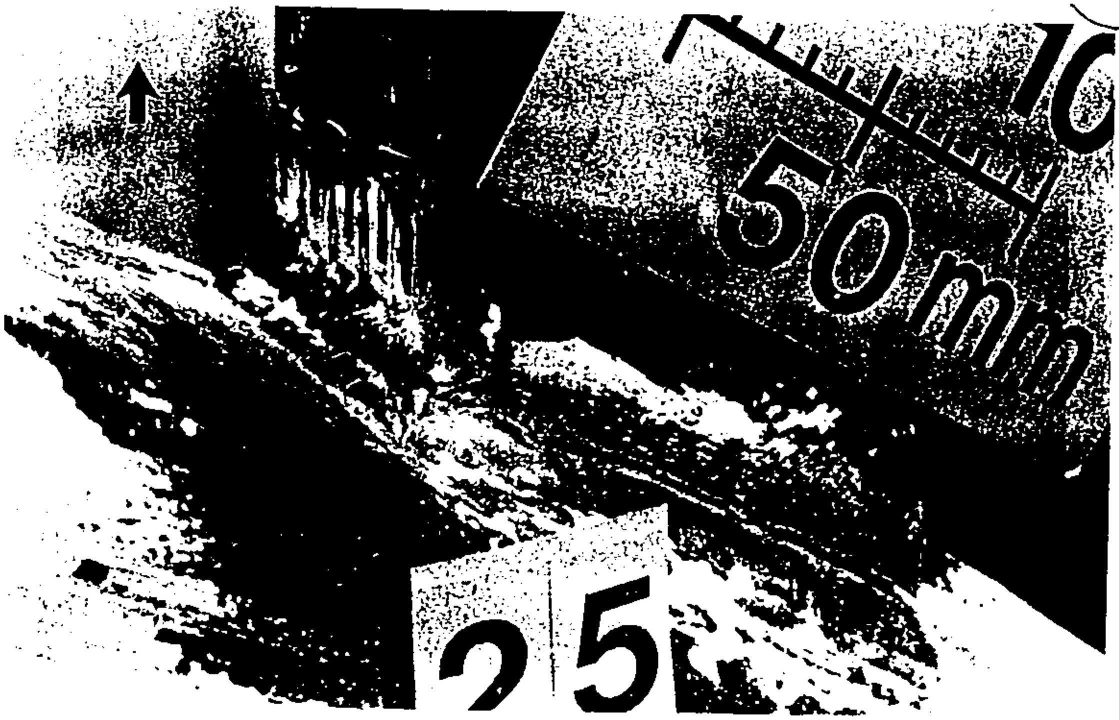

FIGURE 4.35 Failure Mode in Test 25

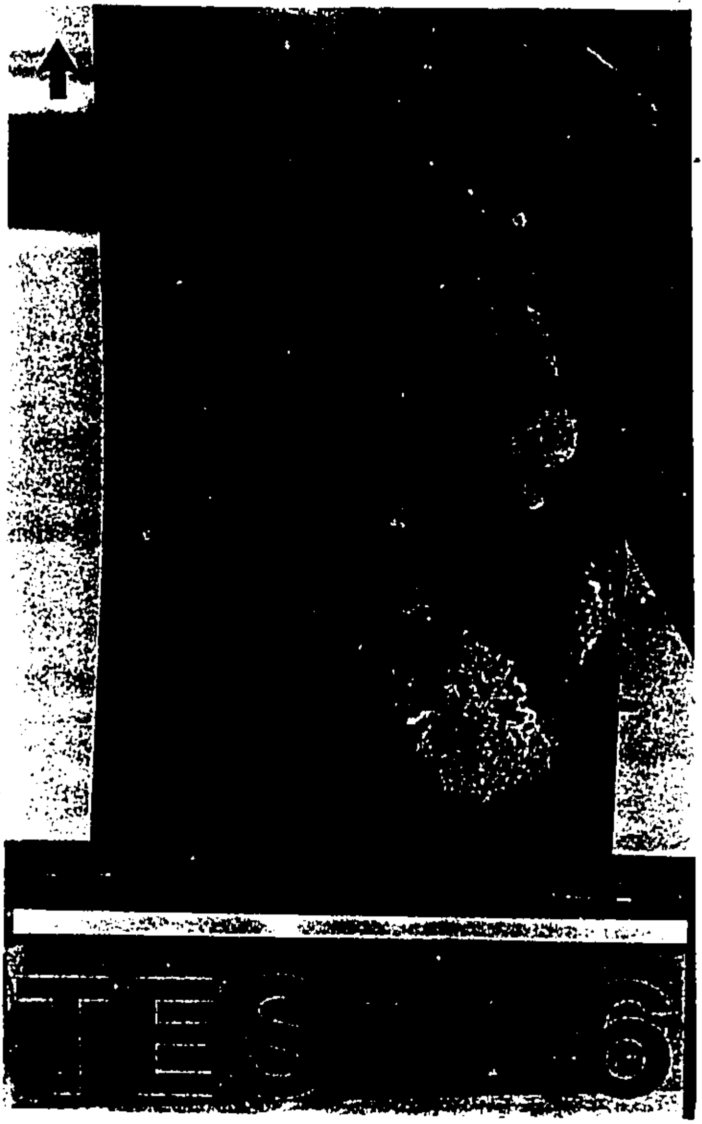

FIGURE 4.36 Failure Mode in Test 26

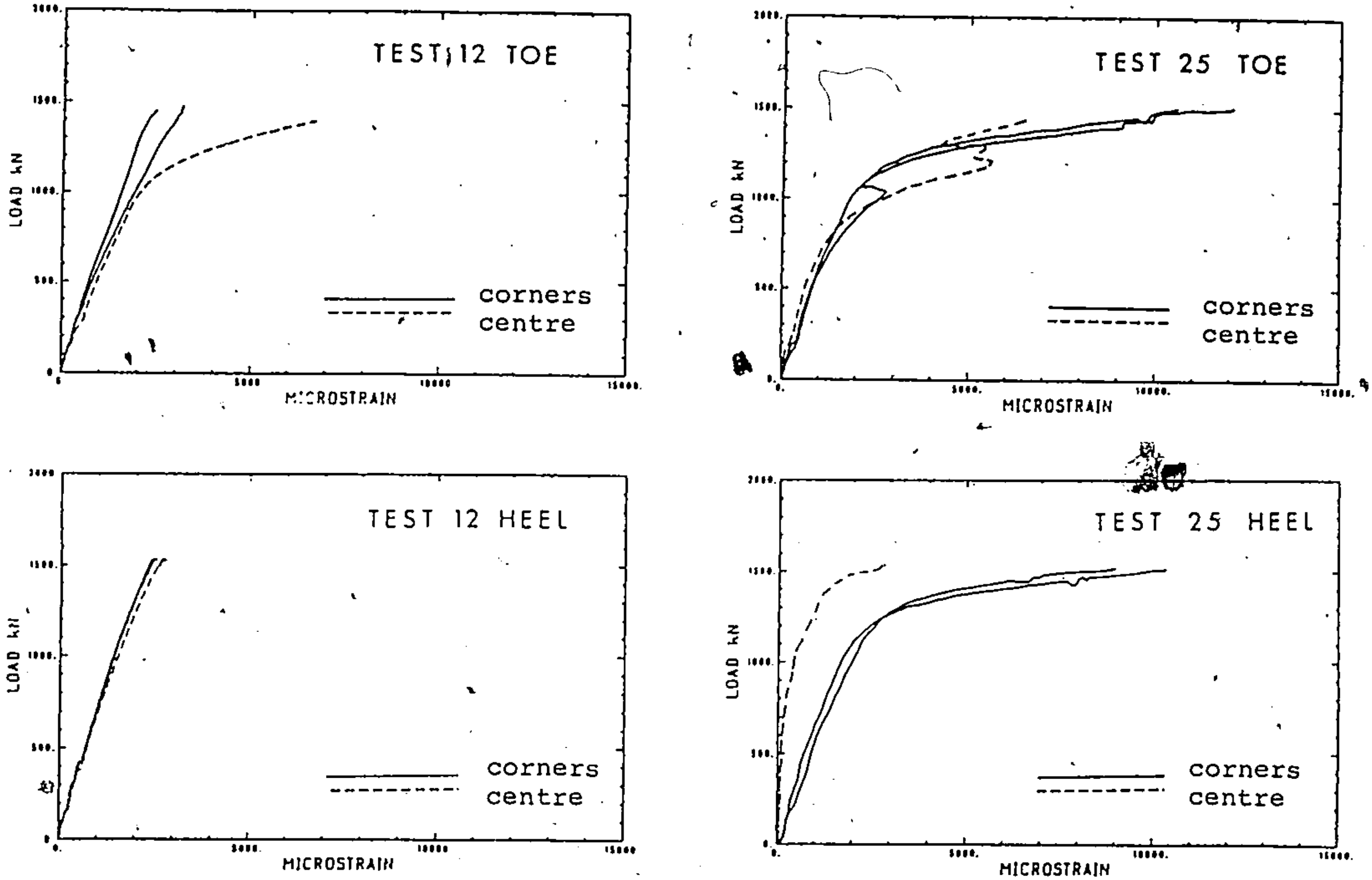

FIGURE 4.37 Comparison of Strains for Rigid Base Conditions (Test 12) and Flexible Base Conditions (Test 25) for Toe and Heel (θ = 60°)

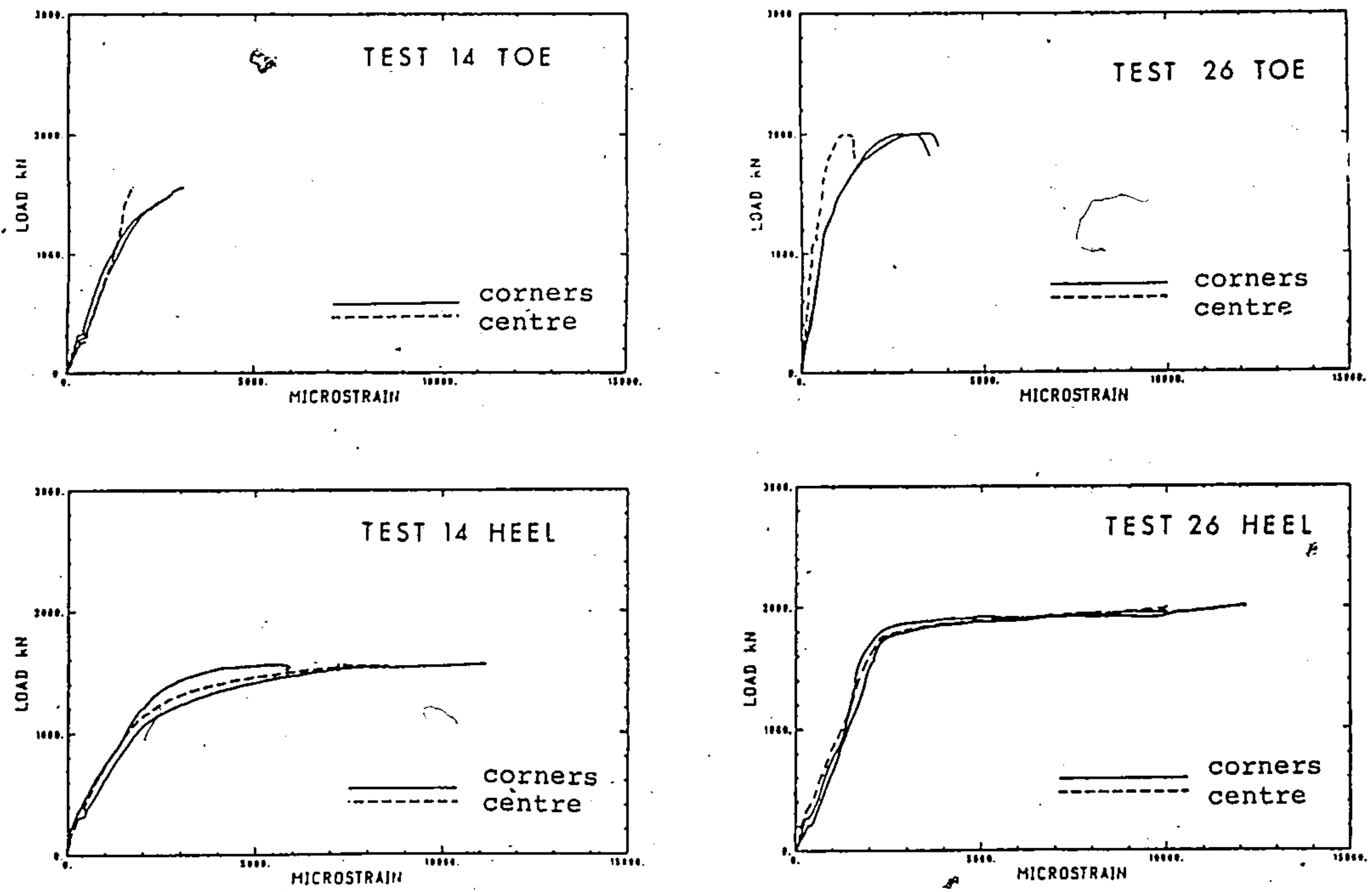

FIGURE 4.38 Comparison of Strains for Rigid Base Conditions (Test 14) and Flexible Base Conditions (Test 26) for Toe and Heel (θ = 30°)

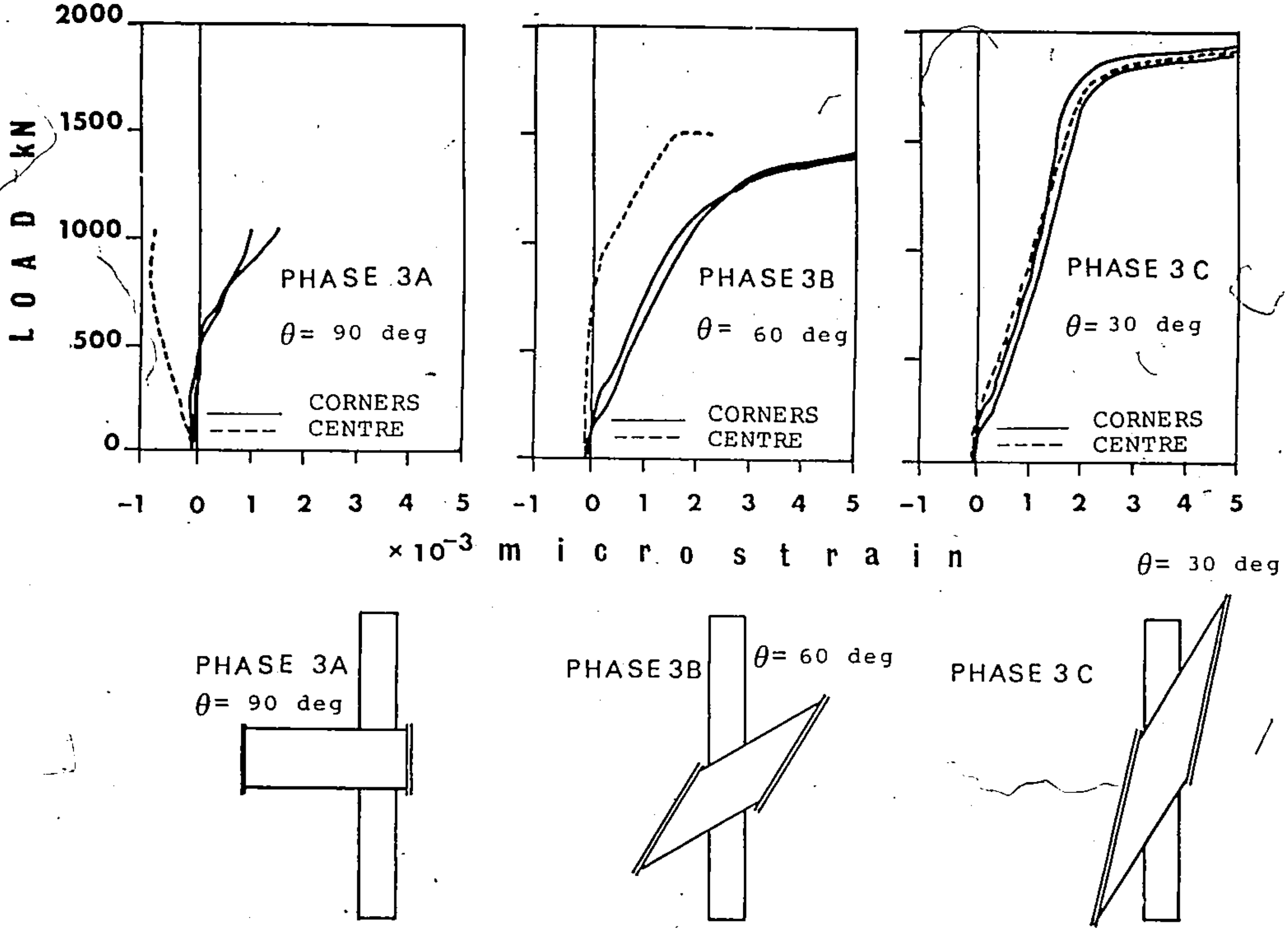

FIGURE 4.39 Comparison of Strain Values at Heel from Phases 3A, 3B and 3C

FIGURE 4.40 Yielding Pattern near Failure in Test 18

FIGURE 4.41 Yielding Pattern near Failure in Test 25

FIGURE 4.42 Yielding Pattern near Failure in Test 26

TABLE 4.1 Summary of Test Results

No	Ult. Load kN	Throat Thickness				Failure Modes	Phase
		a	b	c	d		
1	1020	3.5	3.5	3.5	3.5	WF	1
2	960	3.2	3.2	3.2	3.2	WF	1
3	840	2.8	2.8	2.8	2.8	WF	1
4	1140	4.4	4.4	4.4	4.4	WF	1
5	1200	4.3	4.3	4.3	4.3	WF PF	1
6	1207	4.8	4.8	4.8	4.8	WF PF	1
7	1131	5.0	5.0	5.0	7.3	WF a-c PF d	2A
8	1494	7.1	7.1	7.1	7.1	MPF	1
9	1578	8.1	8.1	8.1	7.1	MPF	1
10	982	3.8	3.8	3.5	4.1	WF c p/a p/b	2A
11	1270	4.4	4.4	4.8	8.4	WF a-c PF d	2A
12	1534	7.2	7.2	5.6	10.2	WF a-c PF d	2A
13	1698	3.8	3.8	n/a	6.7	WF a b	2B
14	1560	5.2	5.2	n/a	8.1	WF a b	2B
15	1857	6.6	6.6	n/a	11.9	PF d SF a-c	2B
16	801	4.6	4.6	4.6	4.6	WF a b p/c p/d	3A
17	1181	8.5	8.5	8.5	8.5	WF a b p/c p/d	3A
18	1023	5.8	5.8	5.8	5.8	WF a b p/c p/d	3A
19	602	3.2	3.2	3.2	3.2	WF	3A
20	1388	11.9	11.9	11.9	11.9	WF a b p/c p/d	3A
21	1140	4.3	4.3	3.8	7.0	WF a CR d	3B
22	1328	7.2	7.2	7.4	11.1	SD c WF a b	3B
23	1788	10.1	10.1	10.1	10.1	MPF	1
24	861	4.3	4.3	3.4	6.9	SD c WF a b	3B
25	1521	11.7	11.7	10.6	15.8	SD c SF a	3B
26	2010	8.0	8.0	n/a	12.2	CR d	3C

Failure Modes : WF - weld failure, WF a b - weld failure along sides a b, PF - plate failure, MPF - mostly plate failure, SF - fracture in sidewalls, CR - chord rupture, SD - shear of a side wall

definition of a, b, c, d :

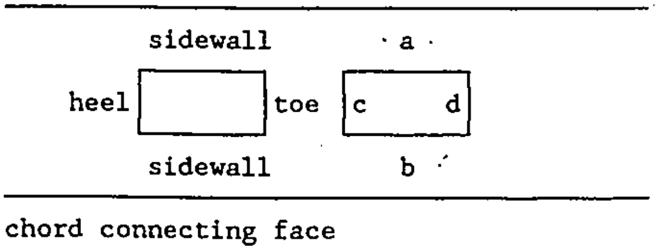

TABLE 4.2 Summary of Instrumentation for Specimens 10-12

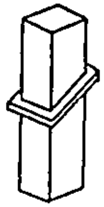 TEST 10	PHASE 2B THETA 30 STRAIN GAUGES 11 ROSETTES 0 LVDT'S 6 FACE		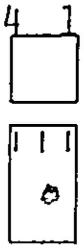		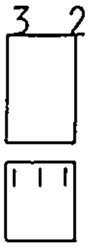
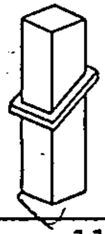 TEST 11	PHASE 2B THETA 30 STRAIN GAUGES 12 ROSETTES 0 LVDT'S 6 FACE		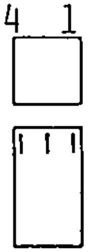		
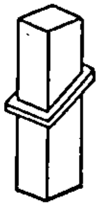 TEST 12	PHASE 2B THETA 30 STRAIN GAUGES 6 ROSETTES 6 LVDT'S 6 FACE	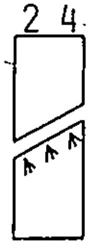	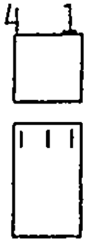		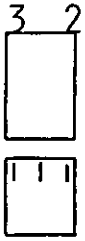

TABLE 4.3 Summary of Instrumentation for Specimens 13-15

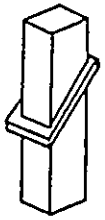 TEST 13	FACE PHASE 2A THETA 60 STRAIN GAUGES 6 ROSETTES 3 LVDT'S 6		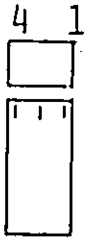	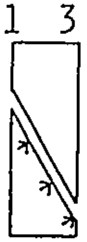	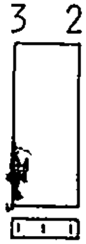
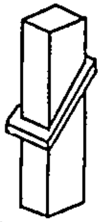 TEST 14	FACE PHASE 2A THETA 60 STRAIN GAUGES 6 ROSETTES 3 LVDT'S 6				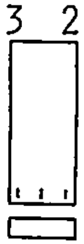
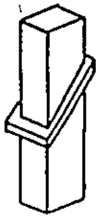 TEST 15	FACE PHASE 2A THETA 60 STRAIN GAUGES 14 ROSETTES 3 LVDT'S 6			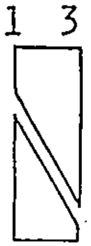	

TABLE 4.4 Summary of Instrumentation for Specimens 16-19

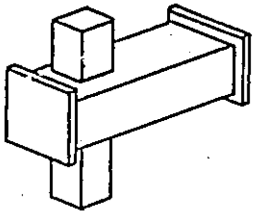 TEST 16	PHASE THETA STRAIN GAUGES ROSETTES LVDT'S	3A 90 6 3 6	FACE	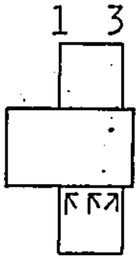	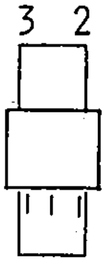	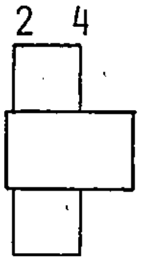	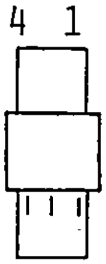
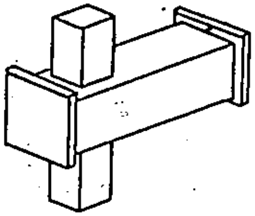 TEST 17	PHASE THETA STRAIN GAUGES ROSETTES LVDT'S	3A 90 6 3 6	FACE	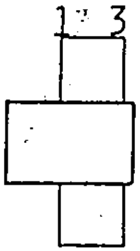	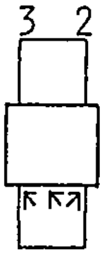	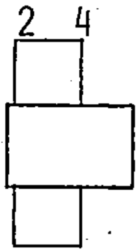	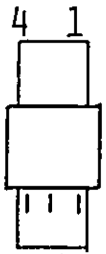
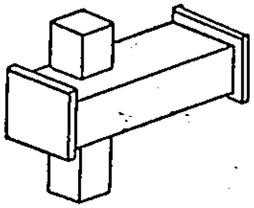 TEST 18	PHASE THETA STRAIN GAUGES ROSETTES LVDT'S	3A 90 6 3 6	FACE	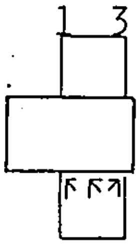	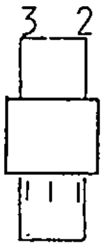	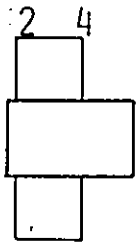	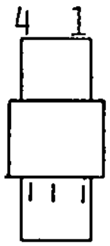
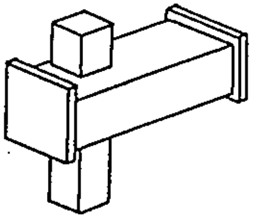 TEST 19	PHASE THETA STRAIN GAUGES ROSETTES LVDT'S	3A 90 8 6 6	FACE	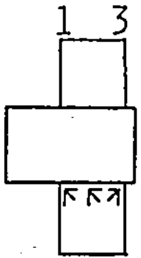	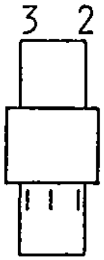	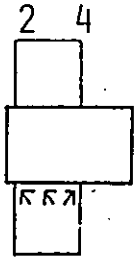	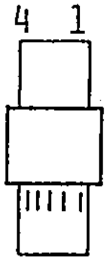

TABLE 4.5 Summary of Instrumentation for Specimens 21,22,24

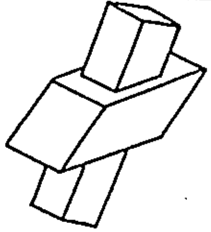 TEST 21	FACE PHASE 3B THETA 60 STRAIN GAUGES ROSETTES LVDT'S 6	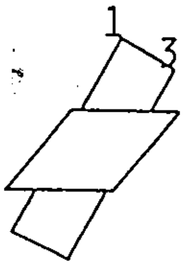	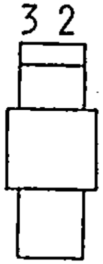	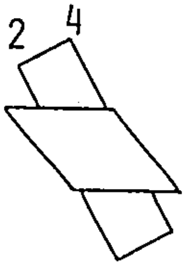	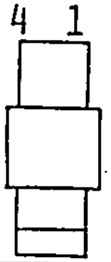
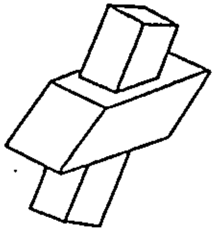 TEST 22	FACE PHASE 3B THETA 60 STRAIN GAUGES 10 ROSETTES 0 LVDT'S 6	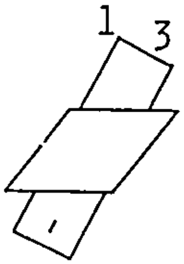	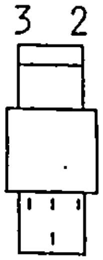	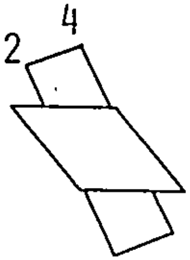	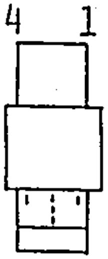
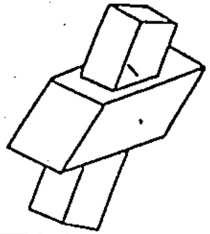 TEST 24	FACE PHASE 3B THETA 60 STRAIN GAUGES 10 ROSETTES 3 LVDT'S 6	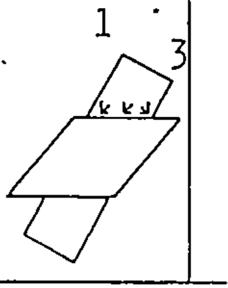	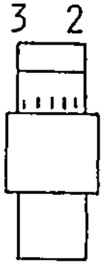	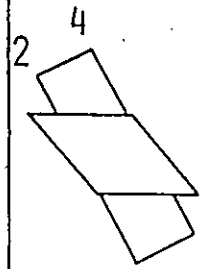	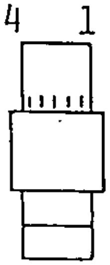

TABLE 4.6 Summary of Instrumentation for Specimens 20,23,25,26

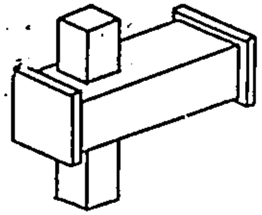 TEST 20	PHASE 3A FACE THETA 90 STRAIN GAUGES 9 ROSETTES 0 LVDT'S 6	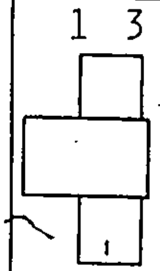	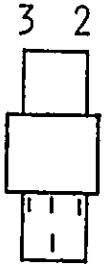	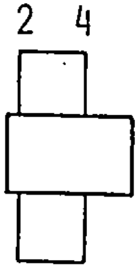	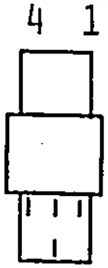
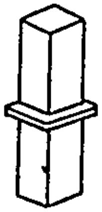 TEST 23	PHASE 1 FACE THETA 90 STRAIN GAUGES 12 ROSETTES 0 LVDT'S 6	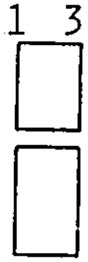			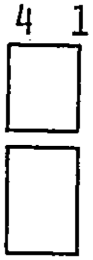
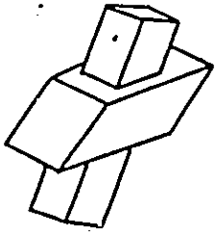 TEST 25	PHASE 3B FACE THETA 60 STRAIN GAUGES 10 ROSETTES 3 LVDT'S 6	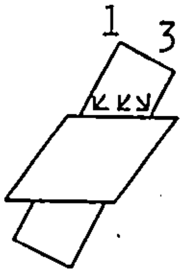	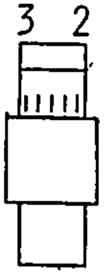	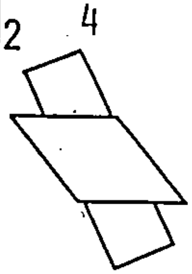	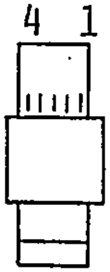
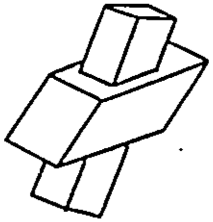 TEST 26	PHASE 3C FACE THETA 30 STRAIN GAUGES 6 ROSETTES 2 LVDT'S 6	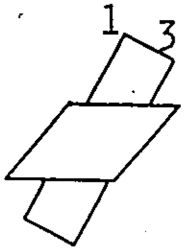	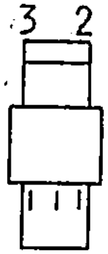	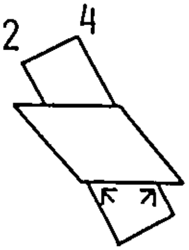	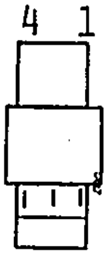

TABLE 4.7 Material Properties (after Frater 1986)

SECTION	NOMINAL GRADE	MILL REPORT VALUES(MPa)		NO. OF COUPONS TESTED	MEASURED(MPa)				E-YOUNG's MODULUS (MPa)	ELONGATION (%)
					INDIVIDUAL COUPONS		AVERAGE			
		F_y	F_u		F_y	F_u	F_y	F_u		
127.0x127.0x9.53 HSS b_1 = 127.6 mm; A_1 = 4296 mm^2; t_1 = 9.54 mm.	350W	428	494	1 corner 2 flat	497 418&434	562 494+505	440 +	512 +	201,164	13*
203.2x203.2x12.7 HSS b_0 = 203.5 mm; A_0 = 9113 mm^2; t_0 = 12.5 mm.	350W	407	505	1 corner 3 flat	440 333,336 &336	538 456,460 &469	352 +	474 +	206,385	37
PLATE(t=19.0 mm)	350W	394	571	3	344,354 &354	546,562 &566	351	558	211,150	36
WELD CONSUMABLE (D=1.2 mm)	E480	607	676	2	627&641	684&690	634	687	212,466	24
WELD CONSUMABLE (D=1.6 mm)	E480	607	676	2	632&651	733&746	641	739	208,465	24

NOTES: (1) F_y was determined from the yield plateau for Plate and HSS, while the 0.2% offset method was used for weld consumables.

(2) + F_y and F_u values shown are "average" values for the whole cross-section computed on the basis of the amount of "corner area" and "flat area" within the HSS cross-section (AISI, 1980).

(3) *.All coupons fractured at the gauge lines, thus giving incorrect elongations.

TABLE 4.8A Simplified Stress-Strain Curve

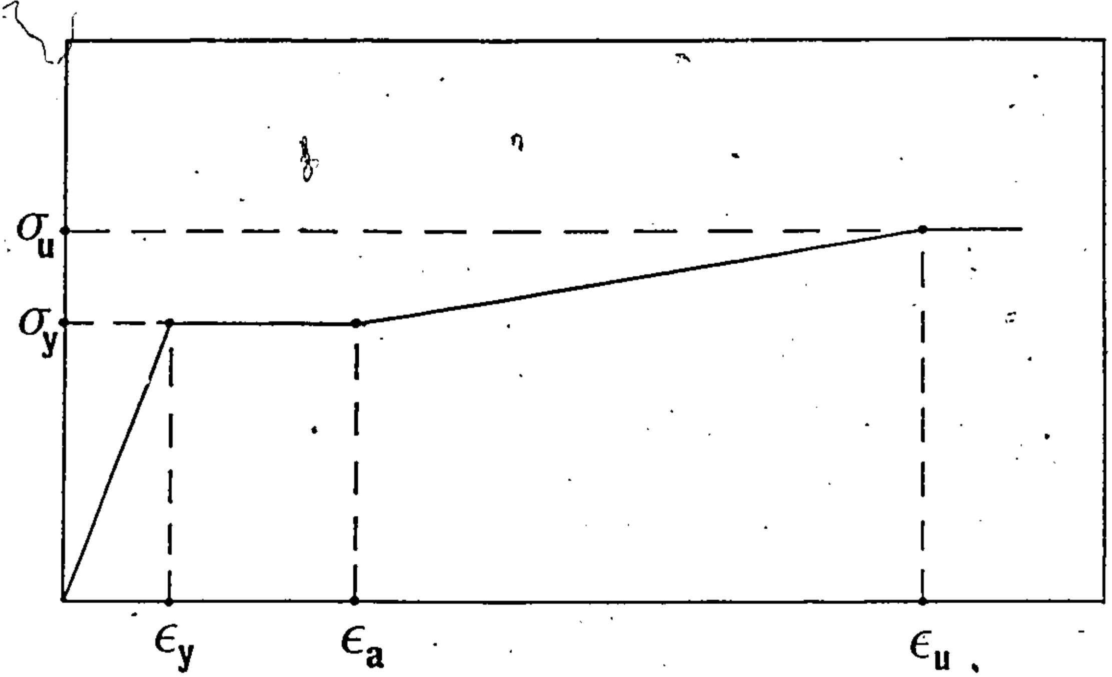

TABLE 4.8B Parameter Values for Simplified Stress-Strain Curve

SECTION	σ_y	σ_u	ϵ_y	ϵ_a	ϵ_u
HSS 127x127x9.53					
flat	426	500	0.0021	0.0125	0.08
corner	497	562	0.0024	0.01	0.08
HSS 203.2x203.2 x12.7					
flat	335	461	0.0017	0.0125	0.12
corner	440	538	0.002	0.0125	0.08
plate 19 mm	351	558	0.0017	0.00675	0.08
weld (d=1.2 mm)	634	687	0.0030	-	0.1
weld (d=1.6 mm)	641	739	0.0031	-	0.1

CHAPTER 5

NUMERICAL SIMULATION OF RECTANGULAR HOLLOW SECTION JOINTS

5.1 Introduction

This chapter presents the results obtained in a numerical simulation of the behaviour of RHS joints which were identical to those in the experimental program described in Chapter 4. The tested joints were divided into phases whereas the joints to be simulated will be grouped in stages. All the joint configurations tested became the subjects of a numerical simulation. In addition, this selection is extended to joints which cover a wider range of joint parameters. The dominant criterion for dividing the numerically simulated joints was a geometrical layout capable of lending itself to the use of the same grid generator within every stage. The relevance between phases and stages is illustrated in Figure 5.1. A brief description of the joints simulated in this numerical study is included below.

The joints from Phases 2A and 2B are equivalent to configurations in Stages 1A and 1C. An additional configuration with $\theta=45^\circ$ was accommodated in the numerical study in Stage 1B. The behaviour of a specimen with $\theta=90^\circ$ was simulated in Stage 1D, but the results are not reported herein because of predictably uniform strain and stress distributions.

The experimental Phase 3A found its counterpart in numerical Stage 2A. The joint configurations from Phases 3B and 3C are simulated in Stages 3A and 3C. As in Phase 1B, a new configuration with θ=45° was added to the numerical simulation in stage 3B.

Stage 4 is exclusive to the numerical work and includes a simulation of the behaviour of an RHS gap K joint which is part of a parametric study to be presented in Chapter 6.

This chapter presents the numerical results for Stages 1, 2 and 3 in Sections 5.3, 5.4 and 5.5. Each section starts with a comparison of numerical results with the experimental measurements. This provides further validation of the finite element model presented in Chapter 3. The numerical results are displayed by means of strains and stresses in the walls of a branch member in the directions normal to and parallel to the weldment. A detailed description of how the results are displayed is presented in the next section.

5.2 Display of Numerical Results

The results of the numerical simulation will be presented by means of the distribution of stresses in the walls of a branch member. All the joint configurations have at least one plane of symmetry and therefore the stress distribution will be shown for one-half of the branch wall at the toe , one of the sidewalls, and for one-half of the wall at the heel. The location of the toe and heel areas for the joints simulated numerically is illustrated in Figure 5.2. The distribution of stresses in the branch member walls will be presented at the sampling points which agree with the Gaussian integration points used for the evaluation of the surface and volume integrals in the numerical model. The sampling points lay on a line which is parallel to the chord connecting face at a distance of 15-30 mm from the intersection of the external surfaces of the chord and the branch. The strain gauges and rosettes mounted on tested specimens, as described in Chapter 4, were positioned along approximately the same line. Hence, the experimental and numerical results can be compared at these locations on the branch member walls. The verification examples presented for Stages 1, 2 and 3 are based on the values of the surface strains in the direction perpendicular to the weldment. The stresses are displayed for two directions: normal and parallel to the weldment. This is illustrated in Figure 5.3. The stresses normal to the weldment are denoted by σ or are called **PERPENDICULAR STRESSES**. This is shortened to SIG PERP in the titles on the graphs. The stresses in the direction parallel to the weldment are denoted by σ or are called **TANGENTIAL STRESSES**. The short form for those stresses is SIG TAN. In addition to the perpendicular stresses and the tangential stresses, the distribution of **EFFECTIVE STRESSES** is also included (short form SIG EFF).

It has been observed that a variation in the stress values existed between the top and bottom surfaces of an element representing the branch member wall in the vicinity of the connection. Typically, it is a result of bending in the branch walls near the weldment. The present numerical model does not reflect the actual weld configuration and it was decided that an average stress across the thickness of the branch wall would be a meaningful representation of numerical results for the purpose of the design of joints. For that reason, the stress values displayed later in this chapter were obtained by a numerical integration of stresses through the branch thickness. Should the displayed stresses be further multiplied by the thickness of the branch wall, one could obtain an average resultant force in the directions normal and parallel to the weldment. This is particularly useful for the design of weldments and for the estimation of bending moments due to the nonuniform stress distribution at an intersection between the branch and the chord.

5.3 Stage 1: Two RHS Sections in Tension Separated by a Plate

The finite element model introduced in Chapter 3 was used to simulate the behaviour of two RHS members separated by a rigid plate. The branch is welded to a thick plate which simulates the condition of a rigid base. The physical dimensions of the joint are the same as in the experimental Phases 2A and 2B which were represented in Chapter 4 by Specimens 12 and 14.

The finite element grid used for a typical case in numerical Stage 1 is shown in Figure 5.4. Each case in Stage 1 required a total of 72 elements and 331 nodes for the discretization of the joint.

The initial interpretation of the numerical results in Stage 1 involved illustration of the axial load vs. axial displacement results as shown in Figure 5.5. Two characteristic points on each load-displacement curve were identified : the first yield and the section yield . The hypothetical first yield (FY) point corresponds to a state in which stresses at any part of a structure reach the value of the yield stress for the material. Such a state was found to depend on the angle of inclination θ. The values of the load P corresponding to the first yield determined numerically for various angles are as follows:

θ degree	30	45	60	90
P kN	1400	1625	1700	1725

The point of a section yield (SY), on the load - displacement curves in Figure 5.5a-d, corresponds to a sudden increase in the axial displacements as a result of the entire cross section of a branch becoming inelastic. Figure 5.5e illustrates the loads associated with FY and SY points as functions of the angle of inclination θ. The difference between FY and SY load levels is most noticeable for θ=30° and diminishes as the angle θ increases up to 90°. The discrepancy between FY and SY load levels for θ=90° is attributed to different values of the yield stress for the corner zones (426 MPa) as opposed to the flat portions (497 MPa) of an RHS. The material properties used in the numerical simulation are identical to those measured in the experiments which were presented in Section 4.7.

A comparison of the load levels corresponding to FY in Stages 1A and 1C with the ultimate load levels attained during the experiment in Phases 2A and 2B (see Chapter 4, Table 4.1) leads to a conclusion that many specimens failed before reaching a hypothetical FY point. Most probably the strength of the weldment is the reason for the observed discrepancy, especially since its size was often smaller than recommended in design practice. The verification of the numerical results of Stage 1 with the experimental measurements of Phase 2 in this section will be carried out using the strains in the walls of a branch at the first yield load level. The verification example for Stage 1 is shown in Figure 5.6. The numerical results are presented by means of the strains in the branch member walls in the direction perpendicular to the weldment. A good agreement between experimental and numerical results is apparent. The strains at the heel are higher than at the toe. A variation of the strain level on the sidewall is evidently leading to smaller values near the heel than near the toe. One can regard the verification of the numerical model for Stage 1 as successful and, therefore, the outcome of further analysis can be presented below.

The results of the numerical simulation of the behaviour of an RHS-to-RHS connection, separated by a plate, are illustrated at the first yield load level. Three different types of stresses are used to demonstrate the behaviour of this configuration: the **perpendicular** stresses (Figure 5.7), the **tangential** stresses (Figure 5.8), and the **effective** stresses (Figure 5.9).

A summary of observations based on the distribution of stresses in the walls of a branch member for Stages 1A , 1B and 1C is listed below.

Perpendicular stresses in Stage 1 (Figure 5.7)

The level of perpendicular stresses in the sidewall is much lower than in either the toe or the heel. The stresses in the sidewall are at a level of about 300 MPa, 200 MPa and 100 MPa for Stages 1A, 1B and 1C respectively. A noticeable variation of the stresses in the sidewall takes place for θ=30° , where their values decrease towards the heel. The values of perpendicular stresses at the heel are higher than at the toe, which is particularly evident for θ=30° and 45°. There is no sign of either the toe or the heel not being fully effective in the transfer of the load from the branch to the plate.

Tangential stresses in Stage 1 (Figure 5.8)

The tangential stresses in the sidewall are much higher than for either the toe or the heel. In Stages 1A and 1B, the stresses in the sidewall remain almost uniform. In Stage 1C, a noticeable increase in the values of stresses in the sidewall can be observed towards the heel. There is no significant variation of stresses at the toe or the heel. The stress levels at both locations remain under the 50 MPa mark.

Effective stresses in Stage 1 (Figure 5.9)

The distribution of effective stresses is represented by an almost perfectly smooth curve. A few points of exception are located near the corners, which are not represented by a sufficient number of discrete points. The distribution of the stresses is highly nonuniform for Stage 1C with the yielding starting on the sidewall near the heel area. In this case the effective stresses in the sidewall decrease towards the toe. In Stage 1B the situation is similar to that in Stage 1C, but the variation of stresses is not as significant. The distribution of effective stresses in the branch walls in Stage 1A is nearly uniform across the section.

This review of the perpendicular, tangential and effective stresses in Stage 1 of numerical analysis suggests the following conclusions:

- the perpendicular stresses are the highest at the toe and the heel;
- the tangential forces are the highest on the sidewall;
- the point of first yielding in a typical joint of Stage 1 is located on the sidewall near the corner at the heel; this is particularly evident for a specimen with θ=30°;
- both the heel and the toe appear to be fully effective in the transfer of perpendicular stresses;
- little variation of the stresses was observed within each of the sidewalls; significant differences develop between the sidewall and either the toe or the heel.

5.4 Stage 2: Two RHS Sections Welded to RHS Chord at 90°

The numerical Stage 2 corresponds to the experimental Phase 3A which was represented by Specimen 18 in Section 3.2 . The finite element grid used for the numerical simulation of the behaviour of this joint is illustrated in Figure 5.10. A total of 102 elements and 451 nodal points were used in the simulation of one-quarter of the joint. The boundary conditions imposed were as listed in Figure 5.10.

The verification example for Stage 2 is shown in Figure 5.11. The strains measured by the strain gauges and rosettes on Specimen 18 in the direction perpendicular to the weldment are compared with the surface strains from the numerical analysis for the same locations. The comparison is made at the load level of P= 540 kN which corresponds to vertical deflections of the chord connecting face of 1% b_o. The agreement between the experimental and numerical results is very good. Both the strain levels and the shape of the strain distribution profile are well duplicated by the numerical simulation of the joint behaviour. The numerical results for Stage 2 are displayed in Figure 5.12 by means of the stress distribution in the branch member walls at the load level corresponding to the local deflections of the chord connecting face reaching 1% b_o.

The perpendicular stresses (Figure 5.12) in the branch member walls are highest near the branch corners. The lowest values of stresses can be found at the midwall location in the heel area, where a level of about -50 MPa indicates compressive forces, despite the branch being loaded in tension. Consequently, the heel area is not fully effective in the load transfer between the branch and the chord top face.

The tangential stresses (Figure 5.12) in the sidewall and the heel area fluctuate around the zero stress level. However, the same stresses reach the value of -300 MPa at the toe, which manifests a sudden increase of compressive forces at this location.

The effective stresses (Figure 5.12) are highest in the centre of the toe. Two other peak points occur at the corners of the branch. The midwall locations in the sidewall and the heel show much lower values of effective stress.

A summary of the numerical results for Stage 2 indicates that the introduction of the flexible base conditions under the branch significantly changes the distribution of stresses in the branch member walls. The difference between the minimum and maximum stress values on any given branch member wall is much higher than in the rigid base conditions in Stage 1 where it is approximately constant. The high values of the tangential stress in the centre of the toe area can be explained by the upward deflection of the chord connecting face which exerts an extra pressure on this branch member wall. The perpendicular stresses peak at the corners of an RHS branch member. The effective stresses are the highest at the midwall location at the toe and around the corners.

5.5 Stage 3: Two RHS Sections Welded to RHS Chord at Angles 60°, 45° and 30°

In Stage 3 of the numerical program, the branch is inclined to the chord at angles other than 90°. Results of Stages 3A and 3C correspond to Phases 3B and 3C of experiments, which were represented in Chapter 4 by Specimens 25 and 26. An example of the finite element grid used for the discretization of the joint is shown in Figure 5.13. The numerical results were verified with Test 25 at a load level of 600 kN, which corresponds to the localised deflections of 1% b_o. The results of a comparison for the surface strains in the direction perpendicular to the weldment are illustrated in Figure 5.14. Reasonable agreement between the experimental and numerical results can be observed. Both numerical and experimental results indicate higher strains at the toe than at the heel.

As before, the numerical results are presented by means of perpendicular, tangential and effective stresses in the branch member walls (see Figures 5.15, 5.16, 5.17). The stresses are displayed at the load levels corresponding to a local deflection of the chord connecting face of 1% b_o which were as shown below:

θ degree	30	45	60
P kN	1247	821	636

Perpendicular Stresses in Stage 3 (Figure 5.15)

In all cases the maximum stress value is at the branch corner near the toe. The significant difference among the stresses for Stages 3A, 3B and 3C is in the values at the toe and the heel. For θ=30° a stress of about -100 MPa occurs at the middle of the toe and stresses at the heel reach 200 MPa. For θ=45° the stresses at both the middle of the toe or the middle of the heel are near zero. For θ=60° the middle of the heel has a stress of -50 MPa whereas the middle of the toe is at the + 50 MPa mark. It appears that the toe is not fully effective for θ=30° and the heel is not fully effective for θ-60°. The resultant force is shifting slightly from the heel for θ-30° to the toe for θ-60°.

Tangential Stresses in Stage 3 (Figure 5.16)

In all cases, the sidewall participates most in the transfer of tangential stresses. For θ-30° a significant difference takes place between the minimum and maximum values of the stresses and is equal to about 400 MPa. For other angles this difference is only about 200 MPa. In all cases the centre of the toe indicates negative stresses.

Effective Stresses in Stage 3 (Figure 5.17)

The stress profiles are similar in all cases. In all cases the maximum values occur at the branch corners; the minimum values are at the centre of the heel; and the stresses at the centre of the toe are near the 400 MPa mark.

5.6 Summary of Numerical Results from Stages 1,2 and 3

In every stage a good agreement was achieved between the numerical and experimental results. Thus the validation of the model has been extended for three RHS joints of various configuration. The joints simulated in Stage 1 represent rigid base conditions. The branch members are welded to a plate at angles θ of 30°, 45° and 60°. The results are presented at the first yield load level. The effective stresses for θ-30° are higher in the heel area than near the toe. For θ-45° or 60° the distribution of effective stresses is almost uniform. The maximum effective stresses for θ-30° and 45° occur on the sidewall near the heel.

This can be explained by high tangential stresses and low perpendicular stresses at this location. It is apparent that the toe and the heel participate mainly in the transfer of perpendicular stresses and the sidewall is effective in the transfer of tangential stresses.

The joint simulated in **Stage 2** is an example of flexible base conditions. The branch member is welded to an RHS at an angle θ=90°. This joint has a strengthening plate welded perpendicular to the chord near the branch which is supposed to reflect the unchanged chord cross section geometry in an RHS gap joint. The presence of this plate is causing high perpendicular stresses in the toe area, low tangential stresses at the same location and higher effective stresses at the toe than at the heel.

Stage 3 is represented by joints similar to a configuration described in Stage 2 but the angles θ are 30° , 45° and 60° . The perpendicular stresses for θ = 30° at the midwall location of the toe are lower than at the midwall of the heel. The opposite is true for θ = 60°. The values of tangential stresses at the toe are all negative which indicates compressive forces. The effective stresses in all cases peak near the corners of the RHS branch member.

Throughout Stages 1,2 and 3 two significant parameters were varied: flexibility of the base under the branch member and the angle of inclination θ .

For the **rigid base conditions** (Stage 1) the perpendicular and tangential stresses are nearly constant within each wall but a substantial difference existed in their levels between two neighbouring walls; the effective stress distribution however is rather smooth and tends to be uniform across the section with increasing θ . For the **flexible base conditions** (Stages 2 and 3) a substantial variation takes place in the stress levels within each wall of the branch member ; the perpendicular and effective stresses peak at the corners of RHS branch member ; and the tangential stresses are negative at the middle of the toe.

The effect of **decreasing** θ (from 60° to 30°) in rigid base conditions leads to : higher values of perpendicular stresses at the heel as compared with the toe, high effectiveness of the sidewall in the transfer of tangential stresses , and to higher effective stresses at the heel than at the toe.

When θ is decreasing in the flexible base conditions the difference between the maximum and minimum values of the perpendicular stresses decreases; the effectiveness of the sidewall in the transfer of the tangential stresses increases ; and the concentration of high effective stresses at the corner near the heel becomes well pronounced.

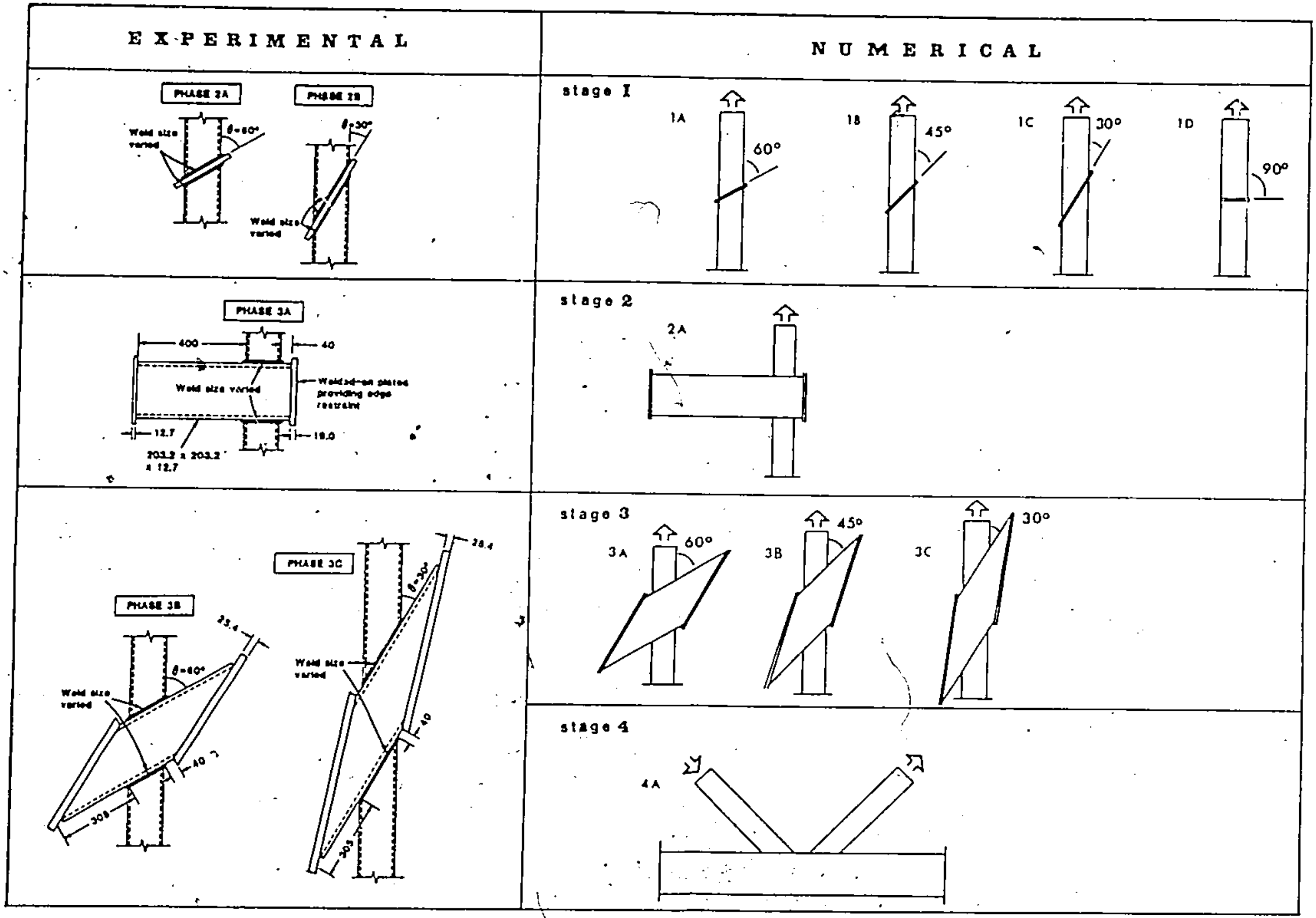

FIGURE 5.1 Comparison of Experimental and Numerical Programs

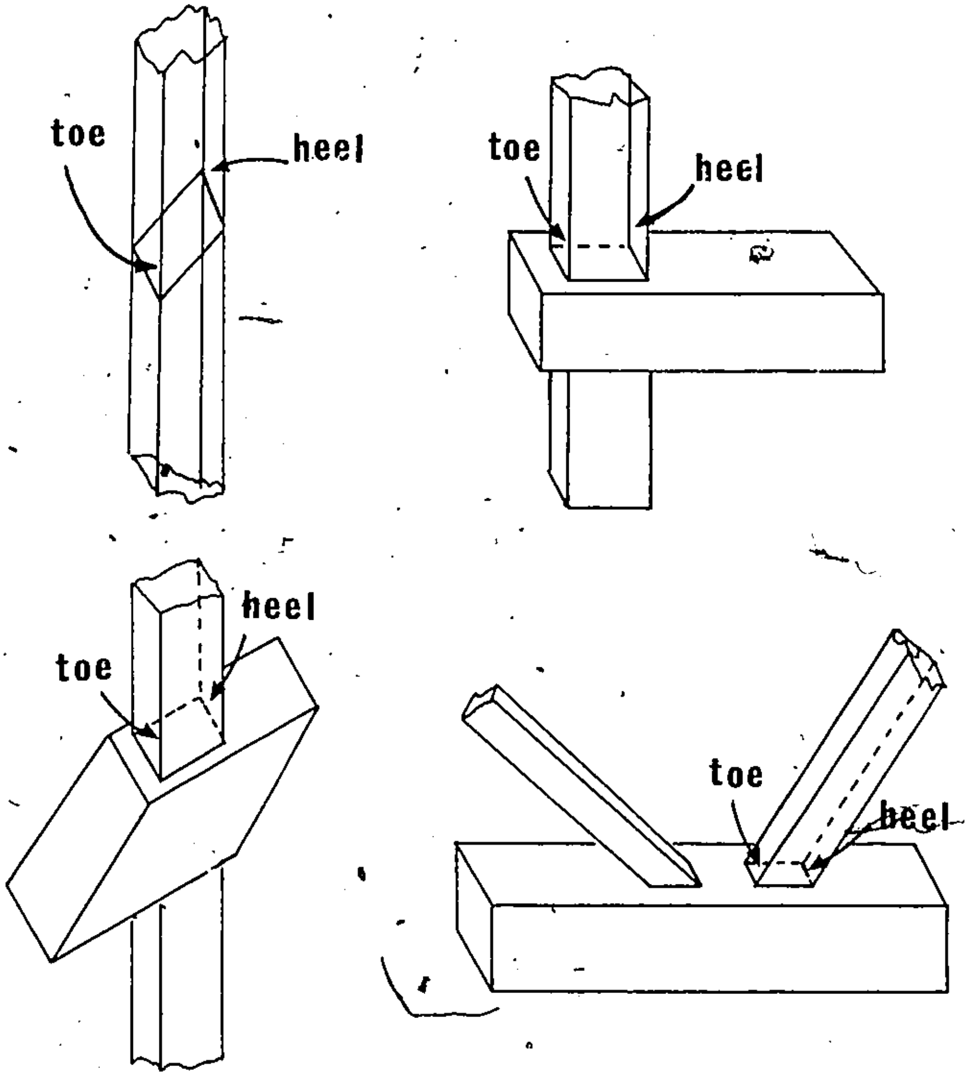

FIGURE 5.2 Locations of Toe and Heel for Stages 1-4

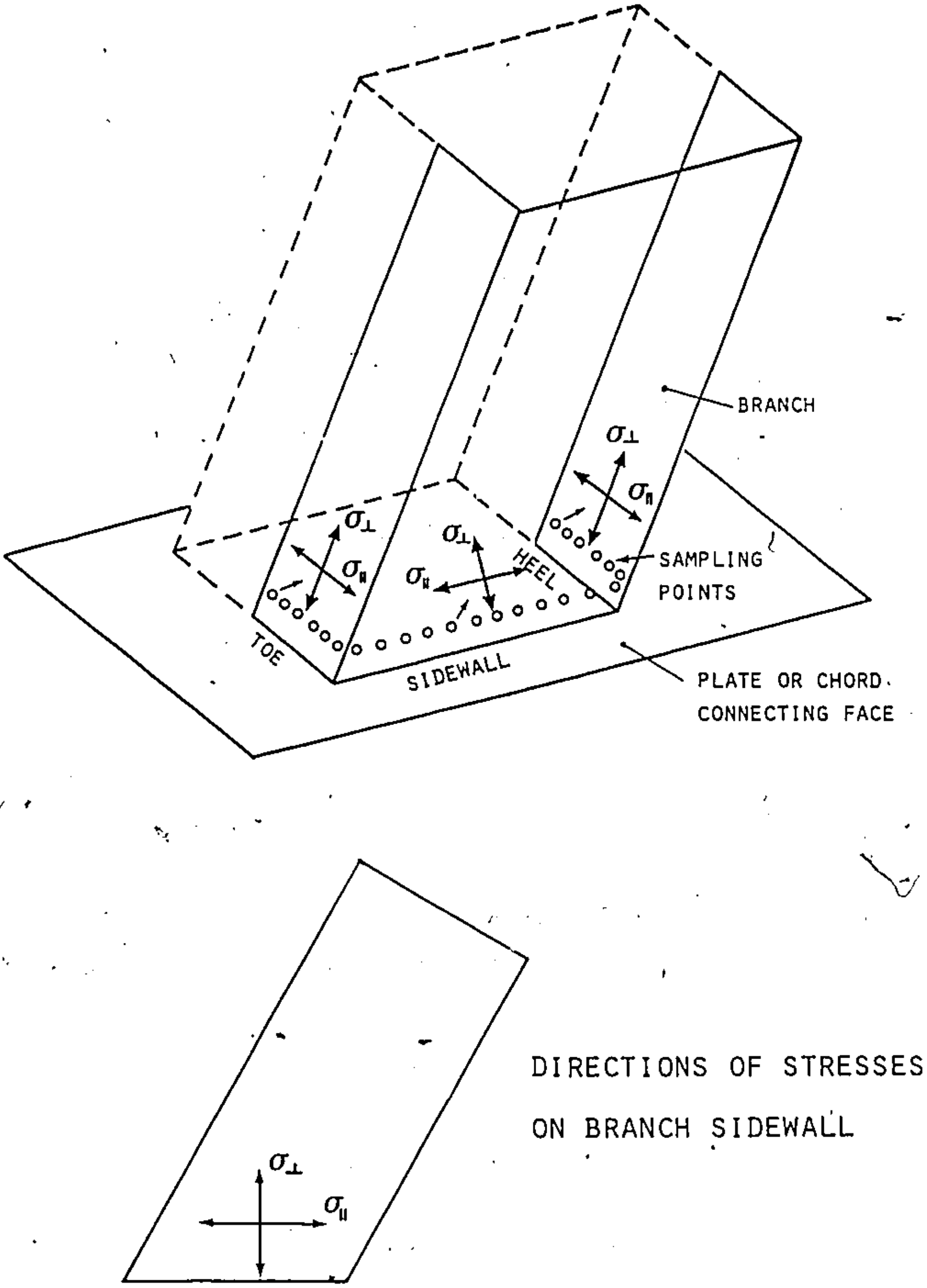

FIGURE 5.3 Convention for Display of Stresses

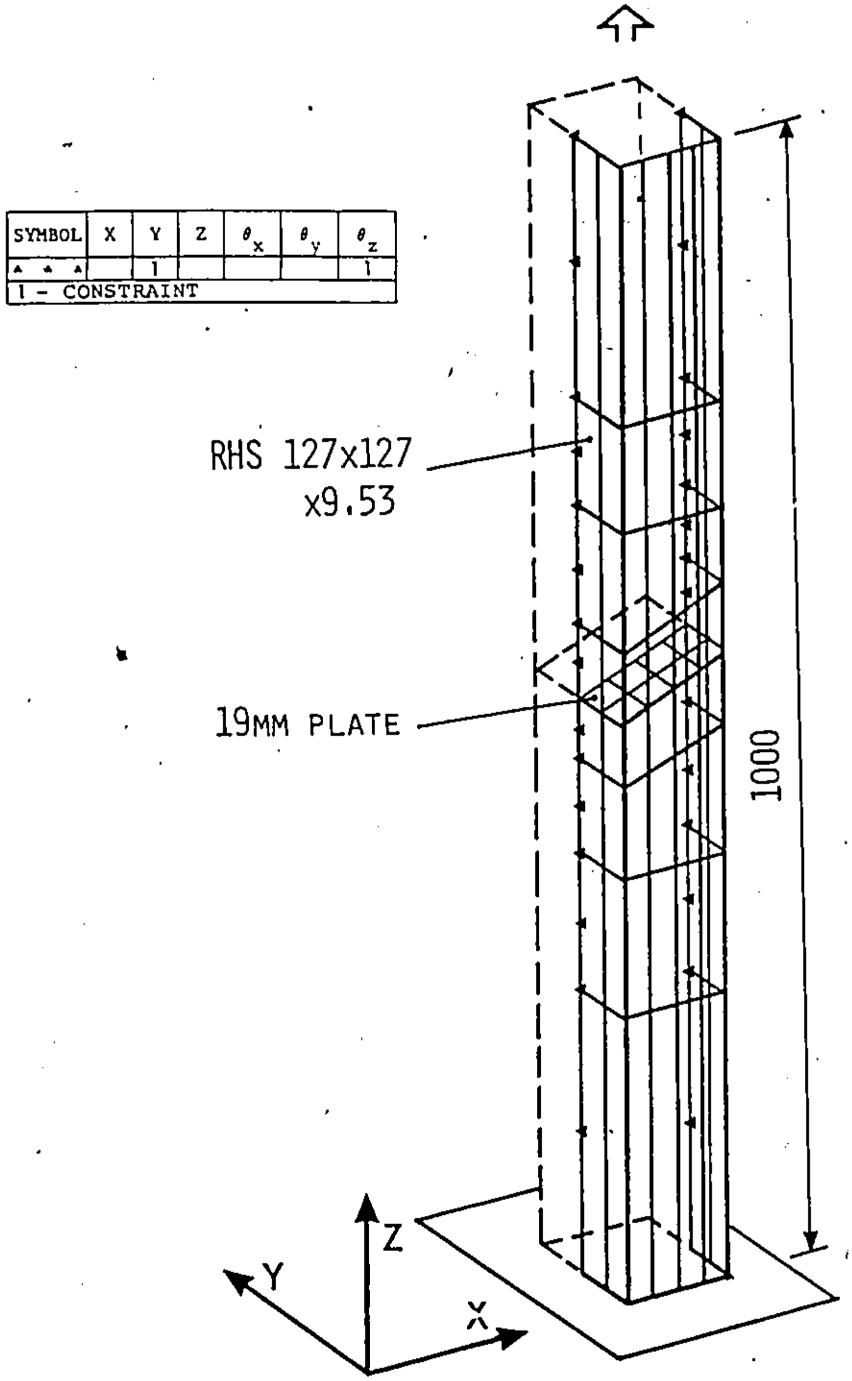

SYMBOL	X	Y	Z	θ_x	θ_y	θ_z
▲ ▲ ▲		1				1
1 - CONSTRAINT						

FIGURE 5.4 Finite Element Grid for Stage 1

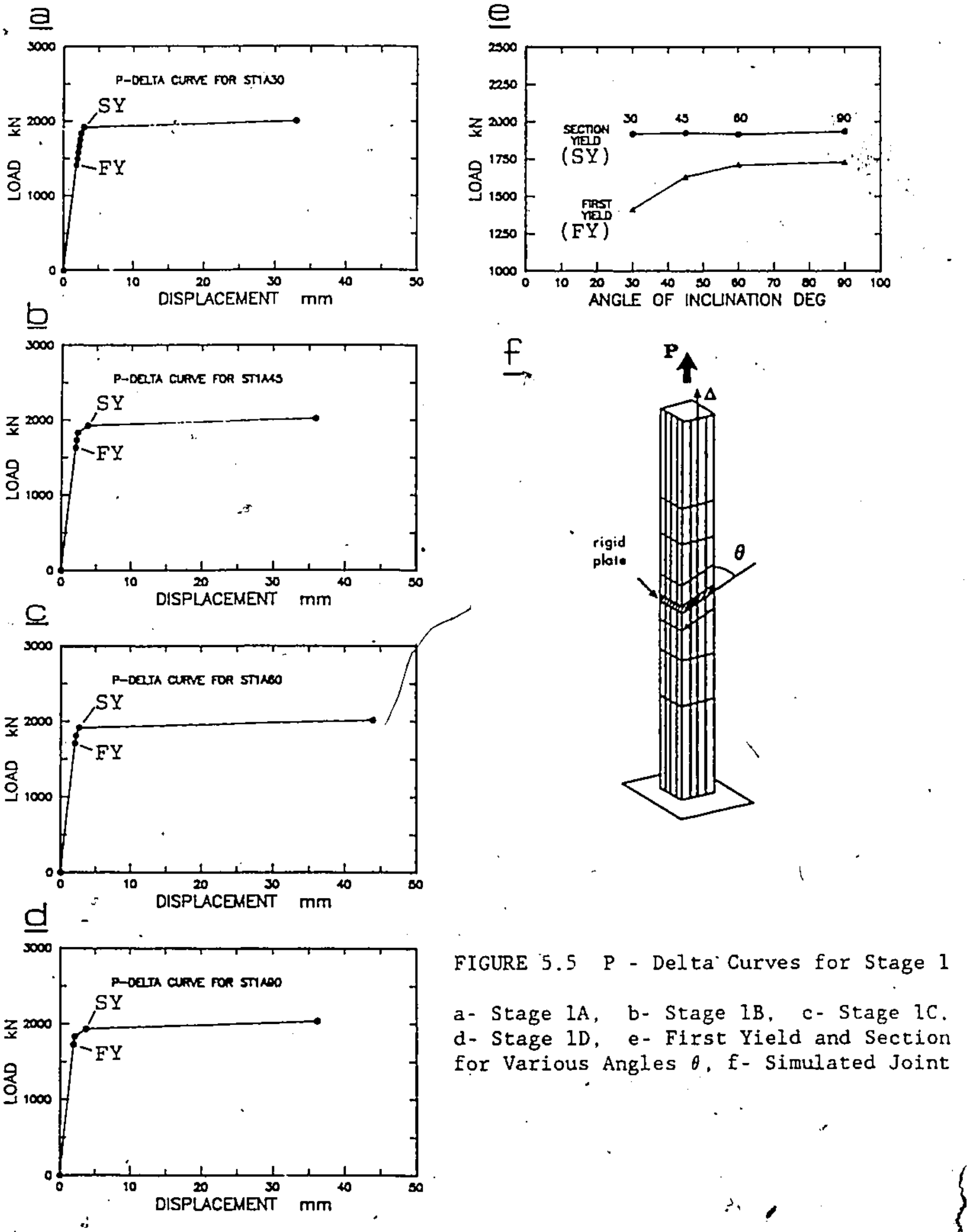

FIGURE 5.5 P - Delta Curves for Stage 1

a- Stage 1A, b- Stage 1B, c- Stage 1C, d- Stage 1D, e- First Yield and Section for Various Angles θ, f- Simulated Joint

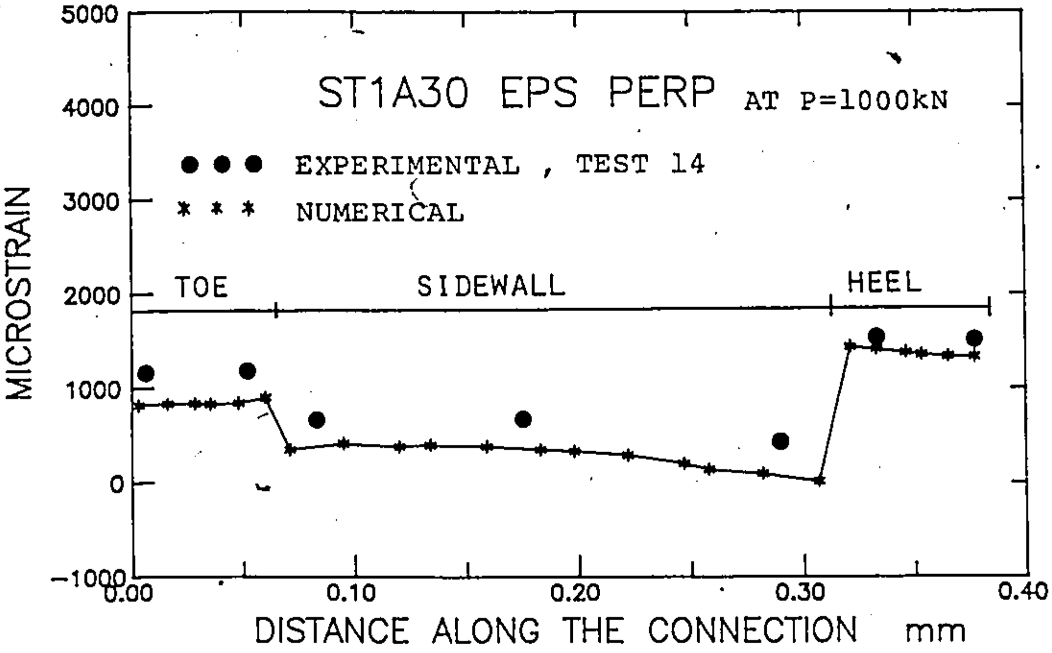

FIGURE 5.6 Verification Example for Stage 1

PERPENDICULAR STRESSES

STAGE 1C
$\theta = 30°$

STAGE 1B
$\theta = 45°$

STAGE 1A
$\theta = 60°$

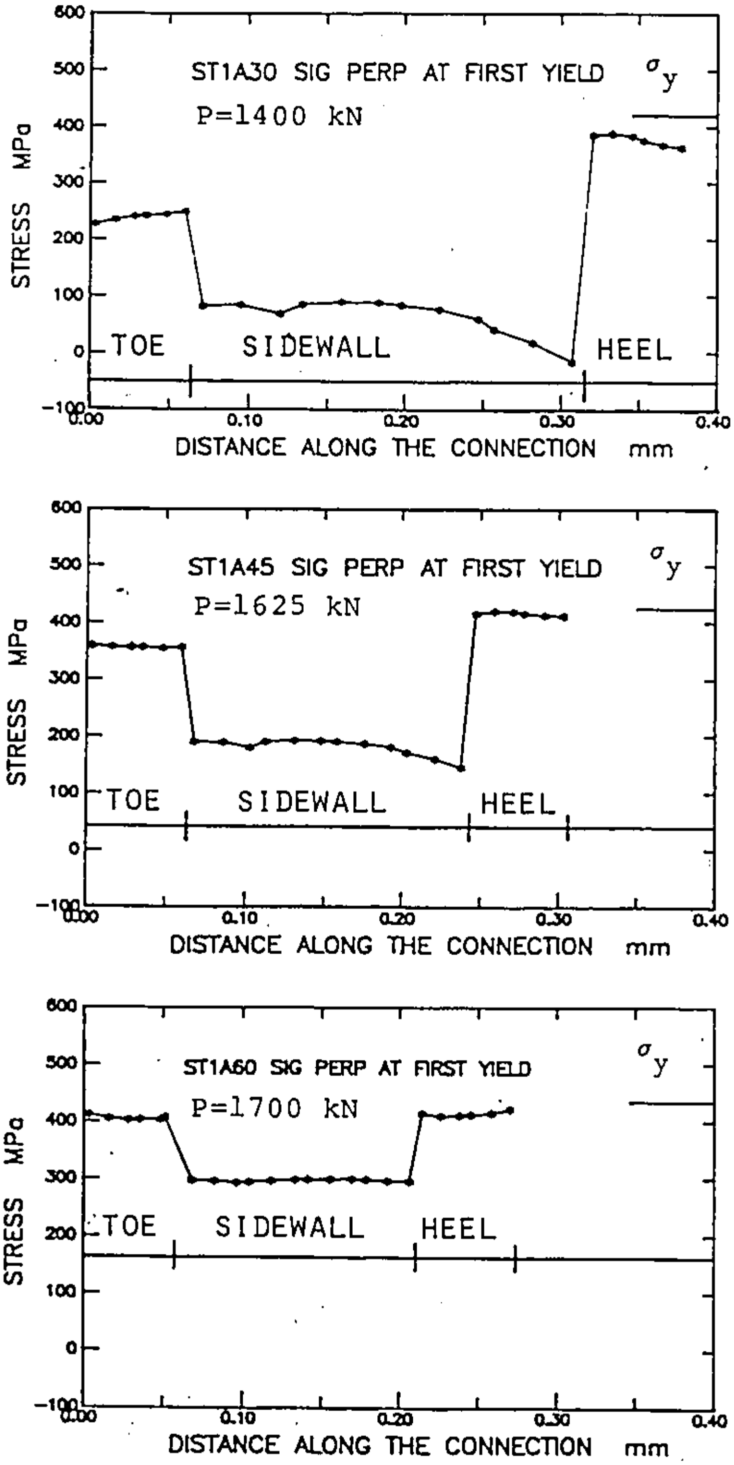

FIGURE 5.7 Display of Perpendicular Stresses in Branch Walls for Stage 1

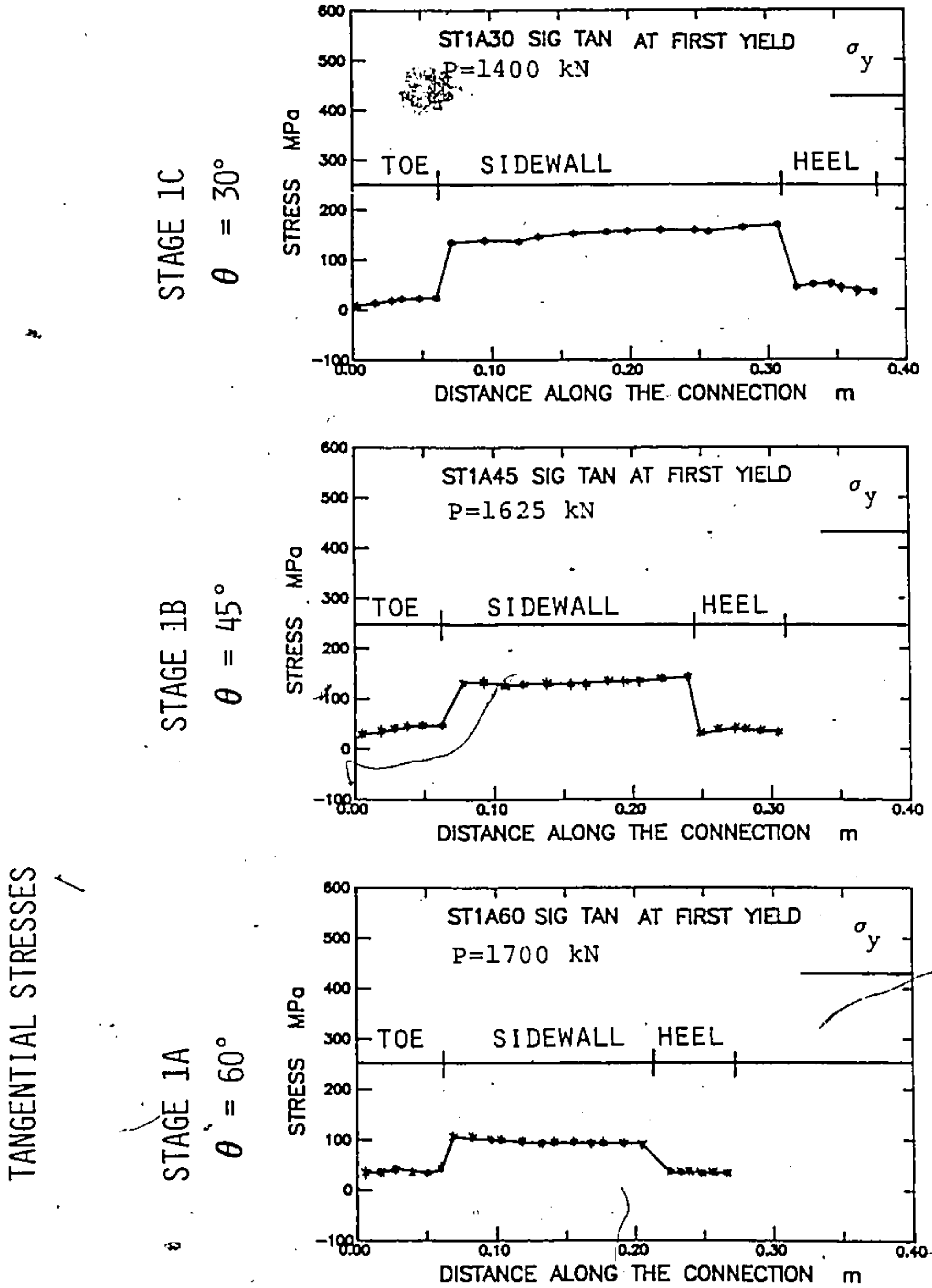

FIGURE 5.8 Display of Tangential Stresses in Branch Walls for Stage 1

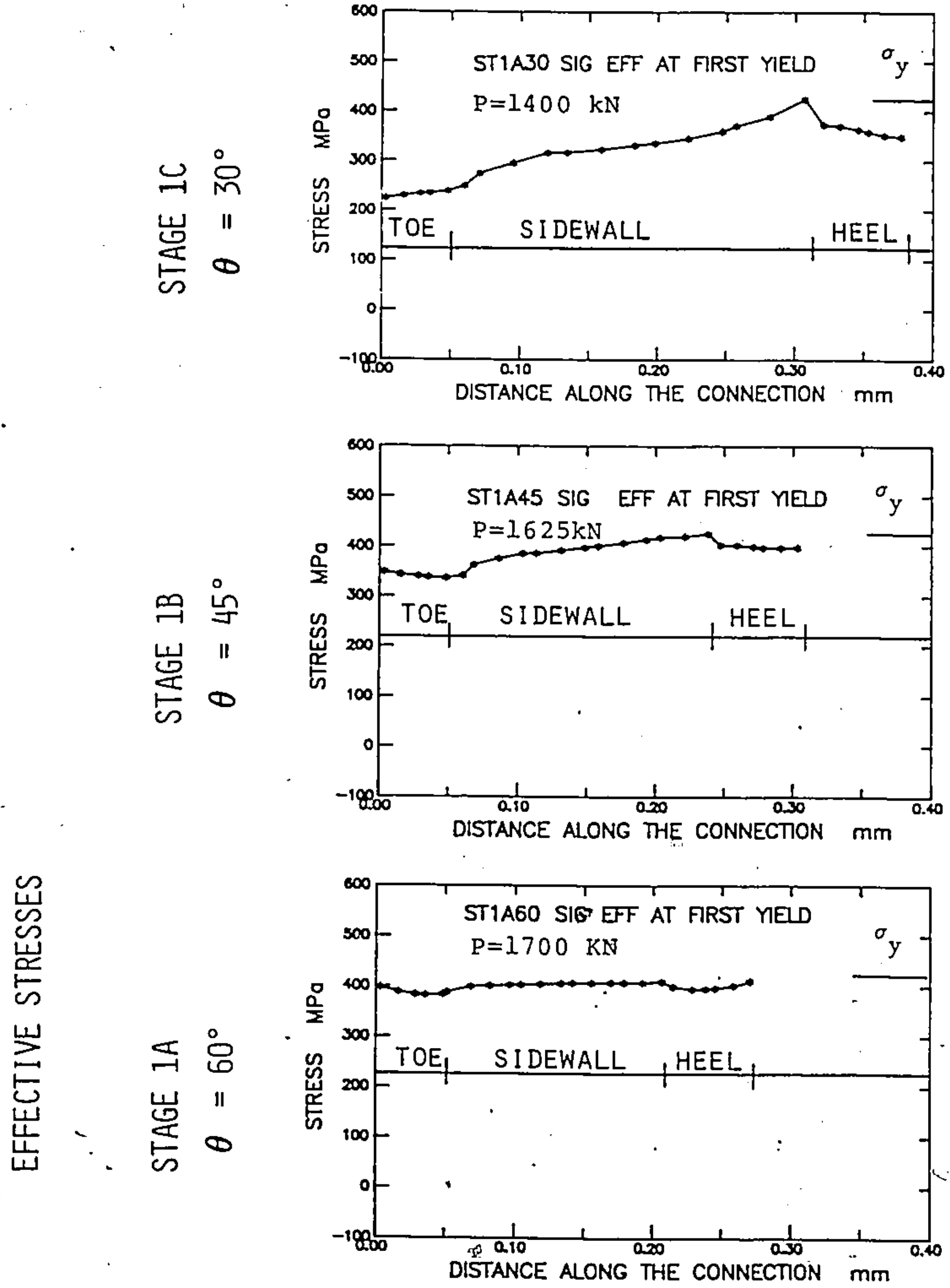

FIGURE 5.9 Display of Effective Stresses in Branch Walls for Stage 1

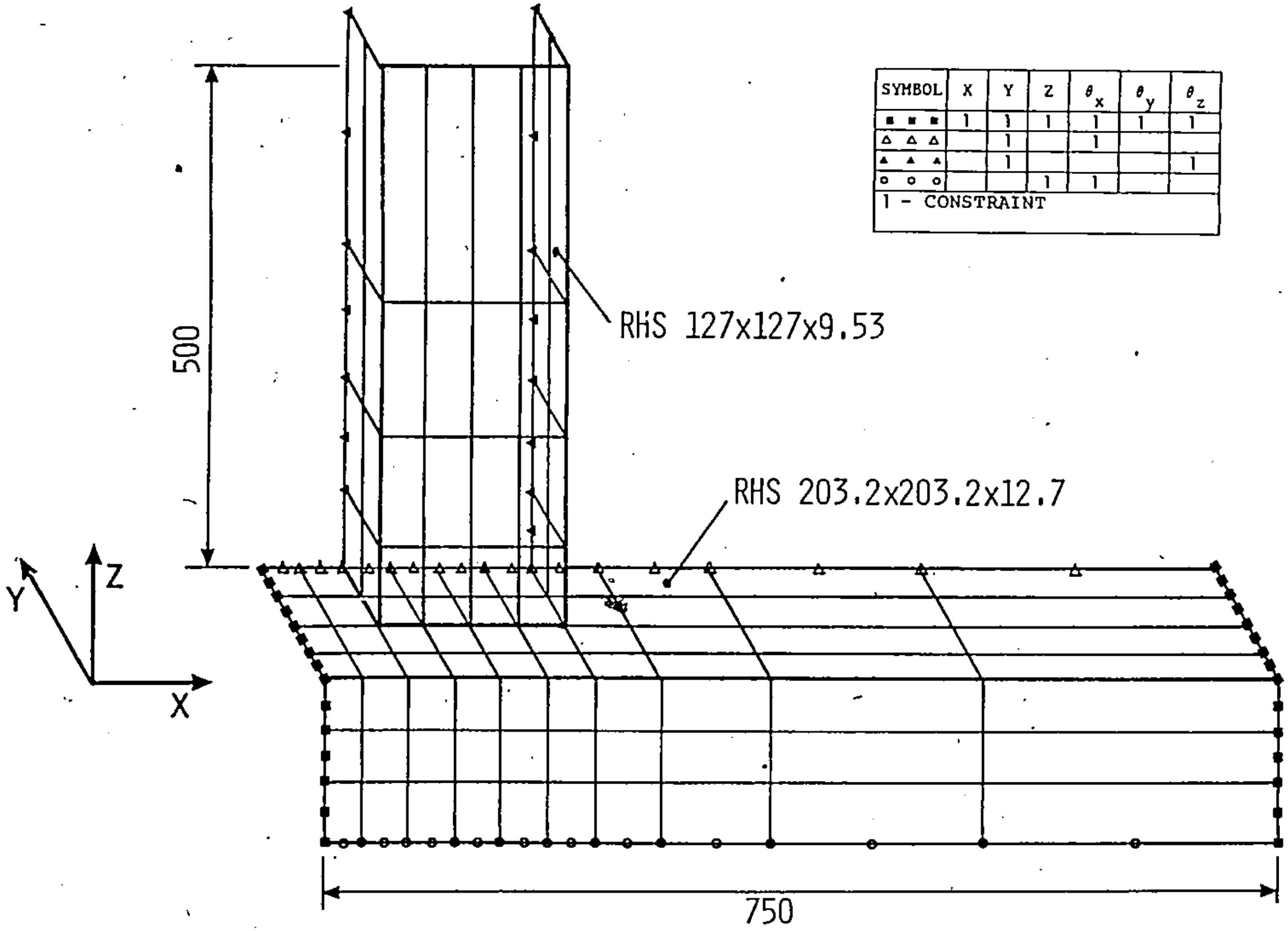

SYMBOL	X	Y	Z	θ_x	θ_y	θ_z
■ ■ ■	1	1	1	1	1	1
△ △ △		1		1		
▲ ▲ ▲		1				1
○ ○ ○			1	1		

1 - CONSTRAINT

FIGURE 5.10 Finite Element Grid for Stage 2

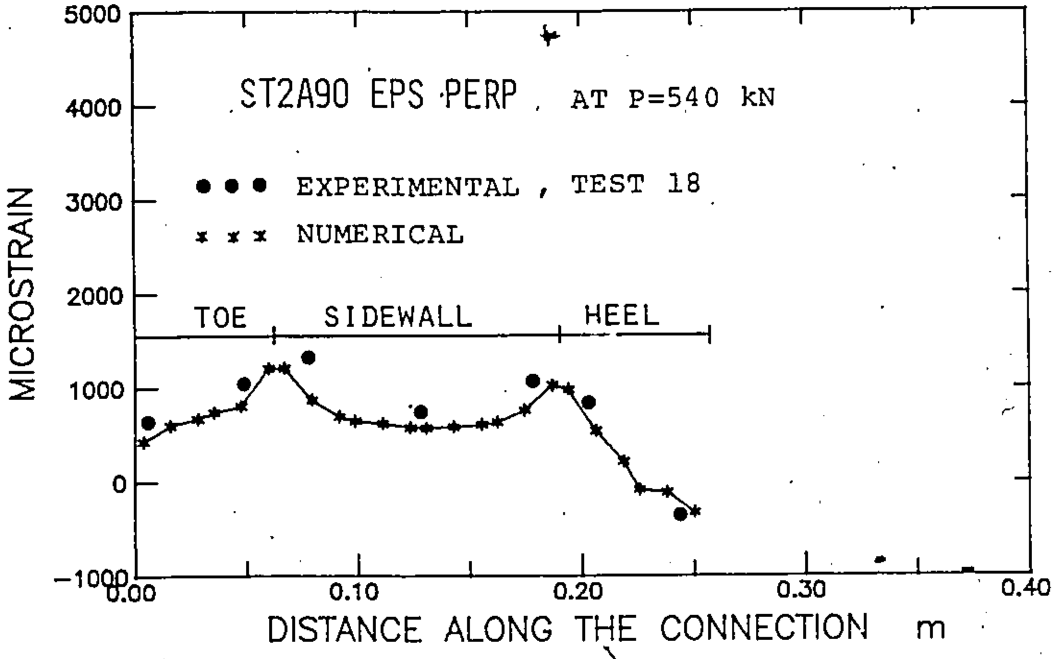

FIGURE 5.11 Verification Example for Stage 2

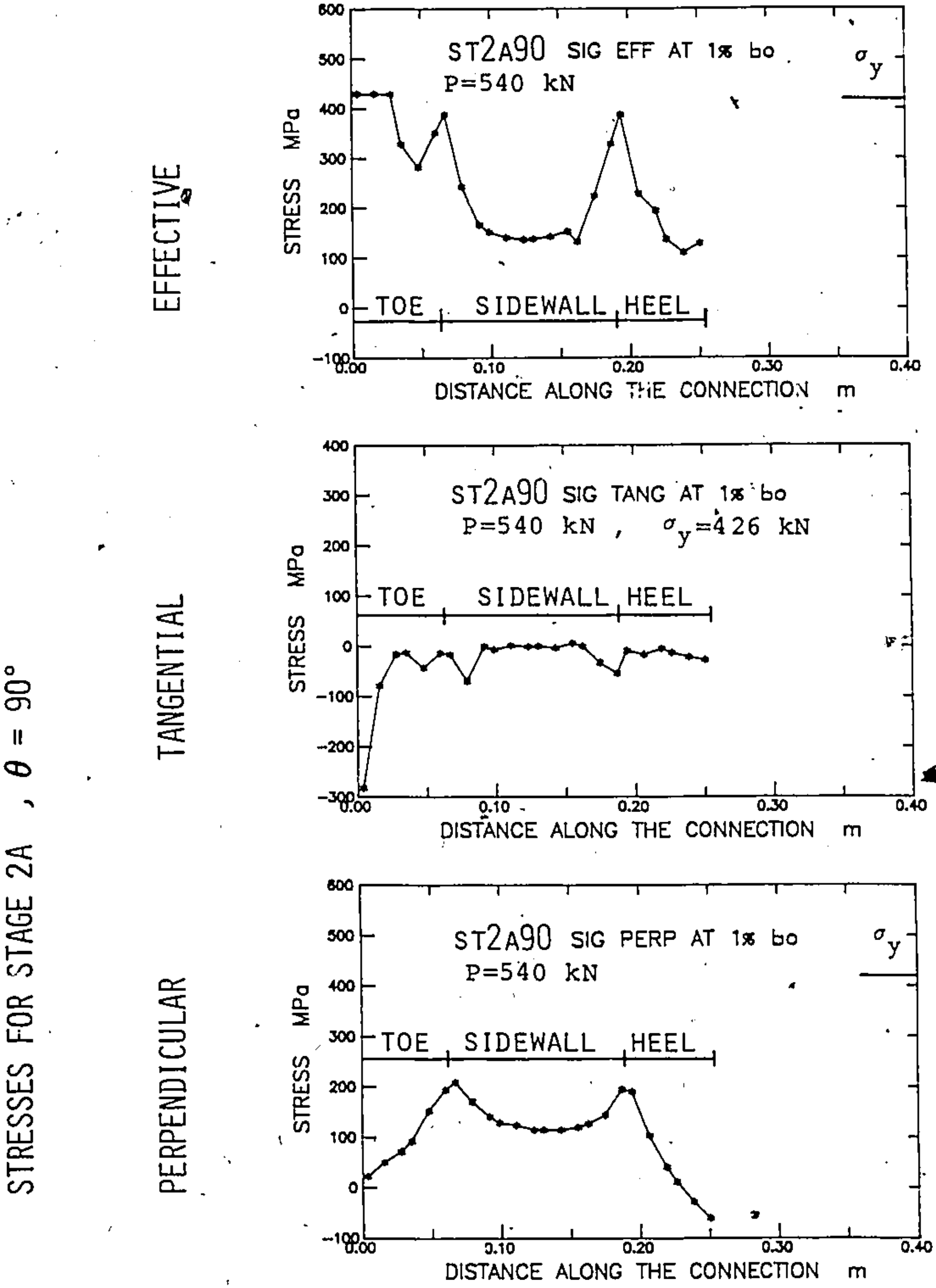

FIGURE 5.12 Display of Stresses in Branch Walls for Stage 2

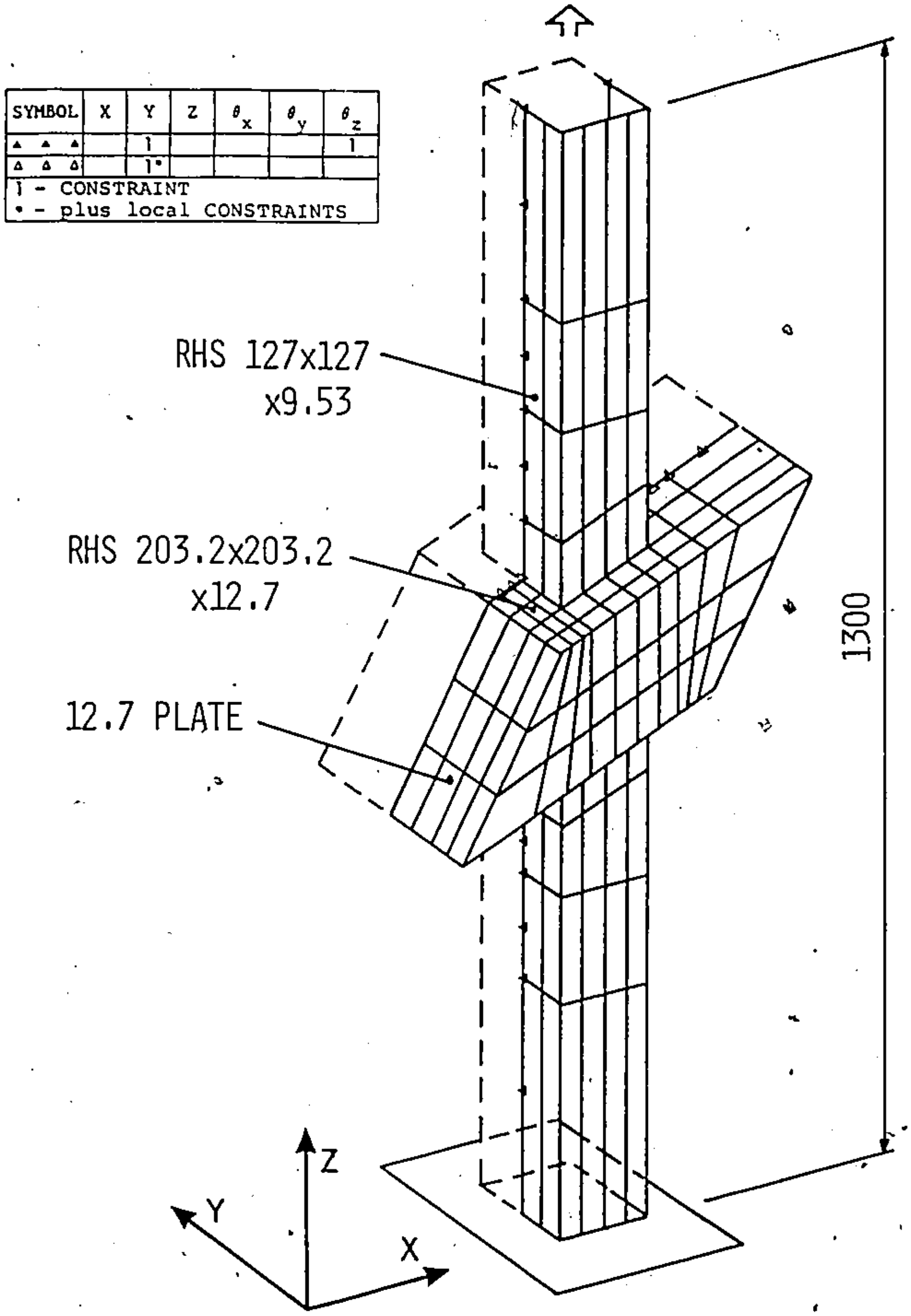

SYMBOL	X	Y	Z	θ_x	θ_y	θ_z
▲ ▲ ▲		]				]
△ △ △		]•				

] - CONSTRAINT
• - plus local CONSTRAINTS

FIGURE 5.13 Finite Element Grid for Stage 3

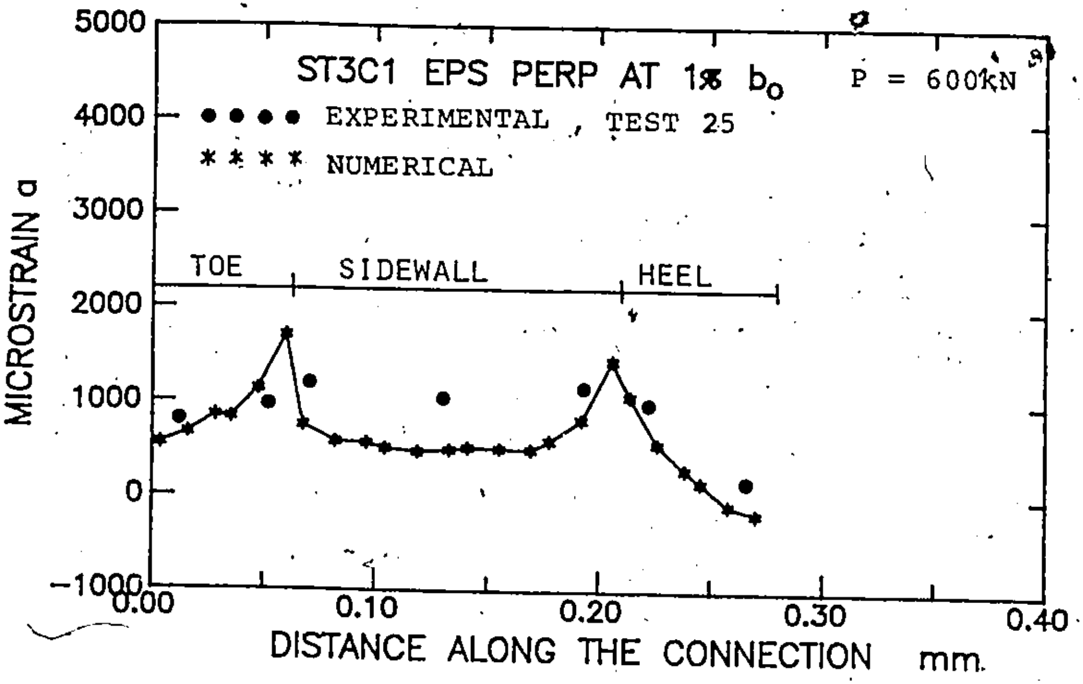

FIGURE 5.14 Verification Example for Stage 3

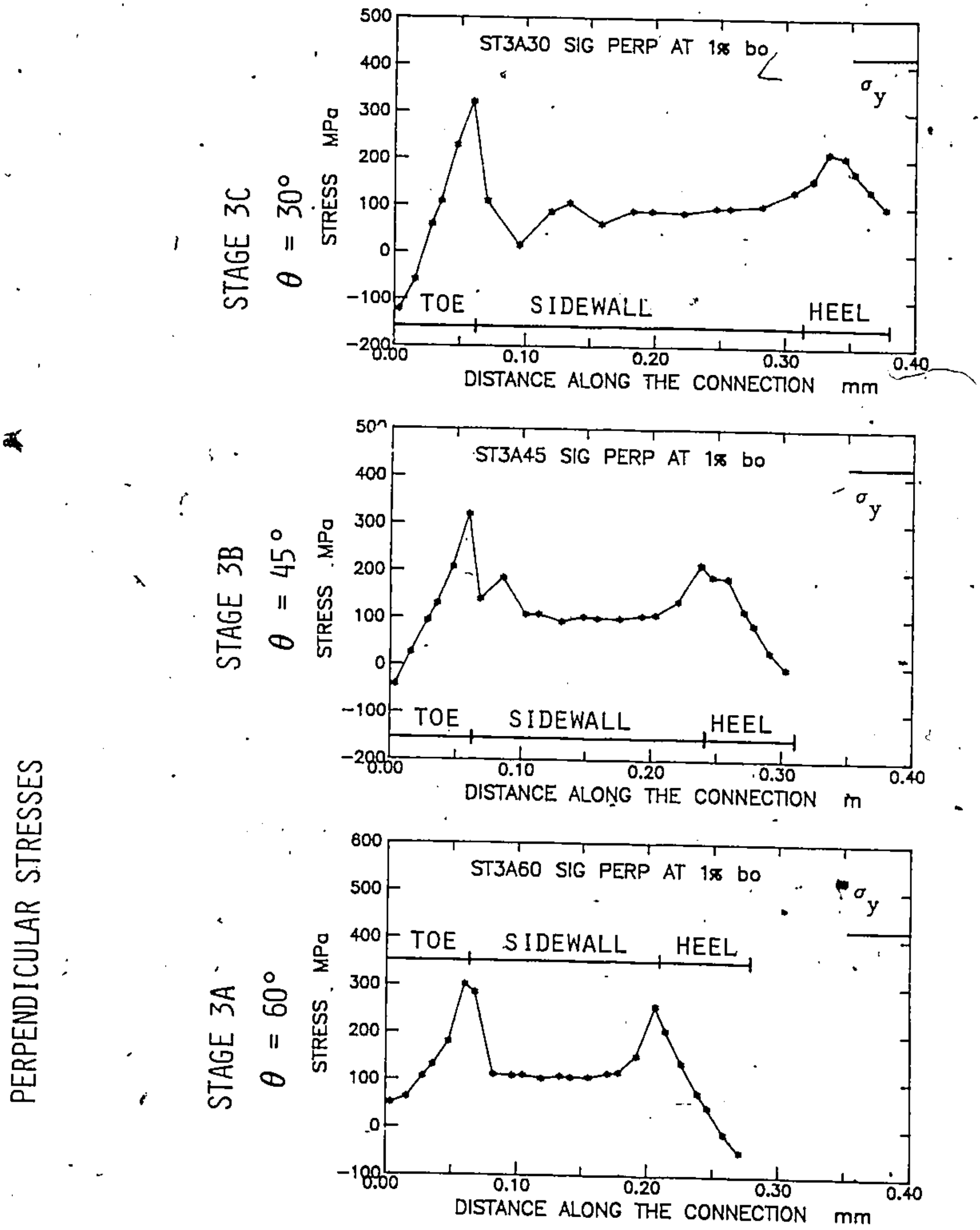

FIGURE 5.15 Display of Perpendicular Stresses in Branch Walls for Stage 3

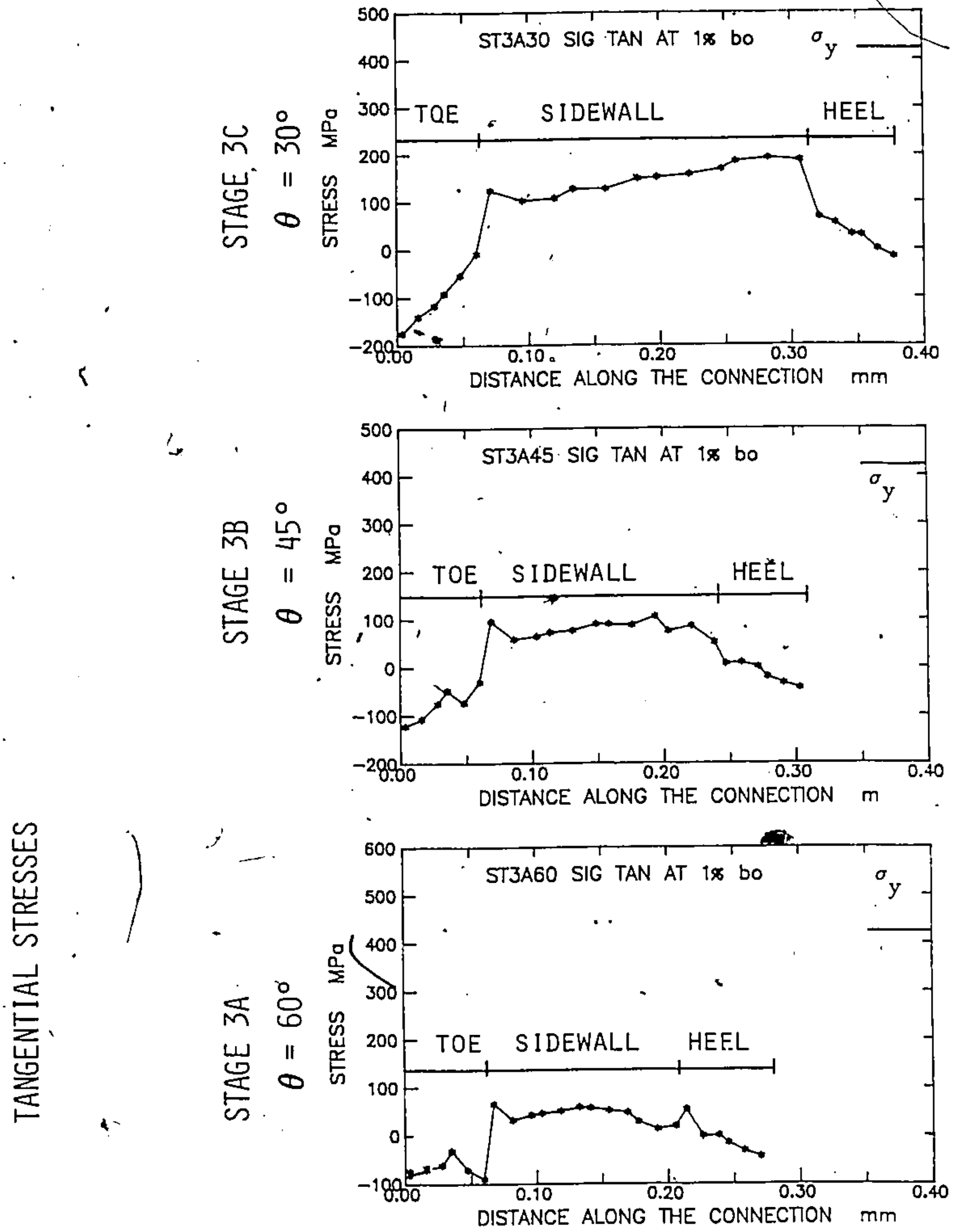

FIGURE 5.16 Display of Tangential Stresses in Branch Walls for Stage 3

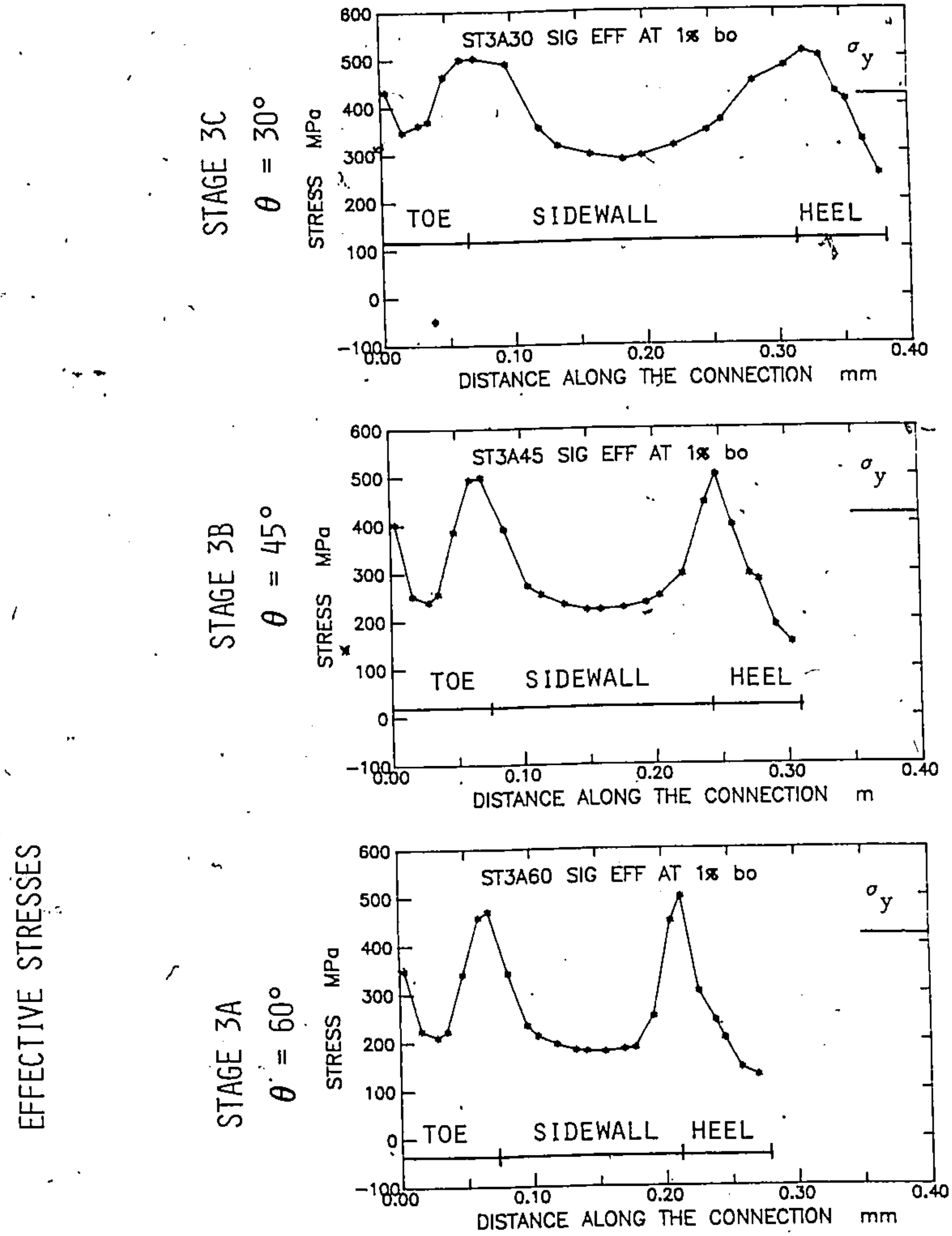

FIGURE 5.17 Display of Effective Stresses in Branch Walls for Stage 3

CHAPTER 6

PARAMETRIC STUDY FOR GAP K-JOINT

6.1 Introduction

The gap K joint has been selected for the parametric study because of its popularity and a very complex behaviour which requires detailed analysis. A finite element grid used for the study is shown in Figure 6.1. A total of 130 elements and 580 nodal points was utilized to discretize the joint. Only one quarter of a gap K joint was analyzed. The joint is symmetrical with respect to a vertical plane passing through the longitudinal axis of the chord member. In addition, the profile of local deflections for the chord connecting face is assumed to be antisymmetrical which is believed to be true within the working load level (see Section 2.5.1). Both branch members are modelled as square RHS of equal size. The rounded corners are approximated by 90° angles.

6.2 Selected Parameters

The most significant parameters which affect the behaviour of an RHS gap K joint are:

- angle of bracing inclination θ,
- width ratio β,
- gap size g,
- chord width to chord thickness ratio b_o/t_o.

Each of the above parameters can be varied within the following limits according to recent design recommendations for RHS joints (IIW 1981):

range of parameters
$30^\circ \leq \theta \leq 90^\circ$
$0.4 \leq \beta \leq 1.0$
$0.5\ (1-\beta) \leq g/b_o \leq 1.5\ (1-\beta)$ $g \geq 2t_o$
$b_o/t_o < 40$

The values of the joint parameters selected for this study were determined using the above table and the sizes of RHS from the experiments reported herein. The following parameter values were used in the numerical analysis:

θ : $\underline{30^\circ}$, 45° , $\underline{60^\circ}$;

β : 0.44 , $\underline{0.63}$, 0.88 ;

g : $0.2\ b_o$, $\underline{0.4\ b_o}$, $0.6\ b_o$;

b_o/t_o : $\underline{16}$, 21 , 32 ;

The underlined values correspond to the joint parameters used during the experiments on subconfigurations of a gap K joint. The parametric study of a gap K joint, presented in this study, consisted of thirteen different cases which used the joint parameters indicated in Figure 6.2 . The geometry of all the joints is described in Table 6.1. Initially the variation of one of the parameters was accompanied by a subset of the following:

$\theta=60^\circ$, $\beta=0.63$, $g=0.4\ b_o$, $b_o/t_o = 16$.

Cases 1,2,3 belong to the first group in which the angle of inclination θ was varied and other parameters were kept constant. Cases 4,3,5 represent a group where the width ratio β was varied. The gap size variation took place among cases 6,3,7. The change in b_o/t_o was accommodated in a batch which included cases 3,8,9. After nine analyses, it was revealed that the effects θ and β are very significant. Hence, four additional cases were added to the parametric study to complete the variation of the two parameters (for a given g and b_o/t_o). Cases 10,2,11 constituted a variation of β at θ=45° and cases 12,1,13 represented the variation of the same parameter at θ=30°. In cases 10 through 13 the values of g and b_o/t_o were kept the same, as in cases 1 to 5.

The results of the parametric study will be displayed in the same way as the results in Chapter 5 (see Section 5.2). All stresses are given at a load level when the local deflections of the chord connecting face reach 1% b_o. Three different types of stresses will be presented : perpendicular, tangential and effective. A complete set of numerical results for cases 1-13 is included in Appendix E. This chapter will contain the same results but in a different order, so that stresses of the same type for three different cases may be presented on one page and compared. Each time the results are compared when only one parameter varies. Hence, it is necessary to extract eight sets from the parametric study which include three different cases each. A list of those sets is shown in Figure 6.3. Each of the effects will be discussed in a separate section below.

6.3 Effect of Angle of Inclination θ

SET I Effect of θ at β=0.44

The following cases are compared (see Figure 6.2) :

case	θ	β	g	b_o/t_o
12	30°	0.44	0.4 b_o	16
10	45°	0.44	0.4 b_o	16
4	60°	0.44	0.4 b_o	16

Perpendicular Stresses (Figure 6.4). The stress profiles are similar in all cases. The minimum value for θ=30° occurs at the toe; for θ=45° the toe and heel midwall values are about the same; for θ=60° the minimum value is at the heel. Maximum value in all cases is at the corner between the toe and the sidewall.

Tangential Stresses (see Figure 6.5). The minimum value is at the toe in all three cases. Maximum value is at the corner between the heel and the sidewall. Noticeable variation of stresses takes place for θ=30°, while for θ=45° and 60° the stresses oscillate near zero.

Effective Stresses (see Figure 6.6). In all cases the profile of stress is alike. Two peak points occur at the branch corners and another point with high stresses is located at the centre of the toe. The minimum value for all cases is at the centre of the heel.

Summary for Set I. The effectiveness of the heel area in terms of the perpendicular stresses decreases with rising θ. Only θ=30° is associated with significant tangential stresses. The critical points with respect to effective stresses are located at the branch corners and the centre of the toe area.

SET II Effect of θ at β=0.63

The following cases are compared (see Figure 6.2) :

case	θ	β	g	b_o/t_o
1	30°	0.63	0.4 b_o	16
2	45°	0.63	0.4 b_o	16
3	60°	0.63	0.4 b_o	16

Perpendicular Stresses (Figure 6.7). The stress profiles are similar in all cases. The maximum stress occurs at the corner between the toe and the sidewall. The minimum values occur at the toe for θ=30° and at the heel for θ=60°. For θ=45° the minimum values are the same as for the toe and the heel.

Tangential Stresses (see Figure 6.8). Only the case with θ=30° demonstrates a significant variation of stresses. They fall into a -120 to 200 MPa range. In the other two cases the stresses are near zero.

Effective Stresses (see Figure 6.9). Two corners of the branch show the highest stresses. The centre point at the toe shows stresses of about 400 MPa. The minimum stress values occur at the centre of the heel. The profiles of stresses for θ=45° and 60° are alike. For θ=30° the yielding around the corners takes place over a more extended area than in other two cases.

Summary for Set II. As in set I.

SET III Effect of θ at β=0.88

The following cases are compared (see Figure 6.2) :

case	θ	β	g	b_o/t_o
13	30°	0.88	0.4 b_o	16
11	45°	0.88	0.4 b_o	16
5	60°	0.88	0.4 b_o	16

Perpendicular Stresses (Figure 6.10). Each stress profile is different. The most significant changes take place at the heel and the sidewall. Stresses at the heel are the highest for θ=30° and gradually drop with rising θ. The level of stresses at the sidewall is about 150 MPa, 200 MPa and 250 MPa for θ= 30°, 45° and 60° respectively. Stresses at the toe remain the same for all cases.

Tangential Stresses (see Figure 6.11). The stresses are significant in all cases but especially for θ=30°. The sidewall experiences the highest stresses in all cases. The toe and the heel show much lower stresses than the sidewall. One exception is for θ=30° where stresses at the heel are almost at the same level as in the sidewall.

Effective Stresses (see Figure 6.12). Almost the entire cross section has yielded for θ=30° . For cases with θ=45° and 60° yielding took place only in the vicinity of the corners. In both cases the values at the heel are as low as 100 MPa .

Summary for Set III. At θ=30° the perpendicular stresses are the highest at the heel. As the angle is rising the same stresses shift from the heel to the sidewall. Both the heel and the sidewall participate in the transfer of tangential stresses for θ=30°. The same θ is associated with yielding of the entire cross section, as opposed to corners only, for θ=45° and 60°.

6.4 Effect of Width Ratio β

SET IV Effect of Width Ratio at θ=30°

The following cases are compared (see Figure 6.2) :

case	θ	β	g	b_o/t_o
12	30°	0.44	0.4 b_o	16
1	30°	0.63	0.4 b_o	16
13	30°	0.88	0.4 b_o	16

Perpendicular Stresses (Figure 6.13). The stress profiles at the toe and the sidewall in all cases are alike. Significant changes take place at the heel where the stress level reaches 400 MPa for β=0.88 and diminishes to zero for β=0.44.

Tangential Stresses (see Figure 6.14). The stress profiles for β=0.44 and 0.63 are almost identical and the maximum stress occurs at the sidewall near the heel. For $\beta = 0.88$ such a point is located on the sidewall near the toe. For all three cases stresses at the centre of the toe are at about the -100 MPa level. The stress levels for $\beta = 0.63$ and 0.88 are much higher than for $\beta = 0.44$.

Effective Stresses (see Figure 6.15). The stress profiles for $\beta = 0.44$ and $\beta = 0.63$ are almost identical. The maximum value of stresses occurs near the corners. High stresses also develop at the centre of the toe. For $\beta = 0.88$ the distribution of stresses is almost uniform.

Summary for Set IV. The change in β at $\theta = 30°$ affects the distribution of perpendicular stresses in the heel area only. The tangential stresses reach 200 MPa at the branch sidewalls with $\beta = 0.63$ and 0.88. The distribution of effective stresses becomes more uniform with higher values of β.

SET V Effect of Width Ratio at $\theta = 45°$

The following cases are compared (see Figure 6.2) :

case	θ	β	g	b_o/t_o
12	45°	0.44	0.4 b_o	16
1	45°	0.63	0.4 b_o	16
13	45°	0.88	0.4 b_o	16

Perpendicular Stresses (Figure 6.16). The stress profiles for all cases are alike. The level of stresses is rising with higher values of β.

Tangential Stresses (see Figure 6.17). The stresses for β= 0.44 and β=0.63 oscillate near zero. For β=0.88 a significant variation in stresses takes place between the minimum value of -100 MPa at the toe and the maximum value of 200 MPa at the sidewall.

Effective Stresses (see Figure 6.18). All stress profiles are alike. For β=0.88 the stresses at the sidewall are higher than for the other two cases and the corner near the heel experiences yielding over a more extended area than in the other two cases.

Summary for Set V. No significant changes are observed in the general form of the stress distribution when the width ratio changes for θ=45°. For β=0.44 and 0.63 the difference is negligible. For β=0.88 the stress levels are higher than in the other two cases but the stress profiles are alike.

SET VI Effect of Width Ratio at θ=60°

The following cases are compared (see Figure 6.2) :

case	θ	β	g	b_o/t_o
4	60°	0.44	0.4 b_o	16
3	60°	0.63	0.4 b_o	16
5	60°	0.88	0.4 b_o	16

Perpendicular Stresses (Figure 6.19). The stress profiles for β=0.44 and 0.63 are almost identical. The peak stress occurs at the corner near the toe. The stress values at the centre of the heel are at about -100 MPA. For β=0.88 the stress profile is different. Much higher stresses of 300 MPa at the sidewall are observed. The stresses at the centre of the toe and heel are about equal and positive.

Tangential Stresses (see Figure 6.20). The stresses for β=0.44 and 0.63 are very low and oscillate near zero. For β=0.88 the stresses reach 140 MPa and are especially high at the sidewall.

Effective Stresses (see Figure 6.21). Three peak values of stresses occur at the corners and at the centre of the toe. High stresses are observed at the sidewall for β=0.88. In all cases the centre of the heel shows low stress values which are between 100-200 MPa.

Summary for Set VI. No significant change in any of the stresses is observed between cases with β=0.44 and 0.63. For β=0.88 both the perpendicular and tangential stresses are very high at the sidewall, which results in the effective stresses being the highest near the branch corners and the sidewall.

6.5 Effect of Gap Size g

SET VII Effect of Gap

The following cases are compared (see Figure 6.2) :

case	θ	β	g	b_o/t_o
3	60°	0.63	0.2 b_o	16
8	60°	0.63	0.4 b_o	16
9	60°	0.63	0.6 b_o	16

Perpendicular Stresses (Figure 6.22). Only the stress profile for g=0.2 b_o is different from the other two. The difference occurs at the toe with the stress levels rising by about 100 MPa as compared with cases where g=0.4 b_o or 0.6 b_o.

Tangential Stresses (see Figure 6.23). There is no noticeable difference among the stress profiles for various g.

Effective Stresses (see Figure 6.24). Only the stress profile for g=0.2 b_o is different. The change takes place in the toe area and is rather insignificant and does not affect either the maximum or minimum values of stress.

Summary for Set VII. No significant change in stress levels was observed due to variation of the gap size.

6.6 Effect of Chord Width to Thickness Ratio b_o / t_o

SET VIII

The following cases are compared (see Figure 6.2) :

case	θ	β	g	b_o/t_o
3	60°	0.63	0.4 b_o	16
8	60°	0.63	0.4 b_o	21
9	60°	0.63	0.4 b_o	32

Perpendicular Stresses (Figure 6.25). The stresses tend to diminish with the rising value of b_o/t_o.

Tangential Stresses (see Figure 6.26). Very low levels of stresses are observed for all values of b_o/t_o.

Effective Stresses (see Figure 6.27). Only the peak stress values are noticeably affected by a change in b_o/t_o.

Summary for Set VIII. The stress profiles remain similar in all cases. The perpendicular stress level at b_o/t_o of 32 is four times the level of b_o/t_o of 16. This indicates that the bending action is dominant in the chord connecting face. All tangential stresses are near zero. The difference in the effective stress levels is about inversely proportional to b_o/t_o.

6.7 P-Delta Curves

The local deflections of the chord connecting face are evaluated in exactly the same manner as stresses were evaluated in Sections 6.3 - 6.6. The load-local deflection curves will be compared for three different cases at a time. The same sets I-VIII as before were selected out of the selection of 13 cases available (see the graphs in Figures 6.28-6.35). The results are presented at the toe and heel of the branch member.

SET I Effect of θ at β= 0.44 (see Figure 6.28)

The deflections for θ=30° are noticeably smaller than in cases where θ=45° or 60° which are very similar. The difference between deflections at the toe and heel is larger for θ=30° than in other two cases. At β=0.44 the deflections for θ=45° and 60° are virtually identical.

SET II Effect of θ at $\beta = 0.63$ (see Figure 6.29)

A recognizable difference exists between all cases. The load levels at which the local deflections reach 1% b_o are 1050 kN, 707 kN and 549 kN for angles 30°, 45° and 60° respectively. The discrepancy between the deflections at the toe and heel increases when θ decreases.

SET III Effect of θ at $\beta = 0.88$ (see Figure 6.30)

At $\beta = 0.88$ the deflections for $\theta = 30°$ and 45° are very small. In both cases the toe experiences deflections that do not reach the level of 1% b_o before 2000 kN. Only for $\theta = 60°$ a significant change in the slope of the load-deflection curves is observed.

SET IV Effect of Width ratio at $\theta = 30°$ (see Figure 6.31)

Every load-deflection curve is different. The width ratio has a very significant effect on local deflections. In all cases a noticeable difference takes place between deflections at the toe and heel, especially in the early stages of loading.

SET V Effect of Width ratio at $\theta = 45°$ (see Figure 6.32)

The deflections are similar to those in Set IV but the load levels for comparable deflections are lower in this set. The load levels associated with deflections of 1% b_o are equal to 466 kN, 707 kN and 1856 kN for $\theta = 30°$, 45° and 60° respectively.

SET VI Effect of Width ratio at θ=60° (see Figure 6.33)

The load-deflection curves for β=0.44 and 0.63 are almost identical. Only the case with β=0.88 is different and reaches about twice the load level for the other two cases at the deflection level of 1% b_o.

SET VII Effect of Gap Size (see Figure 6.34)

Only the smallest gap size of 0.2 b_o has a significant impact on the load-deflection curves. Not only are the load levels higher in this case but the discrepancy between the toe and heel is more noticeable. The other two cases of g=0.4 b_o and 0.6 b_o are alike.

SET VIII Effect of b_o/t_o (see Figure 6.35)

The effect of b_o/t_o on the magnitude of deflections is extremely significant. The deflections decrease when b_o/t_o increases. The load levels corresponding to 1% b_o for b_o/t_o = 16, 21 and 32 are 549 kN, 346 kN and 160 kN respectively.

6.8 Conclusions from Parametric Study

6.8.1 Distribution of Stresses in Branch Walls

The conclusions about the effects of θ and β appear in Table 6.2. A few significant trends are summarized here:

- the behaviour of joints with β of 0.44 and 0.63 is similar and joints with β of 0.88 represent different trends;
- the heel is fully effective for all joints with $\theta=30°$ and for joints with $\beta=0.88$ and 45°;
- the branch corners always exhibit high stress concentration;
- perpendicular stresses peak at the corner near the toe for $\beta=0.44$ and 0.63 whereas for $\beta=0.88$ they peak at the heel for $\theta=30°$, and are equally balanced between the toe and heel for $\theta=60°$;
- high perpendicular stresses occur at the sidewall for $\beta=0.88$ and angles $\theta=45°$ and 60°;
- tangential stresses for $\theta=30°$ and $\beta=0.44$ or 0.63 are relatively high whereas for 45° and 60° and the same width ratios the stresses are near the zero mark;
- for $\beta=0.88$ the sidewall experiences high tangential stresses for all angles; the perpendicular stresses are significant at the sidewall for the same β and $\theta=45°$ and 60°.
- effective stresses are the highest around the branch corners and at the centre of the toe;

A change in the gap size g produces stress changes which are noticeable only at the toe location and only for $g=0.2\ b_o$. It affects the distribution of perpendicular and effective stresses only and does not cause stress variation higher than 50 MPa as compared with the stress distributions for either $g=0.4\ b_o$ or $0.6\ b_o$.

The b_o/t_o effect does not influence the distribution of stresses. The only change results in the magnitude of the stress levels which are much higher for lower values of b_o/t_o. For b_o/t_o equal to 21 and 32 the perpendicular and tangential stresses are almost negligible and the effective stresses remain within the elastic domain.

6.8.2 Local Deflections

The following are the immediate conclusions derived from Figures 6.28 to 6.35 :

- for β-0.44 no difference exists in the load-deflection curves between θ-45° and 60°;
- for β-0.63 the deflections increase with an angle θ;
- for β-0.88 the angles of 30° and 60° are associated with very small deflections which are below the serviceability limit of 1% b_o until the load level of at least 1750 kN;
- for all angles the deflections increase when the width ratio decreases; this increase in deflections, is most noticeable for θ-30°.

The loads attained at 1% b_o for each of the thirteen cases from the parametric study are listed in Table 6.3 (Column 8). They are compared with the working load level obtained by dividing a joint strength for a particular configuration by a load factor of 1.5 (Table 6.3, Column 7).

In most cases the load levels associated with local deflections of 1% b_o are lower than the working load level for that particular joint. This suggests that the deflections at the working load level would be higher than the $0.01b_o$ allowable, which implies that a remedy must be found against excessive service load local deflections before the joint can be regarded as adequate.

6.9 Design Implications

The following are specific implications for the design of RHS gap K joints:

- the effectiveness of the heel should be regarded as equal to the effectivenes of the toe for joints with θ=30°; joints with β=0.8 and θ=45° also have the heel fully effective; very high stresses occur at the heel for high width ratios of 0.80 or above and θ=30° ;
- the effectiveness of the heel should be linked with θ and the width ratio; it should not be calculated based on a model consisting of an assembly of independent plates as is currently done in practice;
- for β=0.8 or higher the sidewall participates equally in the transfer of both the perpendicular and tangential stresses;
- the local deflections are particularly critical for θ = 60°
- for joints with β=0.8 or higher and angles θ=30° or 45°, the local deflections at service load are not critical in the design of joints; for all other cases a designer should check the serviceability condition at the working load level.

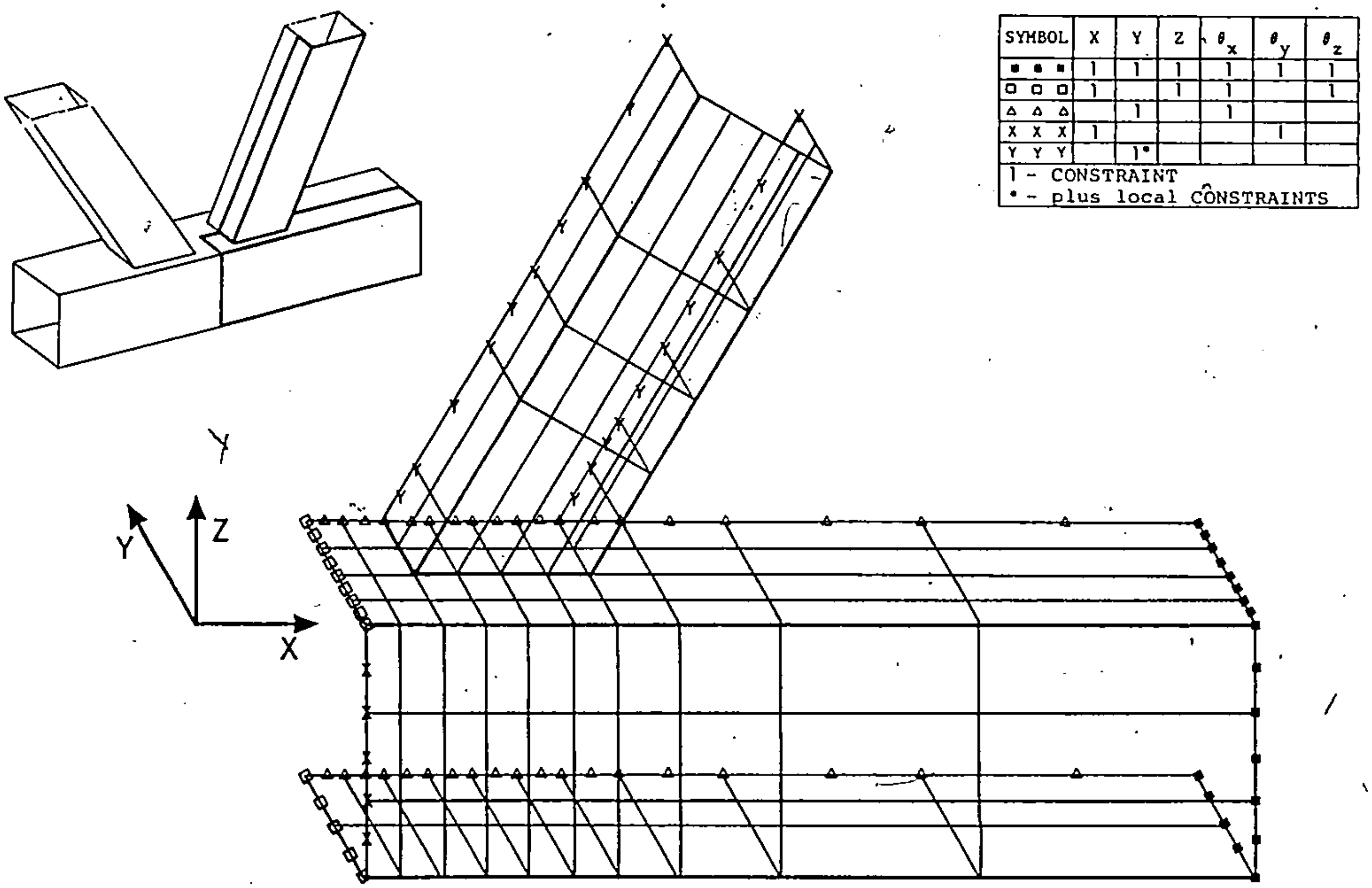

SYMBOL	X	Y	Z	θ_x	θ_y	θ_z
■ ■ ■	1	1	1	1	1	1
□ □ □	1		1	1		1
△ △ △		1		1		
X X X	1				1	
Y Y Y		1*				

1 - CONSTRAINT
* - plus local CONSTRAINTS

FIGURE 6.1 Finite Element Grid for Gap K Joint

FIGURE 6.2 Summary of Parametric Study for Gap K Joints

	θ			β			g			b_o/t_o			comments
run	30°	45°	60°	0.44	0.63	0.88	.2bo	.4bo	.6bo	16	21	32	
1	M				●			●		●			
2		M			●			●		●			
3			M		●			●		●			
4			●	M				●		●			
			●		M			●		●			as in 3
5			●			M		●		●			
6			●		●		M			●			
			●		●			M		●			as in 3
7			●		●				M	●			
			●		●			●		M			as in 3
8			●		●			●			M		
9			●		●			●				M	
10		●		M				●		●			
		●			M			●		●			as in 2
11		●				M		●		●			
12	●			M				●		●			
	●				M			●		●			as in 1
13	●					M		●		●			

M main effect, ● other parameters

FIGURE 6.3 List of Subsets of Parametric Study

SET NO.	CASES SELECTED	EFFECT
I	12 10 4	EFFECT OF θ, WITH β=0.44
II	1 2 3	EFFECT OF θ, WITH β=0.63
III	13 11 5	EFFECT OF θ, WITH β=0.88
IV	12 1 13	EFFECT OF β, WITH θ=30°
V	10 2 11	EFFECT OF β, WITH θ=45°
VI	4 3 5	EFFECT OF β, WITH θ=60°
VII	6 3 7	EFFECT OF g
VIII	3 8 9	EFFECT OF b_o/t_o

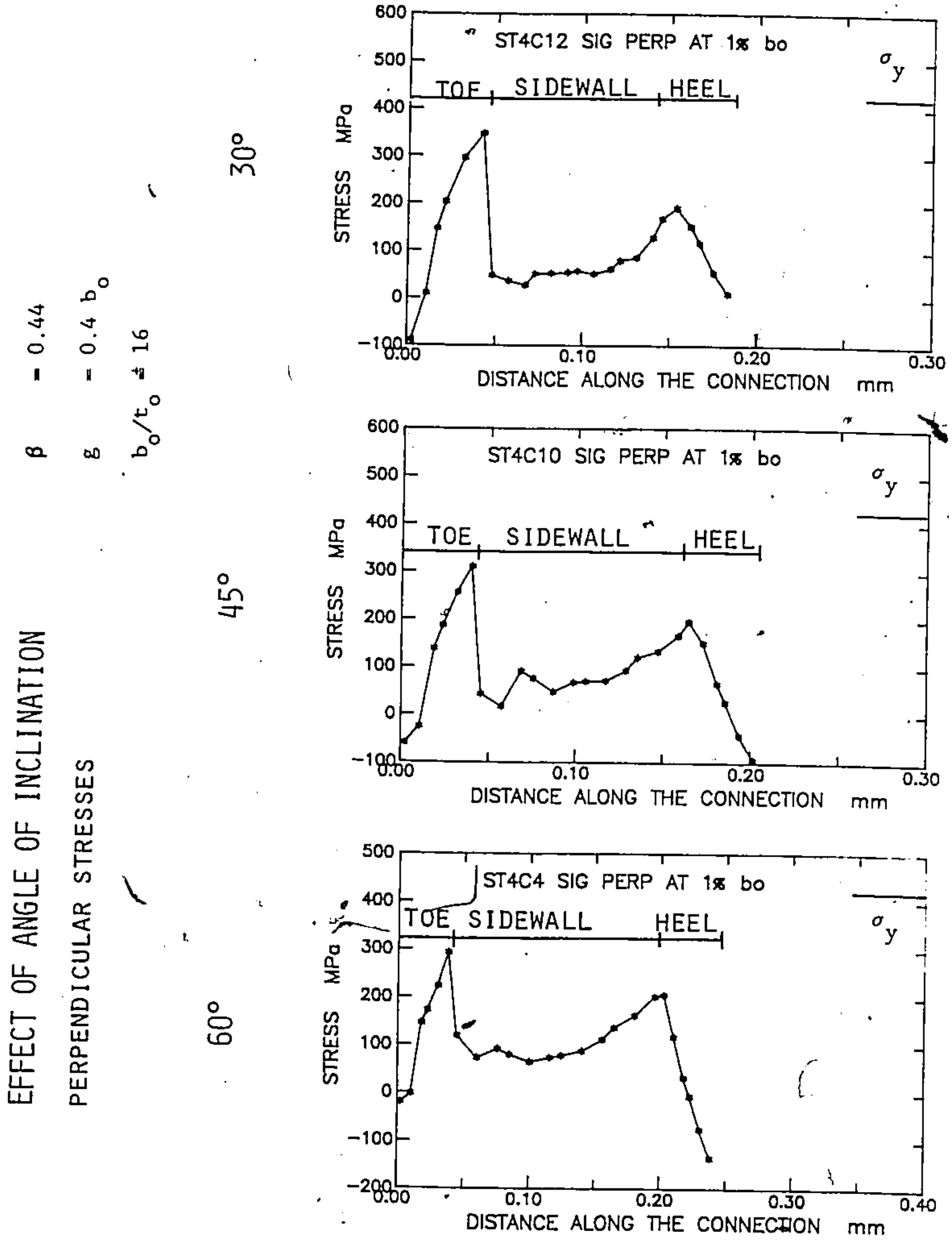

FIGURE 6.4 Effect of Angle θ at β=0.44 , Perpendicular Stresses.

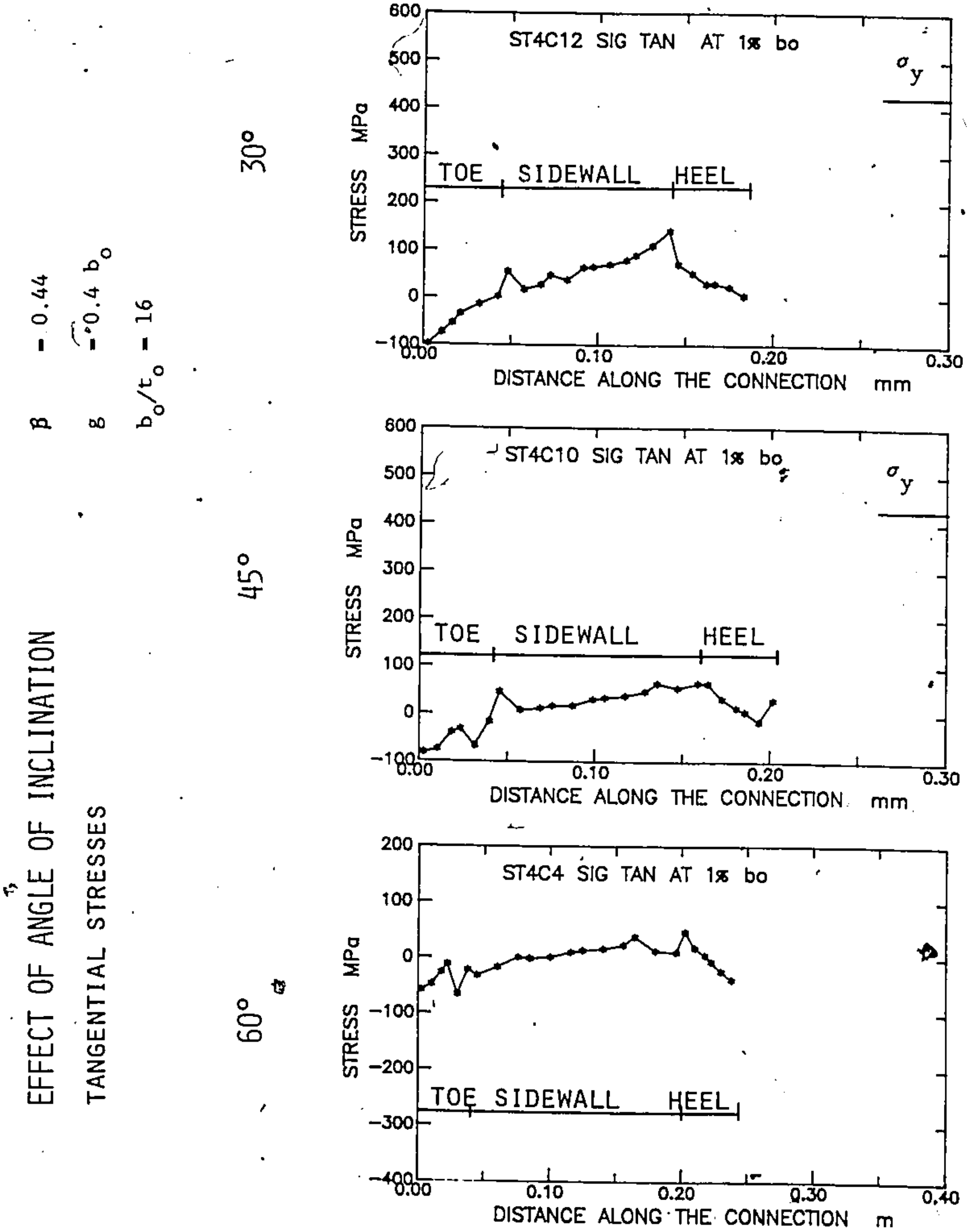

FIGURE 6.5 Effect of Angle θ at β=0.44 , Tangential Stresses.

EFFECT OF ANGLE OF INCLINATION

EFFECTIVE STRESSES

$\beta = 0.44$

$g = 0.4\ b_o$

$b_o/t_o = 16$

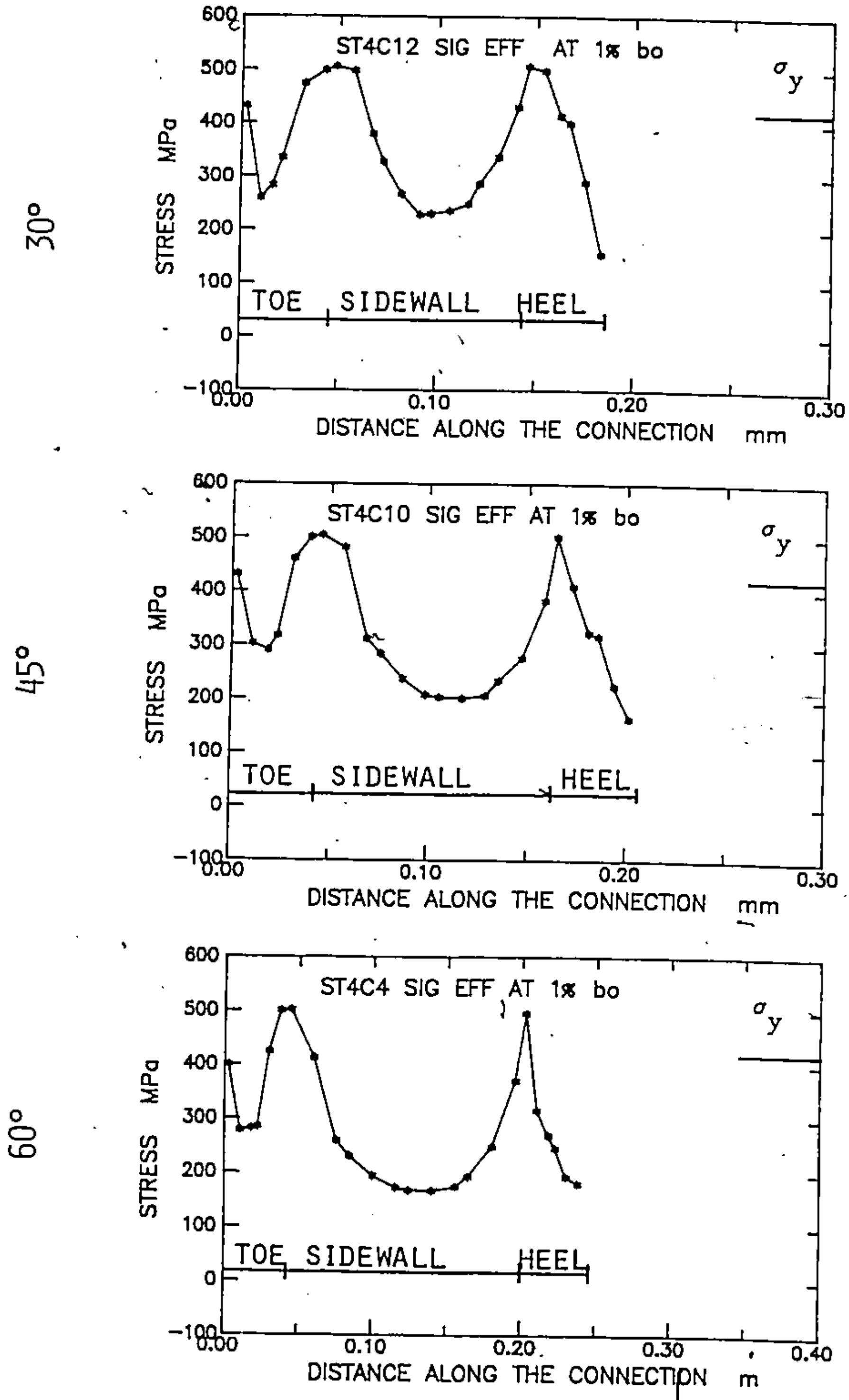

FIGURE 6.6 Effect of Angle θ at β=0.44 , Effective Stresses.

EFFECT OF ANGLE OF INCLINATION

PERPENDICULAR STRESSES

$\beta = 0.63$

$g = 0.4\, b_o$

$b_o/t_o = 16$

30°

45°

60°

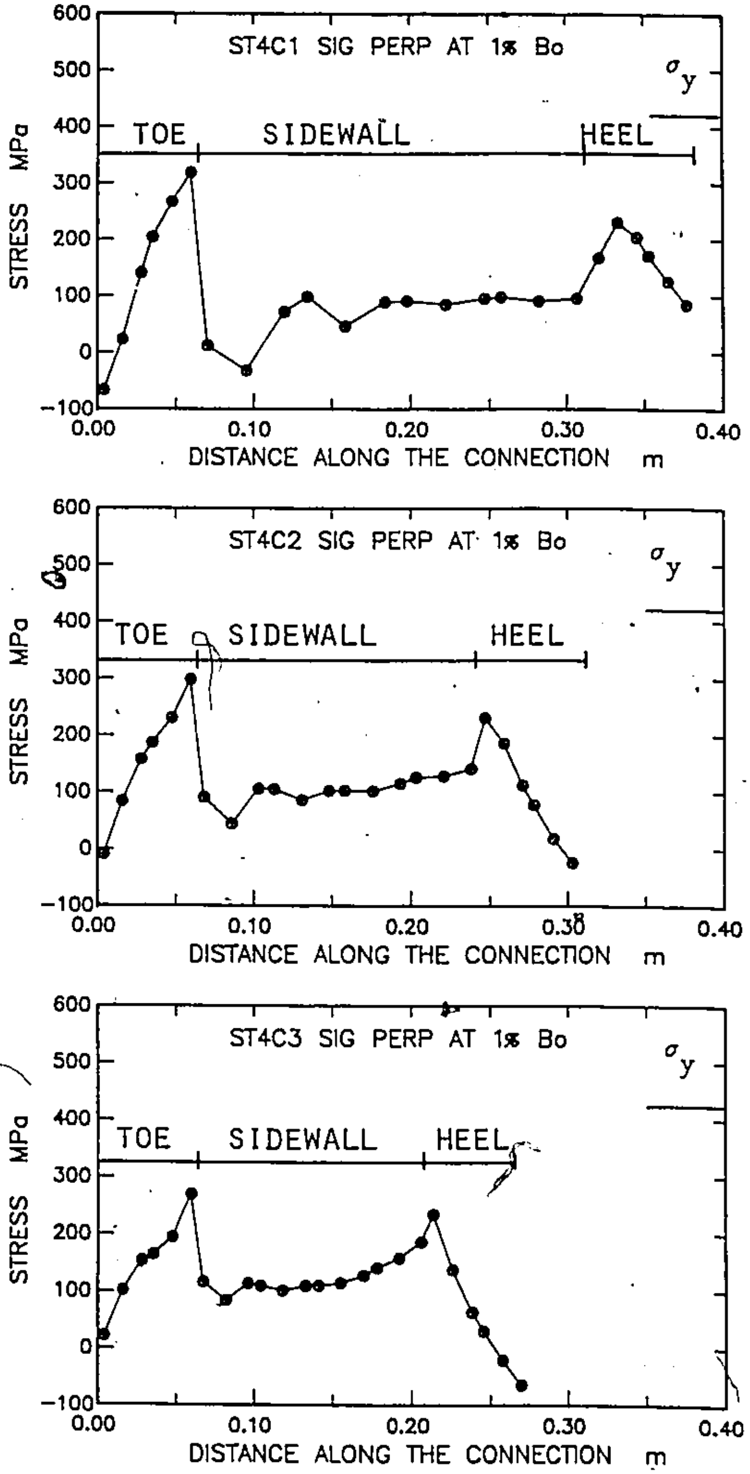

FIGURE 6.7 Effect of Angle θ at β=0.63 , Perpendicular Stresses.

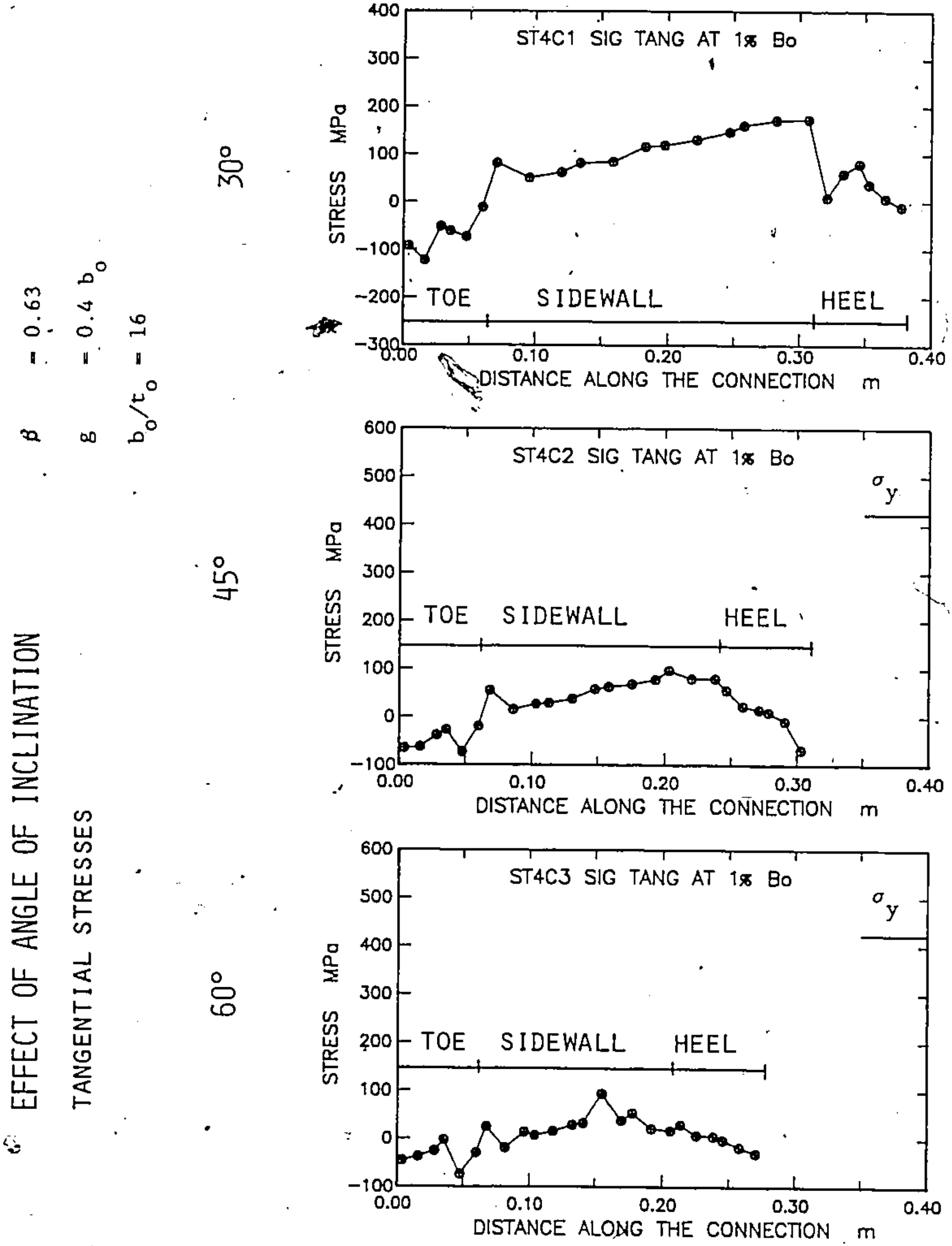

FIGURE 6.8 Effect of Angle θ at β=0.63 , Tangential Stresses.

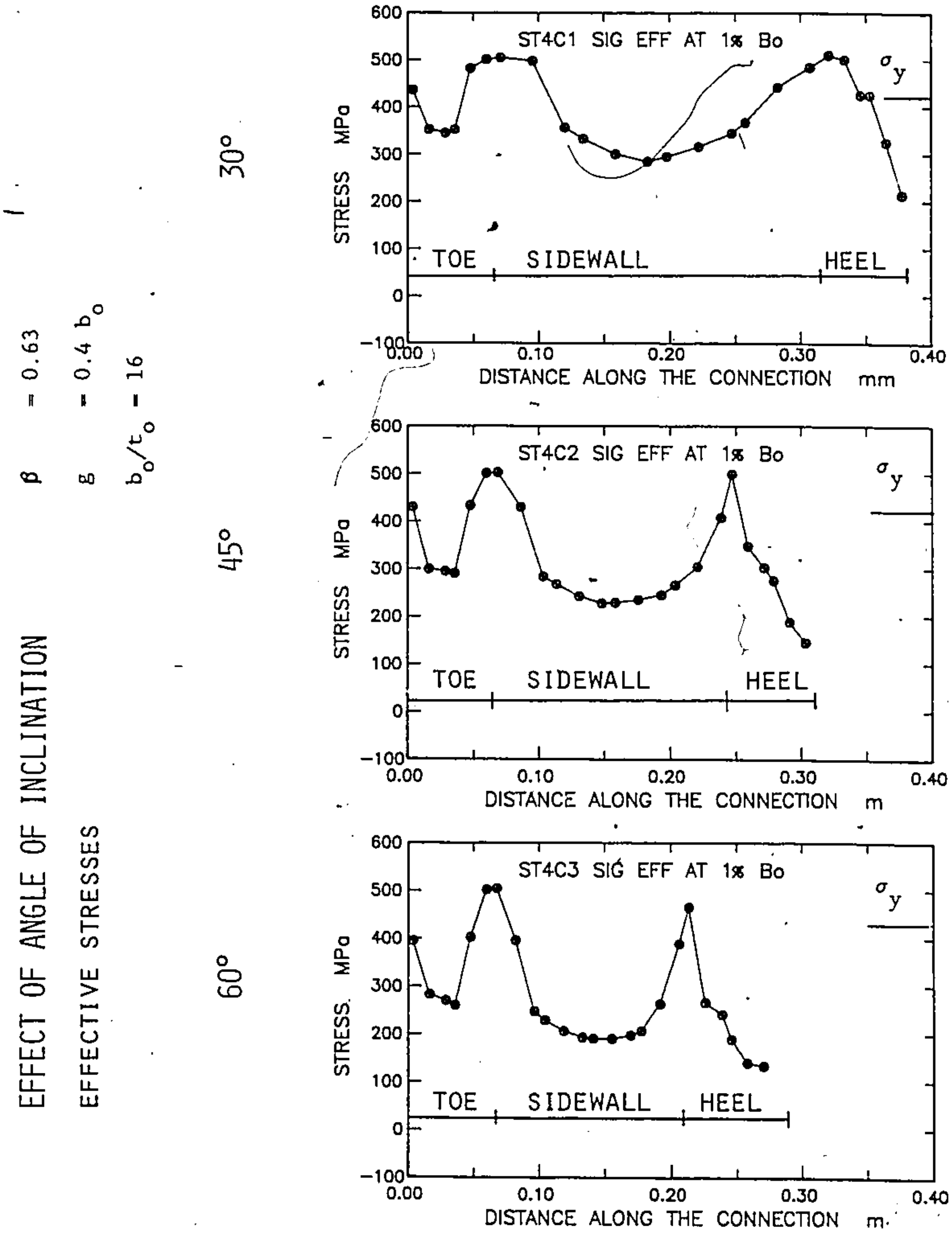

FIGURE 6.9 Effect of Angle θ at β=0.63 , Effective Stresses.

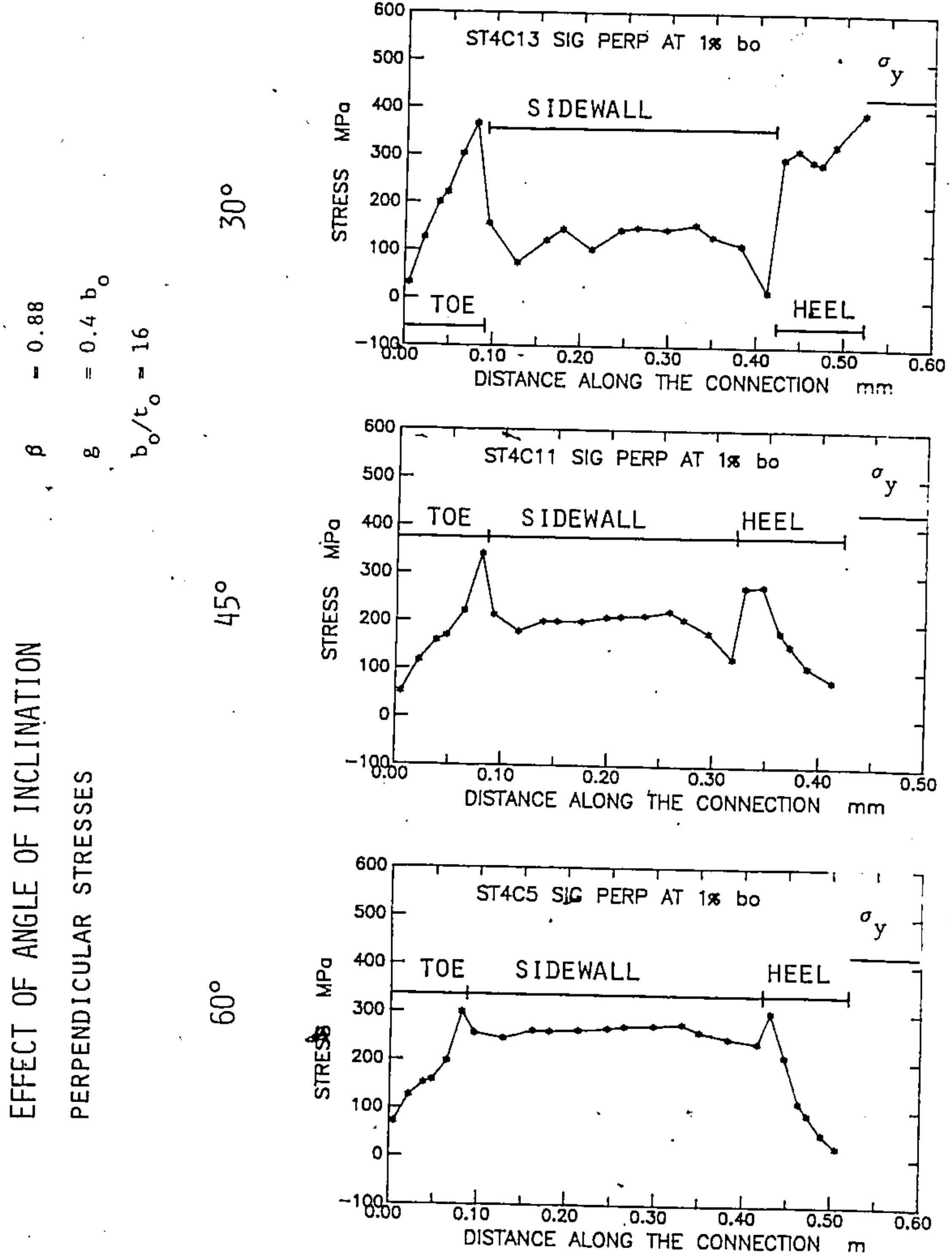

FIGURE 6.10 Effect of Angle θ at β=0.88 , Perpendicular Stresses.

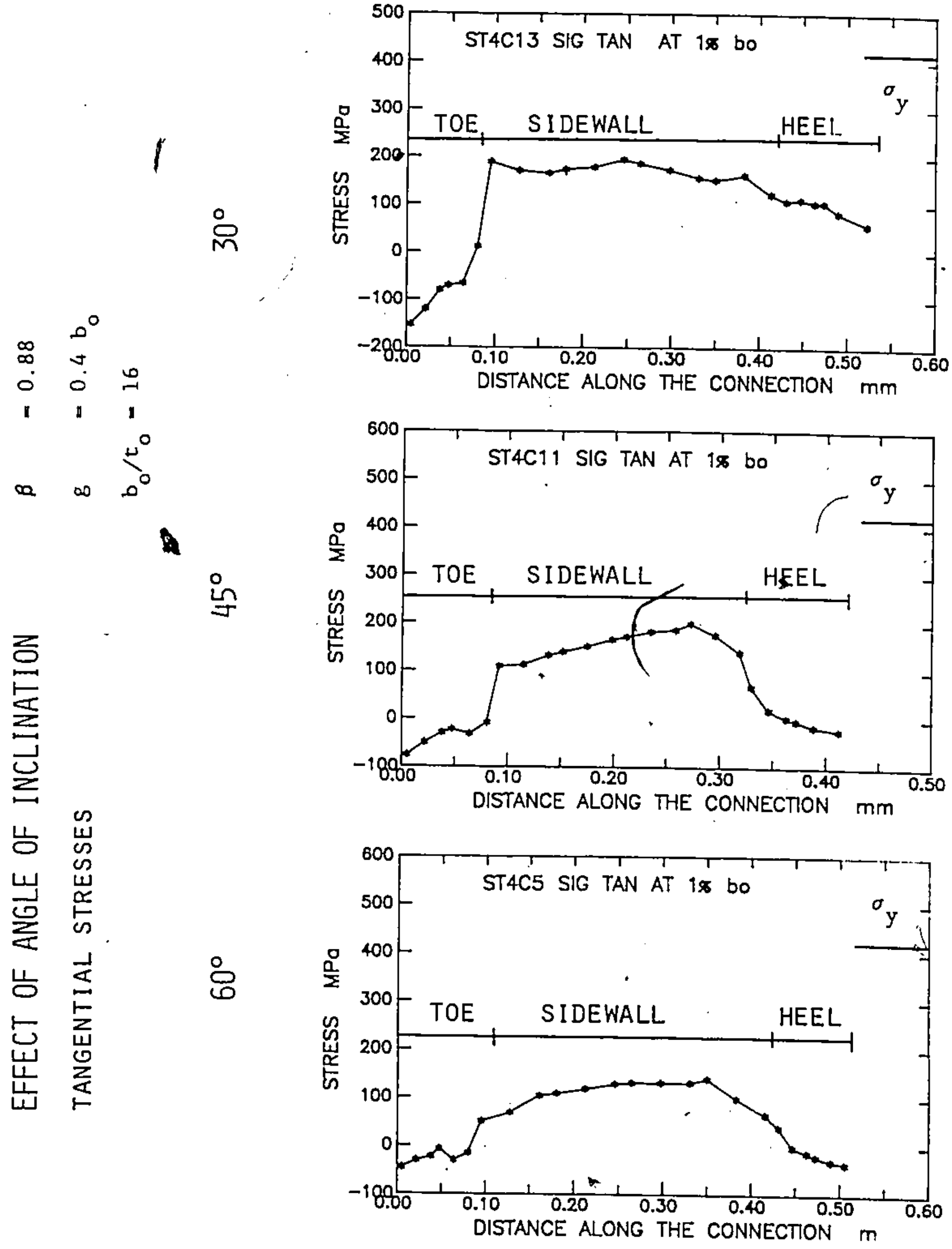

FIGURE 6.11 Effect of Angle θ at β=0.88 , Tangential Stresses.

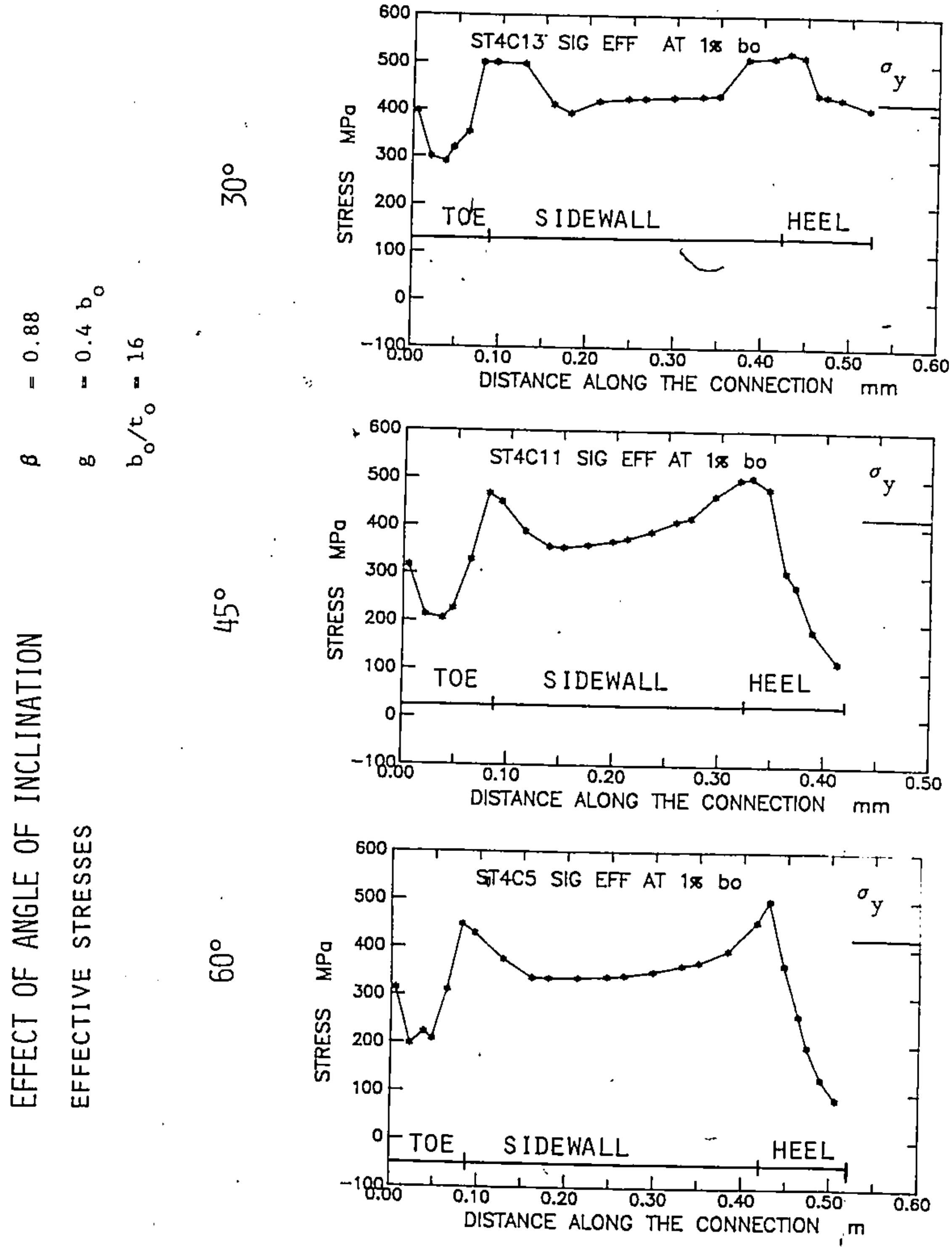

FIGURE 6.12 Effect of Angle θ at β=0.88 , Effective Stresses.

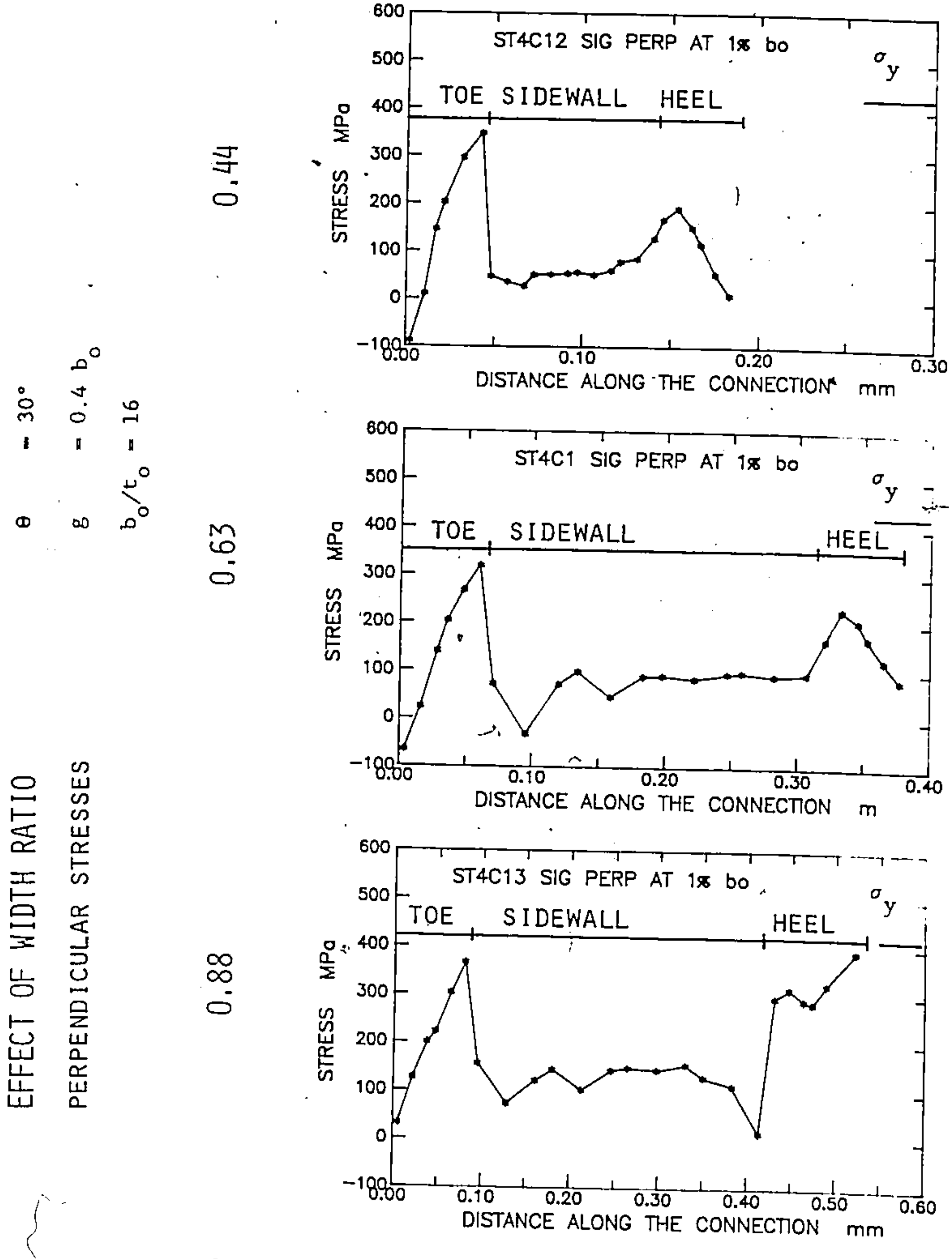

FIGURE 6.13 Effect of Width Ratio β at θ=30° , Perpendicular Stresses.

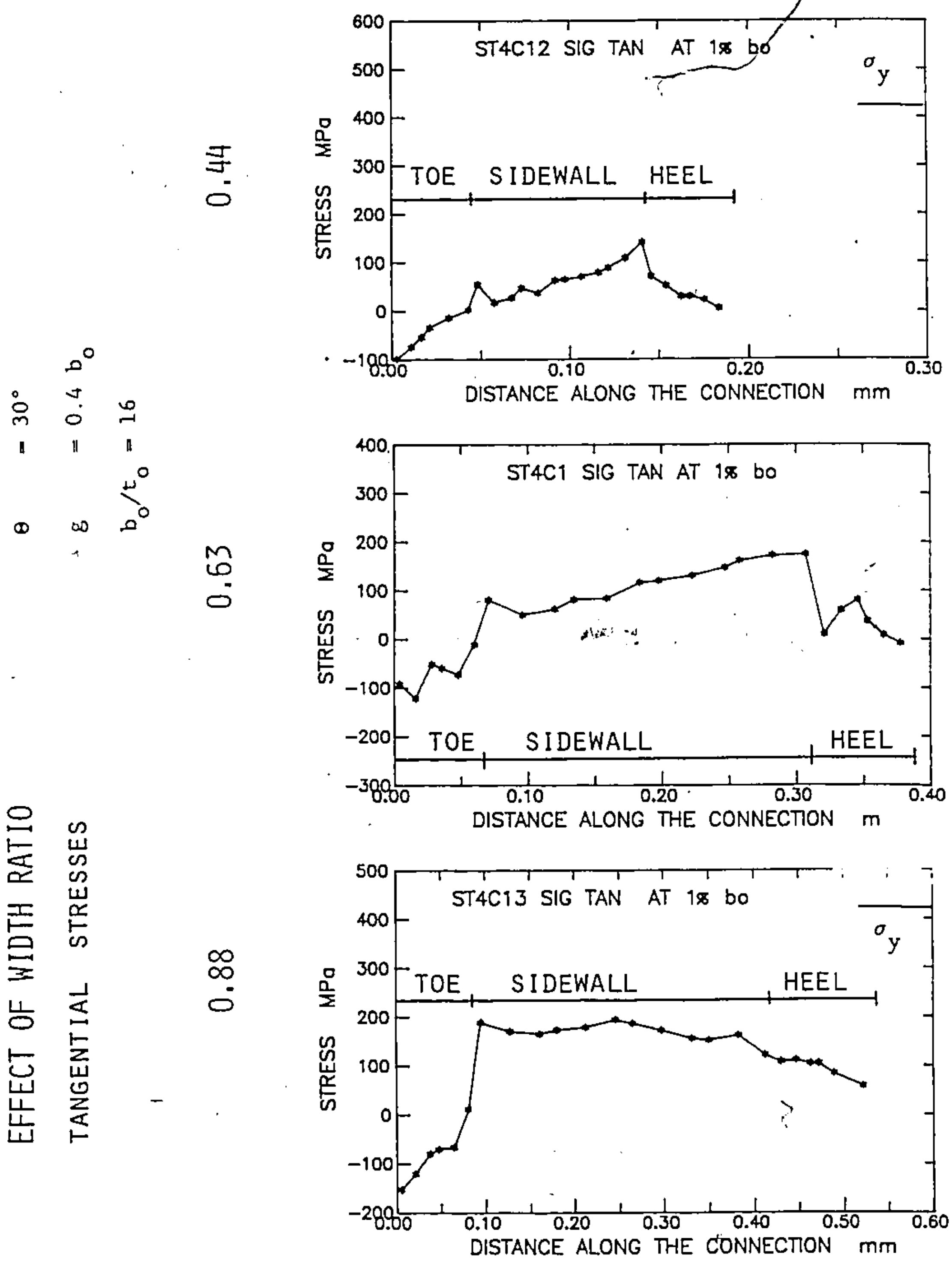

FIGURE 6.14 Effect of Width Ratio β at θ=30° , Tangential Stresses.

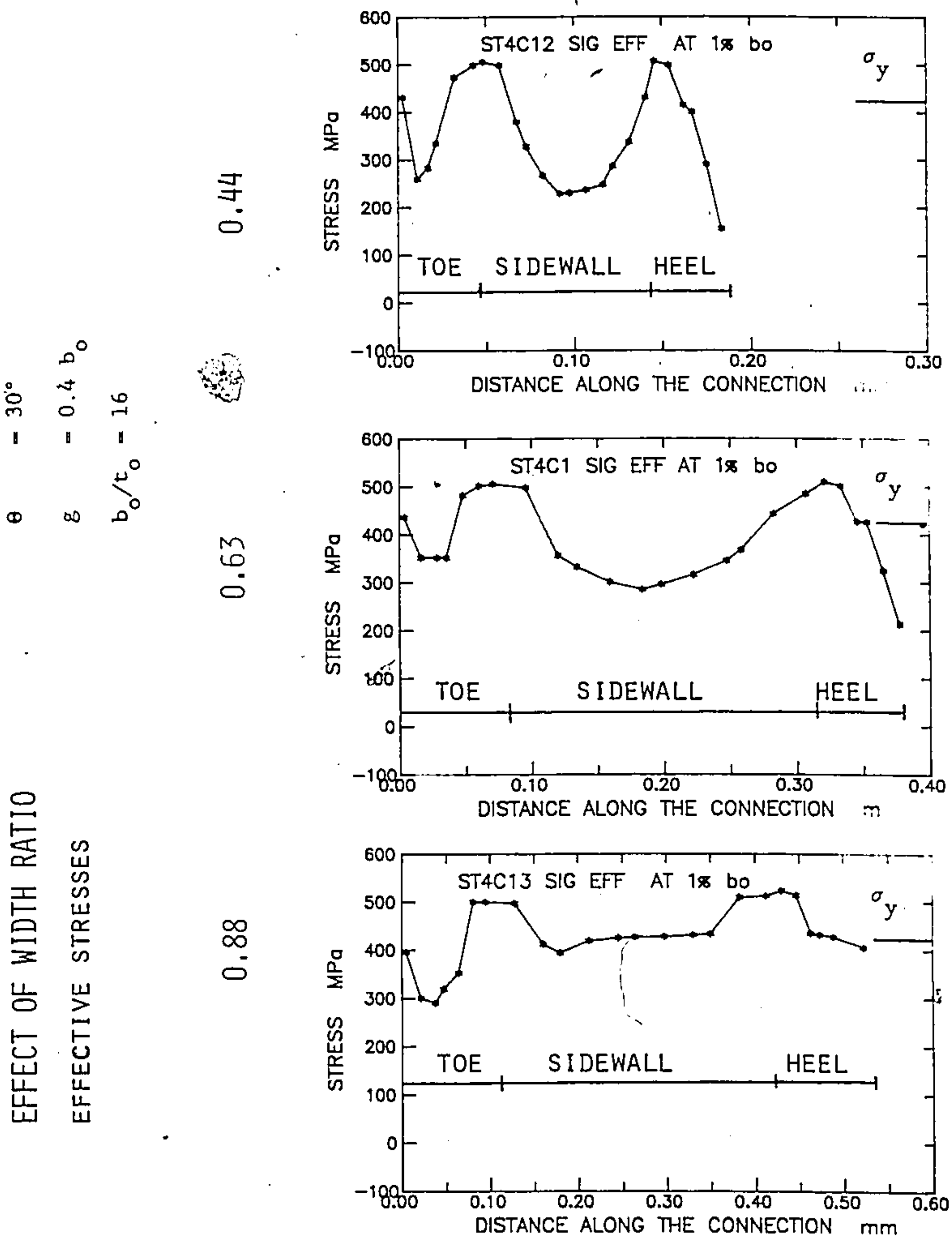

FIGURE 6.15 Effect of Width Ratio β at θ=30° , Effective Stresses

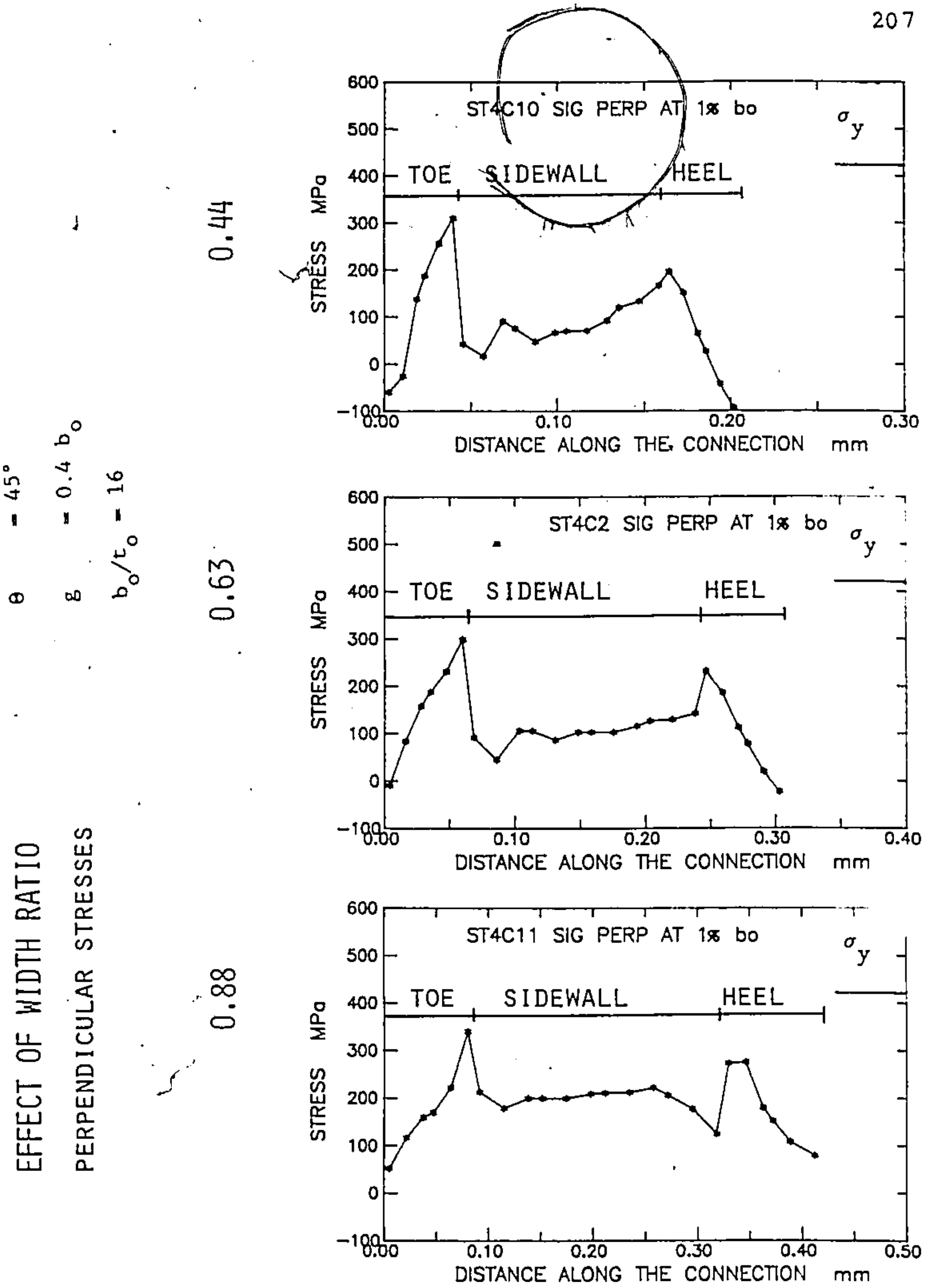

FIGURE 6.16 Effect of Width Ratio β at θ=45° , Perpendicular Stresses.

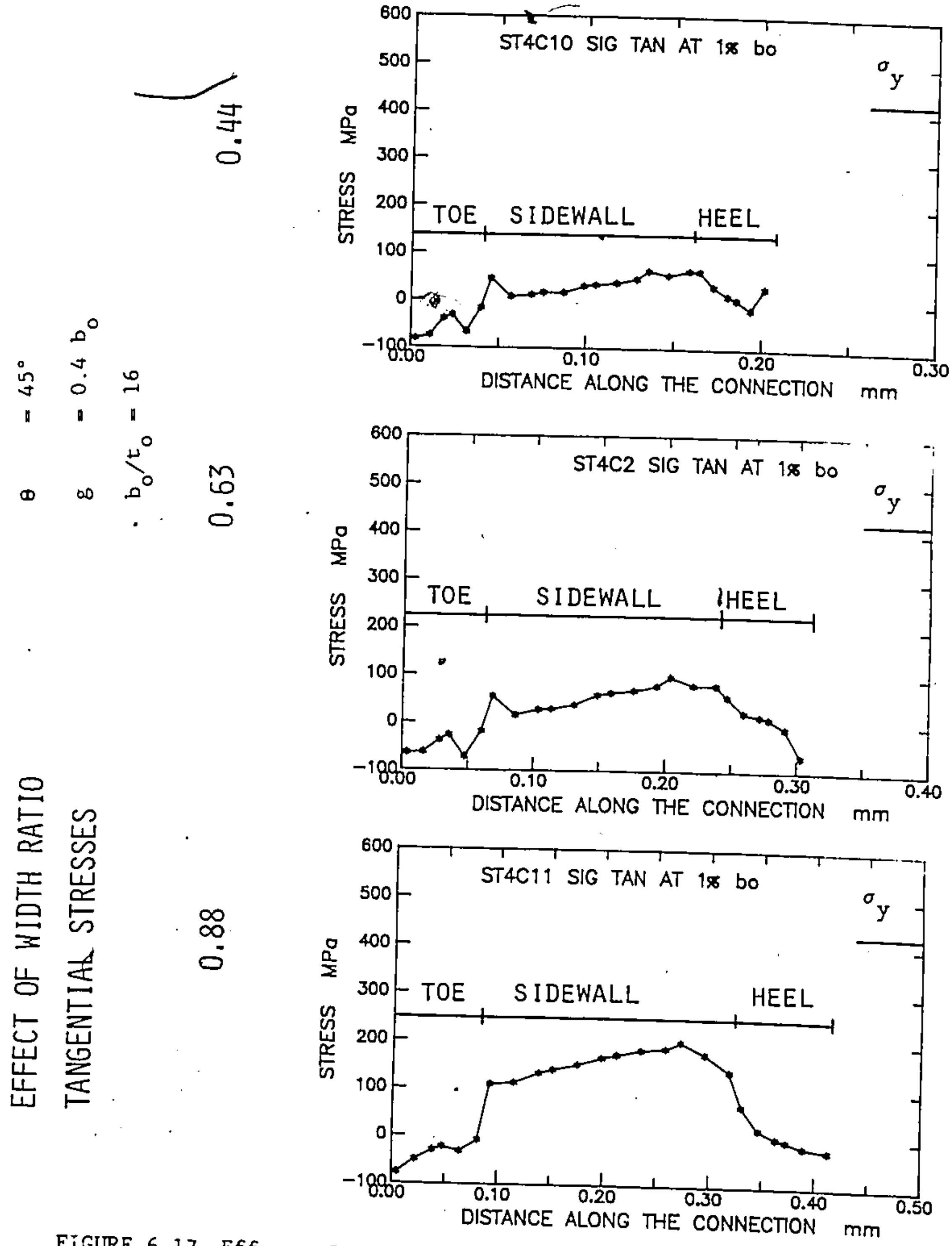

FIGURE 6.17 Effect of Width Ratio β at θ=45° , Tangential Stresses.

EFFECT OF WIDTH RATIO

EFFECTIVE STRESSES

θ = 45°

β = 0.4 b_o

b_o/t_o = 16

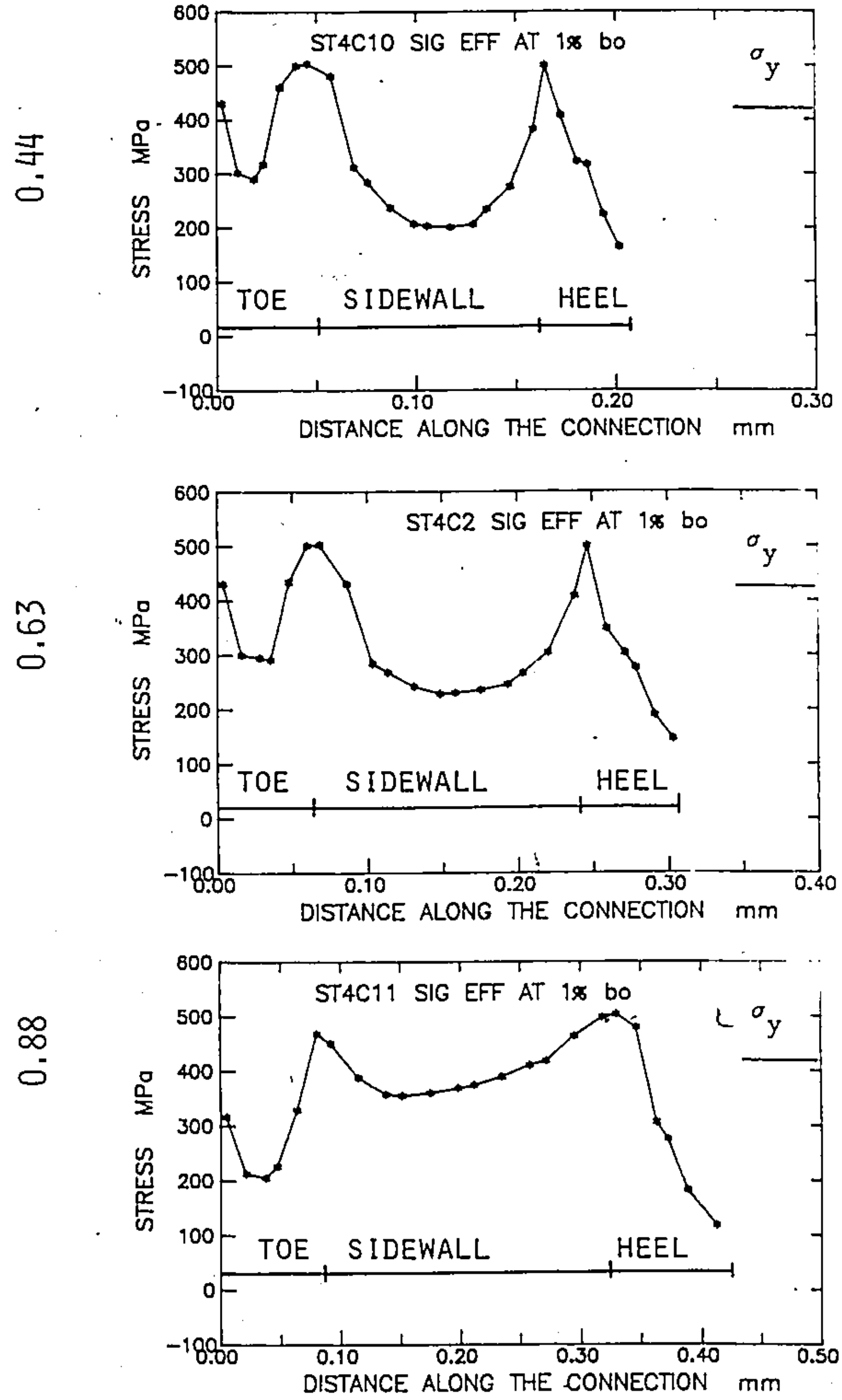

FIGURE 6.18 Effect of Width Ratio β at θ=45° , Effective Stresses.

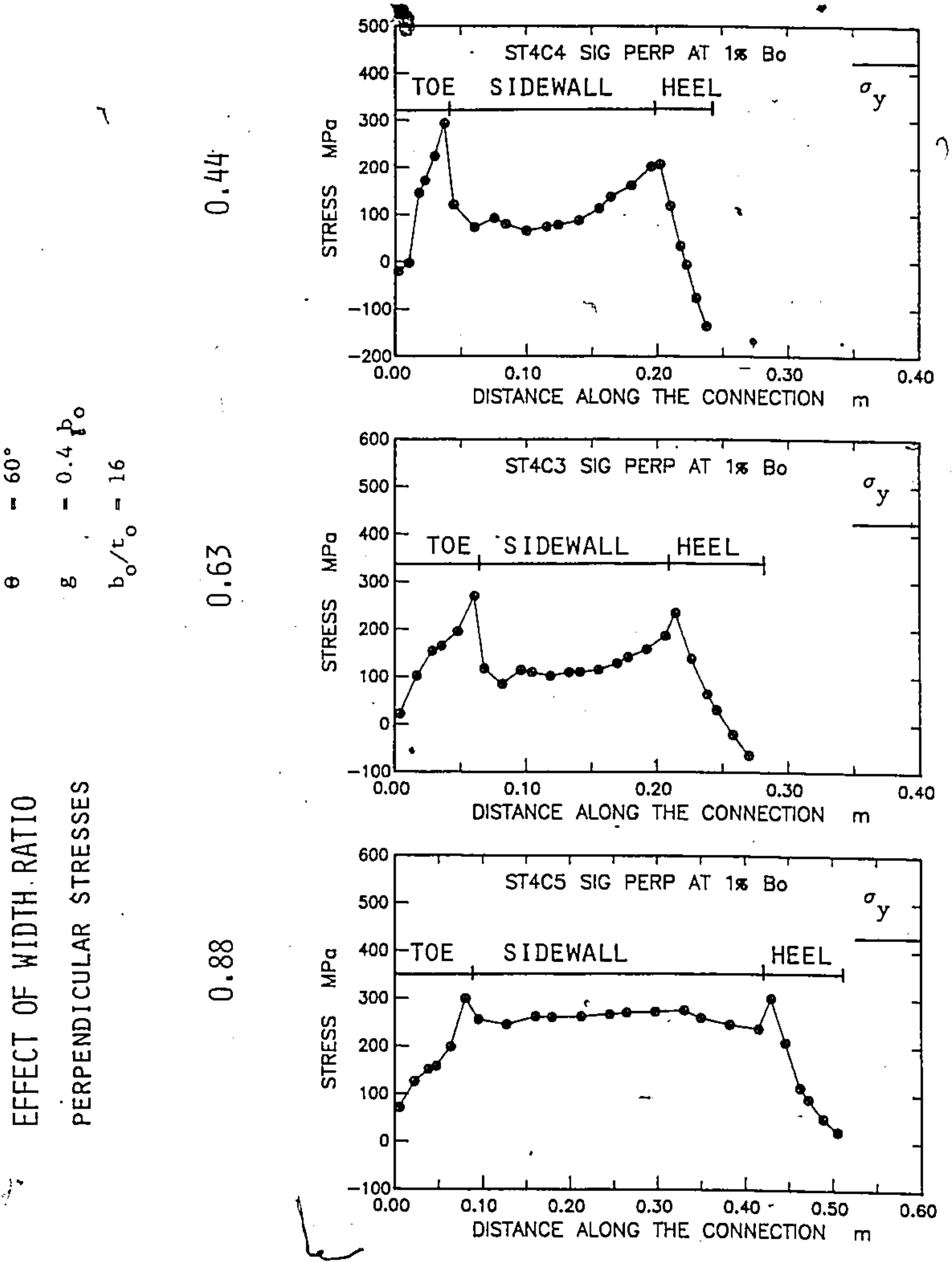

FIGURE 6.19 Effect of Width Ratio β at θ=60°, Perpendicular Stresses.

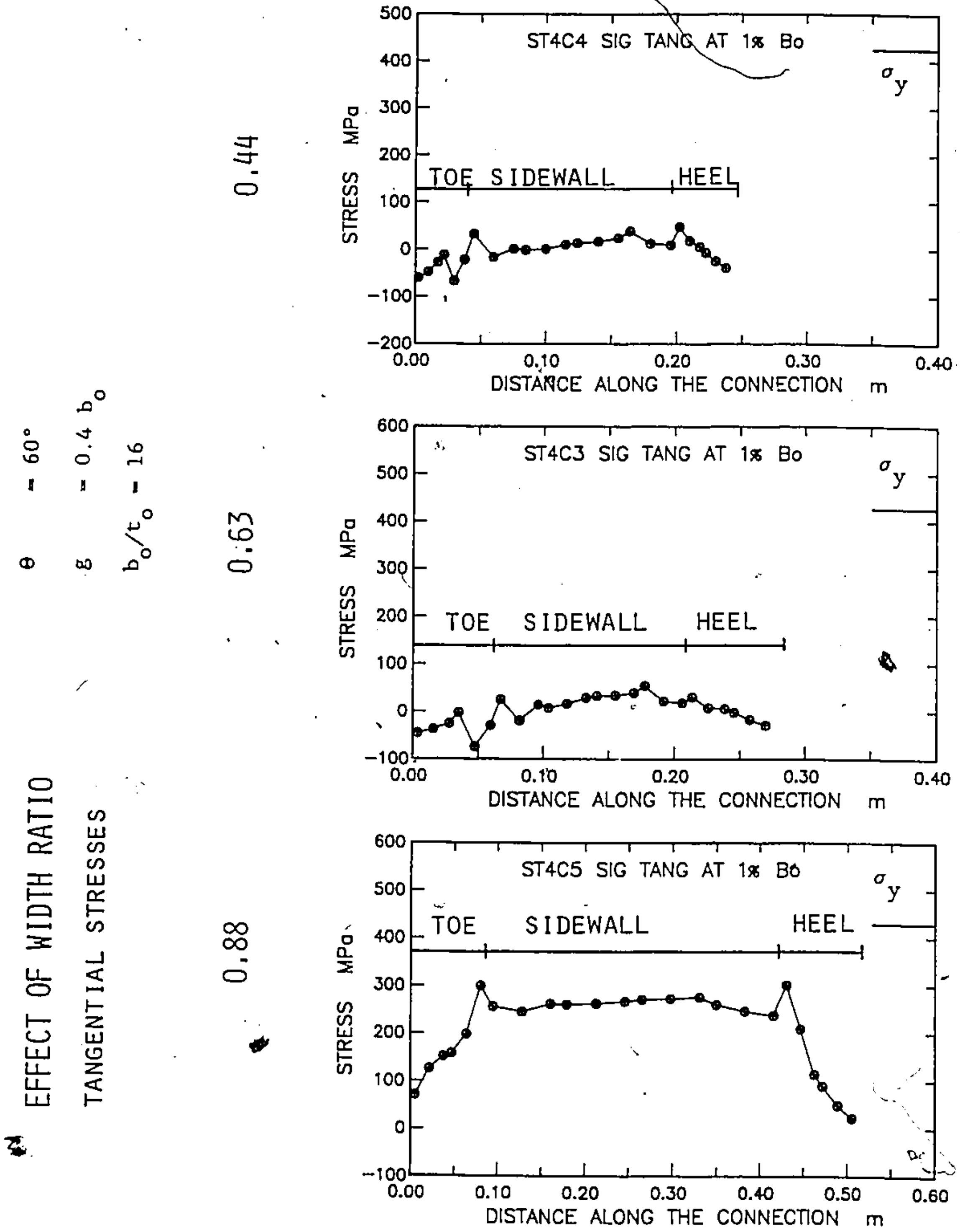

FIGURE 6.20 Effect of Width Ratio β at θ=60° , Tangential Stresses.

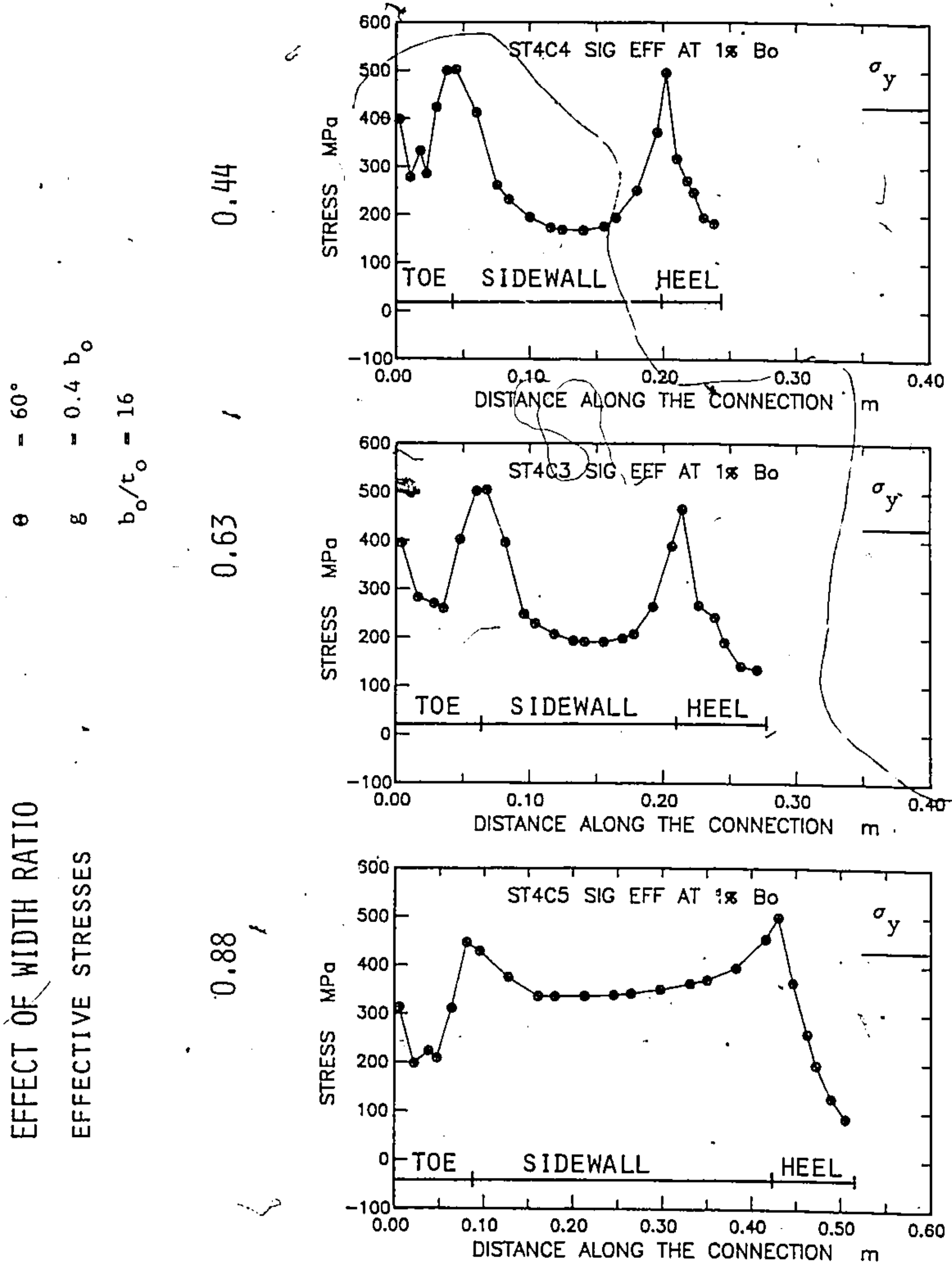

FIGURE 6.21 Effect of Width Ratio β at θ=60° , Effective Stresses.

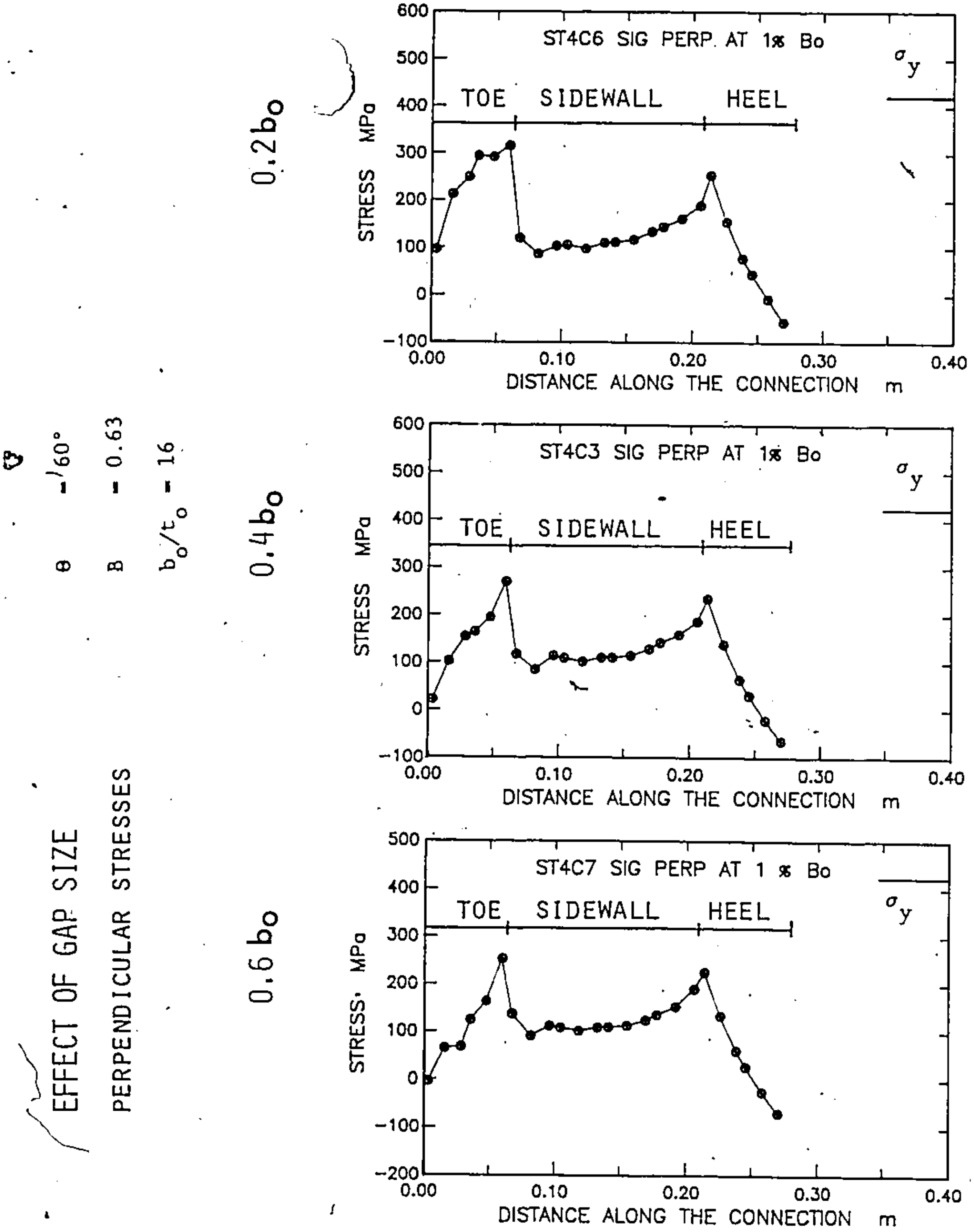

FIGURE 6.22 Effect of Gap Size, Perpendicular Stresses.

EFFECT OF GAP SIZE

TANGENTIAL STRESSES

θ = 60°

B = 0.63

$b_o/t_o = 16$

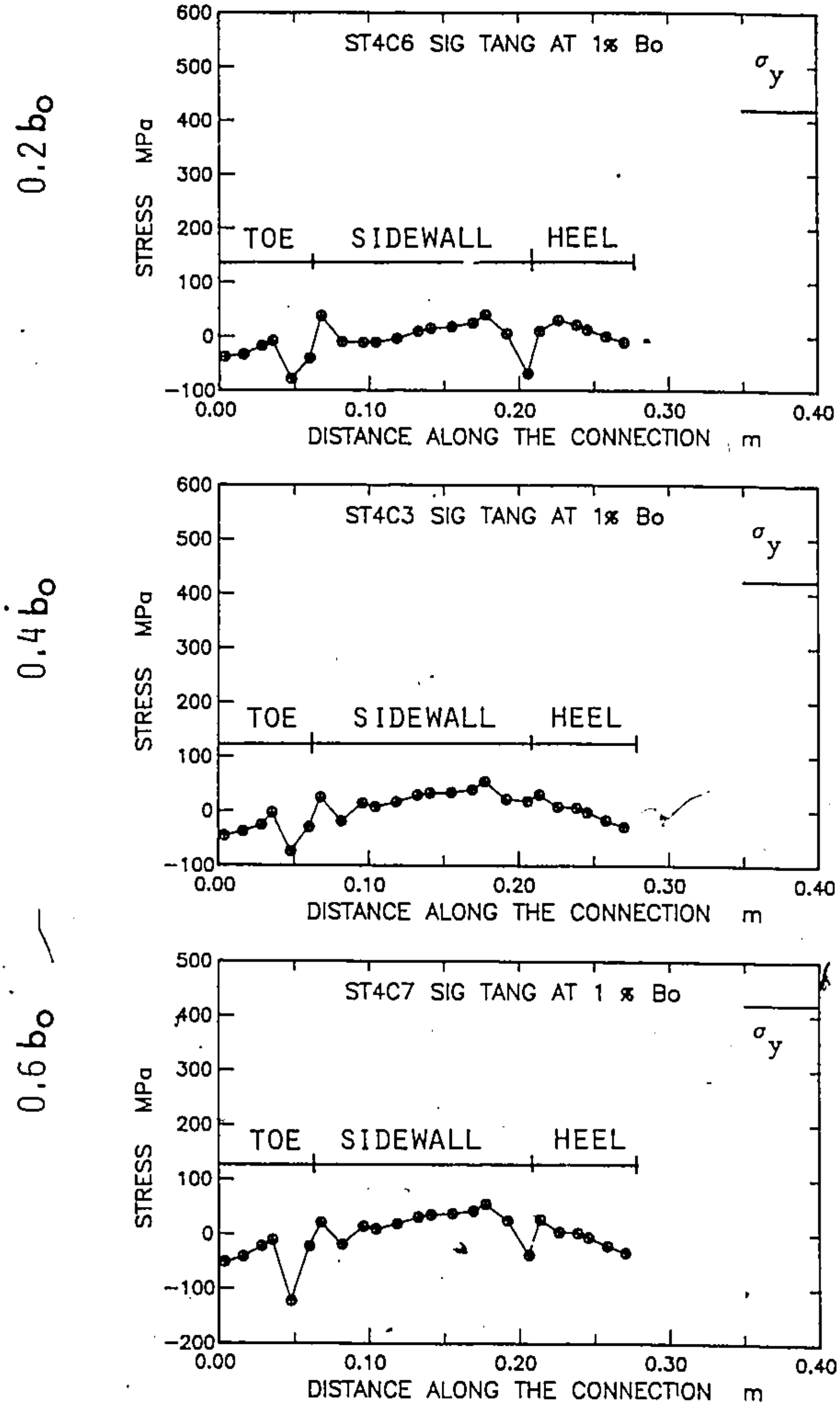

FIGURE 6.23 Effect of Gap Size, Tangential Stresses.

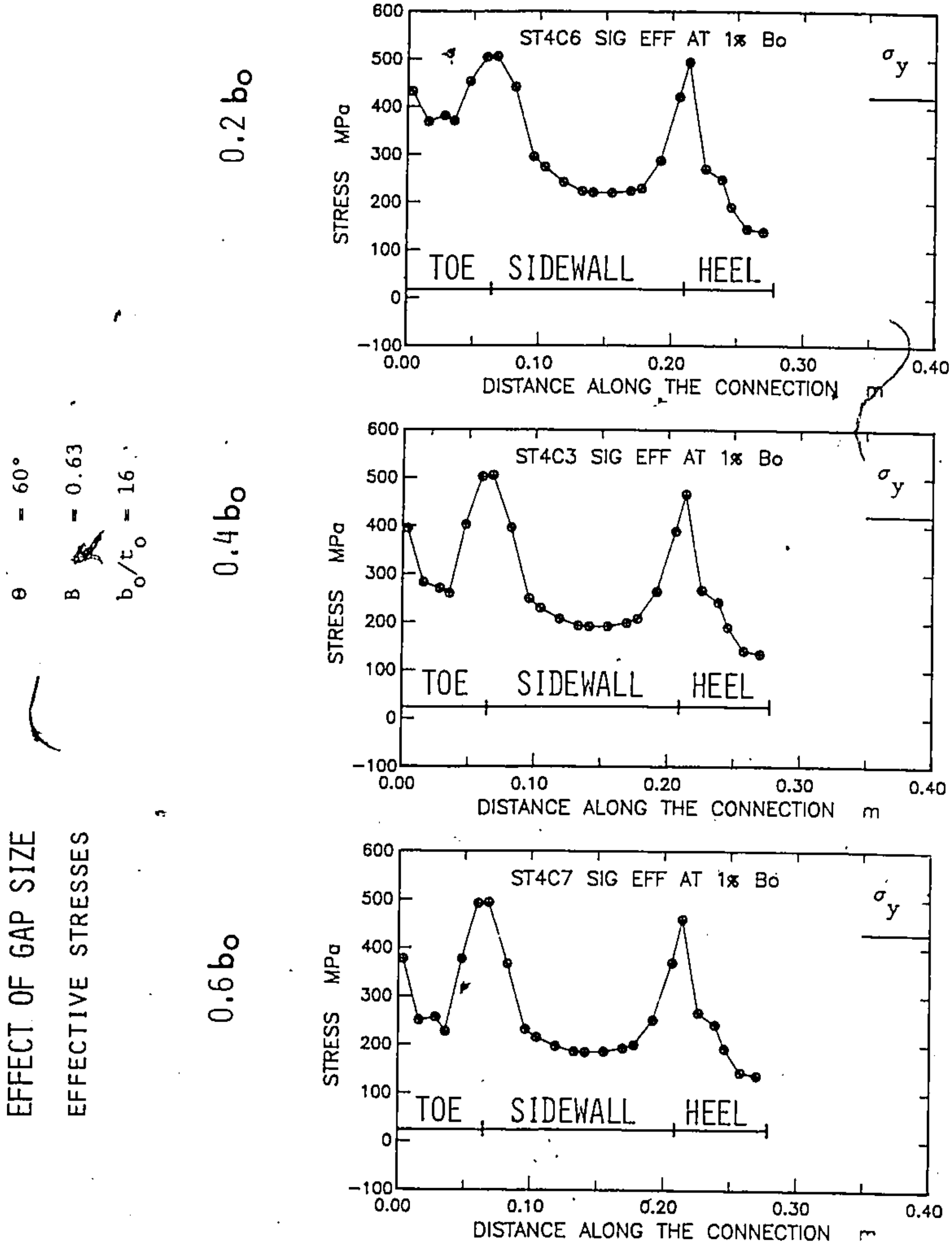

FIGURE 6.24 Effect of Gap Size, Effective Stresses.

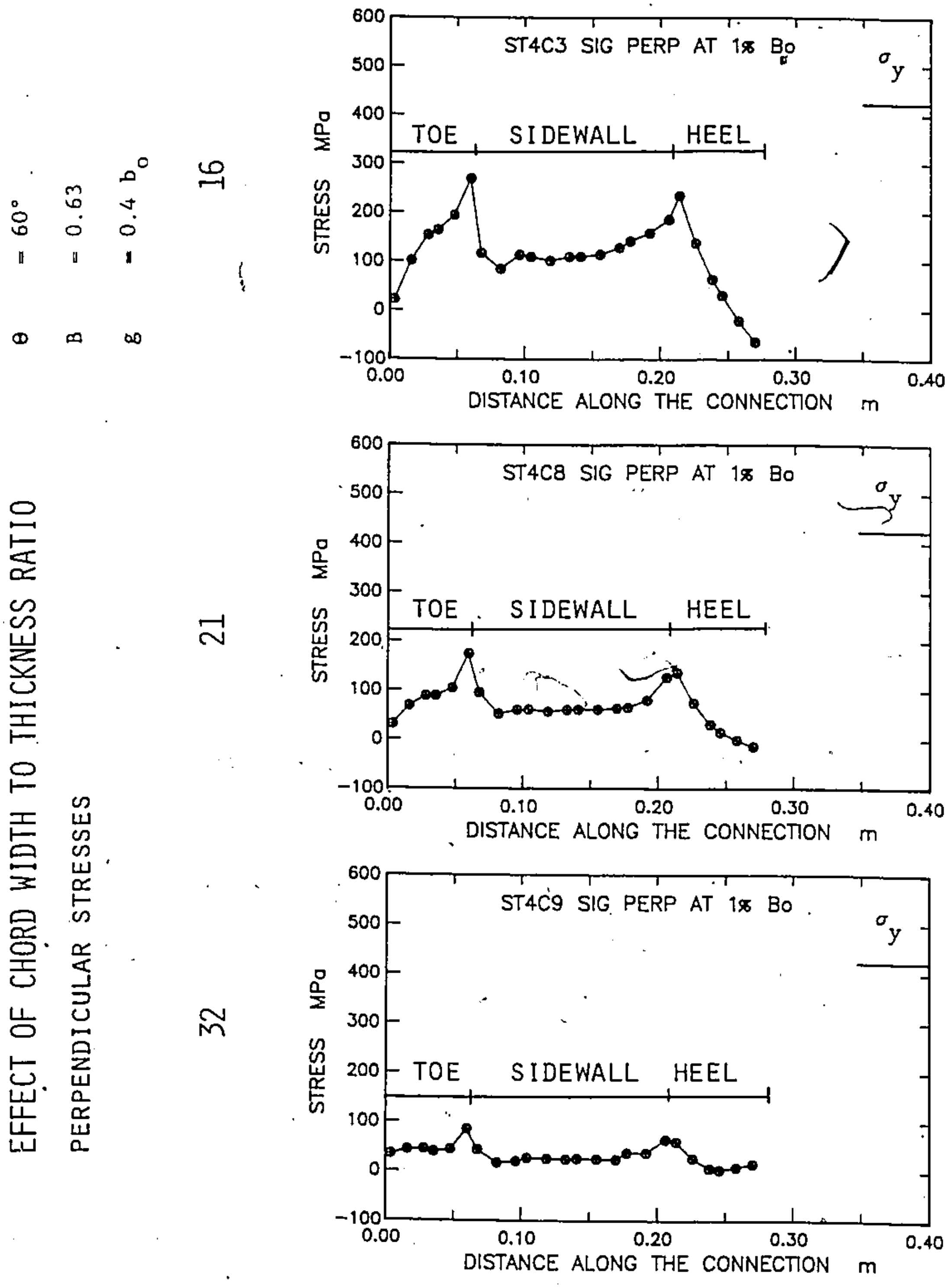

FIGURE 6.25 Effect of b_o/t_o , Perpendicular Stresses.

EFFECT OF CHORD WIDTH TO THICKNESS RATIO

TANGENTIAL STRESSES

$\theta = 60°$

$\beta = 0.63$

$g = 0.4\, b_o$

16

21

32

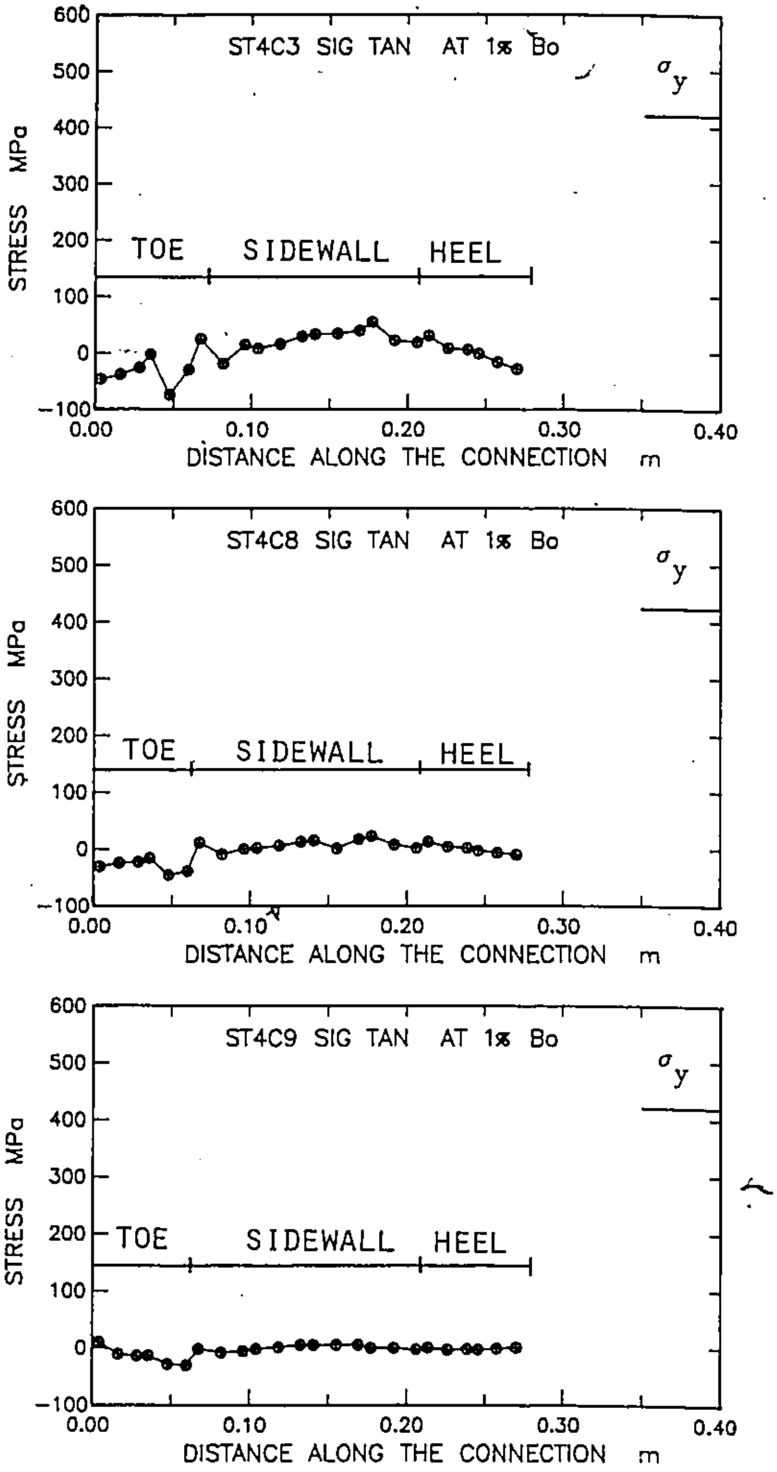

FIGURE 6.26 Effect of b_o/t_o, Tangential Stresses.

EFFECT OF CHORD WIDTH TO THICKNESS RATIO

EFFECTIVE STRESSES

θ = 60°

β = 0.63

g = 0.4 b_o

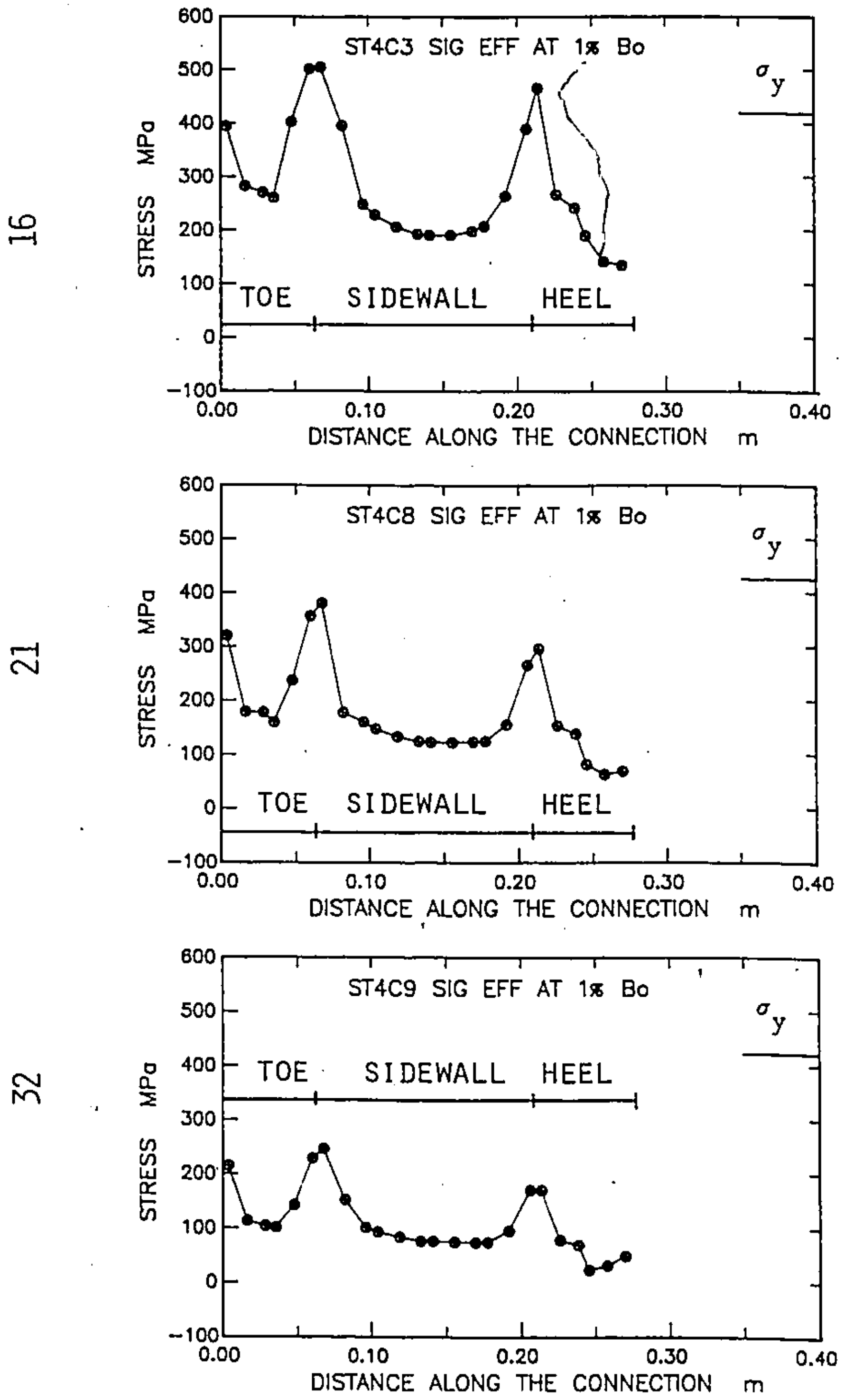

FIGURE 6.27 Effect of b_o/t_o, Effective Stresses.

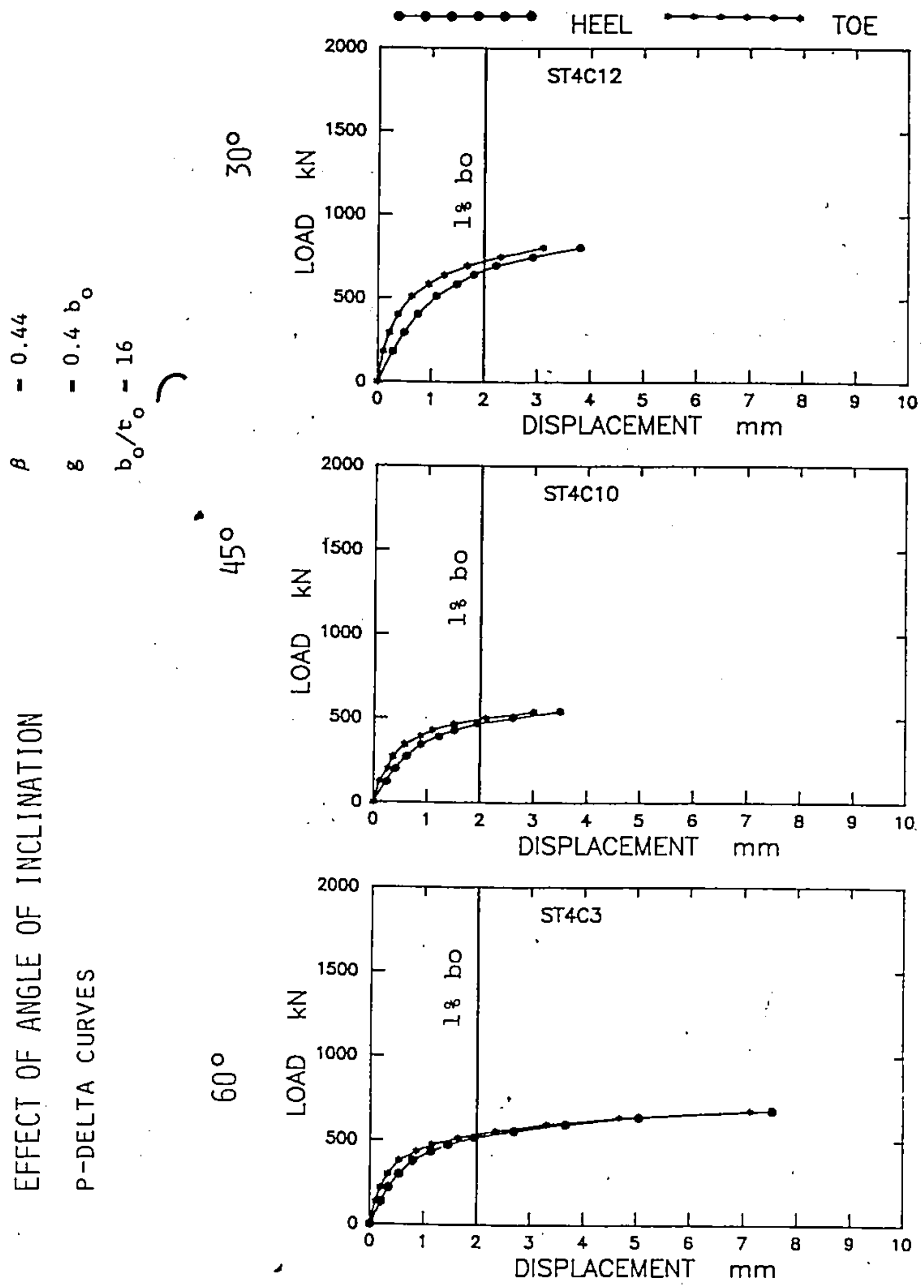

FIGURE 6.28 Effect of Angle θ at β-0.44 , Load-Deflection Curves.

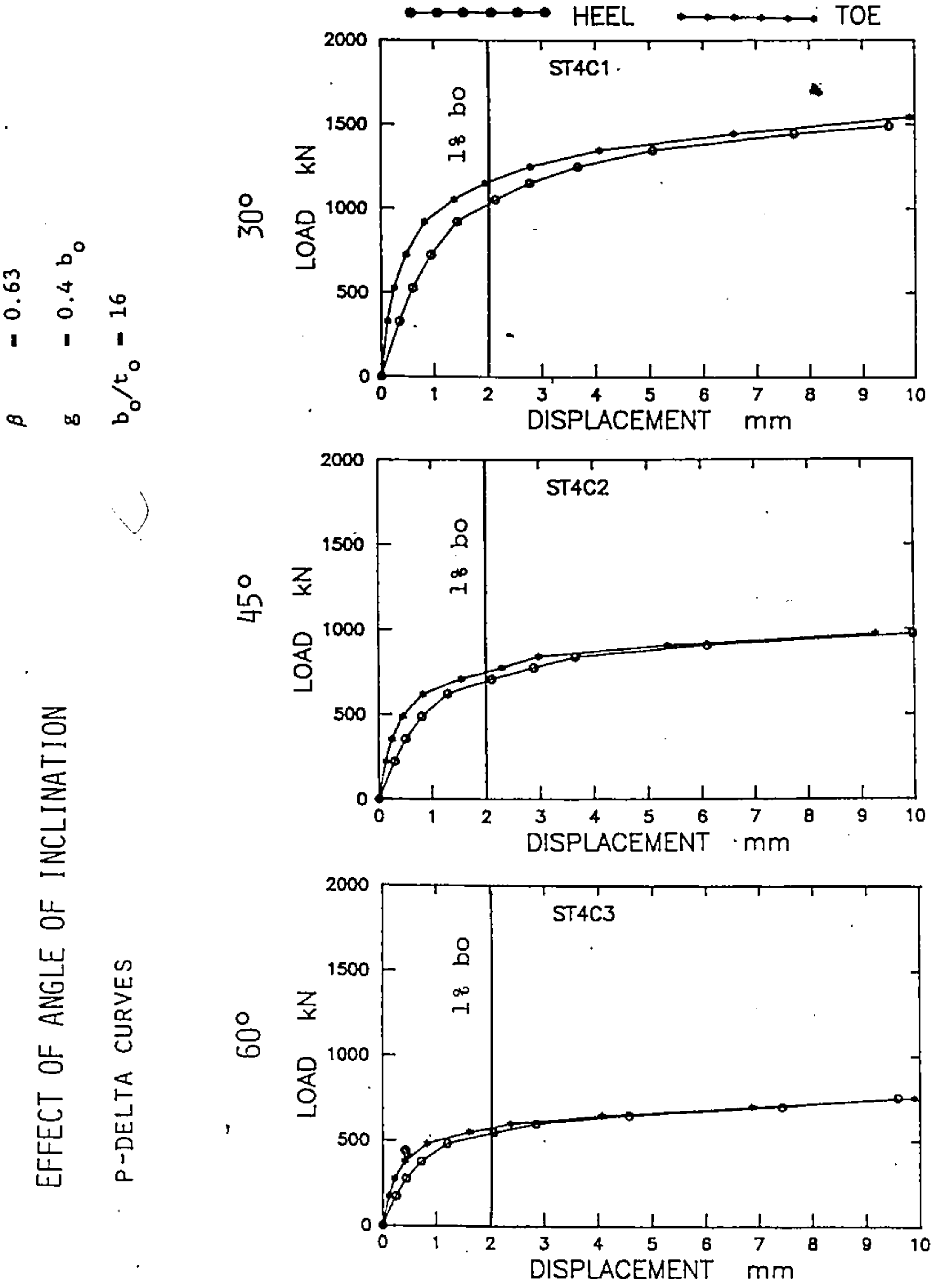

FIGURE 6.29 Effect of Angle θ at β=0.63 , Load-Deflection Curves.

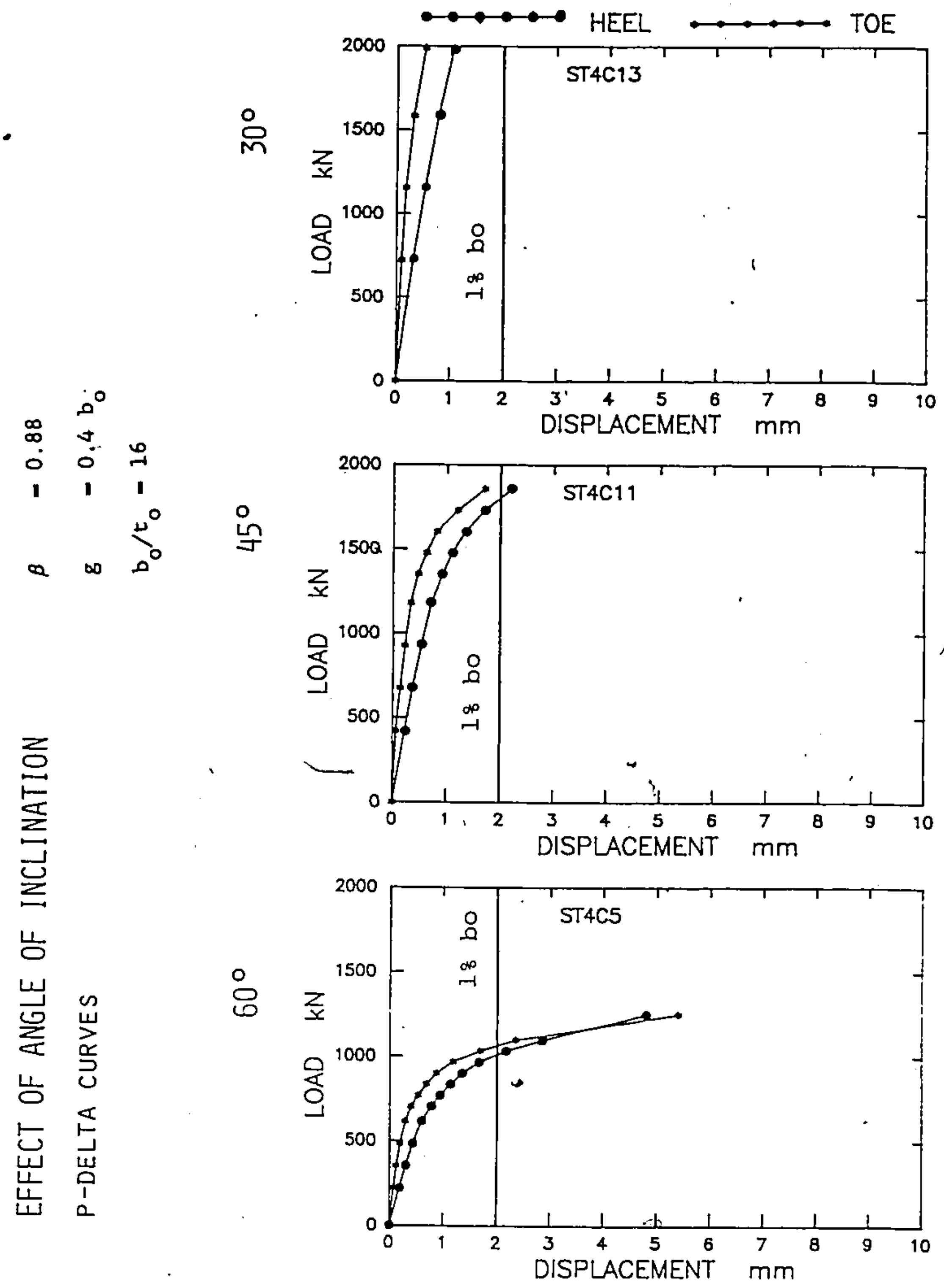

FIGURE 6.30 Effect of Angle θ at β=0.88 , Load-Deflection Curves.

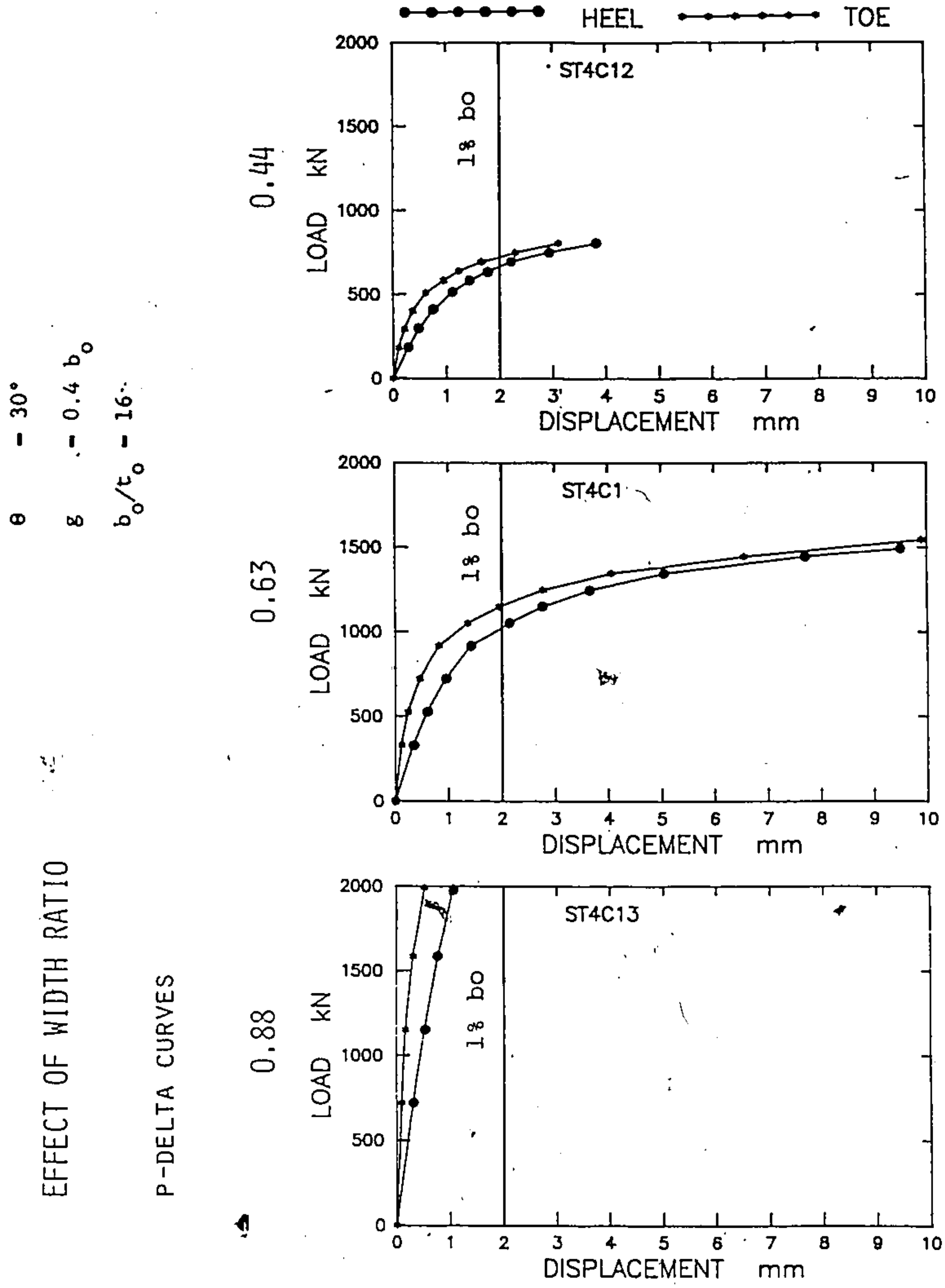

FIGURE 6.31 Effect of Width Ratio β at $\theta=30°$, Load-Deflection Curves.

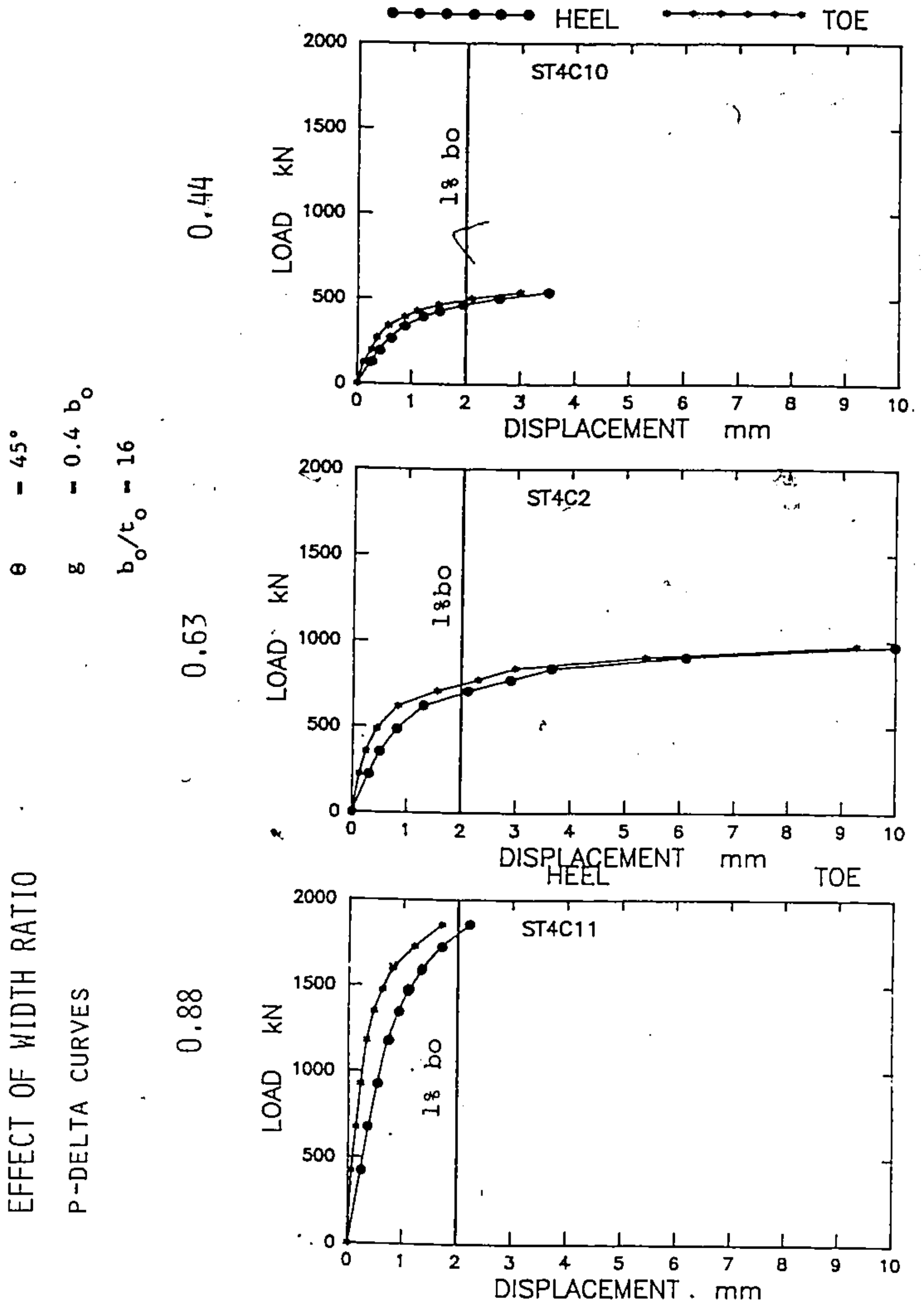

FIGURE 6.32 Effect of Width Ratio β at θ=45° , Load-Deflection Curves.

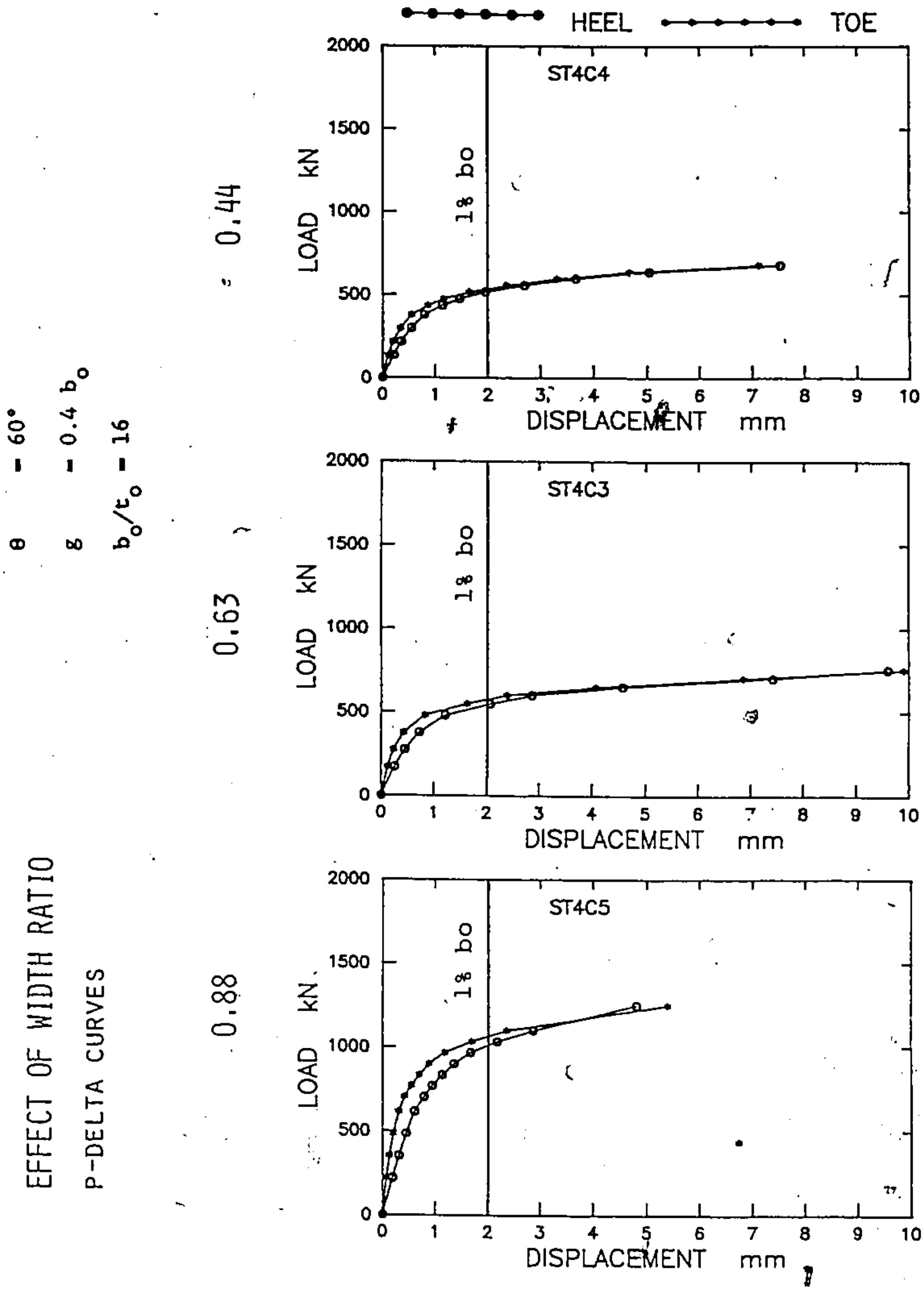

FIGURE 6.33 Effect of Width Ratio β at θ=60° , Load-Deflection Curves.

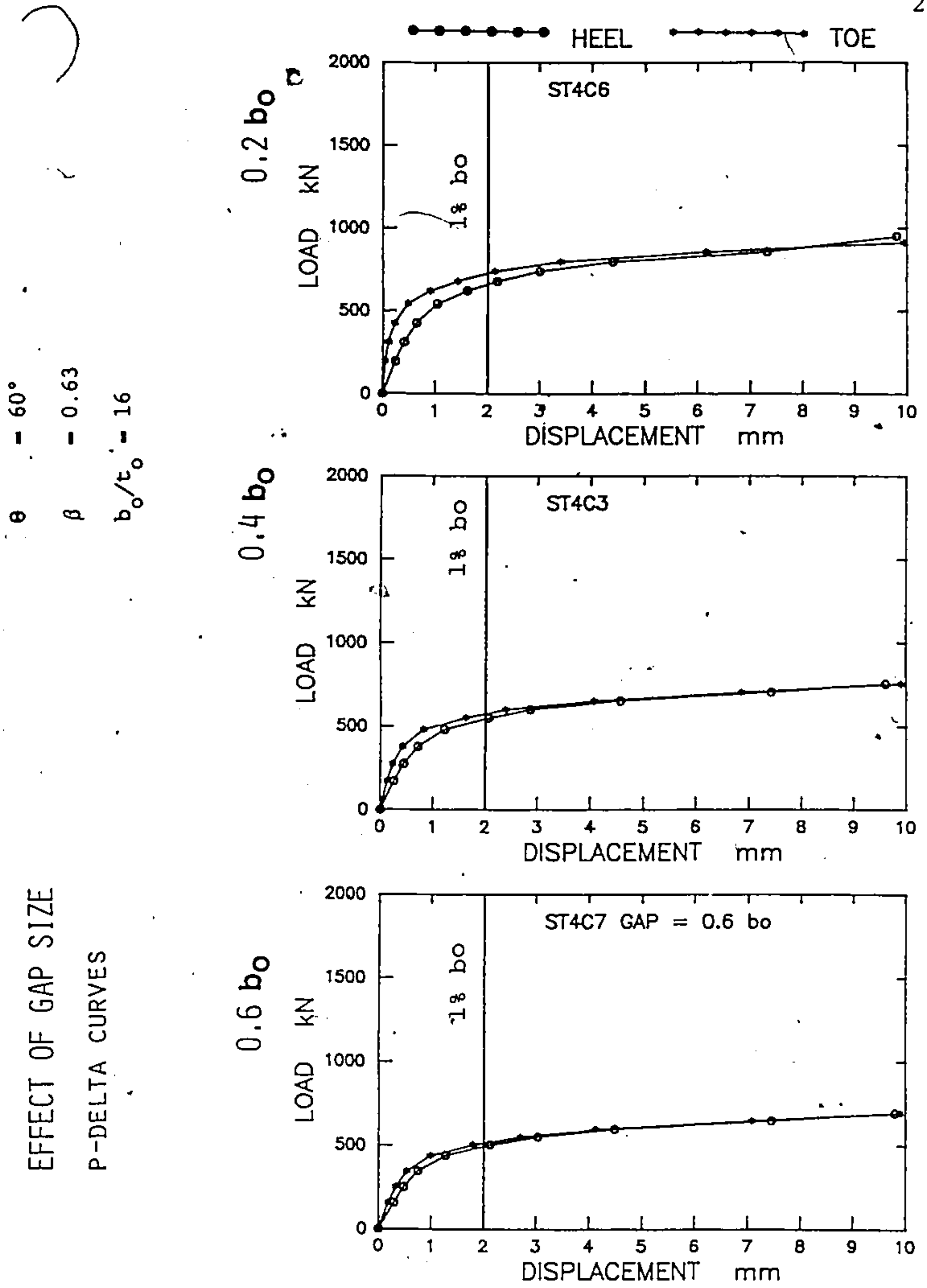

FIGURE 6.34 Effect of Gap Size , Load-Deflection Curves.

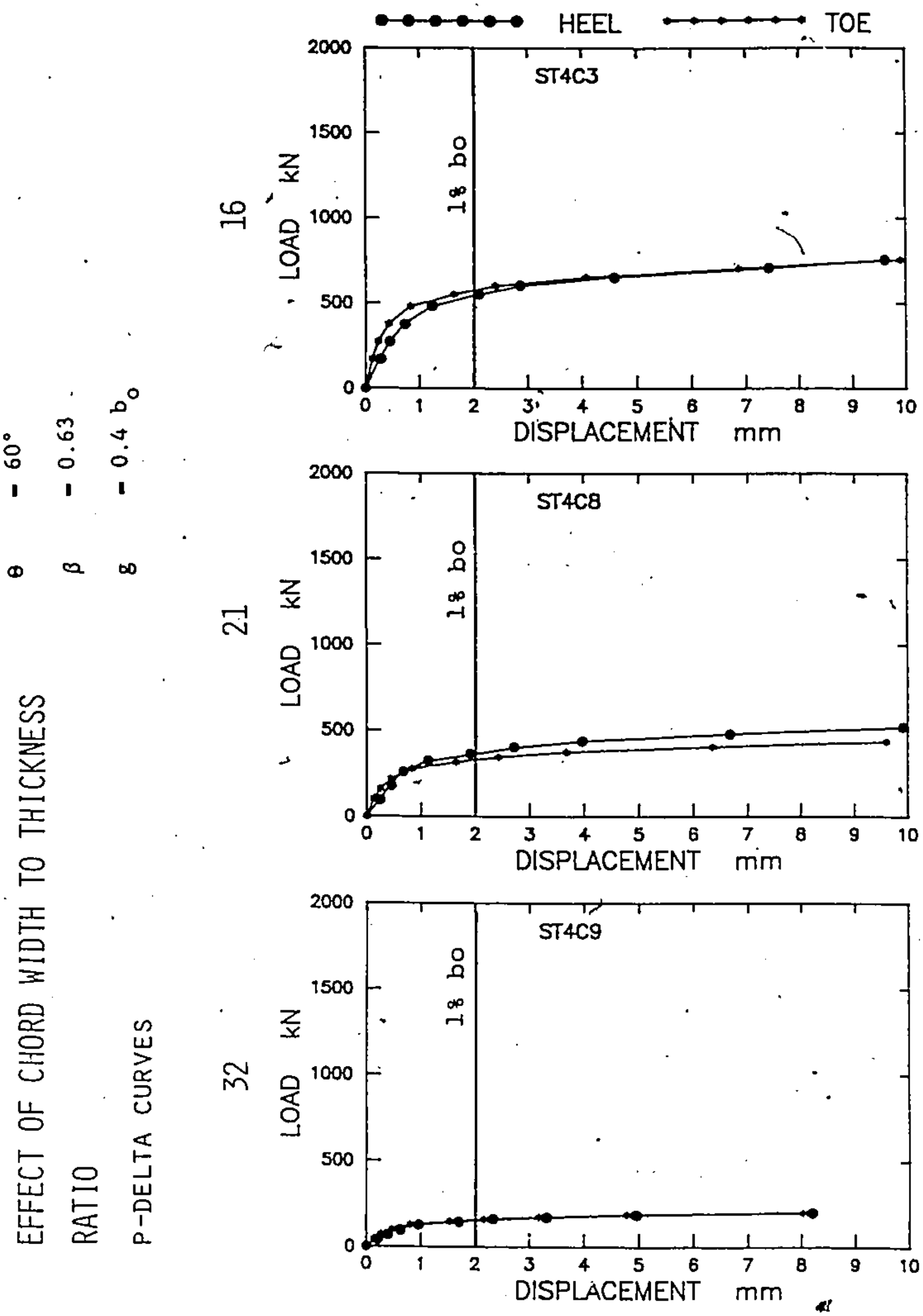

FIGURE 6.35 Effect of b_o/t_o , Load-Deflection Curves.

TABLE 6.1 JOINT CHARACTERISTICS IN PARAMETRIC STUDY

RUN	$b_o \times t_o$ mm	$b_i \times t_i$ mm	θ deg	g mm	min g* mm	max g* mm
1	203.2x12.7	127x9.53	30	81	38	114
2	203.2x12.7	127x9.53	45	81	38	114
3	203.2x12.7	127x9.53	60	81	38	114
4	203.2x12.7	88.9x9.53	60	81	57	171
5	203.2x12.7	177.8x9.53	60	81†	13	38
6	203.2x12.7	127x9.53	60	41	38	114
7	203.2x12.7	127x9.53	60	122†	38	114
8	203.2x9.53	127x9.53	60	81	38	114
9	203.2x6.35	127x9.53	60	81	38	114
10	203.2x12.7	88.9x9.53	45	81	57	171
11	203.2x12.7	177.8x9.53	45	81†	13	38
12	203.2x12.7	88.9x9.53	30	81	57	171
13	203.2x12.7	177.8x9.53	30	81†	13	38

* - min g and max g are determined from the equation (IIW 1982):

$$0.5\ (1-\beta) < g/b_o < 1.5\ (1-\beta)$$

which describes the range of validity for g (see Section 2.4.3)

† - gap sizes outside range of validity

TABLE 6.2 Summary of Results for Effects of θ and β

β \ θ	30°	45°	60°
0.44	Heel fully effective SIG TAN significant	SIG TAN near zero	Heel not fully effective SIG TAN near zero
	<<<<< SIG PERP high at toe corner , SIG EFF high at corners and toe >>>>>		
0.63	Heel fully effective Min. SIG PERP at toe SIG TAN significant	max. SIG PERP at toe corner SIG TAN near zero low SIG EFF at heel	Heel not fully effective Min. SIG PERP at heel SIG TAN near zero
	<<<<< SIG PERP high at toe corner , SIG EFF high at corners and toe >>>>>		
0.88	Heel highly effective SIG PERP are high at toe corner and heel SIG TAN high at sidewall and heel SIG EFF high everywhere <<<<<	Heel fully effective SIG PERP high at sidewall SIG TAN relatively high at sidewall peak SIG EFF at corners low SIG EFF at heel SIG PERP >0 everywhere	Heel not fully effective SIG PERP relatively high SIG TAN very high at sidewall peak SIG EFF at corners low SIG EFF at heel >>>>>

TABLE 6.3 JOINT STRENGTH COMPARED WITH SERVICEABILITY LOAD

<—— in kN ——>							
FAILURE>	A	B	C	D	E	min A-E *ϕ/1.5	Load at 1% b_o
1	1872	3120	1730	2130	1806	1084	1050
2	1324	1689	1730	1506	1806	786	707*
3	1081	1192	1730	1230	1806	641	549*
4	757	834	1164	1230	1188	449	515
5	1513	1669	2464	2230	2633	898	1034
6	1081	1192	1730	1303	1806	641	679
7	1081	1192	1730	1204	1806	641	505*
8	703	895	1582	909	1806	417	346*
9	382	596	1476	596	1806	227	160*
10	927	1182	1164	1506	1188	550	466*
11	1853	2365	2464	1506	2633	1004	1856
12	1310	2184	1164	2130	1189	713	710*
13	2621	3120	1730	2130	1633	980	1304

FAILURE MODES:

A - CHORD FACE , Packer et al. (1984), Eq.1, ϕ=0.89
B - PUNCHING SHEAR , Packer et al. (1984), Eq.9, ϕ=0.95
C - EFFECTIVE WIDTH , Packer et al. (1984), Eq.8, ϕ=0.95
D - CHORD SHEAR , Packer et al. (1984), Eq.4, ϕ=1.00
E - BRANCH YIELDING

* - values lower than the ultimate strength * ϕ / 1.5 , where
φ - resistance factor (Packer et al. 1984, Table 5)
1.5 - dominant load factor (mostly live load)

CHAPTER 7

SUMMARY AND CONCLUSIONS

7.1 Summary

One of the prime objectives of the research presented herein was to study the behaviour of an RHS gap K joint which is one of the most complex joints used in planar trusses. This was achieved by a combination of theoretical and experimental investigations. The analytical part included the development of a general finite element model for RHS joints of various configurations including a gap K joint. The experimental part involved the testing of 26 structural joints, each of them being a subconfiguration of a gap K joint.

The purpose of the numerical analysis was to develop a three dimensional model of RHS joints capable of tracing their behaviour up to the serviceability load level. The essential aspects of the modelling included a derivation of a general shell finite element, implementation of an efficient and accurate elasto-plastic algorithm and a realistic discretization of the joint. The element derived is based on a nine node Ahmad shell element. Instead of five degrees of freedom per node it has six; two local rotations are replaced by three global rotations. The elasto-plastic algorithm is based on the Von Mises yield criterion and the Prandtl-Reuss flow equations. The computer implementation of nonlinear analysis involved the use of a tangential stiffness method and the frontal solution technique. The elasto-plastic numerical algorithm is capable of: accounting properly for strain hardening; allowing the integration point to yield within a load increment; monitoring the evolution of the yield surface; and accommodating the possibility of elastic unloading. The material properties can change within an element and any nonlinear stress-strain relationship can describe the evolution of the yield surface. The presented finite element model can be used in the analysis of a variety of structures such as plates, shells, folded plates and any combination of these. In particular, it may be applied to the analysis of multiple junctions. It is not limited to an intersection between two plates. In the area of hollow section joints either circular or rectangular sections can be used in a discretization of a structural joint.

The experimental program was part of an investigation into the design of weldments in RHS joints which was carried out at the University of Toronto. The purpose of the measurements collected for this study was to gather information about the joint behaviour in order to: obtain a realistic description of the strain distribution in the branch walls; assess the influence of angle θ and the flexibility of the base under the branch; and provide data for verification of the numerical model. This was accomplished by placing numerous strain gauges on the branch member walls in the vicinity of the weldment. The experimental program included testing of two types of joints. Both of them had two RHS branch members loaded in tension and separated by either a thick steel plate or another RHS member of a bigger size. This arrangement involved a variation of the angle of inclination for the branch member.

The numerical analyses presented in this study are focused on modelling of the behaviour of RHS joints. All joint configurations tested became the subjects of a numerical simulation. In addition, this selection was extended to joints with a branch inclination of 45° which was not part of the experimental investigation. After an in-depth validation of the numerical model based on the examples available in the literature and the results of the present experimental program, the numerical effort concentrated on modelling of a gap K joint. The behaviour of this joint was analyzed in a parametric study which included four major effects: the angle of branch inclination, the width ratio, the gap size and the chord width to thickness ratio. The outcome of this study included the distribution of stresses in the branch member walls and the localised deflections of the chord connecting face. The results of the numerical simulation of selected RHS joints add to a better understanding of the behaviour of RHS joints and provide specific design implications.

7.2 Conclusions

The distribution of strains in the walls of a branch near the weld has been found to depend on the angle of inclination and on rigid or flexible base conditions.

Experimental measurements near failure indicated that in both base conditions the heel is the critical area for θ=30° and the toe is critical for $\theta=60°$. This was confirmed by strain gauges at the toe and the heel, rosettes on the sidewall and by inspection of the failure modes. However, the direction of the major principal axis of strain in both cases is different. For a rigid base it is almost parallel to the branch longitudinal axis and for a flexible base it bisects the angle of consideration.

The **strain measurements** in joints with rigid base conditions have shown that both the toe and the heel are fully effective in transferring the load from the branch to the plate within the **service loads**. In joints with flexible base conditions the effectiveness of the toe or the heel varies with the angle of inclination θ. For $\theta=30°$ the entire perimeter of the branch member may be regarded as fully effective.

The **yielding patterns** observed during testing indicate that the branch corners in the vicinity of the weldment become inelastic first. Next, the yielding spreads along the weldment. For the flexible base condition, the yielding also affects the chord connecting face.

The results of the numerical simulation of joints in Stage 2 indicate that for the **rigid base** condition the sidewall does not participate as much in the transfer of perpendicular stresses as the toe or heel; for $\theta=30°$ the heel is more active than the toe. The tangential stresses are predominantly carried by the sidewall and the stresses at either the toe or heel are near zero. It is typical for the rigid base condition that the stresses within each wall of the branch are uniformly distributed. For the rigid base condition the yielding first takes place in the heel area.

For the **flexible base conditions** the variation of stresses within each wall is very significant; the peak values of the effective stresses always occur near the branch corners. In Stage 2 where the branch was welded to the chord at 90° angle the perpendicular stresses are concentrated near the branch corners; the tangential stresses oscillate near zero with the exception of the toe where they reach very low negative values; the highest effective stresses are near the branch toe and around the corners. The distribution of perpendicular stresses for flexible base conditions with a branch inclined to the chord at angles other than 90° indicates that the resultant force is shifting from the heel to the toe as θ increases from 30° to 60° .

The results of a **parametric study of a gap K-joint** (Stage 4) suggest that the **heel** should be considered as **fully effective** in the transfer of load from the branch to the chord for joints with $\theta=30°$ and any width ratios; it is also fully effective for $\theta=45°$ and high width ratios. High **stress concentrations** always occur near the corners of the branch member. **Perpendicular stresses** for low and medium width ratio peak at the branch corner between the toe and a sidewall; for high width ratio the highest stresses take place at the heel for $\theta=30°$ and are equally balanced between the toe and heel for $\theta=60°$. High levels of perpendicular stresses were observed on the sidewall at high width ratio and $\theta=45°$ or 60°. **Tangential stresses** are the highest on the sidewall; for small and medium width ratios they peak near the heel and for high width ratio closer to the toe. High levels of tangential stresses were observed for all angles at high width ratios and for the angle of 30° and small or medium width ratios. Effective stresses always peak near the branch corners and at the centre of the toe.

The gap size has a negligible effect on the distribution of stresses in the branch walls; the only noticeable effect of the gap size parameter, g, is that for small g values the perpendicular and effective stresses are affected.

The b_o/t_o value affects the levels of all stresses; however, for b_o/t_o higher than 20 the distribution of the perpendicular or tangential stresses at the load level corresponding to 1% b_o is very low and does not reach yield levels for the joints considered in this study.

The local deflections at high width ratio and θ=45° or 60° are very small and do not reach the level of 1% b_o within the working load level. For medium width ratio the deflections become excessively large with increasing θ. For small width ratio the deflections for θ=45° and 60° are about the same. An increase in local deflections is associated with with a decrease of the width ratio. A comparison of the load levels at which localised deflections obtained in the numerical analysis reached 1% b_o with the working load levels indicated that for most joints the local chord face deflections become excessive before the joint reaches the service load level.

REFERENCES

Ahmad, S., Irons, B.M. and Zienkiewicz, O.C. 1970. Analysis of Thick and Thin Shell Structures by Curved Finite Elements. International Journal for Numerical Methods in Engineering, Vol.2, pp.419-451.

Bathe, K.-J. and Bolourchi, S. 1980. A geometric and Material Nonlinear Plate and Shell Element. Computers and Structures, Vol. 11, pp.23-48.

Bathe, K.-J. and Ho, L.W. 1980. Some Results in the Analysis of Thin Shell Structures. Proceedings of the Europe-U.S. Workshop on Nonlinear Finite Element Analysis in Structural Mechanics, Ruhr-Universitat Bochum, Germany, July 28-31. Springer-Verlag Berlin, pp. 122-150.

Bathe, K.-J., Chaudhary, A., Dvorkin, E.N. and Kojic, M. 1984. On the Solution of Nonlinear Finite Element Equations. Proceedings, International Conference on Computer-Aided Analysis and Design of Concrete Structures, Split, Yugoslavia, September, pp.221-231.

Bijlaard, P.P. 1955. Stresses from Local Loadings in Cylindrical Pressure Vessels. Transactions of American Society of Mechanical Engineering. August

Blockley, D.I. 1967. Joints between Structural Hollow Sections in Plane Frameworks. Ph.D. Thesis, University of Sheffield, England.

BRITISH STEEL CORPORATION. 1977a . Tests on complete girders. CIDECT Draft Report CE 73/95, Tubes Division, Corby, England.

BRITISH STEEL CORPORATION. 1977b . Tests on Isolated Joints. CIDECT Report CE 73/96/D, Tubes Division, Corby, England.

CIDECT. 1984. Construction with Hollow Steel Sections. British Steel Corporation Tubes Division, Corby, England.

CIDECT. 1986. Monograph No.6 . The Strength and Behaviour of Statically Loaded Welded Connections in Structural Hollow Sections. Giddings, T.W. and Wardenier, J.; (editors), British Steel Corporation, Corby, England.

Coutie, M.G., Davies, G. and Dasgupta, A. 1970. Report on the Research of Tubular Joints in Trusses. Department of of Civil Engineering, University of Nottingham, England.

Crisfield, M.A. 1985. Shear-Constraints and Folded-Plated Structures. Engineering Computation, Vol.2, September, pp. 238-246.

Czechowski, A., Gasparski, T., Zycinski, J. and Brodka, J. 1984. Investigation into the Static Behaviour and Strength of Lattice Girders made of RHS. IIW Doc. XV-E-84-052, Metal Structures Research and Design Centre MOSTOSTAL, Warsaw, Poland

Dasgupta, A. 1970. The Behaviour of Joints in Tubular Trusses, Ph.D. Thesis, University of Nottingham, England.

Davie, J. and Giddings, T.W. 1971. Research into the Strength of Welded Lattice Girder Joints in Structural Hollow Sections, CIDECT Program 5EC, Report CE70/3, British Steel Corporation, Tubes Division, Corby, England, May.

Davies, G. and Roper, C.G. 1975. Gap Joints with Tubular Members - A Yield Line Approach. Building Science, Vol. 10, pp. 199-205.

Davies, G. and Roper, C.G. 1977. Gap Joints with Tubes - A Yield Line Modified by Shear Approach. Building and Environment, Vol. 12, pp. 31-38.

Davies, G., Wardenier, J. and Stolle, P. 1981. The Effective Width of Branch Cross Walls for RR X-Joints in Tension. Stevin Report 6-81.7, TNO/IBBC Report BI-81-18/063.4.3470, Delft University of Technology, Netherlands.

De Koning, C.H.M. and Wardenier, J. 1979. Tests on Welded Joints in Complete Girders made of Square Hollow Sections. CIDECT Program 5Q, CIDECT Report No. 5-Q/79, Stevin Laboratory, Delft University of Technology, Netherlands.

Dixon, D.A. 1982. The effects of transverse compression on RHS, B.A.Sc. Thesis, Department of Civil Engineering, University of Toronto, April.

Donnell, L.H. 1934. Stability of Thin-Walled Tubes under Torsion. National Advisory Committee on Aeronautics (NASA). Report No 479.

Dundrova, V. 1965. Stresses at Intersection of Tubes; Cross and T Joints. Technical Report from Structures Fatigue Research Laboratory, Department of Civil Engineering, University of Texas, Austin.

Eastwood, W. and Wood, A.A. 1970. Recent Research on Joints in Tubular Structures. Proceedings of Canadian Structural Engineering Conference, Toronto.

Flugge, W. 1967. Stresses in Shells. Springer Verlag. Berlin.

Frater, G. 1986. Weldment Design for Hollow Structural Section Joints. M.A.Sc. Thesis, Department of Civil Engineering, University of Toronto.

Greste, O. 1970. Finite Element Analysis of Tubular K Joints. Report SESM 70-11, University of California.

Hoff, N.J. 1953. Deformation and Stresses in Circular Cylindrical Shells caused by Pipe Attachments. Knolls Atomic Power Laboratory, Reports KAPL 921, 922, 923, 924, 925, 926 and 1025. November.

IIW (International Institute of Welding). 1981. Sc.XV-E *, Design Recommendations for Hollow Sections Joints - Predominantly Statically Loaded", IIW Annual Assembly, Oporto, Portugal, Doc. XV-491-81 Revised.

Irons, B. and Ahmad, S. 1980. Techniques of Finite Elements. Ellis Horwood. Chichester, UK.

Irving, D.J. 1982. Large Deformation Elasto-Plastic Finite Element Analysis of Plates, Shells and Tubular Joints Using Semiloof Shell Elements. Ph.D. Thesis, Faculty of Engineering, Kingston Polytechnic, England.

Johansen, K.W. 1962. Yield Line Theory. Cement and Concrete Association, London, England.

Kellogg, M.W. 1956. Design of Piping Systems. 2nd Ed., Wiley.

Korol, R.M. 1972. The Plastic Behaviour of Hollow Structural Sections with Implications for Design. Canadian Structural Engineering Conference, Toronto.

Korol, R.M. and Mansour M.H. 1979. Theoretical Analysis of Haunch-Reinforced T Joints in Square Hollow Sections. Canadian Journal of Civil Engineering, Vol.6, pp.601-609.

Krakeland, B. 1978. Large Displacement Analysis of Shells Considering Elasto-Plastic and Elasto-Viscoplastic Materials. Ph.D. Thesis, Norwegian Institute of Technology, Division of Structural Mechanics.

Makino, Y., Kurobane, Y. and Ochi, K. 1984. Ultimate Capacity of Tubular Double K-Joints. Proceedings of 2nd, International Conference on Welding of Tubular Structures, Boston,USA,July.

Mang, F., Bucak, O. and Hummel, T. 1978. Investigations into the Behaviour of High Tensile Steel Joints of Rectangular Hollow Sections, University of Karlsruhe, West Germany, IIW DOC. XV-416-78, May.

Mang, F., Bucak, O. and Striebel, A. 1978. The Load Carrying Behaviour of Unstiffened K-Joints of Large Sized Thin Walled Rectangular Hollow Sections of Steel Grade St 42 and St 52, University of Karlsruhe, West Germany,IIW Doc.XV-417-78,XIII-932-79.

MANNESMANN Research Institute. 1968. Tests on RHS Joints.

Markarian, D. 1977. The Behaviour of Welded Joints in Complete Lattice Girders with RHS Chords (Tests on Isolated Joints). British Steel Corporation, Tubes Division, Report CE 73/3, Corby, England, May.

Mee, B.L. 1969. The Structural Behaviour of Joints in Rectangular Hollow Sections. Ph.D. Thesis, University of Sheffield, England.

Mirza, F.A. and Korol, R.M. 1982. Finite Element Analysis of RHS T Joints. Journal of Structural Division, Proceedings of ASCE, Vol. 108, pp. 2081-2098.

Mirza, F.A., Shehata, A.A. and Korol, R.M. 1982. Modelling of Double Chord Rectangular Hollow Section T Joints by Finite Element Method. Computers and Structures, Vol. 15, pp. 123-129.

Mouty, J. 1976. Ultimate Load Calculations for Welded Joints Comprising Rectangular and Square Hollow Sections. Construction Métallique, No.2.

Niemi, E. 1983. The Effect of Gap Size on Static Strength of K-Joints in Rectangular Hollow Section Trusses - a Modified Yield Line Approach. Department of Mechanical Engineering, Lappeenranta University of Technology, Finland, IIW Report XV-537-83.

Ogle, R.B. and Kulak, G.L. 1981. Fatique Strength of Trusses made from Rectangular Hollow Sections. Department of Civil Engineering, University of Alberta.

Ostrowski, P. 1984. "Finite Element Modelling of Single Chord RHS Gap K Joints", M.Eng. Thesis, McMaster University, Hamilton.

Ostrowski, P.K., Korol, R.M., Mirza,F.A. and Packer, J.A. 1985. Deformation of Gap K-Joints. 10th Canadian Congress of Applied Mechanics, London, Ontario, Proceedings, pp. A355-A356.

Owen, D.R.J. and Hinton, E. 1980. Finite Elements in Plasticity, Theory and Applications. Pineridge Press Limited . Swansea, UK.

Packer, J.A. 1978. Theoretical Behaviour and Analysis of Welded Steel Joints with RHS Chords. CIDECT Report 5U-78/19, Department of Civil Engineering, University of Nottingham, England.

Packer, J.A., Davies, G. and Coutie, M.G. 1982. Ultimate Stength of Gapped Joints in RHS Trusses. Journal of the Structural Division, ASCE, Vol. 108, pp. 411-431.

Packer, J.A., Birkemoe, P.C. and Tucker, W.J. 1984. Canadian Implementation of CIDECT Monograph No. 6. Department of Civil Engineering, University of Toronto, Publication No. 84-04, CIDECT Report NO. 5AJ-84/9-E.

Packer, J.A. and Frater, G.S. 1986. Performance of Fillet Weldments in Hollow Section Connections. Safety Criteria in Design of Tubular Structures, ed. Y.Kurobane and Y,Makino, Proceedings of International Meeting, Tokyo, Japan, Maruzen Co. Ltd.,pp.139-148.

Packer, J.A. and Frater, G.S. 1987. Weldment Design for Hollow Section Joints. Department of Civil Engineering, University of Toronto, Publication No. 87-01, CIDECT Report NO. 5AN-87/1-E.

Packer, J.A., Korol, R.M., Mirza F.A. and Ostrowski P.K. 1984. A Finite Element Study of the Flexibility of Rectangular Hollow Section Truss Gapped K-Joints", 9th Australasian Conference on the Mechanics of Structures and Materials, University of Sydney, Australia.

Panagiotopoulos, G.D. 1986. A Finite Element Procedure for the Stress Analysis of Tubular Joint Connections. International Journal for Numerical Methods in Engineering, Vol. 23, pp.317-329.

Patel, N.M., Graff, W.J. and White, A. 1975. Punching Shear Characteristics of RHS Joints. ASCE National Structural Engineering Meeting, San Francisco.

Ramm, E. 1977. A Plate/Shell Element for Large Deflections and Rotations. in Formulations and Computational Algorithms in Finite Element Analysis. Bathe, K.-J. and Oden, J.T. Editors. M.I.T. Press.

Redwood, R.G. 1965. The Behaviour of Joints between Rectangular Hollow Structural Members. Civil Engineering and Public Works Review, Vol. 60, pp. 1463-1469.

Rolloos, A. 1969. The Effective Weld Length of Beam to Column Connnections without Stiffening Plates. TNO / Delft University of Technology, Report 6-69-7-HL 12, IIW Doc. XV-276-69.

Roper, C.G. 1974. An Analytical Study on the Strength and Flexibility of Tubular Joints. M.Phil. Thesis, University of Nottingham.

SONCO Steel Tube Ltd. 1983. Hollow Structural Sections (product brochure). Brampton, Ontario.

Stanton, E.L. and Schmit, L.A. 1970. A Discrete Stress and Displacement Analysis of Elastoplastic Plates. AIAA Journal, Vol.8, pp.1245-1251.

Stein, E. Lambertz, K.H. and Plank, L. 1985. Ultimate Load Analysis of Folded Plate Structures with Large Elasto-Plastic Deformations - Theoretical and Practical Comparisons of Different FE algorithms. Proceedings of the International Conference on Numerical Methods in Engineering: Theory and Applications. Swansea, UK, January.

STELCO Inc. 1981. Hollow Structural Sections Design Manual for Connections. 2nd ed. Hamilton, Canada.

Strommen, E.N. 1982. Ultimate Strength of Welded K-Joints of Rectangular Hollow Sections. Ph.D. Thesis, Norwegian Institute of Technology, Division of Steel Structures, Trondheim, Norway.

UEG (Underwater Engineering Group). 1985. Design of Tubular Joints for Offshore Structures. Vols 1-3, London, England.

Wardenier, J. 1982. Hollow Section Joints. Delft University Press, Delft University of Technology, Delft, Netherlands.

Wardenier, J., Davies, G. and Stolle, P. 1981. The Effective Width of Branch Plate to RHS Chord Connections in X-Joints. Stevin Report 6-81.6, TNO/IBBC Report BI-81-17/063.4.3470, Delft University of Technology, Netherlands

Wardenier, J. and Stark, J.W.B. 1978. The Static Strength of Welded Lattice Girder Joints in Structural Hollow Sections: Parts 1-10. CIDECT Final Report 5Q/78/4, Stevin Laboratory, Delft University of Technology, Netherlands.

Wardenier, J. and De Koning, C.H.M. 1976. Rig Comparison Tests. CIDECT Report No. 76-24(5S). Stevin Laboratory. Delft University of Technology, Netherlands.

Yeomans, N.F. 1977. Fatique Strength of SHS Welded Joints - Isolated Static RHS Joints Tests (CIDECT Programme 7A). Summary of Results for CIDECT Fatigue Group. Report CE 75/32, British Steel Corporation, Tubes Division, January.

Zienkiewicz, O.C. 1977. The Finite Element Method. 3rd Edition. McGraw Hill, New York.

Zycinski, J., Czechowski, A. and Brodka, J., 1982. Investigation into the Static Strength of Welded K-Type Joints in Rectangular Hollow Sections. Metal Structures Research and Design Centre "Mostostal" Report, Warsaw, Poland.

APPENDIX A SHAPE FUNCTIONS FOR 9 NODE SHELL ELEMENT

$N_1 = \xi\eta/4\ (1-\xi)(1-\eta)$

$N_2 = -\xi\eta/4\ (1+\xi)(1-\eta)$

$N_3 = \xi\eta/4\ (1+\xi)(1+\eta)$

$N_4 = -\xi\eta/4\ (1-\xi)(1+\eta)$

$N_5 = -\eta/2\ (1-\xi^2)(1+\eta)$

$N_6 = \xi/2\ (1-\eta^2)(1-\xi)$

$N_7 = \eta/2\ (1-\xi^2)(1+\eta)$

$N_8 = -\xi/2\ (1-\eta^2)(1-\xi)$

$N_9 = (1-\eta^2)(1-\xi^2)$

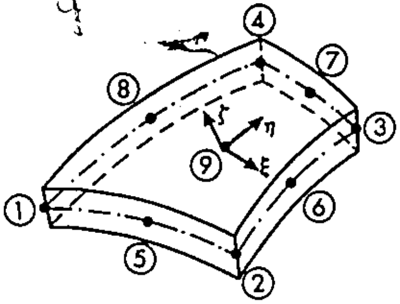

APPENDIX B ALGORITHM LEADING TO FORMATION OF THE ORTHOGONAL BASIS $[v_{1i}\ v_{2i}\ v_{3i}]$

The local Cartesian axes x′, y′, z′ are defined relative to the curvilinear coordinates for the element. Local axis z′ is normal to surface $\zeta = 0$. Vector $\mathbf{v}_3$ along this axis is defined in the following way:

$$\mathbf{v}_3 = (X,_\xi \times X,_\eta)/|X,_\xi \times X,_\eta|$$

where:

$$X,_n = \left[\frac{\partial X}{\partial \xi} \quad \frac{\partial Y}{\partial \xi} \quad \frac{\partial Z}{\partial \xi} \right] \ , \quad X,_\eta = \left[\frac{\partial X}{\partial \eta} \quad \frac{\partial Y}{\partial \eta} \quad \frac{\partial Z}{\partial \eta} \right]$$

It is assumed that x′ concides with ξ axis. Hence

$$\mathbf{v}_1 = X,_\xi \ / \ |X,_\xi|$$

$\mathbf{v}_2$ can be obtained as the following cross product:

$$\mathbf{v}_2 = \mathbf{v}_3 \times \mathbf{v}_1$$

Finally , the transformations θ , ϕ , χ used in Chapter 3 can be expressed by the following:

$$\theta = [\mathbf{v}_1\ \mathbf{v}_2\ \mathbf{v}_3]$$

$$\phi = [-\mathbf{v}_2\ \mathbf{v}_1]$$

$$\chi = [\mathbf{v}_1\ \mathbf{v}_2]$$

APPENDIX C TRANSFORMATION MATRICES

The transformations θ , Φ used in Chapter 3 are expressed by the following:

$$\theta = [v_1 \; v_2 \; v_3]$$

$\Phi = \phi \, \chi^T$, where $\phi = [-v_2 \; v_1]$ and $\chi = [v_1 \; v_2]$

After some algebraic manipulations Φ can be expressed by :

$$\Phi = \begin{bmatrix} 0 & v_{33} & -v_{23} \\ -v_{33} & 0 & v_{13} \\ v_{23} & -v_{13} & 0 \end{bmatrix}$$

where

$$v_1 = \begin{bmatrix} v_{11} \\ v_{12} \\ v_{13} \end{bmatrix} , \quad v_2 = \begin{bmatrix} v_{21} \\ v_{22} \\ v_{23} \end{bmatrix} \quad v_3 = \begin{bmatrix} v_{31} \\ v_{32} \\ v_{33} \end{bmatrix}$$

APPENDIX D EXPERIMENTAL RESULTS FOR SPECIMENS 17 AND 19

In Test 17 the rosettes were positioned in the toe area. The main objective was to check the direction of the major principal axis in the corner positions of the toe. The strain levels in all three legs of rosettes 1 (gauges 1,2,3) and 3 (gauges 7,8,9) are shown in Figures D1-D2. It is apparent that no substantial difference exists among the strain levels on each graph. All three directions: parallel to the longitudinal branch axis, parallel to the weldment, and bisecting the angle of consideration, show comparable strain levels in both rosettes. This is confirmed by the load vs. the angle of inclination graph for the major principal axis as illustrated in Figure D4. At a relatively low load level both rosettes indicate that the major principal axis of strain is inclined to the longitudinal branch member axis at an angle of about 45°. In addition to the load vs. strain graphs in the toe area, a set of strain measurements at the heel is presented in Figure D5. The same tendency as for Specimen 18 (Section 4.4, Figures 4.15-4.19), where only the corner positions are effective in the load resistance at the heel, is visible here. However, because the failure load for Specimen 17 was higher than for Specimen 18 (presented in Chapter 4), it was possible to collect the strain measurements beyond the 1000 kN mark. In that region the middle gauge indicates a change in the slope of the load vs. strain curve with the strain values near the limit becoming close to zero.

The findings reported for Test 18 (Section 4.4, Figures 4.15-4.19) have also been confirmed by strain measurements on Specimen 19 (Figure

D6), which carried strain gauge rosettes on both branch sidewalls. The object was to check for symmetry in the distribution of strains on both sides of the branch. In addition, five strain gauges were positioned at the branch heel (instead of the previous three), to monitor the effectiveness of this area with better accuracy. Specimen 19 had relatively small weld sizes and failed at a load level of 602 kN. Nevertheless, it was possible to document the essential trends in the strain distribution. The load vs. strain graphs for Specimen 19 are included in Appendix D (Figures D7-D9). First, the strains at the heel and toe areas are presented (see Figures D7 and D8). It is evident that, at the heel, only the corners participate in load resistance. For the toe, no substantial difference among the strain values is observed. Next, the load vs. strain graphs for the major and minor principal axes on both sides of the branch are shown in Figures D9, D10 and D12 and D13. It is worth pointing out that the load vs. minor principal strain curves for rosettes positioned in the corners suddenly change their slopes at the load level of about 500 kN, indicating the same trend as in Test 18. Also included in Appendix D are graphs of the load vs. the angle of inclination for the major principal axis of strain, shown in Figures D11 and D14. Near the failure, the middle rosette on a sidewall reveals that the principal axis of strain being parallel to the branch axis. The rosettes positioned in the corners indicate that the direction of the same axis bisects the angle of consideration, as illustrated previously for Test 18 in Figure 4.33 (Section 4.4).

TEST 17

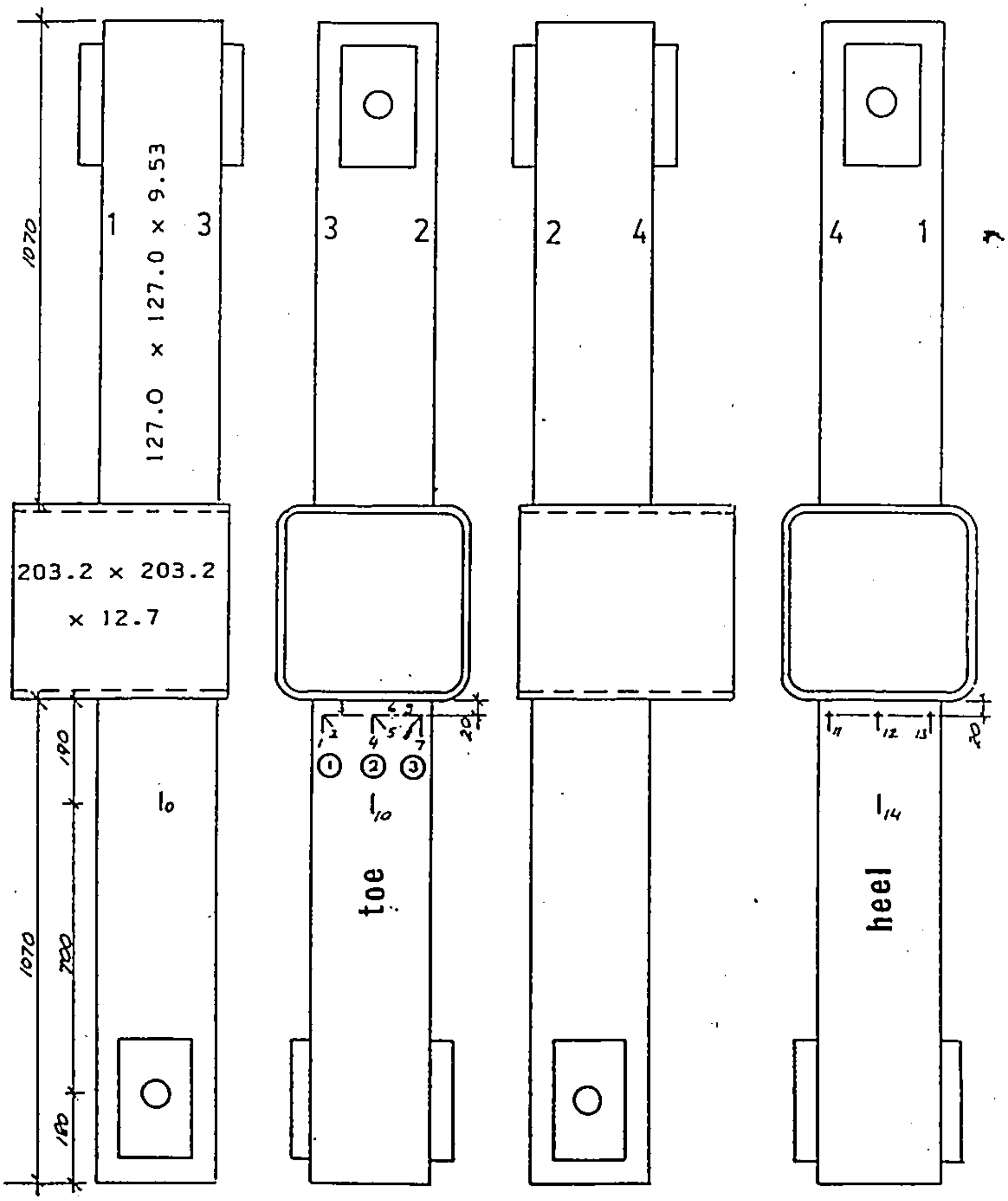

FIGURE D1 Specimen 17

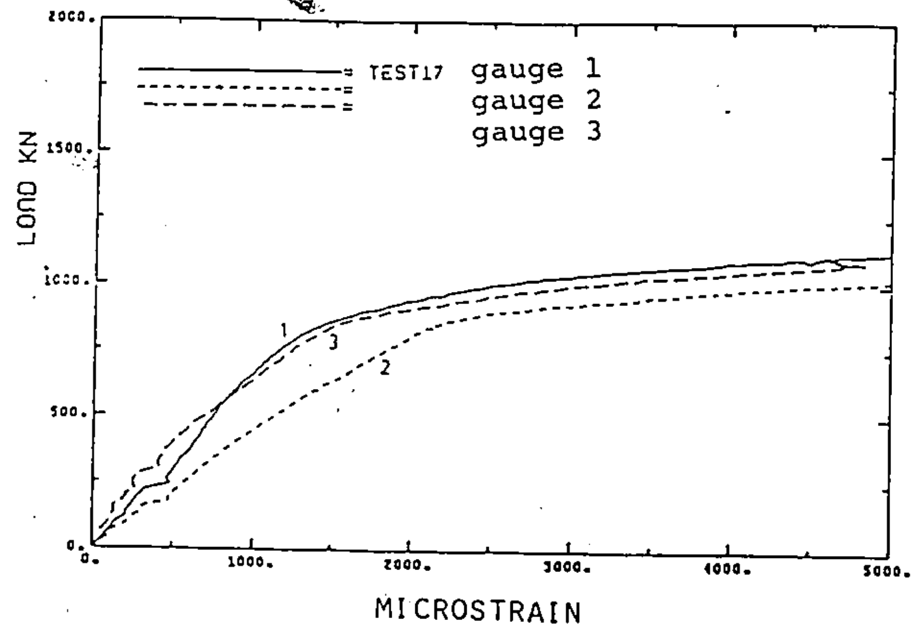

FIGURE D2 Load-Strain Graph for Gauges 1,2,3 of Specimen 17

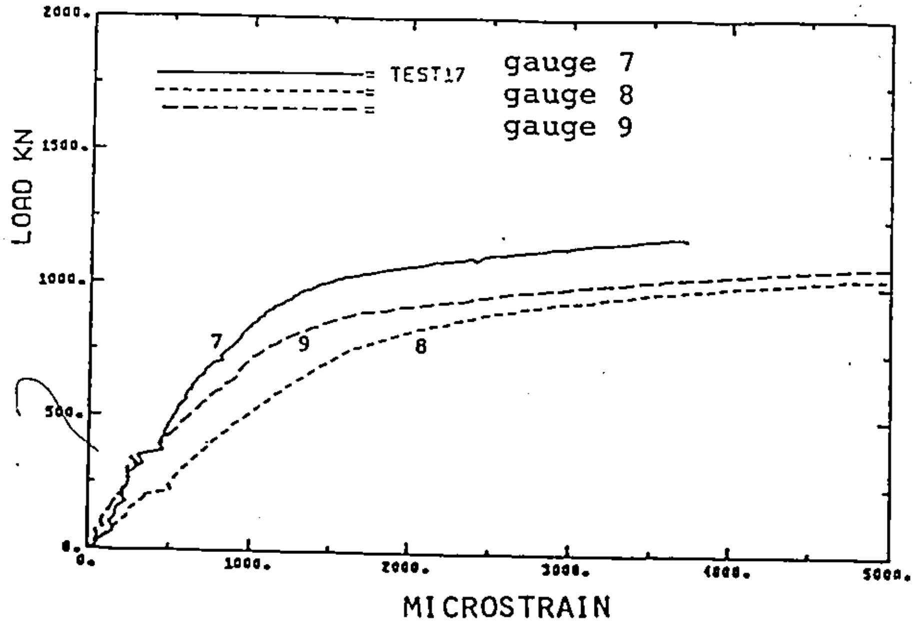

FIGURE D3 Load-Strain Graph for Gauges 7,8,9 of Specimen 17

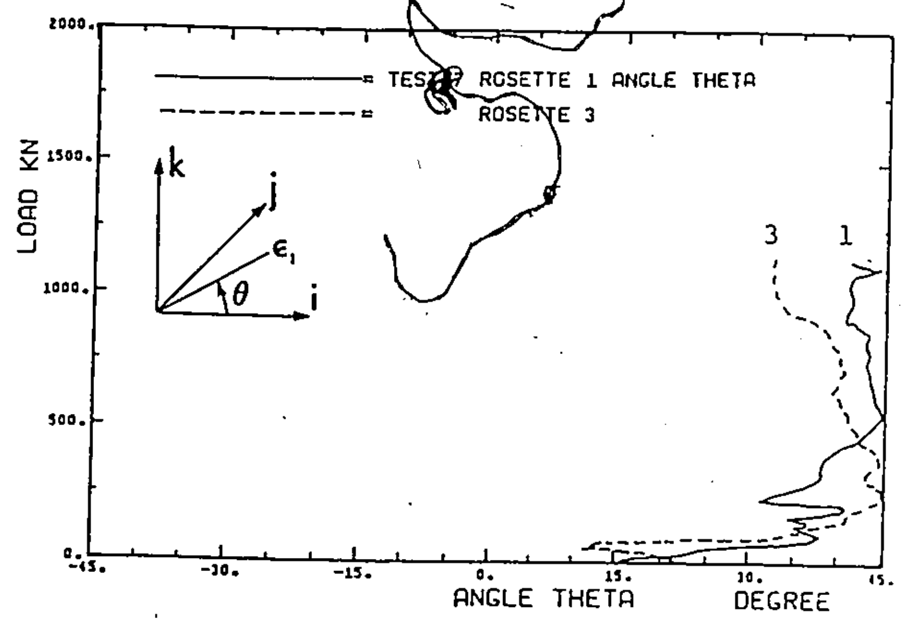

FIGURE D4 Load-Angle of Inclination Graph for Major Principal Direction in Rosettes 4,5,6

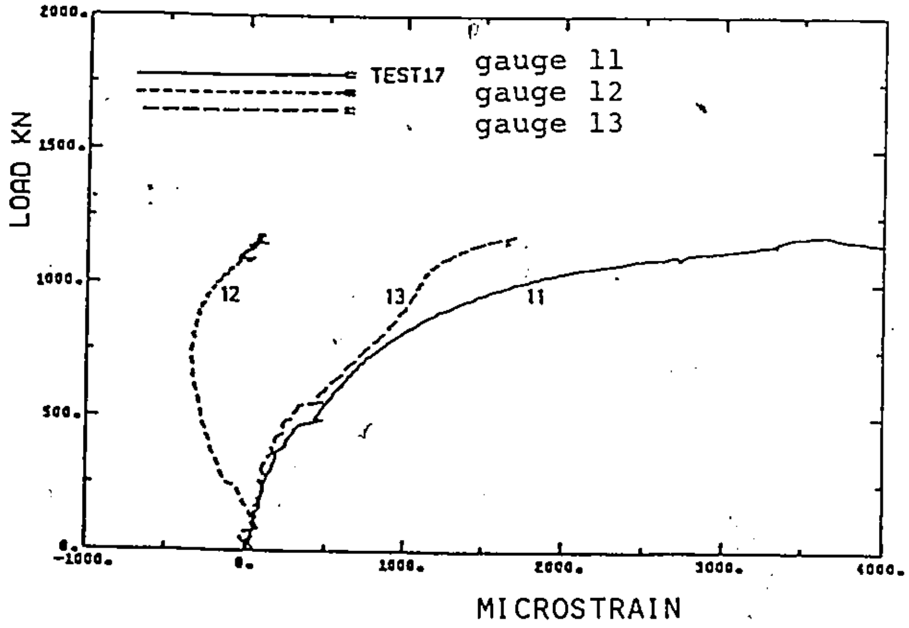

FIGURE D5 Load-Strain Graph for Gauges 11,12,13 of Specimen 17

TEST 19

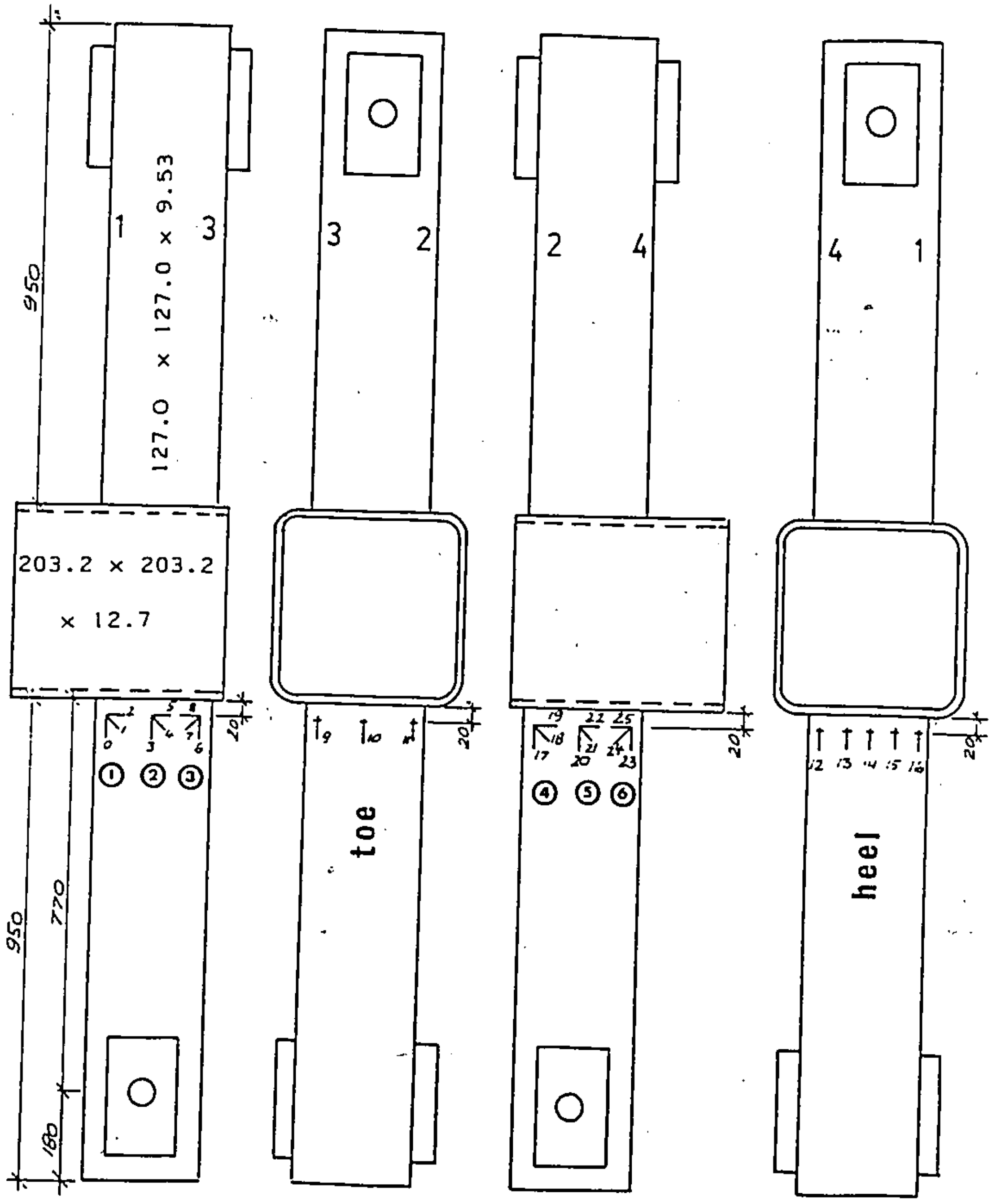

FIGURE D6 Specimen 19

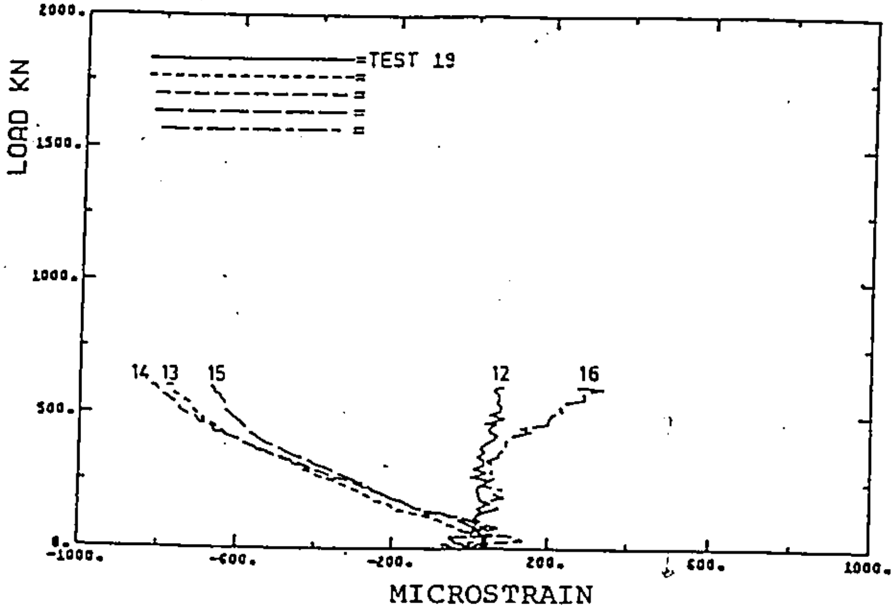

FIGURE D7 Load-Strain Graph at Heel of Specimen 19

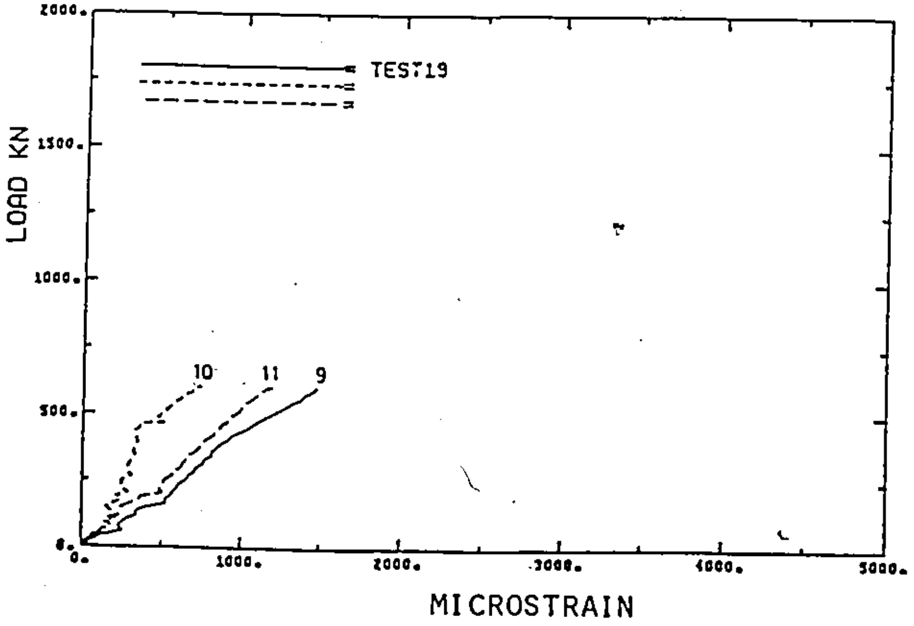

FIGURE D8 Load-Strain Graph at Toe of Specimen 19

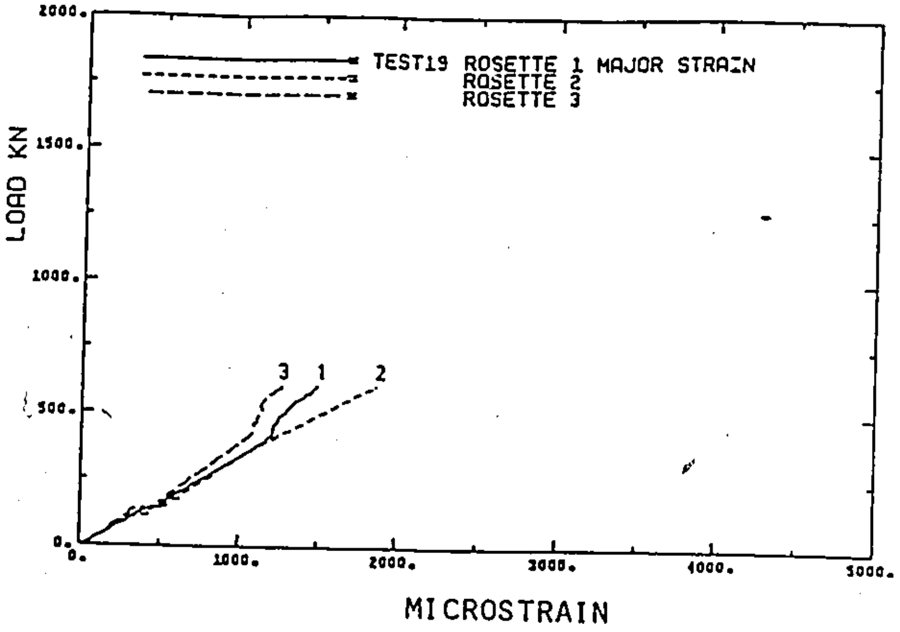

FIGURE D9 Load-Major Principal Strain Graph for Rosettes 1,2,3 in Test 19

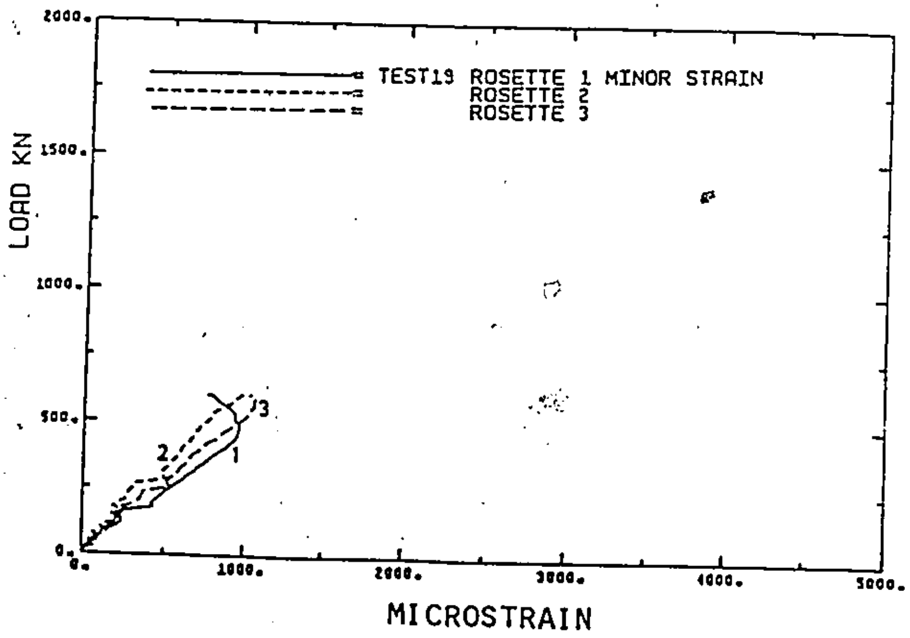

FIGURE D10 Load-Minor Principal Strain Graph for Rosettes 1,2,3 in Test 19

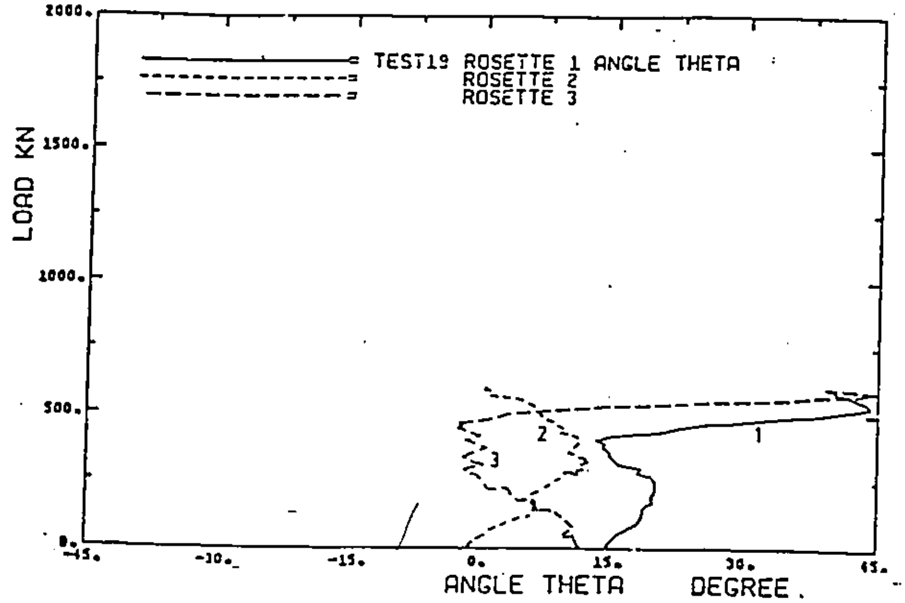

FIGURE D11 Load-Angle of Inclination Graph for Major Principal Direction for Rosettes 1,2,3

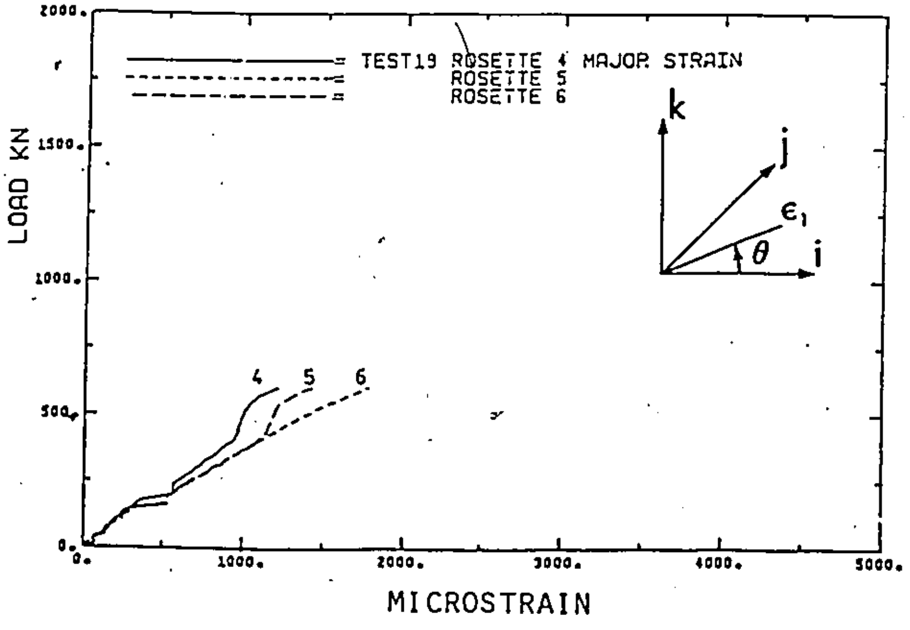

FIGURE D12 Load-Major Principal Strain Graph for Rosettes 4,5,6 in Test 19

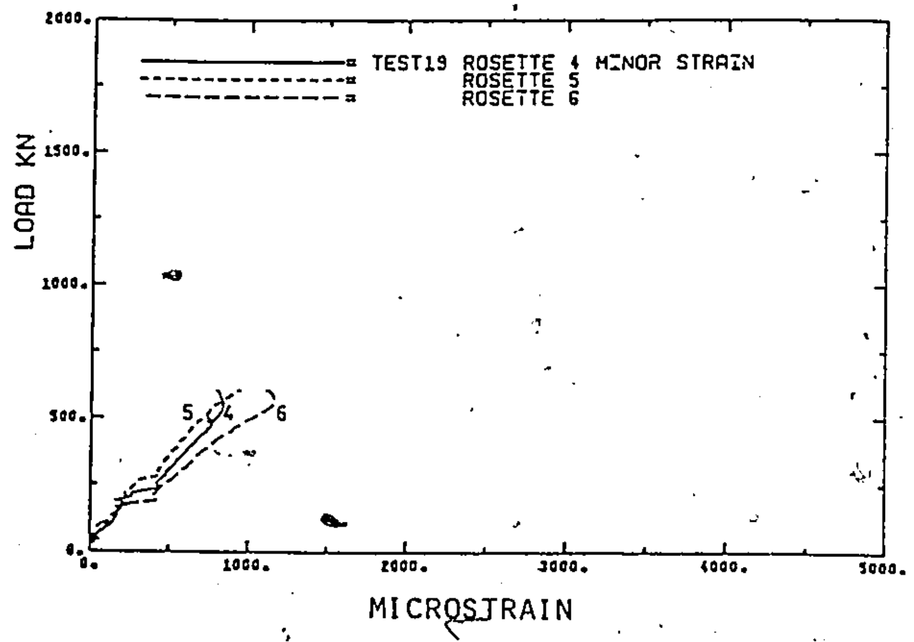

FIGURE D13 Load-Minor Principal Strain Graph for Rosettes 4,5,6 in Test 19

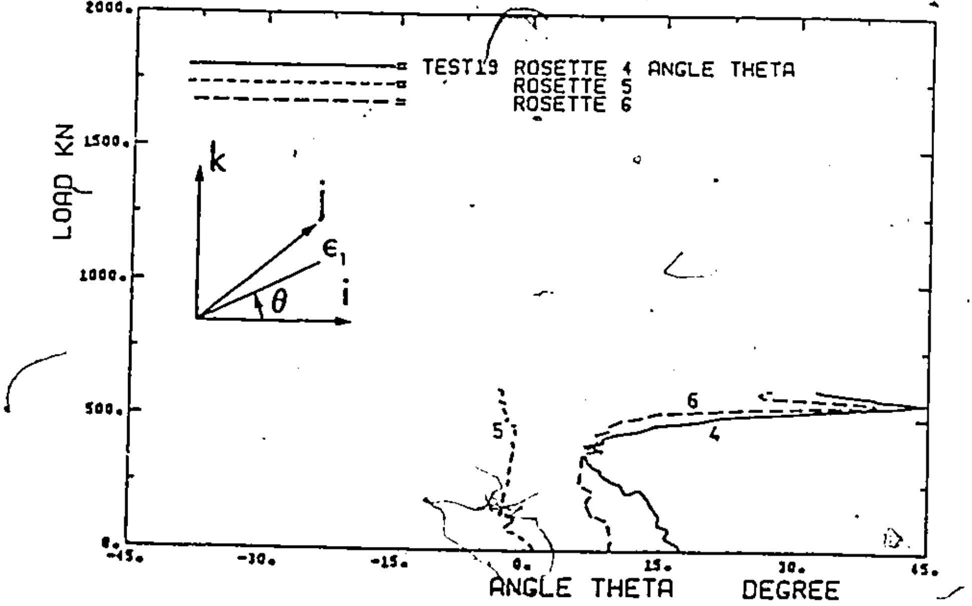

FIGURE D14 Load-Angle of Inclination Graph for Major Principal Direction for Rosettes 4,5,6

APPENDIX E RESULTS OF A PARAMETRIC STUDY

STRESSES FOR STAGE 4 CASE 1

$\beta = 0.63$ $\theta = 30°$

$g = 0.4\, b_o$ $b_o/t_o = 16$

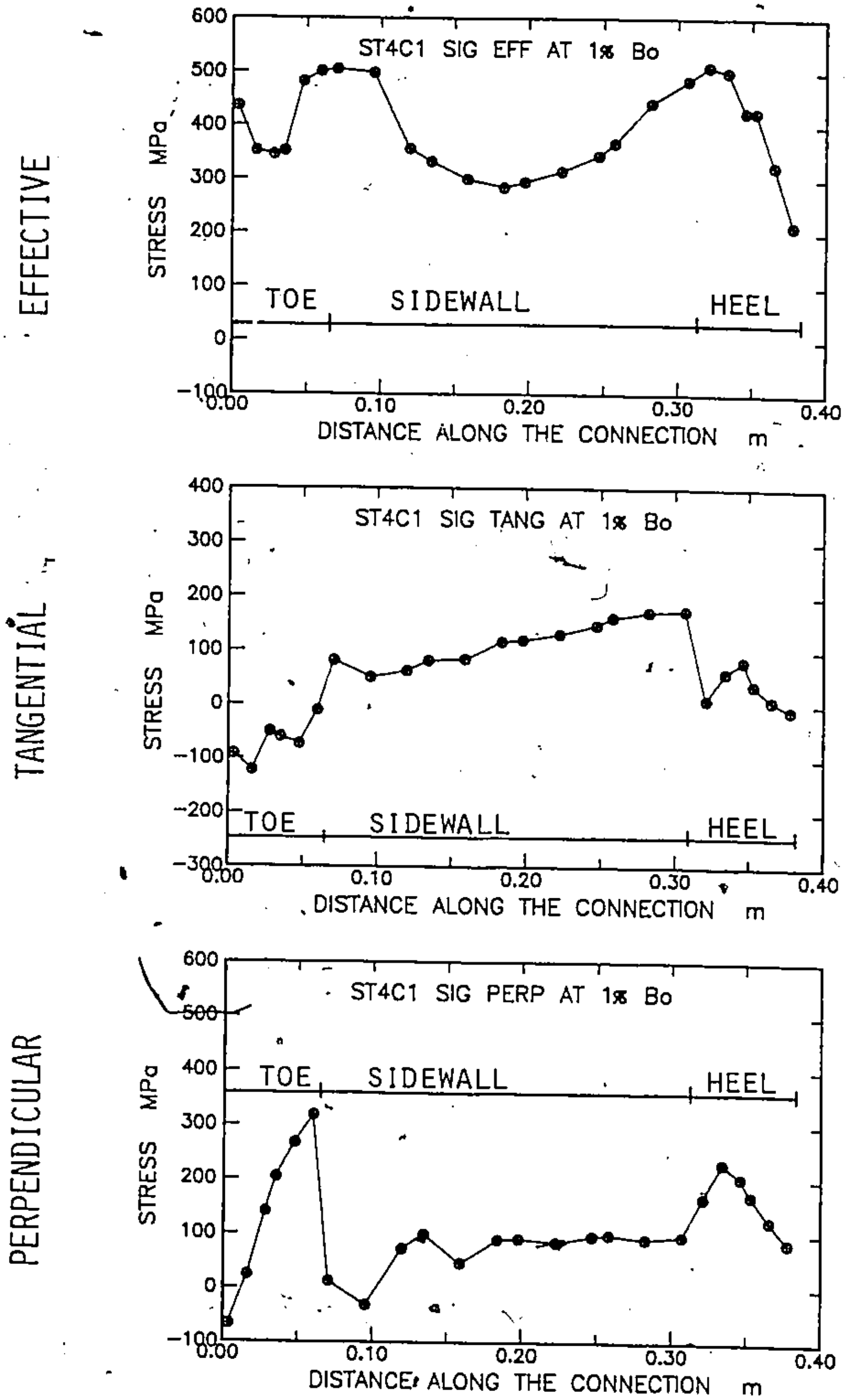

FIGURE E1 Stresses for Stage 4 Case 1

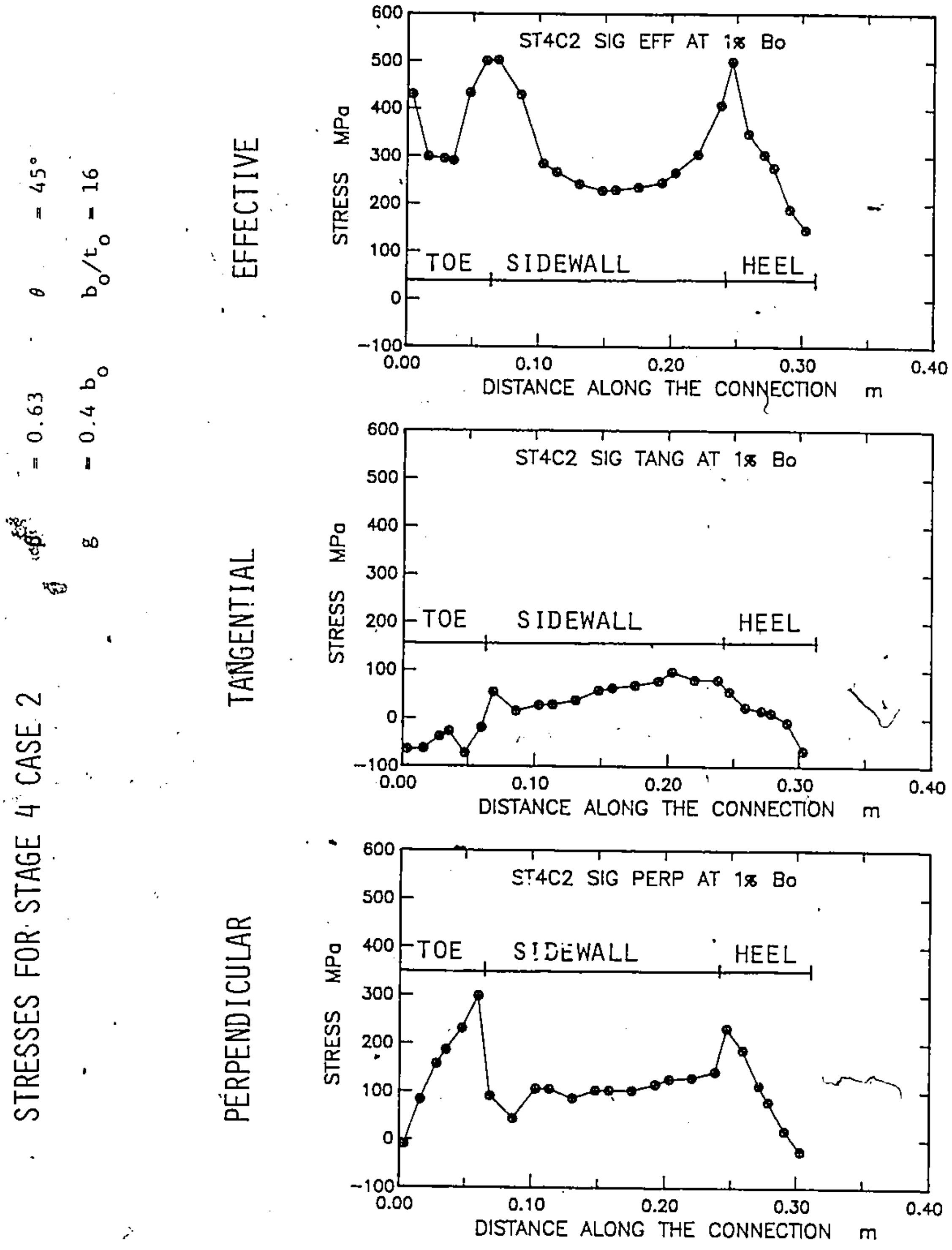

FIGURE E2 Stresses for Stage 4 Case 2

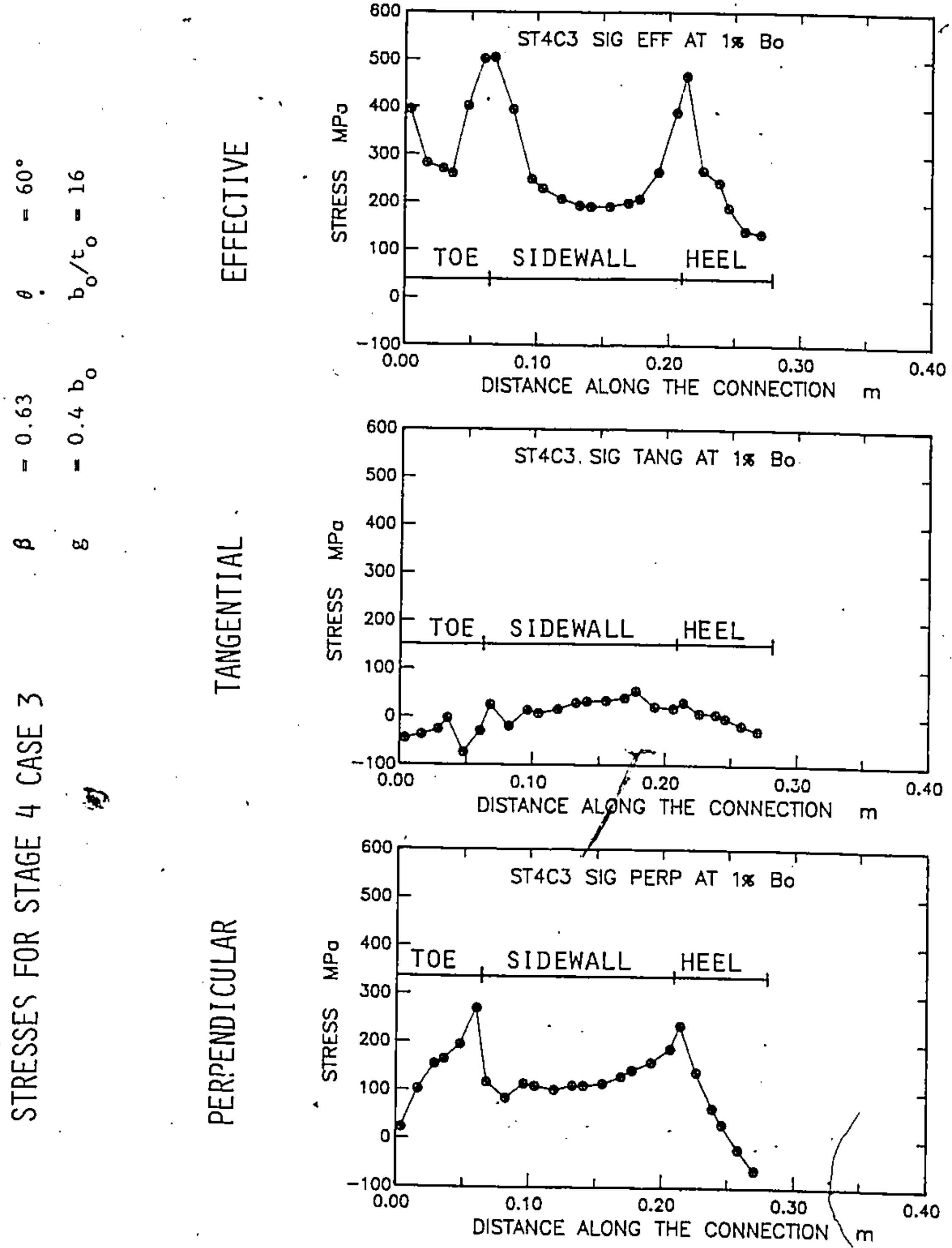

FIGURE E3 Stresses for Stage 4 Case 3

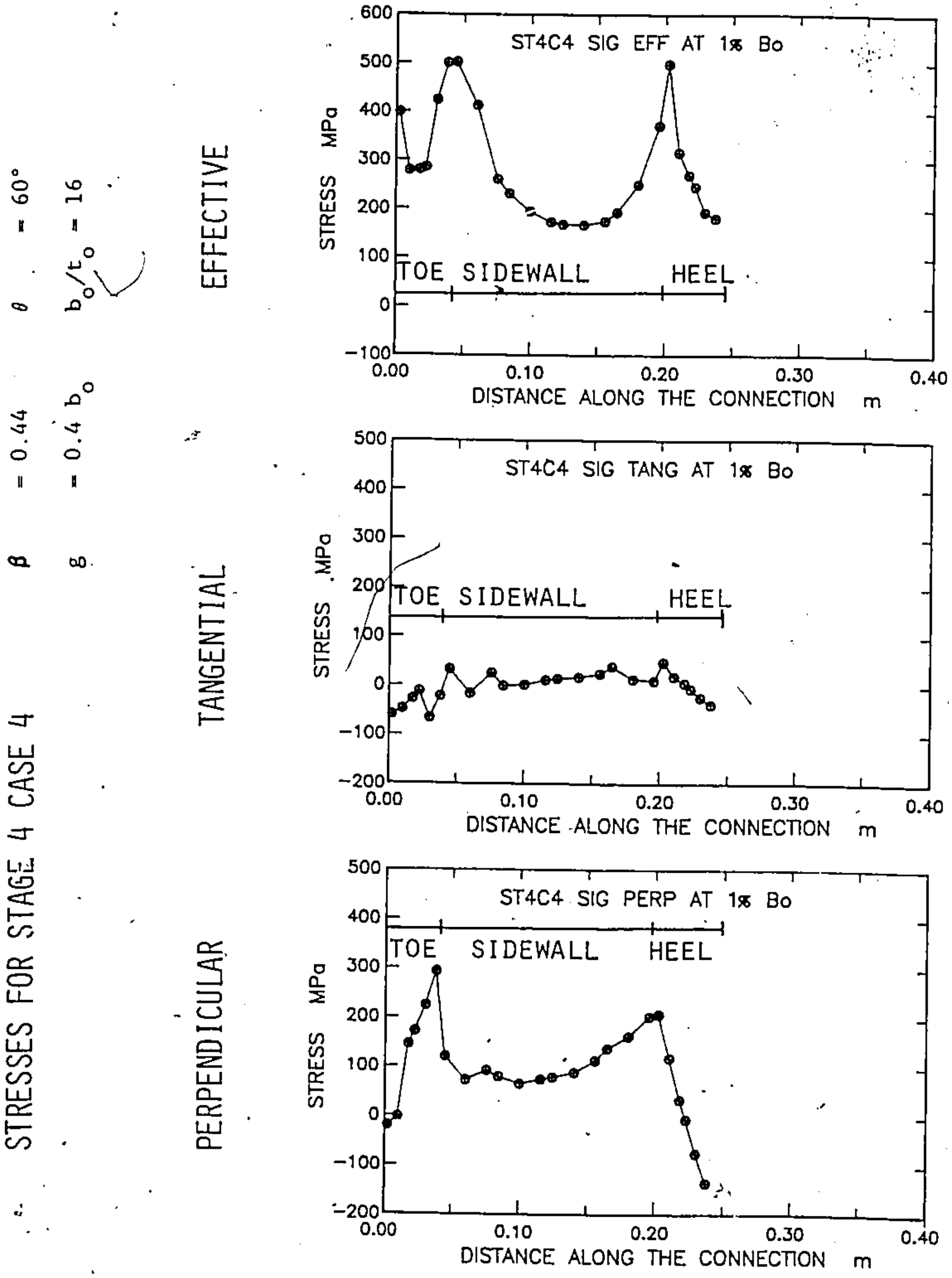

FIGURE E4 Stresses for Stage 4 Case 4

STRESSES FOR STAGE 4 CASE 5

$\beta = 0.88$ $\theta = 60°$

$g = 0.4\ b_o$ $b_o/t_o = 16$

EFFECTIVE

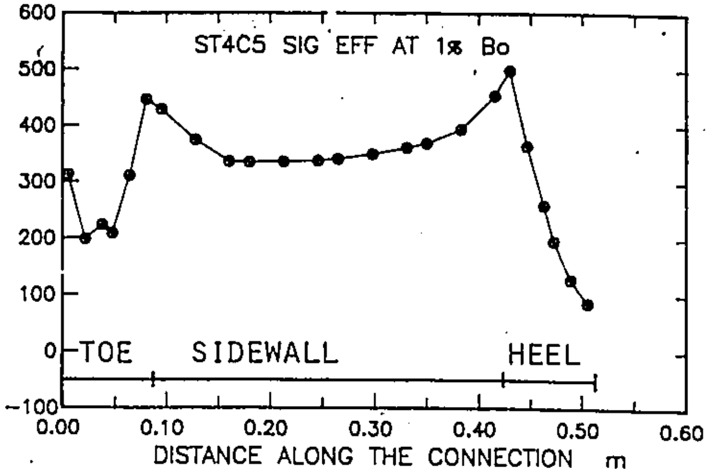

TANGENTIAL

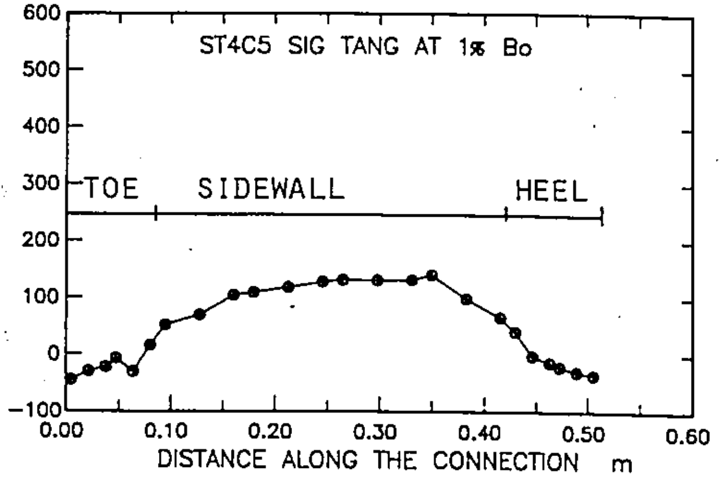

PERPENDICULAR

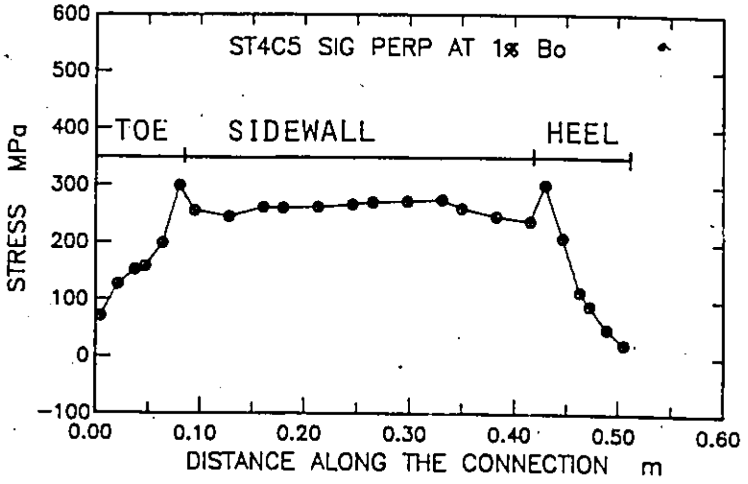

FIGURE E5 Stresses for Stage 4 Case 5

STRESSES FOR STAGE 4 CASE 6

$\beta = 0.63$ $\theta = 60°$

$g = 0.2\ b_o$ $b_o/t_o = 16$

EFFECTIVE

TANGENTIAL

PERPENDICULAR

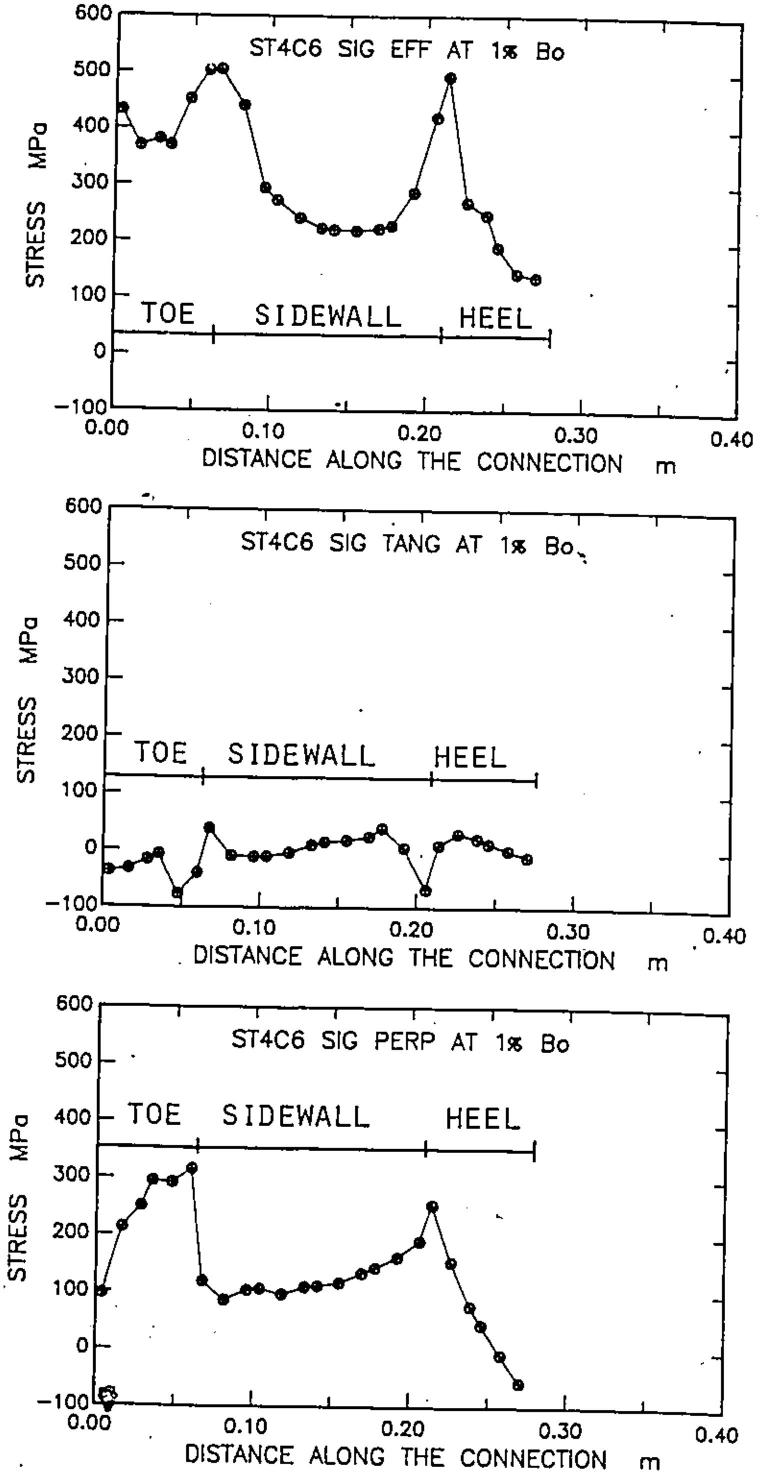

FIGURE E6 Stresses for Stage 4 Case 6

STRESSES FOR STAGE 4 CASE 7

$\beta = 0.63$ $\theta = 60°$

$g = 0.6\, b_o$ $b_o/t_0 = 16$

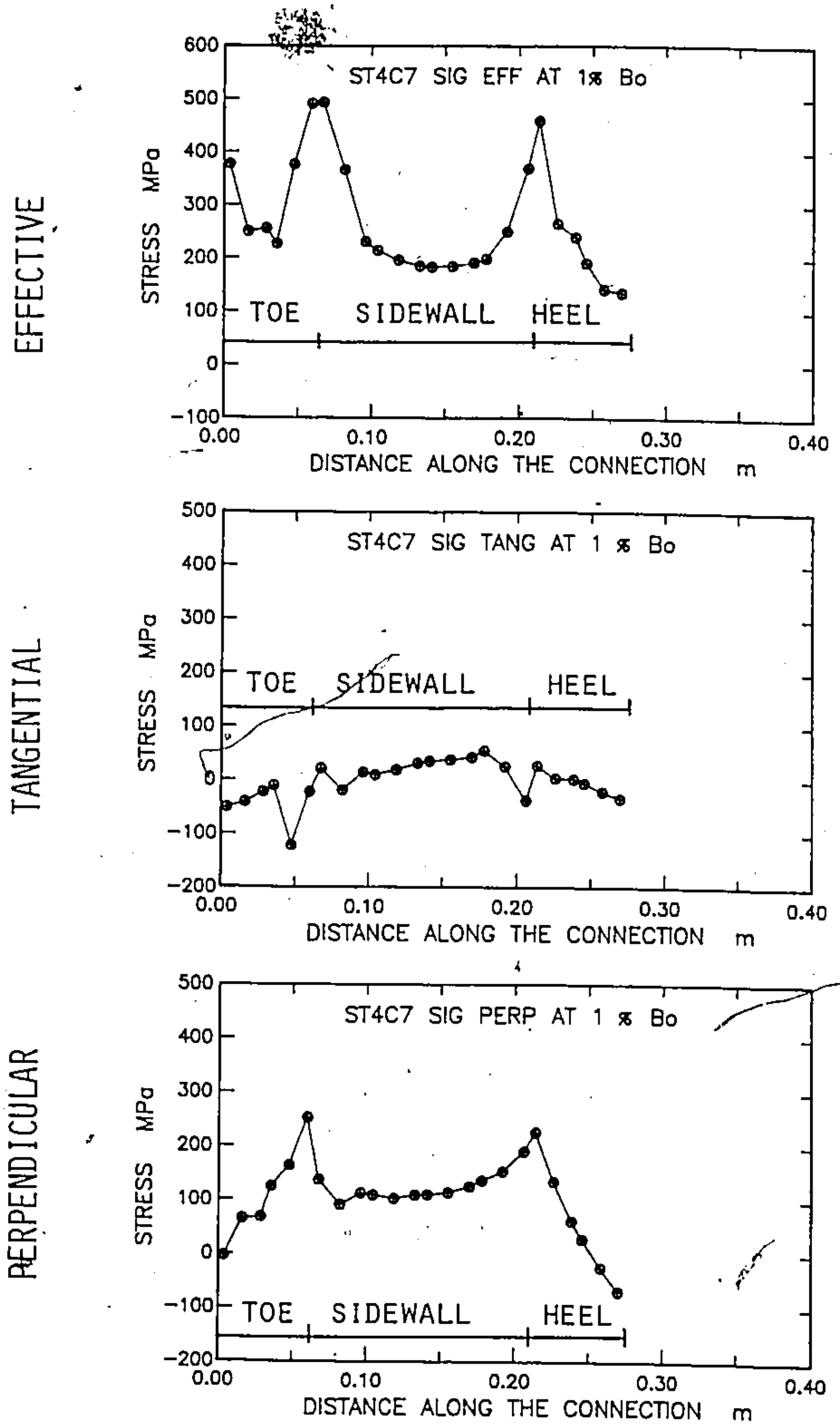

FIGURE E7 Stresses for Stage 4 Case 7

STRESSES FOR STAGE 4 CASE 8

$\beta = 0.63 \qquad \theta = 60°$

$g = 0.4\ b_o \qquad b_o/t_o = 21$

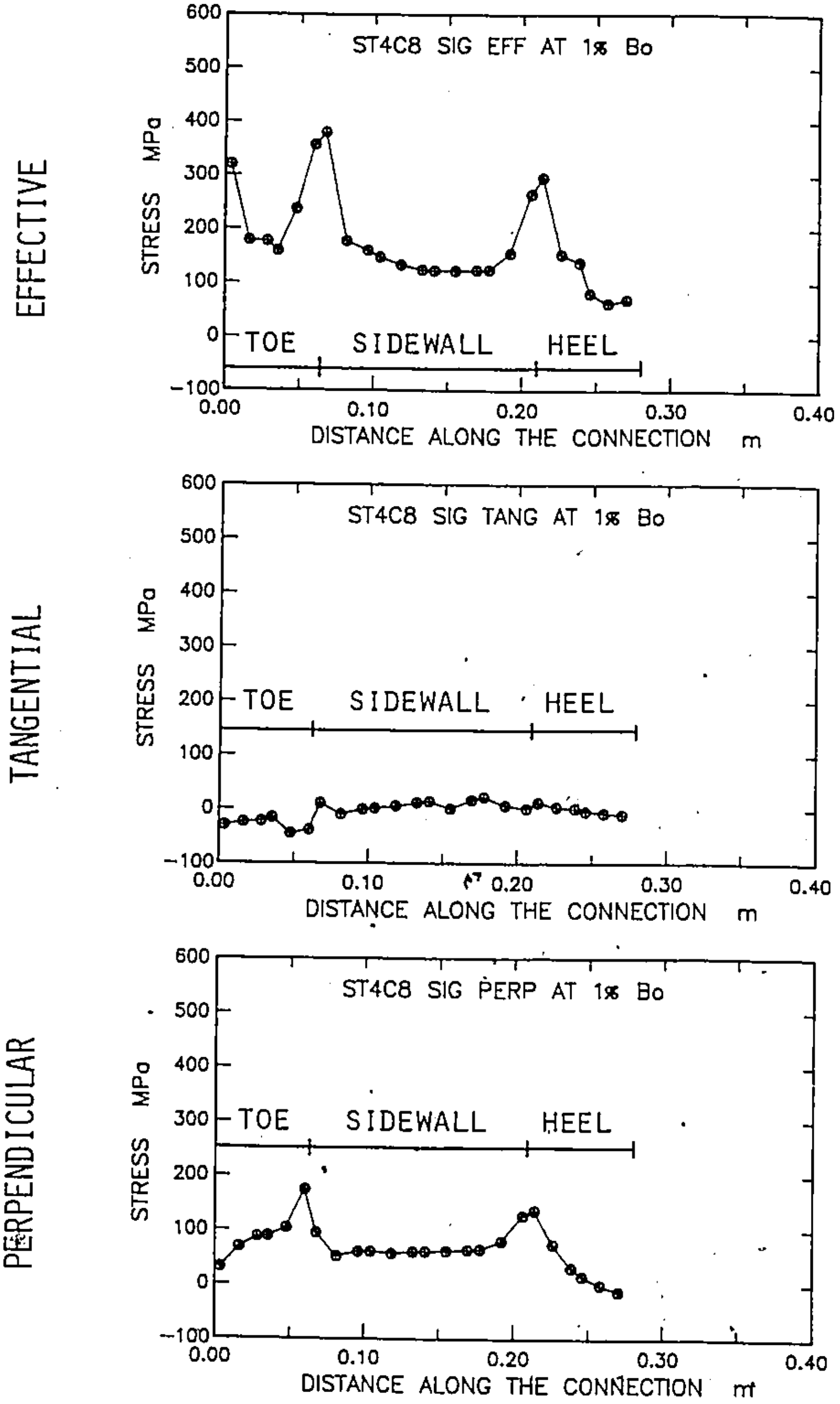

FIGURE E8 Stresses for Stage 4 Case 8

STRESSES FOR STAGE 4 CASE 9

$\beta = 0.63$ $\theta = 60°$

$g = 0.4\ b_o$ $b_o/t_o = 32$

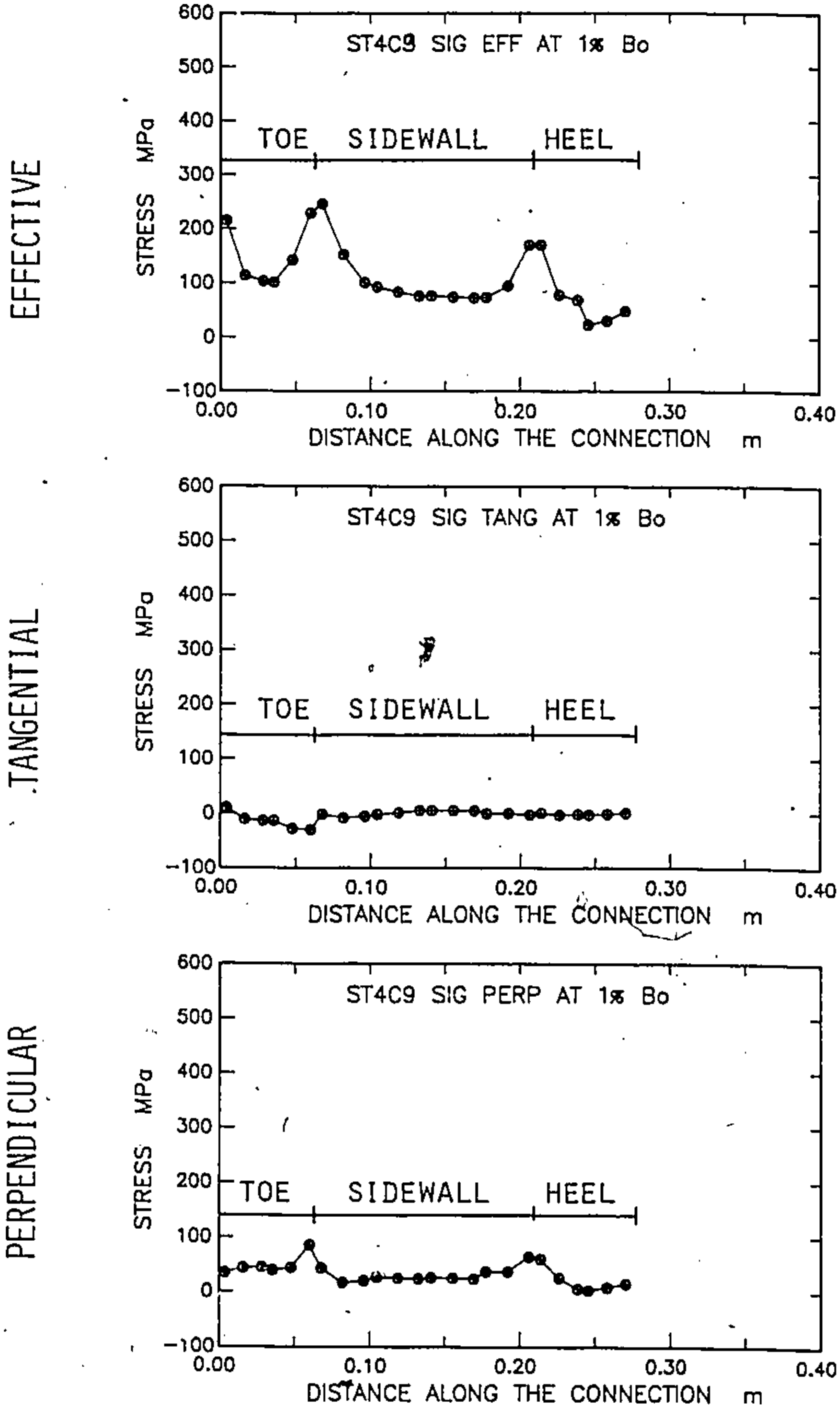

FIGURE E9 Stresses for Stage 4 Case 9

STRESSES FOR STAGE 4 CASE 10

β = 0.44 θ = 45°

g = 0.4 b_o b_o/t_o = 16

EFFECTIVE

TANGENTIAL

PERPENDICULAR

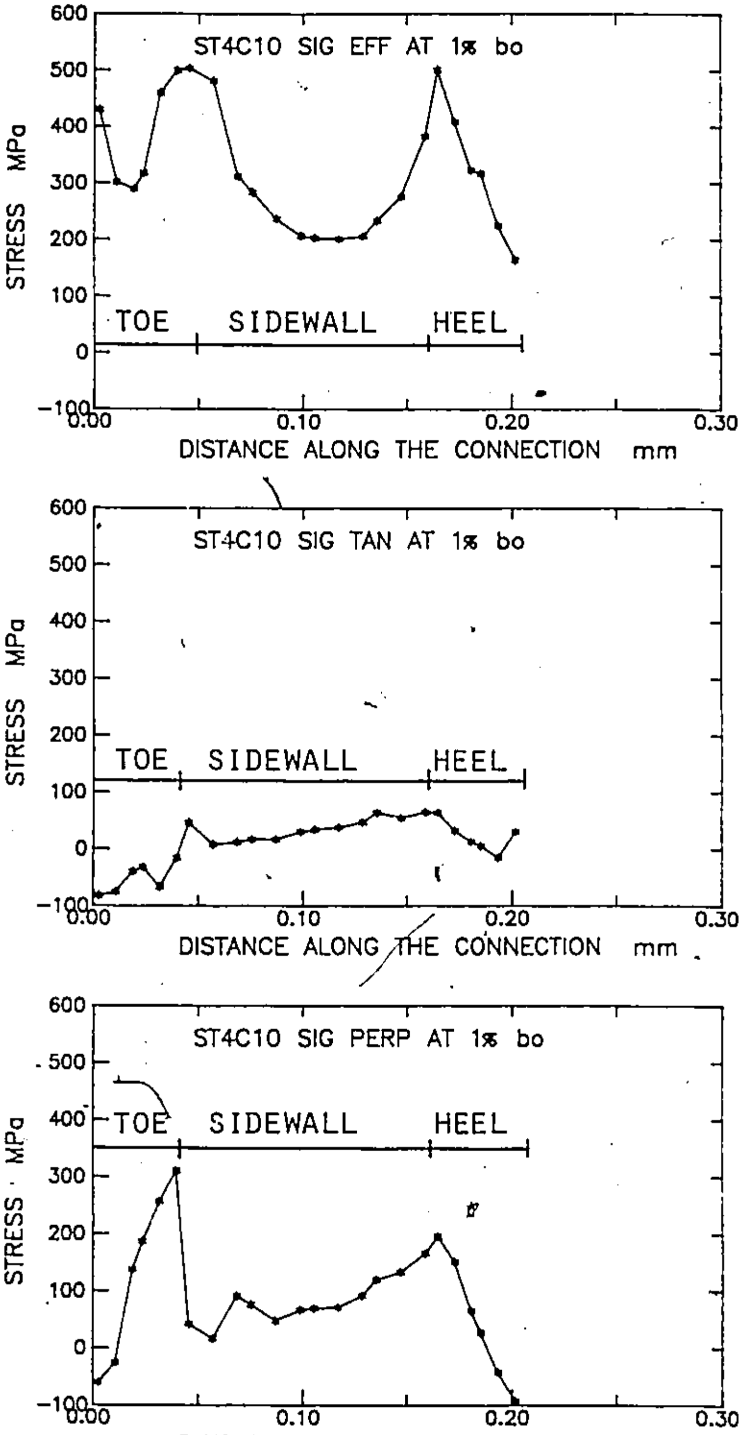

FIGURE E10 Stresses for Stage 4 Case 10

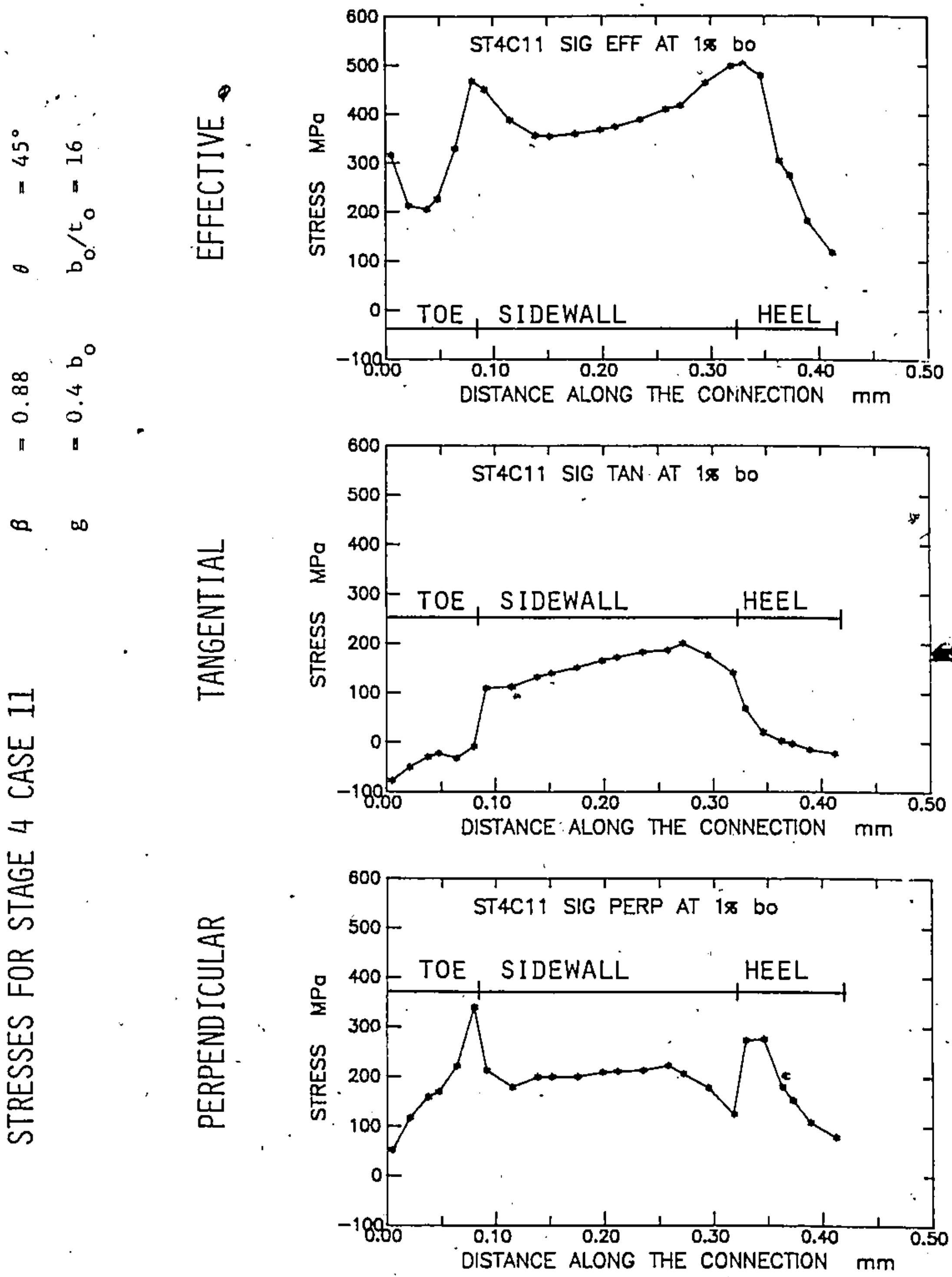

FIGURE E11 Stresses for Stage 4 Case 11

STRESSES FOR STAGE 4 CASE 12

β = 0.44 θ = 30°

g = 0.4 b_o b_o/t_o = 16

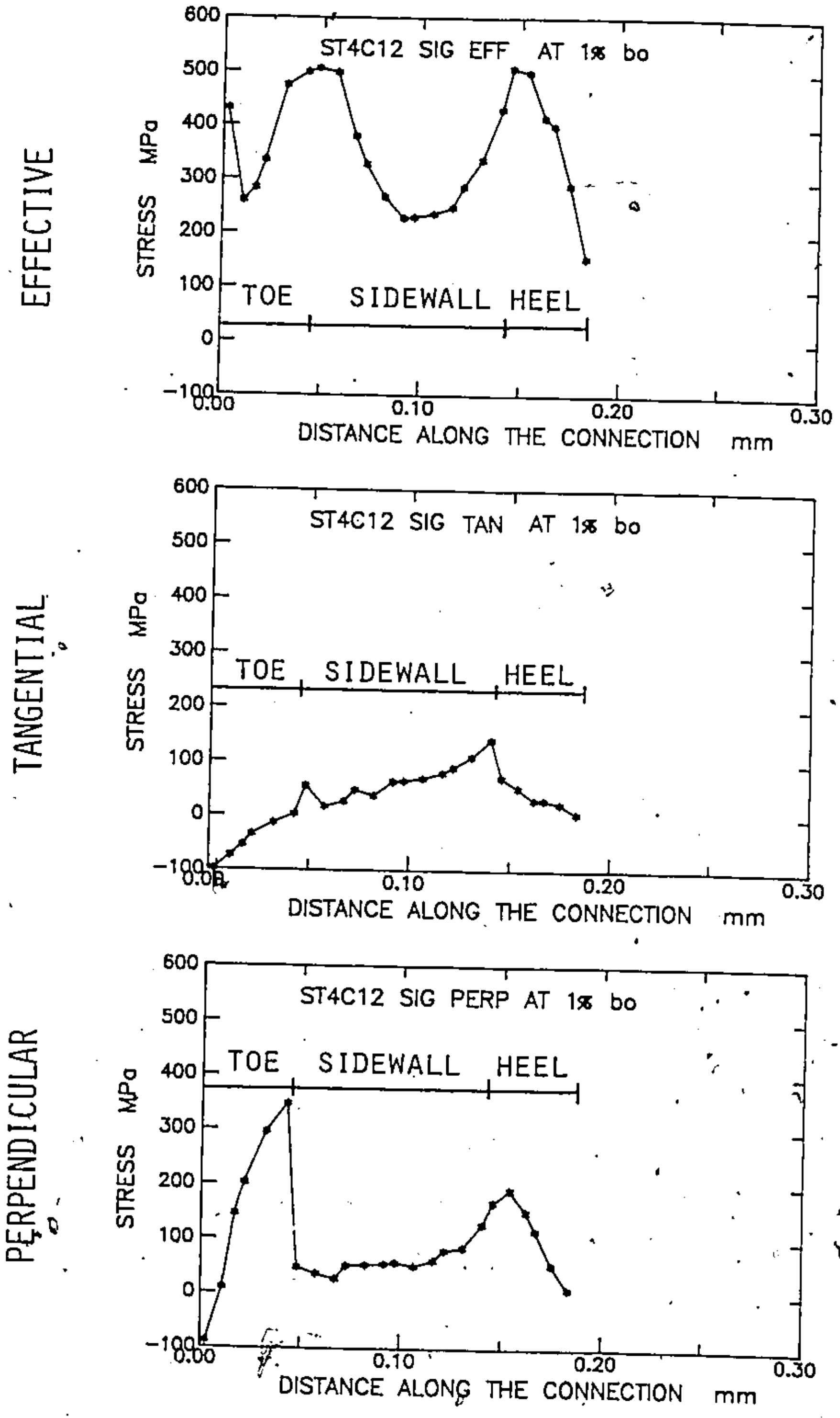

FIGURE E12 Stresses for Stage 4 Case 12

STRESSES FOR STAGE 4 CASE 13

β = 0.88 θ = 30°

g = 0.4 b_o b_o/t_o = 16

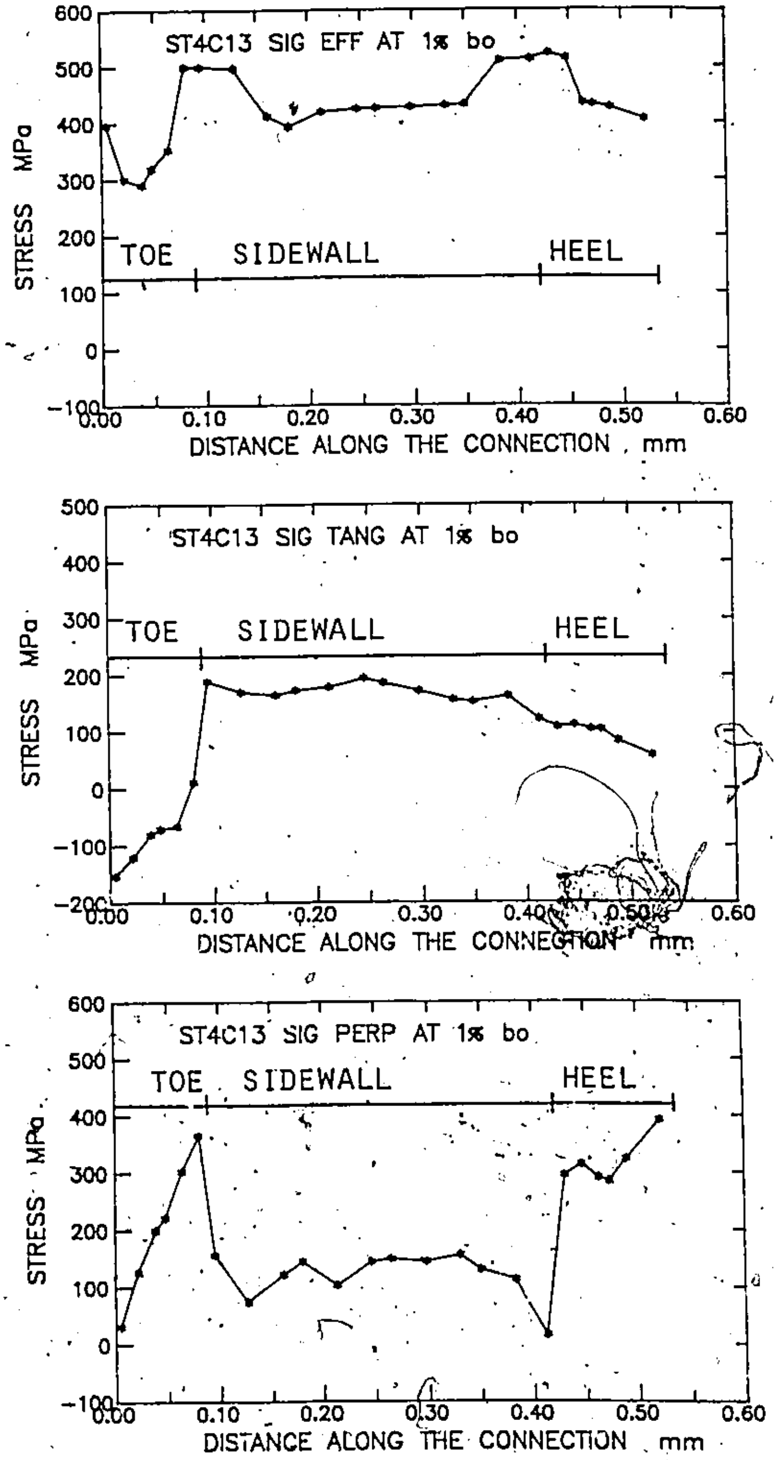

FIGURE E13 Stresses for Stage 4 Case 13